Title
The Design, Synthesis, and Characterization of Open Sites on Metal Clusters

Author
Nigra, Michael Mark

Publication Date
2013

Peer reviewed|Thesis/dissertation

The Design, Synthesis, and Characterization of Open Sites on Metal Clusters

By

Michael Mark Nigra

A dissertation submitted in partial satisfaction of the

requirements for the degree of

Doctor of Philosophy

in

Chemical Engineering

in the

Graduate Division

of the

University of California, Berkeley

Committee in charge:

Professor Alexander Katz, Chair
Professor Enrique Iglesia
Professor Kenneth Raymond

Fall 2013

The Design, Synthesis, and Characterization of Open Sites on Metal Clusters

Abstract

The Design, Synthesis, and Characterization of Open Sites on Metal Clusters

by

Michael Mark Nigra

Doctor of Philosophy in Chemical Engineering

University of California, Berkeley

Professor Alexander Katz, Chair

Coordinatively unsaturated corner and edge atoms have been hypothesized to have the highest activity of sites responsible for many catalytic reactions on a metal surface. Recent studies have validated this hypothesis in varied reaction systems. However, quantification of different types of coordinatively unsaturated sites, and elucidation of their individual catalytic rates has remained a largely unresolved challenge when understanding catalysis on metal surfaces. Yet such structure-function knowledge would be invaluable to the design of more active and selective metal-surface catalysts in the future. I investigated the catalytic contributions of undercoordinated sites such as corner and edge atoms are investigated in a model reaction system using organic ligands bound to the gold nanoparticle surface. The catalyst consisted of 4 nm gold nanoparticles on a metal oxide support, using resazurin to resorufin as a model reaction system. My results demonstrate that in this system, corner atom sites are the most undercoordinated sites, and are over an order of magnitude more active when compared to undercoordinated edge atom sites, while terrace sites remain catalytically inactive for the reduction reaction of resazurin to resorufin.

Catalytic activity has been also demonstrated for calixarene-bound gold nanoparticles using the reduction of 4-nitrophenol. With the 4-nitrophenol reduction reaction, a comparative study was undertaken to compare calixarene phosphine and calixarene thiol bound 4 nm gold particles. The results of the study suggested that a leached site was responsible for catalysis and not sites on the original gold nanoparticles. Future experiments with calixarene bound gold clusters could investigate ligand effects in reactions where the active site is not a leached or aggregated gold species, possibly in oxidation reactions, where electron-rich gold is hypothesized to be a good catalyst.

The results that emphasize the enhanced catalytic activity of undercoordinated sites led me to synthesize small gold clusters consisting of a high fraction of coordinatively unsaturated open sites. This was enabled through an approach that utilized bulky calix[4]arene ligands that are bound to a gold core. Since the size of the calix[4]arene ligand is commensurate with the size of the gold cluster core, the calix[4]arene ligand does not pack closely together on the gold cluster surface. This in turn results in areas of accessible gold atom sites between ligands. Additionally, these calix[4]arene ligands prevent cluster aggregation and electronically tune the gold core in a manner conceptually similar to enzymes affecting reactivity through organic side-

chains acting as ligands. I quantified the number of open sites that result from this packing problem on the gold cluster surface, using fluorescence probe chemisorption experiments. The results of these chemisorption measurements support the mechanical model of accessibility whereby accessibility is not dependent on the identity of the functional group, whether it be calixarene phosphines or N-heterocyclic carbenes, bound to the gold surface, but rather to the relative radii of curvature of bound ligands and the gold cluster core.

Additional materials characterization was completed with transmission electron microscopy in both bright-field imaging of zeolites, in MCM-22 and delaminated ITQ-2 and UCB-1 materials, and in dark field imaging of glucan coatings on oxide particles. These materials could prove to be interesting materials as to use as supports for the calixarene-bound metal clusters described above or for other metal clusters.

.

To my family, friends, and all whom I love and hold dear.

Table of contents

Acknowledgements

There are many, many people that I would like to thank who have helped me along the way to finishing this dissertation. First, I would like to thank my parents, Mark and Kathleen. Put simply, without them, I wouldn't be here. Thank you to them for their constant love and encouragement. I would also like to thank my brother, Alex, who has been a source of support and fun. Thank you, Dad, Mom, and Alex, and the rest of my extended family.

I would like to express my appreciation for my advisor, Professor Alexander Katz and to other members of the Katz group for their mentorship and assistance. Professor Katz has been an excellent advisor and has helped me to grow to become a much better scientist. Specifically, amongst Katz group members, I would like to thank the researchers with whom I have worked the most: Dr. Andrew Solovyov, Dr. Alexander Okrut, Dr. Namal de Silva, Dr. Isao Ogino, and Dr. Jeong-Myeong Ha. Thank you, Professor Katz and the Katz group members.

An important person in my career has been Mr. John Varine. Mr. Varine was my high school chemistry teacher, and I give him credit for fostering a love of chemistry in me starting in tenth grade. He was also instrumental in teaching me how to use Microsoft Excel for many spreadsheet calculations. I use every day in the laboratory the many skills that I learned from him. Thank you, Mr. Varine

I would also like to thank my friends from the San Francisco Bay Area, particularly ones who have "adopted" me as part of their family. Your care and encouragement for me means so very much to me. A particular heartfelt thank you goes to Tom and Katie Scarry and their young family. They have been exceptionally great friends since shortly after I moved to California and were always willing to have me visit for a few days for mini-retreat at their farm. Thank you, friends, and "adopted" families.

Thank you also to Adriana for your love and support at the end of my dissertation to help me to cross the finish line of my Ph. D. joyfully.

Science isn't without materials costs, and due to the generous grants and fellowships, all of this work was made possible. Thank you, Chevron Corporation and to the National Science Foundation for the financial support that I have received through many sources to fund my research here.

CHAPTER 1:

Identification of binding and reactive sites in metal cluster catalysts: homogeneous-heterogeneous bridges

a collaboration between Michael Nigra and Alexander Katz

1.1 Introduction

The concept of only a minority fraction of catalyst sites on a surface exhibiting most, if not all, of a catalyst's activity for certain reactions has been hypothesized since the early part of the twentieth century, when Sir Hugh Taylor postulated this in 1925. [1] The challenge remained almost a century later to identify which of these sites are the most active, though significant progress has been made in years since. Taylor also postulated that there must be "varying degrees of saturation" present when comparing a metal atom on the surface or even in the gas phase versus interior metal atoms in the bulk. He additionally postulated that these "varying degrees of saturation" can control catalytic activity. Another concept presented by Taylor was that the amount of surface that is active for a particular reaction is reaction-dependent. Taylor's distinguished student, a giant of catalysis on solid surfaces, Michel Boudart, classified heterogeneous metal-catalyzed reactions as being either "structure-sensitive" or "structure-insensitive" later in the 1960's. [2] Structure-sensitive reactions were observed to be heavily influenced by the particle size, as the particle size influences which crystallographic faces are present on the surfaces of metal particles and the number of coordinatively unsaturated atoms as described by Taylor. During this time period, kinetic measurements of catalysis demonstrated that reactions such as ring opening and hydrogenation of alkenes were structure-insensitive, while reactions such as hydrogenolysis, isomerization, and ammonia synthesis were found to be structure-sensitive. [3] This chapter will examine catalytic performance of coordinatively unsaturated metal atoms in catalytic systems that have benefited from atomic-scale imaging and draws on examples drawing from many decades of catalysis research into the creation and characterization of such active sites.

One method of synthesizing a greater fraction of coordinatively unsaturated sites in a metal catalyst is to create smaller particles or clusters of the metal, since more of the atoms will be on the surface versus on the inside of such a particle. There are several geometry-based correlations between the different populations of corner, edge and terrace atoms as a function of particle size on variously shaped clusters. [4], [5] These correlations demonstrate that the number density of the most coordinatively unsaturated surface atoms (the corner atoms) increases sharply as a fraction of the total atoms, for particle sizes less than 2 nm. On the other hand, the same data demonstrate that the number density of less coordinatively unsaturated edge sites decreases gradually as particle sizes increases over 2 nm. As the particle size increases further beyond 2 nm, almost all of the surface atoms are located on terraces, which are the most coordinatively saturated of the surface atoms. [4], [5]

Seminal kinetic measurements of Wei and Iglesia [6] unequivocally demonstrate the effect of cluster size/metal dispersion on methane reforming catalysis. The number of undercoordinated sites was varied by synthesizing catalysts with different particle sizes for Pt and other Group VIII metals such as Rh, Ru, and Ir. This allowed control over the fraction of surface atoms relative to the total. This quotient represents the fractional metal dispersion. Data in Figure 1.1 from the Wei and Iglesia study show how the turnover rate when normalized per surface atom for methane reforming reactions using CO_2 or H_2O as co-reactants increases with dispersion. This demonstrates structure sensitivity for this reaction, where more coordinatively unsaturated (open) sites possess higher catalytic activity. In the opposite case of a structure-insensitive reaction, the data in Figure 1.1 should be represented by a flat horizontal line. This structure-sensitive reaction does not appear to be support dependent within the cluster-size regimes investigated, given the similar rates for various supports for a given metal. [6] However,

below in this chapter, we also present an example of ethylene hydrogenation catalysts consisting of much smaller Ir clusters from the Gates research group, where support effects play a significant role.

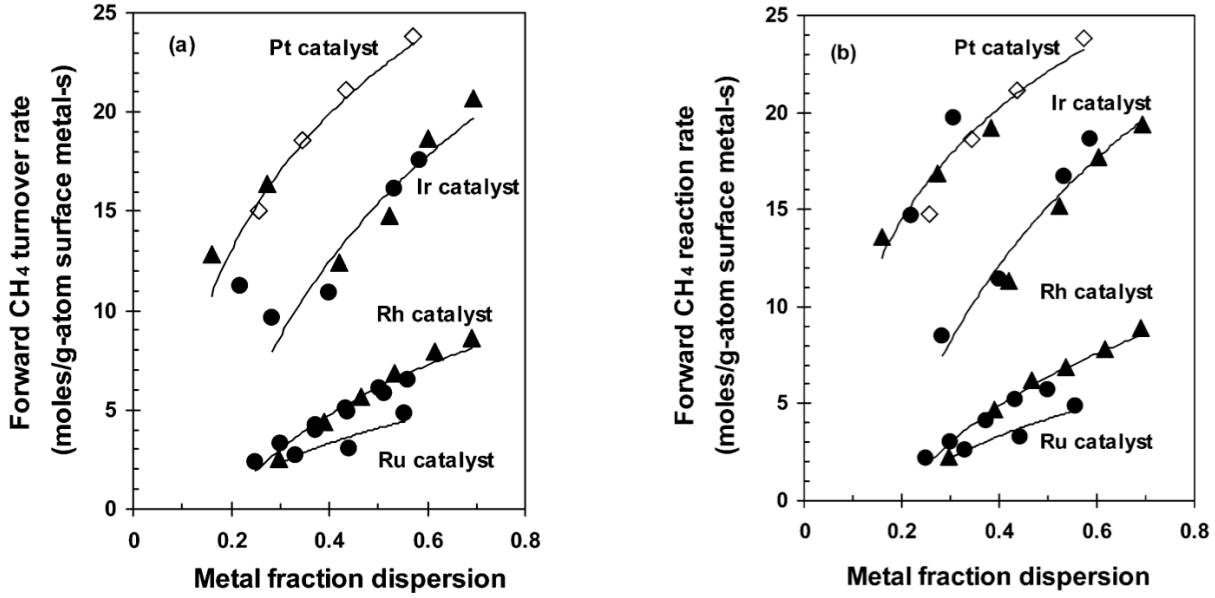

Figure 1.1: Forward CH_4 turnover rates for CO_2 (a) and H_2O (b) reforming of CH_4 as a function of metal dispersion on various supports (873 K, 20 kPa CH_4, (▲) ZrO_2 (●) γ-Al_2O_3, (◇) ZrO_2-CeO_2 support). [6]

Temperature can also be used to affect the number of undercoordinated sites in heterogeneous catalysis. This is elegantly shown in the case of a chromia metal oxide catalyst, where in this context, an undercoordinated site represents an oxygen vacancy (or equivalently, a site where an oxygen ligand has been removed thereby exposing an undercoordinated Cr atom). Burwell *et al*. [7] showed that by heating chromia to temperatures greater than 400°C, coordinatively unsaturated sites are synthesized via -OH condensation and water release, which are active for olefin hydrogenation catalysis as well as CO and O_2 chemisorption. In comparison, untreated chromic gel is unable to perform such chemisorption and is catalytically inactive at 150°C for olefin hydrogenation. Burwell *et al*. controlled the number density of undercoordinated sites by varying the temperature of the chromia gel pre-treatment. Representative data show the increased capacity for carbon monoxide and oxygen chemisorption sites as chromia gel pretreatment temperature increases, and are shown in Figure 1.2. [7]

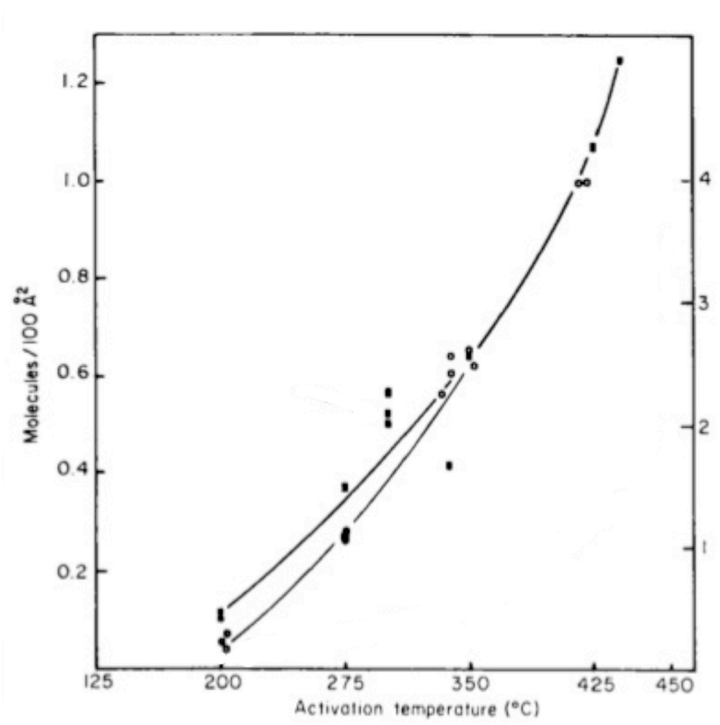

Figure 1.2: Amount of chemisorbed carbon monoxide and oxygen as a function of chromic gel pretreatment temperature. Carbon monoxide: squares, oxygen: open circles. [7]

More contemporary examples of synthesizing coordinatively unsaturated or open sites via heating have followed. Vidruk *et al*. [8] were able to increase the number of low coordinated aluminum ions along grain boundaries in γ-Al_2O_3 using thermal treatments at 1073K. Evidence for the increased number of Al ions in open coordination environments after thermal treatment came from a variety of complimentary techniques including ^{27}Al magic angle spinning nuclear magnetic resonance (MAS NMR), which probes the number and environment of tetrahedral and octahedral aluminum sites; high-resolution transmission electron microscopy (HRTEM), which images the disorder at the grain boundaries; X-ray photoelectron spectroscopy (XPS), which monitors the surface O/Al ratio; and powder X-ray diffraction, which is sensitive to changes in crystal size and morphology. The catalytic ramifications of the synthesis of these coordinatively unsaturated sites was shown in the increased activity for isopropanol dehydration, which was an order of magnitude greater for the high temperature-treated sample relative to a commercial γ-Al_2O_3. [8] In a separate example, Vidruk *et al*. [9] show that by controlling the contact interface between MgO nanocrystals and the magnesium hydroxide precursor, that the number of undercoordinated sites can be controlled. In samples with high contact interfaces, distortion zones were formed at the grain boundaries. These zones led to more coordinatively unsaturated surface ions and oxygen vacancies on the surface, and were characterized using similar methods as were used with the γ-Al_2O_3 system described above. The sample with more coordinatively unsaturated sites again exhibited higher catalytic activity, in this case, for the Knoevenagel condensation reaction. [9]

While particle size and catalyst pretreatment temperature can be used as methods to increase catalytic activity by creating a greater number density of coordinatively unsaturated active sites, there are also ongoing efforts to translate molecular-scale control in the design and synthesis of these sites. Molecular-scale control affords the possibility of synthesizing active sites with a greater information density that can perform multiple functions such as controlling the relative strength of binding and selectivity in a catalyst, and preventing the more open/coordinatively unsaturated active sites from deactivating via sintering/aggregation. Also, when using molecular-scale synthetic approaches for tailoring active site properties, the Sabatier principle suggests an optimum degree of openness of the site for catalysis. [10] Reactants that bind too strongly often lead to catalyst deactivation, while reactants that do not bind strongly enough cannot be catalytically activated.

The need for molecular-level design of catalysts to control binding energies is nicely demonstrated by the electrochemical reduction of carbon dioxide to hydrocarbons: an example of current relevance in the emerging fields of catalysis for carbon management and CO_2-based liquid fuel production. [11] Currently, large overpotentials must be used for this reaction, which makes it prohibitive to perform on a large scale even with the best catalysts currently available. The catalyst for these transformations to reduce CO_2 into compounds that could be building block materials for fuels must be able to (i) catalyze the protonation of adsorbed CO to CHO or COH while simultaneously (ii) suppressing the hydrogen evolution reaction that competes with it. This requires the effective catalyst to have a lower binding energy for CO relative to CHO, in order to avoid the hydrogen evolution reaction. A bound organic ligand based approach is one proposed route for tuning the open catalyst active site to alter the binding energy of the reactants on the molecular level. Other methods of tuning the active site include adding other metals to form alloys or adding promoters. [11]

A rich source of inspiration for molecular-scale design of open catalytically active sites comes from catalysts of biological relevance such as enzymes. Enzymes are particularly proficient at controlling accessibility to an active site through molecular-scale control of the environment that surrounds the active site. Consider the case of the multicopper oxidase laccase enzyme active site, which consists of four copper cations, possessing a total +4 charge, and catalyzes the reduction of molecular oxygen to water. In order to function, the enzyme active site must disfavor the binding of water and favor instead the binding of molecular oxygen, in order to reduce oxygen to water and subsequently remove the water product from the active site, thereby regenerating the catalyst. This is exactly opposite to what would typically occur at such a copper cluster active site based on enthalpic considerations, which favor the adsorption of water to molecular oxygen and would lead to a catalytically inactive cluster site. [12] However, the enzyme active site uses a clever organization of neutralized by the enzyme active site uses a clever organization of negatively charged aspartic and glutamic acid residues within 12Å of the copper cluster active site. These negatively charged residues are thought to disfavor the binding of water relative to molecular oxygen.[12]

The open nature of the copper cluster core of the active site intrigued us, given the fact that this positively charged core is surrounded by anionic residues. The intriguing aspect to us is what prevented the collapse of the oppositely charged residues onto the cluster, which would result in inaccessible (to small molecule reactants) and dense active sites? We formulated a hypothesis based on accepted biophysical modeling of the protein backbone. This backbone (see Figure 5 of [13]) can be modeled as a connected series of rigid tubes, each of which have a minimum characteristic length of 2-3 nm. [13] Our hypothesis was that the characteristic length

of a rigid tube prevented the backbone from bending back on itself on the length scale of 2-3 nm, thus (i) making the mutual annihilation of positive and negative charges in a dense structure impossible and (ii) enabling synthesis of accessible active site cluster cores as shown in the left panel of Figure 1.3. The schematic representation in this figure shows that when the rigid length of the ligand is significantly larger than that of the cluster core, a degree of accessibility to the metal core can result.

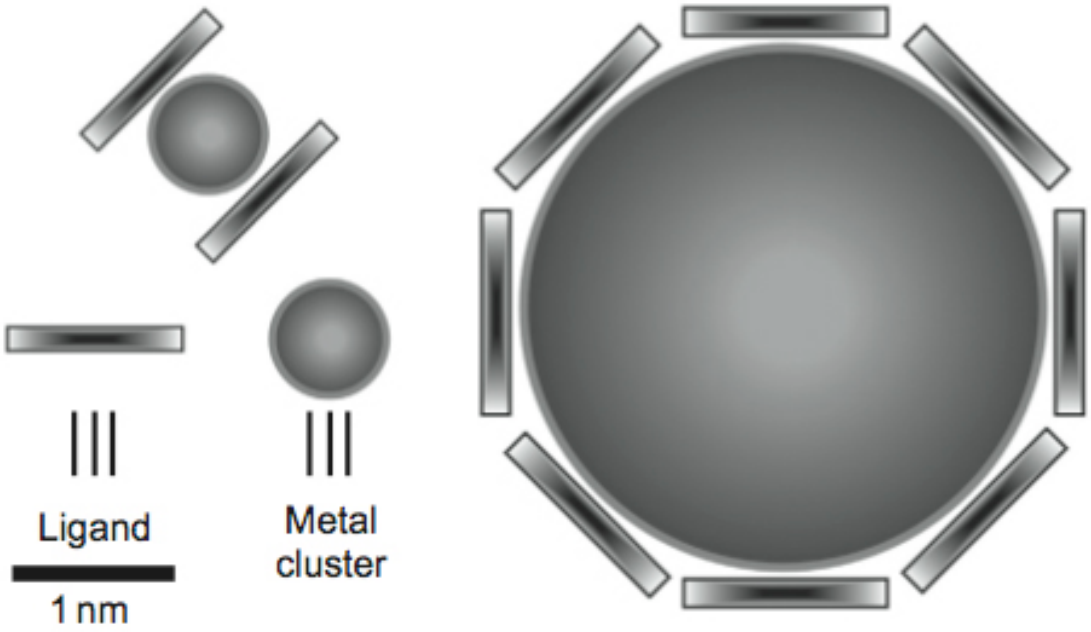

Figure 1.3: Schematic of sub-nanometer gold core (left) and larger (4 nm) gold nanoparticle (right), which are both bound with rigid bulky organic ligands. The sub-nanometer gold particle exhibits open sites on the metal cluster surface that are accessible to small reactant molecules, while the ligands on the larger gold particle are able to pack more densely on the gold surface and result in a closed site, which virtually eliminates accessibility to small-molecule reactant molecules. [14]

Furthermore, our hypothesis was that the type of metal cluster shown in the left panel of Figure 1.3 would not only prove to be chemically accessible, but it would also be mechanically stable. The latter was qualitatively justified by the role of the sterically bulky ligands as barriers for aggregation/coalescence properties. [14] This is peripherally related to the role of sterically bulky ligands in protecting unstable mononuclear metal complexes in synthetic chemistry such as Cp*, neopentyl, norbornyl, di-*tert*- butylphospinoethane, tris-pyrazolylborate, and tris-*tert*-butylsiloxane, which are used for stabilizing complexes against aggregation, as well as large anionic ligands that disfavor coordination based on their electron delocalization properties and steric bulk, such as $[B[3,5\text{-}(CF_3)_2C_6H_3]_4]^-$ ($[BAr^F{}_4]^-$) and tris(pentafluorophenyl)boron. However, the other function of the rigid sterically bulky ligands in the left panel of Figure 1.3 is to provide

small molecule reactant accessibility to the underlying metal cluster surface, and is unique to metal clusters as shown in Figure 1.3. [14]

We recently reported the synthesis and characterization of the most accessible and stable metal clusters in solution using the construct shown in the left panel of Figure 1.3. This approach used bulky and rigid cone calix[4]arene phosphine ligands as crude mimics of a protein backbone segment. [14] The metal core in these systems is enveloped within a permeable monolayer consisting of the adsorbed organic ligands, which prevents cluster aggregation as a surface-passivating layer, while facilitating accessibility to the metal core. [14], [15] Our data in Figure 1.4 demonstrate that the degree of metal core accessibility when using this approach critically relies on the rigid organic ligand to be larger than the size of the metal cluster core, in order to facilitate accessible regions on the metal surface, which are slightly smaller than the size of the organic ligand. [14]

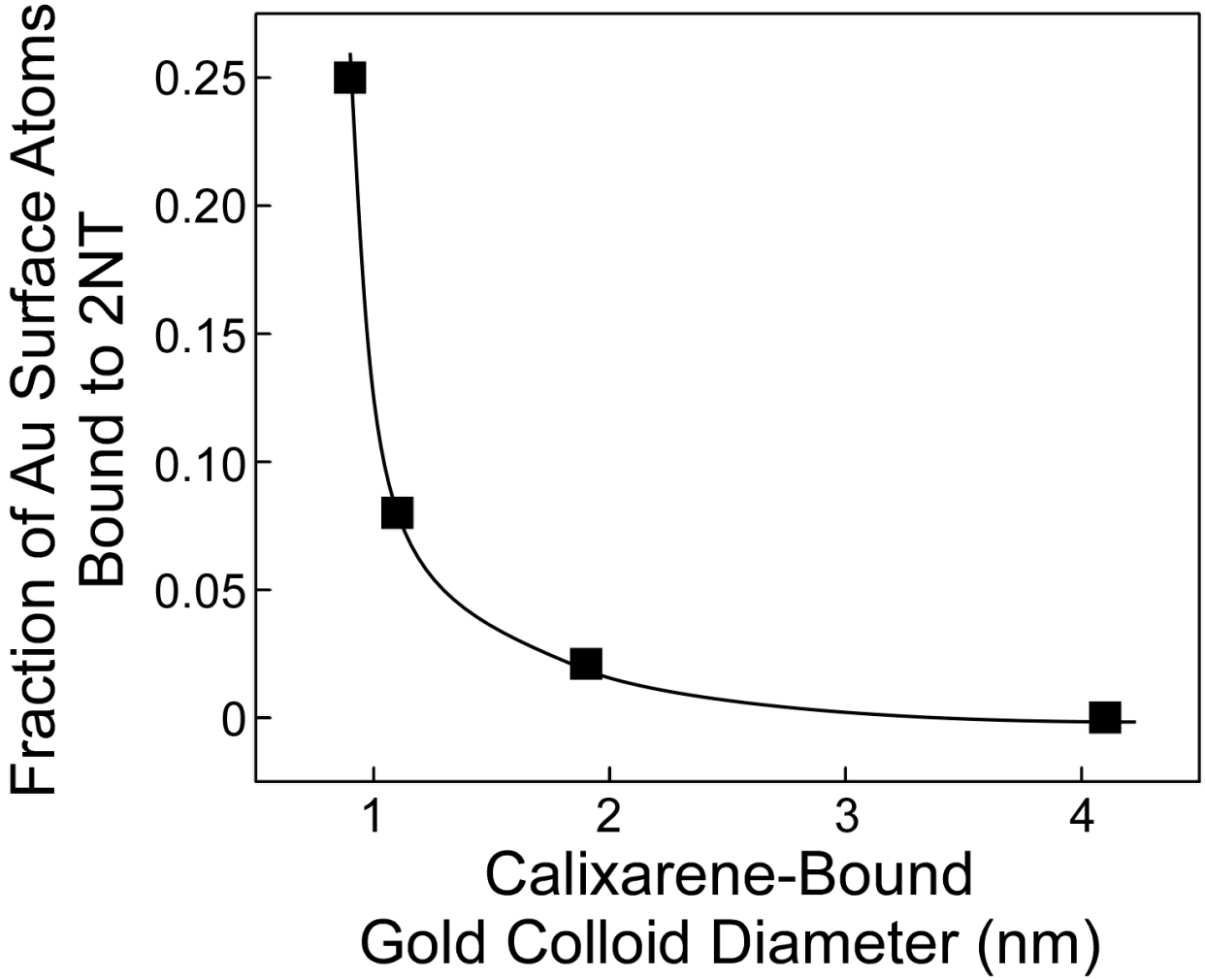

Figure 1.4: Correlation of accessibility of a 2-napthalenethiol (2-NT) probe molecule as a function of calix[4]arene-bound gold nanoparticle core size. Significant amounts of accessibility to 2-NT are afforded by a small sub-nanometer particle size. [14]

Another example of the effect of active site environment in biological systems is shown with Fe-S clusters, which are known to be effective electron transfer agents in applications as varied as nitrogen fixation and photosynthesis. Depending on the particular protein environment where the Fe-S cluster is situated, the cluster redox potential can vary within a span of approximately 0.4 V as shown in Figure 1.5. This paradigm reveals the possibility of tuning cluster active sites for pressing and relevant applications, using earth-abundant materials, by adjusting the active site environment. [16]

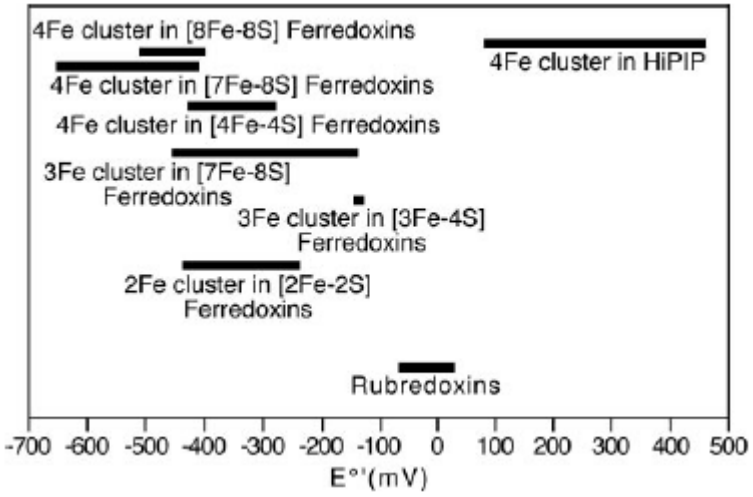

Figure 1.5: Ranges of reduction potentials for Fe-S clusters depend on protein environment [16]

In this chapter, our goal is to present examples of well-characterized systems where structure-function relationships can be realized on the molecular level. We will discuss further examples of controlling binding and reactivity on well-characterized metal cluster catalysts, which involves characterization using imaging. Emphasis is placed on drawing parallels and distinctions between homogeneous and heterogeneous catalysts. The first examples will illustrate how metal-carbonyl binding can be tuned through use of electron donating ligands, which are bound to the metal cluster surface. Subsequent examples leverage on this information and focus on imaging of CO binding on noble metal clusters such as gold. Catalytic systems where characterization of open-site catalysis is possible will be discussed, and systems that utilize molecular clusters that incorporate aspects of binding and site openness will be described.

1.2 Control of binding in metal-carbonyl clusters via ligand effects

As suggested in the CO_2 reduction example from Peterson and Norskov [11] discussed earlier, there is great potential in using organic ligands to tune catalytic activity. One effect that bound organic ligands can have on an active site is electronic tuning of the metal core as demonstrated in the Fe-S cluster example above [16]. For example, phosphines are known to be electron-donating ligands. Ha *et al*. demonstrate electronic tunability using calix[6]arene phosphine molecules bound to 4 nm gold particles. [17] XPS data in Figure 1.6 demonstrate a slight lowering of the gold binding energy, which illustrates an organic ligand effect even in

large nanoparticles which electronically are nearly identical to bulk gold (84.0 eV binding energy is observed in absence of organic ligand). [17]

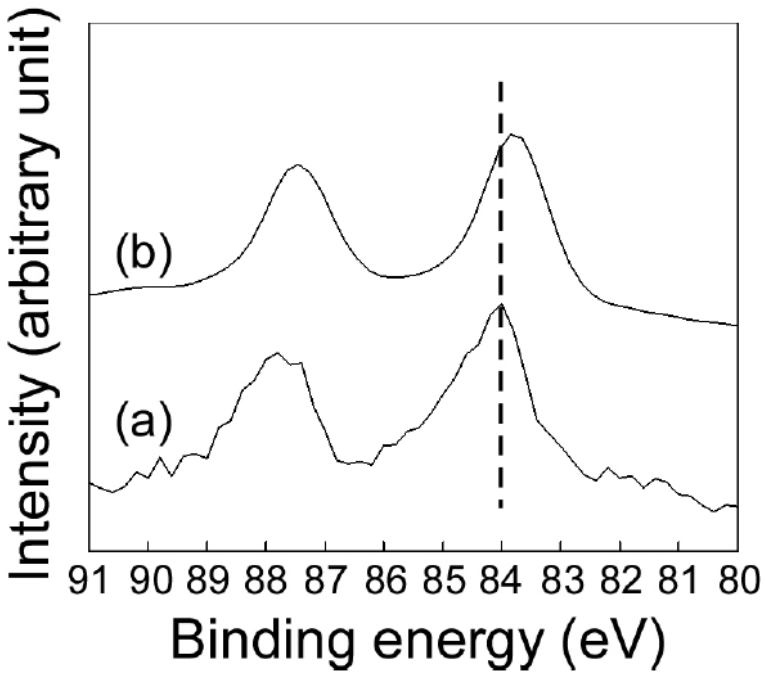

Figure 1.6: Representative Au 4*f* XPS spectra of gold nanoparticles (a) without calix[6]arene triphosphine binding (tetraoctylammonium bromide surfactant only) and (b) with calix[6]arene triphosphine (2 μM for 200 μM of gold atoms) binding. Nanoparticles are deposited on surface-oxidized (~100 nm oxide layer thickness) silicon wafer. [17]

With the construct of Figure 1.3 in mind, calix[4]arene phosphine-substituted Ir_4 carbonyl clusters were synthesized by de Silva *et al*. [18] and Okrut *et al*., [15] and are shown in Figure 1.7. As with the phosphine-bound gold nanoparticles discussed previously, it is expected that these calix[4]arene phosphine (L) bound Ir_4 carbonyl clusters will also benefit from a sterically bulky calixarene ligand for stabilizing open sites in a metal cluster. A reliable method of probing the electron richness of the Ir metal core is through infrared spectroscopy of the cluster, by observing the frequencies of bound carbonyl ligands. Figure 1.8 illustrates that as the number of calix[4]arene phosphine ligands increases, the electron richness of the cluster increases. This increase in electron richness is manifested in the red-shifting of the terminal and bridging CO bands in the IR spectra shown in Figure 1.8. Another example in the literature of using CO as a probe molecule for electron-richness was shown by Lin *et al*. with gold clusters. [19] Gold clusters that were deposited on a defect-free MgO surface were found to have the same stretching frequency of single-crystalline Au at 2120 cm^{-1}, while for gold clusters on an electron-bombarded MgO surface which forms F centers (oxygen vacancies), the CO stretching frequency is red-shifted to 2070 cm^{-1}. [20] The reason behind the red shift in the IR spectra of electron-rich clusters can be explained through the Blyholder model of metal-CO bonding. [21], [22], [23]

This model requires that as the metal d orbital occupancy increases, the amount of backbonding from the metal to the bound CO increases, which is observable by a decrease in the CO stretching frequency (*i.e.* red-shifted CO bands in infrared region), due to weakening of the C-O bond of the bound CO ligand. According to the Blyholder model, there are two main components of the metal-carbon bond. The first component is carbon-to-metal σ-bonding due to overlap between the filled 4σ and 5σ states of the carbon with the empty *d* orbitals of the metal atom. The second component is a π-backbonding interaction of the filled metal *d* orbitals and the 2π* antibonding orbitals of the carbon monoxide leading to more electron density in the 2π* antibonding orbital. Addition of phosphine ligands to the metal cluster will increase the electron-richness of the Ir_4 core and consequentially increase the amount of metal-to-CO backbonding. This further shifts the CO bands in the IR spectra as shown in Figure 1.8. The experimental results are also supported by simulated spectra that are also included in Figure 1.8. [15]

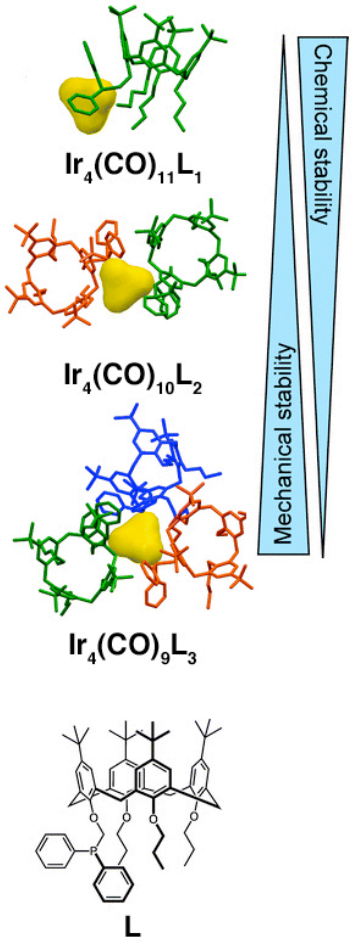

Figure 1.7: Calix[4]arene phosphine (L) substituted Ir_4 clusters and their relative mechanical and chemical stabilities. [15]

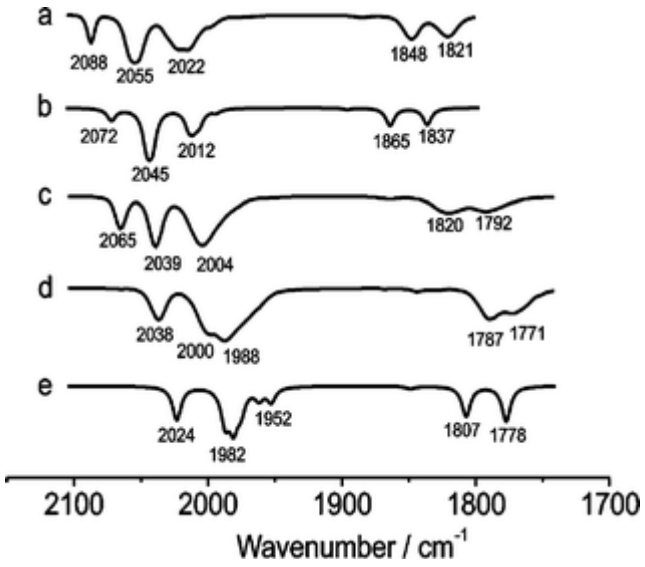

Figure 1.8: Experimental and simulated FTIR spectra for the cluster compound series corresponding to: (a) 1 calix[4]arene phosphine ligand (experimental), (b) 1 calix[4]arene phosphine ligand (simulated), (c) 2 calix[4]arene phosphine ligands (experimental), (d) 3 calix[4]arene phosphine ligands (experimental), (e) 3 calix[4]arene phosphine ligands (simulated). Intensity plotted in arbitrary units. Mechanical stability within this context refers to resistance against aggregation whereas chemical stability refers to resistance to CO loss (decarbonylation). [15]

The data from Figure 1.8 unambiguously demonstrate that the calix[4]arene phosphine substituted clusters are electron rich, but where is the most electronically rich site on the cluster? Infrared measurements only provide sample-averaged measurements. Insight into the location of the most electron rich site in these clusters on the molecular level must come from another source, and in this case it can come from single-crystal X-ray diffraction. Previous studies in the literature have shown that monosubstituted Ir_4 clusters with electron donating ligands exhibit higher electron density on the carbonyl substituted Ir atom. [24] The X-ray crystal structure of the monosubstituted Ir_4 cluster with one calix[4]arene phosphine ligand and 11 carbonyl ligands ($Ir_4(CO)_{11}L_1$, where L is the calixarene phosphine ligand) contains significant asymmetry in the Ir-C bond distances of the two bridging CO ligands that are attached to the substituted Ir atom. The Ir-C bond distances involving the substituted Ir atom are shorter despite the steric bulk presented by the calixarene ligand. [18] There is no observed asymmetry present in the third CO bridging ligand that is not attached to the substituted Ir atom. Chini observed a similar shortening of the Ir-C bond with tetraphenylphosphine substituted Ir clusters. [24] The shorter bond distances are indicative of stronger π-bonding of the bridged CO ligand on an electron-rich Ir atom. Additionally, it is evident that the Ir-C-O bond angles for the bridging CO atoms that are attached to the substituted Ir atom have changed versus on the unsubstituted atom and also exhibit asymmetry. Figure 1.9 shows data from the X-ray crystal structure indicating this change in angles. The angles involving the substituted Ir atom have all increased versus the Ir-C-O angles involving the unsubstituted Ir atoms. This increase in Ir-C-O angle is due to unfavorable

sterics due to the bulky nature of the calix[4]arene phosphine, which favors the bridging carbonyls to point away from the substituted Ir atom, despite the pull of the more electron-rich Ir atom described above. [18]

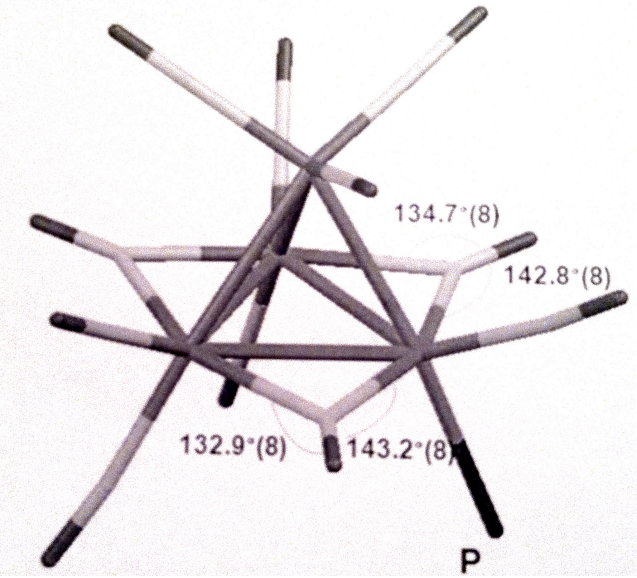

Figure 1.9: Bond angles in $Ir_4(CO)_{11}L_1$ illustrating the asymmetry of the bridging CO ligands around the substituted Ir atom as well as the unfavorable sterics because of the bulky calixarene that favor the CO ligands to point away from the substituted Ir atom. [18]

What is the consequence of the increased electron density on the Ir_4 core to the strength of the metal-carbon bond? Van Santen and Neurock investigate the binding of a terminal CO on an apex and an edge site of a cobalt cluster. [25] When there is binding of a terminal CO to a metal atom, there is a combination of the donation from the CO (5σ) orbital to the *d* orbital on the metal atom and the backbonding between the $2\pi^*$ antibonding orbitals and the *d* orbitals of the metal. In the case of the electron-rich metal core, there are significant sigma Pauli repulsion forces working against sigma electron donation of the terminal CO to the metal. It is calculated by DFT that the CO will bind more weakly to the edge sites as a result of this repulsion. This can be rephrased that the larger Pauli repulsion at the edge sites weakens the M-C bond. There is less *d* orbital occupancy at the apex site than there is in the edge sites because there are more neighboring metal atoms at the edge sites. This effectively explains why terminal CO has a greater binding affinity to lower coordination sites (apex sites) versus higher coordination sites (edges) on Ir as well as on other late metals. [25] The trend of lower coordination number leading to stronger binding energies as observed with Co is also shown for CO and O binding to gold clusters by Lopez *et al*. in Figure 1.10. [26]

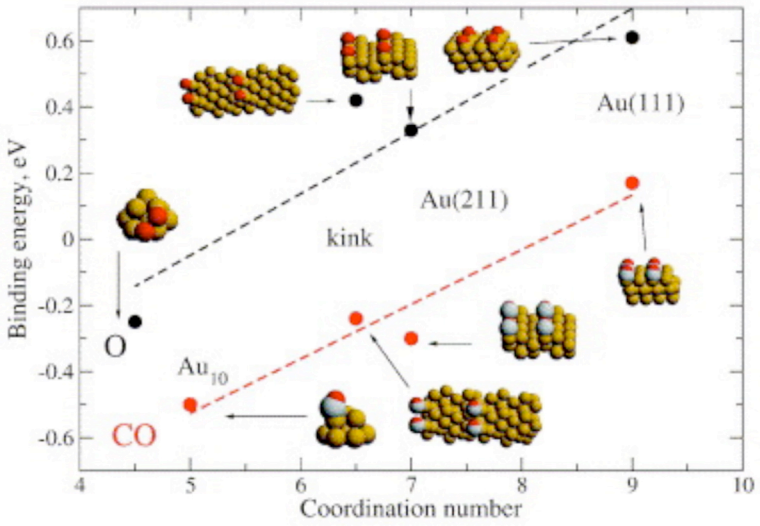

Figure 1.10: Binding energy of CO and O as a function of coordination number on gold clusters. Stronger binding is observed at lower coordination numbers (smaller particles). [26]

The first experimental demonstration of the effect of the consequences of Pauli repulsion on the metal-carbon bond was by Okrut *et al*. [15] Up to this point all studies of this phenomena had been from calculations. For the series of electron-rich calix[4]arene phosphine substituted Ir_4 carbonyl clusters previously described in this chapter, where the number of calix[4]arene phosphines varies from 1 to 3 per Ir_4 cluster, the CO desorption temperature was measured as a function of highest energy terminal CO infrared band (Figure 1.11). Pauli repulsion predicts that more electron-rich clusters lose carbonyl ligands more easily, corresponding to lower T_{decomp} in Figure 1.11 relative to the less electron-rich clusters. This prediction is borne out experimentally for the family of clusters shown in Figure 1.7, and the data is shown in Figure 1.11. The results of Okrut *et al*. [15] above correlate more labile CO ligands and increased *d*-orbital occupancy of the Ir_4 core. They can be used to elucidate previously observed kinetic 3500-fold rate enhancement of CO decarbonylation for $Ir_4(CO)_{10}(PPh_3)_2$ relative unsubstituted $Ir_4(CO)_{12}$. [28]

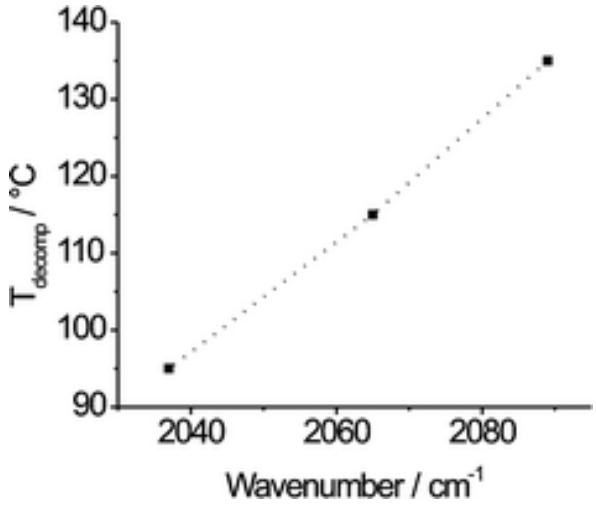

Figure 1.11: Temperature probe desorption experiments of calix[4]arene phosphine-Ir_4 carbonyl clusters as a function of electron richness. Electron richness decreases moving from left to right on the *x*-axis. [15]

1.3 Imaging of CO binding on Noble Metal Clusters

The previous sections discussed using CO as a reporter on the electron richness/deficiency of Ir_4 clusters as well as the effect of electron richness itself on the binding energy of CO. This next section investigates CO binding on gold clusters as well as mentioning a relevant catalytic application of these studies: CO oxidation.

As mentioned previously with reference to the Sabatier principle, there is a delicate balance that must be achieved between a reactant binding too strongly or too weakly to a catalyst. Norskov *et al*. [29] performed a DFT study that correlated the activation energies of N_2, CO, NO, and O_2 dissociation with the heat of adsorption on a variety of different metal surfaces. These relations are structure-sensitive (closed-packed surfaces versus steps) due to the dependence of the transition-state barrier on the openness of the metal surface. The relationship shows that the activation energy decreases as the binding energy of adsorbate increases. [29] Another example of structure-sensitive CO binding is from Iwasawa *et al*., which shows that the adsorption of CO on platinum surfaces occurs associatively on terraces, while dissociative chemisorption dominates on step and kink sites. [30]

Though the binding energy for terminal CO decreases for increasing electron richness of gold [26], it has been observed by various groups [31], [32], [33], [34] that the binding energy for dioxygen increases with increasing electron richness. This relationship between electron richness and binding energy for molecular oxygen is due to the greater electron accepting nature of the oxygen molecule. Due to this favorable binding of molecular oxygen to electron-rich gold clusters, electron-rich gold is a desirable catalyst for CO oxidation based on the results of DFT calculations. [34], [35], [36], [37] Electron richness is extremely important for this reaction as clusters that are less than 8 atoms are generally catalytically inactive; however, negatively charged Au dimers are active for CO oxidation. [36]

Scanning tunneling microscopy (STM) can be used to image the active sites on gold catalysts. Lin *et al*. studied the adsorption of CO on electron-donating MgO/Ag(001) thin films

using STM techniques. [19] Edge gold sites appear bright in Figure 1.12, and this indicates an increased number of electronic states that must exist to accommodate electrons from the MgO/Ag support at these sites. It would be expected that for a non-interacting support or for a homogeneous case in solution that these coordinatively unsaturated sites would be the most electron-poor sites. [25], [26] However, in a supported particle system, the edge sites are where the support is most likely to ligate to the cluster. The support in this case can be electron-donating due to either F-band defects or tunneling effects. [20] The negative charge stays localized on the edge atoms that are ligated to the support just as the negative charge was largest on the phosphine-substituted Ir atom in the clusters discussed earlier. [18] The location of the brightness due to the electron richness of these atoms on the edges is shown in Figure 1.12a. This location of excess charge on the edge is also advantageous from a simple electrostatic charge point of view where charge is distributed throughout the largest perimeter thereby avoiding more repulsion due to localized charge build up.

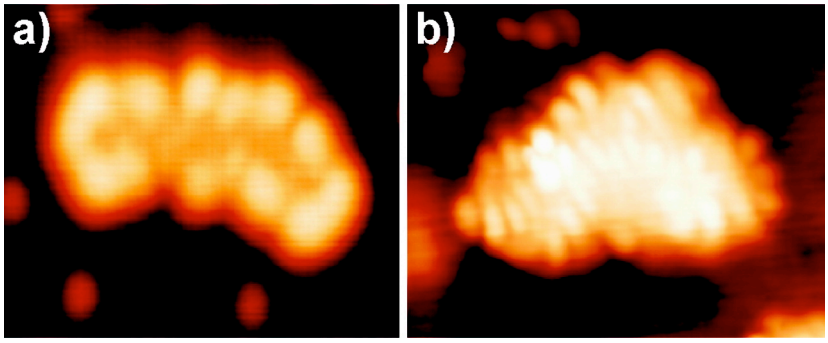

Figure 1.12: STM topographic image of a) bare and b) CO saturated Au island (7.0 x 5.5 nm, 150 mV). [19]

Infrared spectra of the adsorbed CO on the gold clusters are shown in Figure 1.13. [19] This figure shows that the terminal CO stretch vibration is red-shifted as one would predict for increased backbonding for an adsorbed CO on a more electron rich metal. From this spectrum in Figure 1.13 there appears to be no bridging CO present. Additionally, the STM image shows bound CO on the perimeter of the particle rather than on the interior sites (Figure 1.14). [19] This result is surprising in that based on previous calculations [26] terminally bound CO would bind most weakly to the most electron-rich sites, and, in order to decrease aforementioned Pauli repulsion, CO would be expected to bind in either a bridging configuration or on the interior of a cluster. A possible explanation for this system is that CO may prefer to bind to the edge sites due to possible favorable interactions with the support on these edge sites and/or sterics (gold atoms have less neighbors). In order to minimize the unfavorable Pauli repulsion, the binding of CO to these edge sites results in an unprecedented redistribution of charge away from the edge CO binding sites, as shown in Figure 1.12b. The sites that used to be electron rich before CO binding are now electron poor and vice versa, as a result of this charge redistribution upon CO binding. [19]

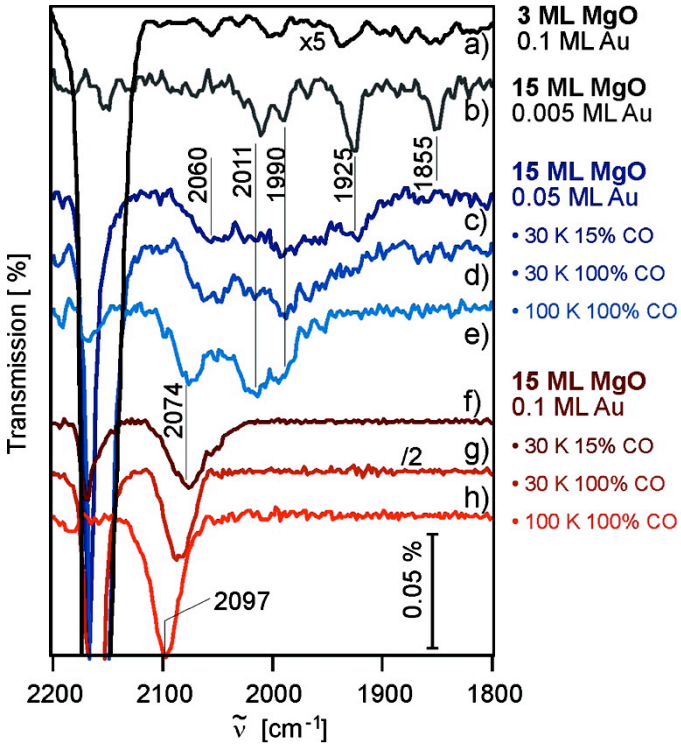

Figure 1.13: Infrared spectra for different sizes of gold islands on MgO. Note the red-shift in the terminal CO bands due to the electron donating nature of the MgO support. [19]

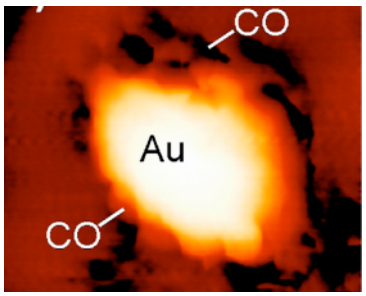

Figure 1.14: STM image that illustrates CO saturated Au island using a CO covered STM tip (4 x 4 nm, 100 mV, 3pA) [19]

1.4 Imaging of open sites in metal cluster catalysis

Observations of catalytic events on a single particle/single catalytic event level show promise in building structure-function relationships in catalysis. If one could resolve the precise location(s) of reaction events on a particle's surface, that would provide extremely valuable information for the molecular design of catalysts. Peng Chen's group at Cornell University has elegantly investigated single nanoparticle catalysis for nearly a decade, in part using the conversion of resazurin to the fluorescent resorufin product on gold nanoparticles and carbon nanotubes with fluorescence microscopy techniques. [38], [39], [40], [41] The molecular-level

mechanism for this reaction is not well-understood; [42] however, the kinetics follow a Langmuir-Hinshelwood profile, consistent with reactant adsorption to the catalyst surface. [38], [39], [40], [41] A hypothesis could be proposed that this adsorption event could benefit from having an open/coordinatively unsaturated site present on the surface to facilitate reactant binding. This would lead to kinetics that are controlled by the degree of coordinative unsaturation of the surface. In recent spatial mapping experiments with gold nanorods, the rate of the gold-catalyzed conversion of Amplex red to resorufin was measured on different regions of the gold nanorods. [43] The ends of the rods were observed to have the fastest rates as shown in Figure 1.15. The ends of the rods are also known to have a greater number density of coordinatively unsaturated sites, as compared to the center of the rods. Due to constraints in the spatial resolution of these measurements, quantification of the number of active sites as a fraction of the total surface or as a fraction of the total activity could not be achieved. [43] Later work by Nigra *et al*., as will be described later in the chapter and in more detail in Chapter 2, will use an organic ligand titration method to quantify the number and the activity of the sites on gold nanoparticles for resazurin reduction. [44]

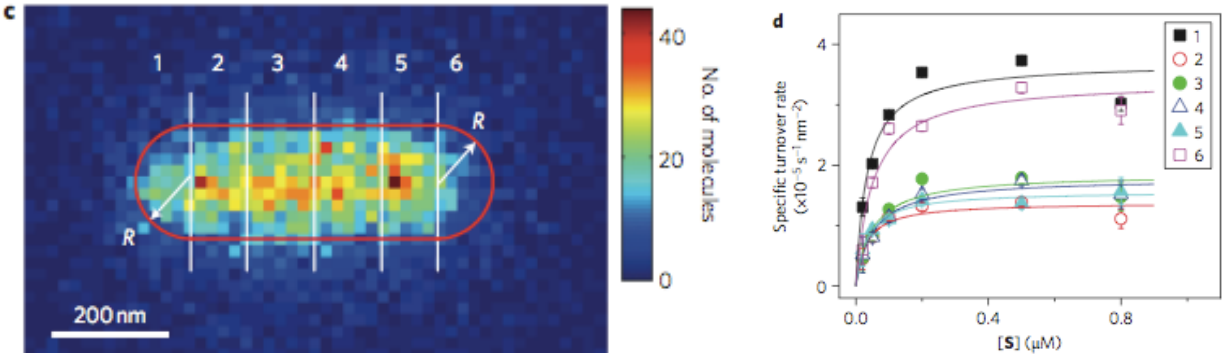

Figure 1.15: Kinetics of the conversion of Amplex Red to resorufin as a function of location on gold nanorods. A) numbered slices of gold nanorods where the kinetics was measured. B) kinetics as a function of location on the gold nanorod [43]

1.5 Elucidating kinetic contributions of open sites: kinetic poisoning experiments using organic ligands

The work of Nigra *et al*. [44] with supported gold nanoparticles was able to determine the individual contributions of different undercoordinated sites such as corners and edges. Using the resazurin reduction reaction studied by Chen *et al*., [38], [39], [40], [41] the different catalytic contributions of the terrace, edge, and corner sites were investigated. This was the first instance in the literature of deconvoluting the separate catalytic contributions of corner and edge sites using a kinetic poisoning experiment.

This study provided additional insight into the reaction that the fluorescence microscopy studies could not provide, due to the lack of spatial resolution in the microscopy images. Using a conventionally synthesized gold nanoparticle supported on silica catalyst, the gold surface was titrated with strongly binding triphenylphosphine (TPP) and dodecanethiol (DDT) ligands to

block surface sites at submonolayer coverages. The titrated catalysts were then used for resazurin reduction catalysis. Figure 1.16 illustrates the dependence of the reaction rate as a function of the fraction accessible surface area, which is one minus the fraction of the surface blocked by organic ligands. There are three distinctly linear regions that are present in this graph. One at fractions from 1 to 0.99 of accessible surface (shaded in green), the next from 0.99 to 0.7 of accessible surface (shaded in purple), and the last region extends from 0.7 to 0 of accessible surface (shaded in yellow). The distinctly linear regions indicate a single type of site blocked in each of the regions. The most active sites (shaded in green), comprising 1% of the accessible surface, contribute to 30% of the total activity of the catalyst. The next most reactive sites (shaded in purple), comprise 29% of the total gold nanoparticle surface and were responsible for 55% of the activity of the catalyst. The rest of the surface (shaded in yellow), approximately 70%, is inactive for this reaction. If the slopes of the linear regions are measured for a TOF-based comparison, it was calculated that the difference in activity between the different active sites was a factor of approximately 17. We hypothesized that these different linear regions of Figure 1.16 corresponded to corner sites as the region from 1 to 0.99 on the *x*-axis, edge sites were in the region from 0.99 to 0.7, and terrace sites in the region from 0.7 to 0 on the *x*-axis. These numbers correlate well with aberration corrected HAADF-STEM electron micrographs of the supported gold nanoparticles. From the micrographs, it was estimated that approximately 2.5% of the surface gold atoms were corner atoms, and approximately 24% of the surface atoms were edge atoms on the gold nanoparticle surface. The micrographs are shown in Figure 1.17. Calculations with geometric models of idealized nanoparticle geometries such as tetrahedron, octahedron, and cubo-octahedron were used to also estimate the number of corner, edge, and terrace sites as a function of the total gold surface area for the average gold nanoparticle size used in this study. The range of the number of corner sites was between 0.5% and 8.3% of the surface, and the number of edge sites ranged from 12.5% to 46.7%. The number of corner and edge sites corresponds in these geometric calculations and in the aberration-corrected HAADF-STEM corresponds with the measured values from catalytic experiments. [44] Previously published data from Chen *et al*. with different gold particle sizes exhibiting different TOF numbers can be explained using this new understanding of the reactivity of edge and corner sites for this reaction. [42] This organic ligand based approach of titration of metal surfaces used in this paper opens the door to wider opportunities to better control and understand catalyst activity and selectivity. One could envision selectively blocking very active sites that produce undesired products and leaving only the sites that produce the desired product(s). [44]

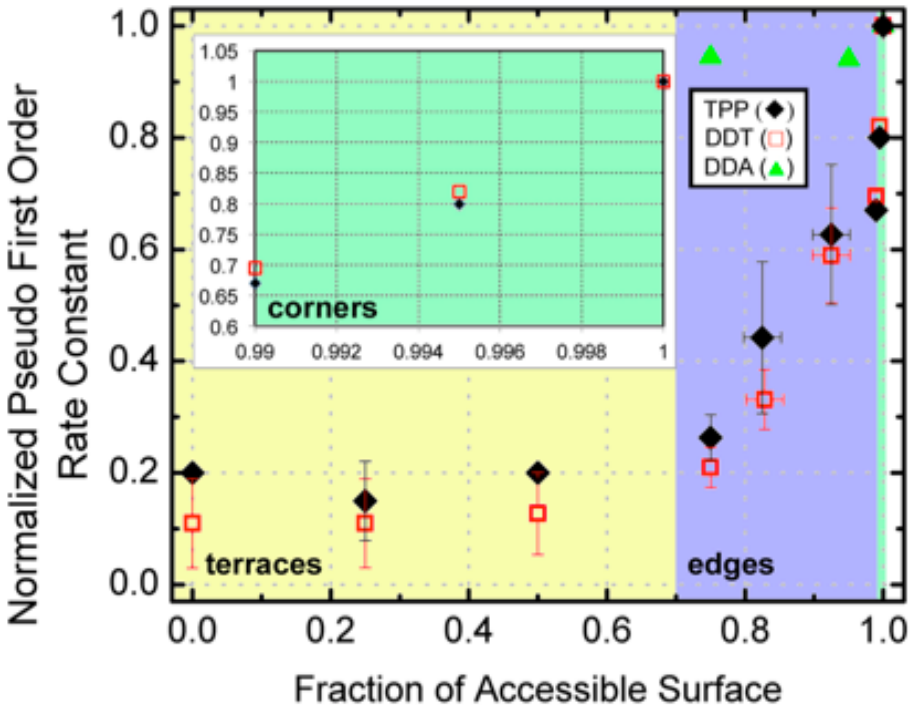

Figure 1.16: Normalized pseudo first-order rate constant for the reduction of resazurin to resorufin on organic ligand-bound Au nanoparticles supported on TMS-capped silica, with varying degrees of accessible gold surface. TPP (♦), DDT (□), and DDA (▲) are used as ligands to block gold surface active sites during the course of kinetic poisoning experiments. (Inset) Represents a zoom into the high fraction of accessible surface region of main figure for TPP (♦) and DDT (□). [44]

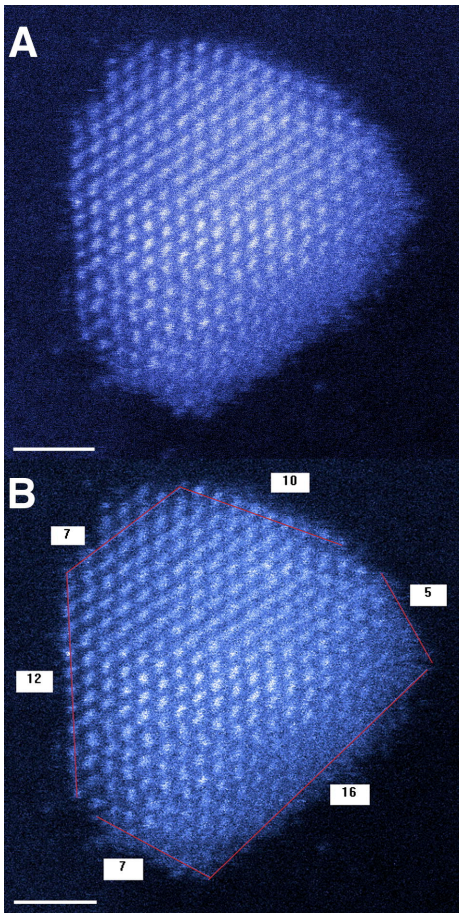

Figure 1.17: (A and B) Aberration-corrected HAADF-STEM images of a representative Au nanoparticle in our catalyst with atomic resolution. (B) The counted number of edge atoms for this particle. The scale bar in each panel represents 1 nm. [44]

1.6 More approaches to poisoning open catalytic active sites to obtain structure function relationships

Poisoning open sites on metal nanoparticles provides a method to observe how the activity and/or selectivity changes as function of the amount of openness of the site. The next few examples illustrate how different poisoning experiments can lead to information about the identity of the catalytic active site.

1.6.1 Using atomic layer deposition of Al_2O_3 to block sites on Pd/Al_2O_3 catalysts

The role of coordinatively unsaturated sites or open sites as the sites responsible for coking, and subsequent deactivation, as well as in sintering in palladium catalysts was further elucidated by Lu *et al*. in 2012. [45] This work demonstrated an excellent example of

manipulation of the catalyst's structure to achieve the desired functionality, namely to be both sinter and coking-resistant in the oxidative dehydrogenation of ethane. It had been known previously that the CUS sites were the active centers for coke formation and that CUS sites in general are unstable through the mechanism of Ostwald ripening. [46] An elegant aspect of this work was the development of an atomic layer deposition method of alumina to selectively block the CUS sites. This resulted in the amelioration of both the problems of coking and particle sintering. Previous work in this field was not successful in addressing both of these problems simultaneously and often used small amount of another alloying metal, poison such as sulfur, or inorganic oxide overlayer (See references found in [46]). Particle size as verified by transmission electron microscopy indicated no sintering of the particles after reaction, and gravimetric analysis indicated a 94% decrease in the amount of coke produced on the surface of the catalyst versus a non-overcoated sample. [46]

1.6.2 Bromide poisoning of active sites on Au/TiO_2 catalysts for CO oxidation reactions

While the number of surface sites on supported gold nanoparticles can be measured using CO chemisorption methods at low temperature, the fraction of those surface sites that are active sites for CO oxidation was determined by the Kung group at Northwestern University. [47] Bromide anion was chosen as the halide poison over chloride due to the fact the chloride is known to sinter the gold particles and have great mobility on support materials. It is also not understood if chloride electronically modifies the catalyst in addition to blocking Au sites. A small fraction of bromide does bind to the support; however, careful XANES measurements are able to correlate the nominal Br to Au ratio versus the actual amount of Br bound to Au. [47] In the Au/TiO_2 catalyst used for this study, the poisoning experiments reveal that only a fraction of the surface atoms are active sites for CO oxidation as compared to sites that are able to chemisorb CO. Catalytic activity was completely suppressed when 35% of the surface sites could still chemisorb to the Au/TiO_2 catalyst, with 5-10% of the gold atoms bound to Br as shown in Figure 1.18. The question can then be asked, where are these active sites located on the nanoparticle? Oxford *et al*. hypothesize that these sites are located at or near the perimeter of the particle and the support. [47] This hypothesis comes from the fact that the bromide ions are bound to Au^0, and there must be a counter cation present to balance the charge. The cation could come from either the sodium cation from NaBr used to poison the catalyst or from the support (latter should be favored based on entropic considerations). The authors cite work by Carlsson *et al*. showing that approximately 6% of the total Au atoms are located on the perimeter, which would account for the suppression of catalytic activity when 5-10% of the total Au atoms are bound to Br. [48] This study provides yet another example where only a fraction of the surface is active for catalysis, and furthermore, the amount of active surface for CO oxidation is quantified.

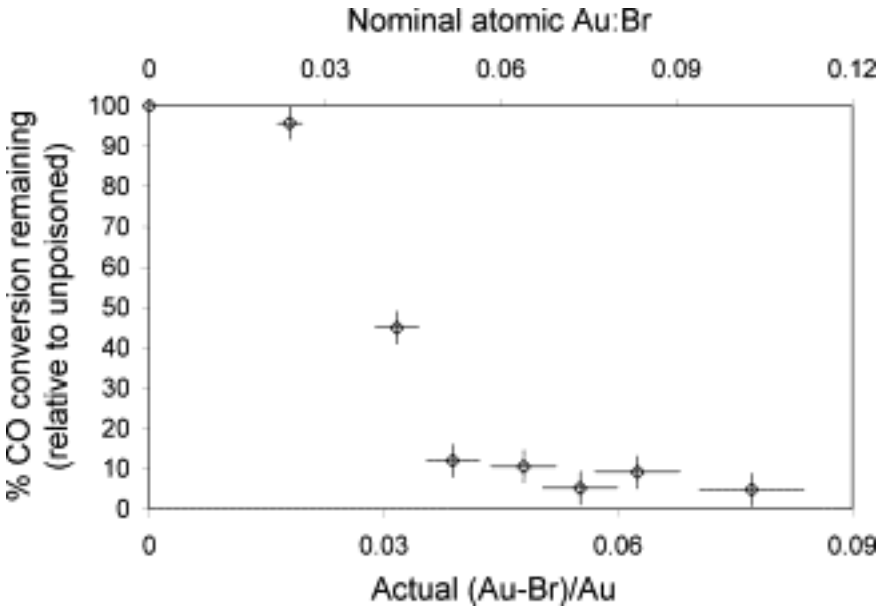

Figure 1.18: CO conversion remaining relative to poisoned Au/TiO_2 catalyst as a function of Br poison added. [47]

More recent work also uses NaBr as a poison for Au/TiO_2 catalysts in work performed by Chandler *et al*. [49] The hypothesis presented in this work is that the corner and edge sites are the active sites for CO oxidation and is supported by previous hypotheses suggested in the literature,[50] which disagrees with the hypothesis that the perimeter sites are the active sites in Oxford *et al*. [47] A careful comparison of the data shows that both publications agree that there are only one type of active site for this reaction due to the fact that they both observe that the activity decreases linearly as more bromide is added to the catalyst. Both studies come to the conclusion that ~10% of the total Au atoms are active for this reaction, but the difference is in the interpretation of the data. Chandler *et al*. use data from DFT calculations to show that bromide binds more strongly to undercoordinated sites such as corners and edges than terrace sites on Au nanoparticles. They use additional evidence based on geometric calculations based on particle size that the corner and edge sites should comprise approximately 30% of the surface atoms to further support their hypothesis that corner and edge sites are the catalytically active sites. [49] A possible hypothesis to reconcile both hypotheses is that a large fraction of the undercoordinated corner and edge sites are present on the perimeter between the particle and the support. To check the validity of this hypothesis, a system could be developed where the particles are not in contact with the support to determine if there is catalytic activity without support contact.

1.6.3 Bromide poisoning of active sites on Au/TiO_2 catalysts for water-gas shift reactions

In a different reaction using Au/TiO_2 catalysts, the role of the coordinatively unsaturated corner sites as the active surface species on supported gold catalysts for the water-gas shift (WGS) reaction was by Ribeiro *et al*. at Purdue. [51] While the absolute number of corner atoms does not vary significantly for particle sizes greater than 1 nm, the relative population

decreases with increasing particle size. Experimental data follow the same trend as the model of the relative population of corner atoms as a function of nanoparticle size, indicating that corner sites are the active sites for this reaction. [52] Additional research using bromide anion as a poison reveals that only the corner sites comprising approximately 2% of the catalyst surface are the active sites for water-gas shift catalysis. The decrease in rate due to bromide poisoning is shown in Figure 1.19. [51] Future opportunities lie here in creating stable sub-nanometer particles where the number of corner atoms is largest per particle.

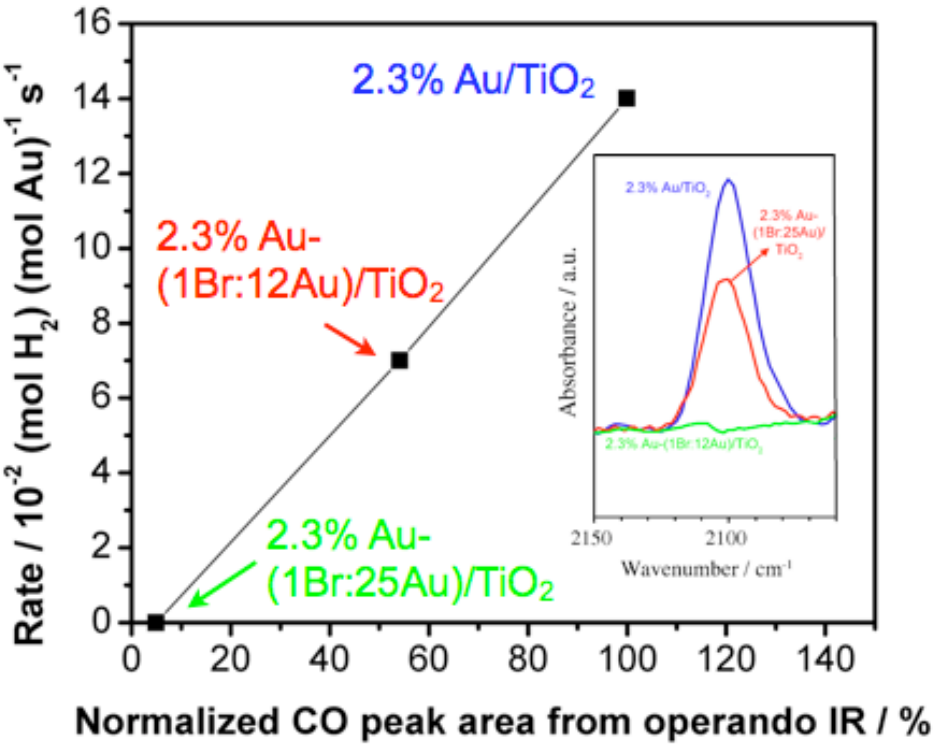

Figure 1.19: Data showing rate as a function of CO peak area that is bound to gold. The amount of bromide poisoning is shown beside each data point. [51]

1.7 Supported molecular iridium clusters for ethylene hydrogenation

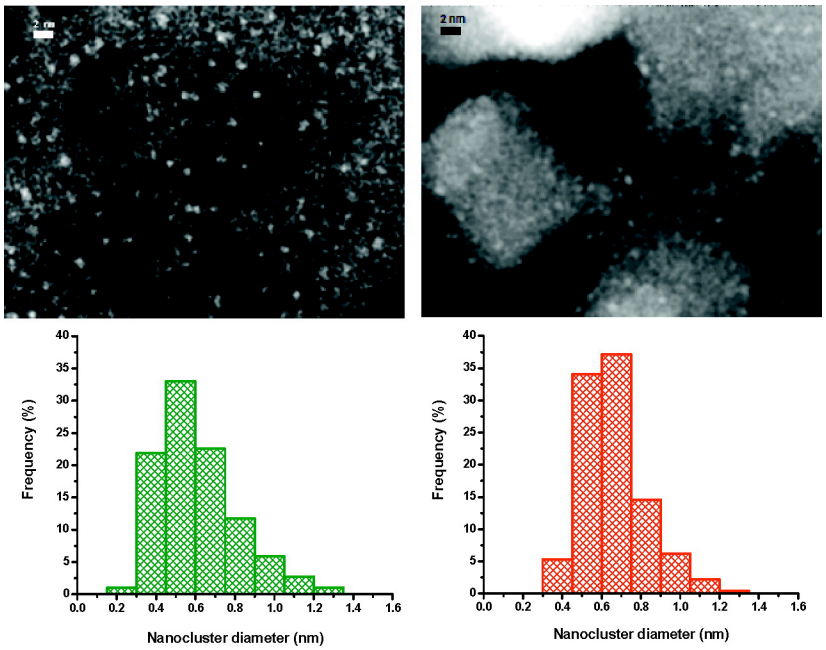

Figure 1.20: HAADF-STEM images of the Ir_4 cluster species supported on DAY zeolite (left) and MgO (right). The images show the presence of nearly uniform iridium clusters approximated as Ir_4 on both supports. [53]

An elegant example of a surface-as-macroscopic-ligand effect in catalysis is shown featuring results from the Gates research group. [53] The Gates group performed studies on both nuclearity and support effects in H_2—D_2 exchange and ethylene hydrogenation reactions with mononuclear and tetranuclear iridium clusters supported on either electron-withdrawing DAY zeolite or electron-donating MgO. HAADF-STEM, in-situ infrared spectroscopy, and EXAFS measurements gave valuable insight into the various active site interactions (metal-metal, metal-ligand/reactant, metal-support) that are important to make structure-function relationships. The appropriate controls were in place that verified using EXAFS and HAADF-STEM that the particle size does not change after catalysis with both the mononuclear and tetranuclear clusters, regardless of the support (Figure 1.20)

Two effects were noted in this study with regard to nuclearity and support effects. [53] Ir_4 clusters versus mononuclear Ir species had faster rates for both ethylene hydrogenation and H—D exchange reactions on both supports. The explanation behind this was that the Ir_4 cluster had more metal surface area available for both hydrogen dissociation and activation of the ethylene on nearby metal sites, two required processes for catalysis, relative to the mononuclear Ir complexes. [53]

The above observation has a direct bridge to homogeneous systems consisting of Wilkinson's catalyst $Rh(PPh_3)_3Cl$,[54] and the Ir analog of Wilkinson's catalyst $Ir(PPh_3)_3Cl$.[55] Wilkinson's catalyst is known to easily release a single phosphine to synthesize $Rh(PPh_3)_2Cl$, a metal complex consisting of an open site (vacancy) previously occupied by the phosphine. Both $Rh(PPh_3)_2Cl$ as well as $Ir(PPh_3)_3Cl$ are able to easily chemisorb and dissociate hydrogen, to form the dihydrido complexes. [54], [55], [56] However, $Ir(PPh_3)_3Cl$ does so to form a closed

(coordinatively unsaturated) six-coordinate Ir center, and is catalytically inactive for olefin hydrogenation. In stark contrast, the open remaining site in $Rh(PPh_3)_2(H)_2Cl$, which remains after hydrogen chemisorption, is able to interact with incoming olefin during hydrogenation catalysis. This results in a highly active olefin hydrogenation catalyst (save for ethylene which binds so strong that it competitively poisons the hydrogen binding site). [54], [55], [56] Thus, this last example demonstrates the crucial aspect of having olefin and hydrogen binding sites proximal to each other for olefin hydrogenation catalysis.

The support effects on the rate are more pronounced and more complicated. At cluster sizes this small, the support truly acts as a ligand by donating and accepting charge from the Ir core. Infrared spectra confirm the MgO-supported clusters had red-shifted CO ligands, consistent with its previously described role as electron donor ligand for noble metals. [53] It was observed that the rates of ethylene hydrogenation were higher on an electron-withdrawing DAY zeolite-supported catalyst than on an electron-donating MgO catalyst by a factor of 4.7-fold. H-D exchange was a factor of 15.8 greater on the DAY zeolite-supported catalyst. [53] IR spectroscopic evidence elucidated that there was no hydride visibly present on the MgO-supported catalysts while there were hydride species present on the zeolite-supported catalysts. EXAFS and IR spectroscopy both show adsorbed ethylene blocking sites on the MgO supported catalyst. The MgO-supported sample was therefore limited in its ability to dissociate hydrogen and was poisoned by ethylene reactant. Additionally, the H—D exchange reaction is much slower on the MgO-supported sample than on the zeolite-supported sample. [53] This observation suggests that hydrogen activation and not ethylene activation is the rate-limiting step with the MgO-supported catalysts.

There is a stark and direct contrast on the ethylene binding ability when comparing Gates's MgO-supported Ir mononuclear complex catalyst [53], which strongly binds ethylene over molecular hydrogen, and the homogeneous $Ir(PPh_3)_3Cl$, which binds hydrogen strongly but is unable to interact with ethylene. [55]

On the other hand, hydride and ethyl species were observed using IR on the zeolite-supported catalyst. The Gates group demonstrated that the zeolite support is able to facilitate hydrogen spillover whereas MgO does not do so as readily. [53] This contribution effectively demonstrates that while a reaction such as ethylene hydrogenation, as investigated here, may be structure-insensitive for larger particles (>2 nm), at molecular-level sizes, the reaction exhibits structure-sensitivity when ligands have a large effect on the metal. [53]

1.8 Summary and outlook

Beginning with Taylor's hypothesis stating that a minority of a metal surface is catalytically active to more recent examples showing that for some reactions open, undercoordinated sites are the most active, though not always the most selective sites, there is still much work left to undertake in catalyst design to achieve greater activities and more selectivity. New methods in catalyst synthesis such as changing the active site environment to modify existing heterogeneous catalysts through different organic or inorganic ligands show promise and may lead to more selective catalysts, which is a crucial area of focus in catalytic science in the 21st century. Novel organic ligand-bound catalysts with cluster sizes reaching sub-nanometer measurements have the potential to be very active catalysts not only by virtue of their small particle sizes but also by providing opportunities through the bound organic ligands to stabilize the open cluster sites as well as change the electronic state of the metal clusters. The

electronic tuning of the active site has the potential to favor the formation of one product over another leading to a more selective catalyst which could have broad impacts in reaction of current importance such as CO_2 reduction. [11]

1.9 References

[1] H.S. Taylor. *Proc. R. Soc. Lond. A* 108 (1925) 105.
[2] M. Boudart. *American Scientist* 57 (1969) 97.
[3] G.A. Somorjai, J. Carrazza. *Ind. Eng. Chem. Fundamen.* 25 (1986) 63.
[4] R. Van Hardeveld, F. Hartog. *Surf. Sci.* 15 (1969) 189.
[5] T.V.W. Janssens, B.S. Clausen, B. Hvolbaek, H. Falsig, C.H. Christensen, T. Bligaard, J.K. Nørskov. *Top. Catal.* 44 (2007) 15.
[6] J. Wei, E. Iglesia. *J. Phys. Chem. B* 108 (2004) 4094.
[7] R.L. Burwell, Jr., G.L. Haller, K.C. Taylor, J.F. Read. *Adv. Catal.* 20 (1969) 1.
[8] R. Vidruk, M.V. Landau, M. Herskowitz, V. Ezersky, A. Goldbourt. *J. Catal.* 282 (2011) 215.
[9] R. Vidruk, M.V. Landau, M. Herskowitz, M. Talianker, N. Frage, V. Ezersky, N. Froumin. *J. Catal.* 263 (2009) 196.
[10] A.B. Laursen, I.C. Man, O.L. Trinhammer, J. Rossmeisl, S. Dahl. *J. Chem. Educ.* 88 (2011) 1711.
[11] A.A. Peterson, J.K. Nørskov. *J. Phys. Chem. Lett.* 3 (2012) 251.
[12] L. Quintanar, J. Yoon, C.P. Aznar, A.E. Palmer, K.K. Andersson, R.D. Britt, E.I. Solomon. *J. Am. Chem. Soc.* 127 (2005) 13832.
[13] J.R. Banavar, A. Maritan. *Annu. Rev. Biophys. Biomol. Struct.* 36 (2007) 261.
[14] N. de Silva, J.-M. Ha, A. Soloyvov, M.M. Nigra, I. Ogino, S. Yeh, K. Durkin, A. Katz. *Nature Chem.* 2 (2010) 1062.
[15] A. Okrut, O. Gazit, N. de Silva, R. Nichiporuk, A. Solovyov, A. Katz. *Dalton Trans.* 41 (2012) 2091.
[16] H. Beinert. *J. Biol. Inorg. Chem.* 5 (2000) 2.
[17] J.-M. Ha, A. Solovyov, A. Katz. *Langmuir* 25 (2009) 10548.
[18] N. de Silva, A. Soloyvov, A. Katz. *Dalton Trans.* 39 (2010) 2194.
[19] X. Lin, B. Yan, H.-J. Benia, P. Myrach, M. Yulikov, A. Aumer, M.A. Brown, M. Sterrer, O. Bondarchuk, E. Kieseritzky, J. Rocker, T. Risse, H.-J. Gao, N. Nilius, H.-J. Freund. *J. Am. Chem. Soc.* 132 (2010) 7745.
[20] G. Pacchioni, H. Freund. *Chem. Rev.* 113 (2013) 4035.
[21] S. Shetty, S. Strych, A.P.J. Jansen, R.A. van Santen. *Can. J. Chem.* 87 (2009) 824.
[22] G.J. Blyholder, *Phys. Chem.* 68 (1964) 2772.
[23] A. Fielicke, G. von Helden, G. Meijer, D.B. Pedersen, B. Simard, D.M. Rayner. *J. Chem. Phys.* 124 (2006) 194305.
[24] P. Chini. *J. Organomet. Chem.* 152 (1978) C35–C38.
[25] R. Van Santen, M. Neurock, *Molecular Heterogeneous Catalysis*, WILEY-VCH Verlag GmbH & Co. KGaA, Weinheim, 2006.
[26] N. Lopez, T.V.W. Janssens, B.S. Clausen, Y. Xu, M. Mavrikakis, T. Bligaard, J.K. Norskov. *J. Catal.* 223 (2004) 232.
[27] G.F. Stuntz, J.R. Shapley, *J. Am. Chem. Soc.* 99 (1977) 607.
[28] D.C. Sonnenberger, J.D. Atwood, *J. Am. Chem. Soc.* 104 (1982) 2113.

[29] J.K. Norskov, T. Bligaard, A. Logadottir, S. Bahn, L.B. Hansen, M. Bollinger, H. Bengaard, B. Hammer, Z. Sljivancanin, M. Mavrikakis, Y. Xu, S. Dahl, C.J.H. Jacobsen. *J. Catal.* 209 (2002) 275.
[30] Y. Iwasawa, R. Mason, M. Textor, G.A. Somorjai, *Chem. Phys. Lett.* 44 (1976) 468.
[31] M. Okurmura, M. Haruta, Y. Kitagawa, K. Yamaguchi, *Gold Bulletin* 40 (2007) 40.
[32] B. Yoon, H. Hakkinen, U. Landman, *J. Phys. Chem. A* 107 (2003) 4066.
[33] A. Franceschetti, S.J. Pennycook, S.T. Pantedlides *Chem. Phys. Lett.* 374 (2003) 471.
[34] H. Hakkinen, S. Abbet, A. Sanchez, U. Heiz, U. Landman. *Angew. Chemie Int. Ed.* 42 (2003) 1297.
[35] A. Sanchez, S. Abbel, U. Heiz, W. D. Schneider, H. Hakkinen, R.N. Barnett, U. Landman. *J. Phys. Chem. A* 103 (1999) 9573.
[36] I.D. Socaciu, J. Hagen, T.M. Bernhardt, L. Woste, U. Heiz, H. Hakkinen, U. Landman, *J. Am. Chem. Soc.* 125 (2003) 10437.
[37] L.M. Molina, B. Hammer, *J. Catal.* 233 (2005) 399.
[38] P. Chen, X. Zhou, H. Shen, N. M. Andoy, E. Choudhary, K.-S. Han, G. Liu, W. Meng. *Chem. Soc. Rev.* 39 (2010) 4560.
[39] W. Xu, J.S. Kong, Y.-T.E. Yeh, P. Chen. *Nat. Mater.* 7 (2008) 992.
[40] W. Xu, J.S. Kong, P. Chen. *Phys. Chem. Chem. Phys.* 11 (2009) 2767.
[41] X. Zhou, W. Xu, G. Liu, D. Panda, P. Chen. *J. Am. Chem. Soc.* 132 (2010) 136.
[42] C.J. Bueno, Alejo, C. Fasciani, M. Greiner, J.C. Netto-Ferreira, J.C. Scaiano. *Catal. Sci. Technol.* 1 (2011) 1506.
[43] X. Zhou, N.M. Andoy, G. Liu, E. Choudhary, K.-S. Han, H.S. Chen, P. Chen. *Nat. Nanotechnol.* 7 (2012) 237.
[44] M.M. Nigra, I. Arslan, A. Katz *J. Catal.* 295 (2012) 115.
[45] J. Lu, B. Fu, M.C. Kung, G. Xiao, J. W. Elam, H.H. Kung, P. Stair. *Science* 335 (2012) 1205.
[46] S. Helveg, C. Lopez-Cartes, J. Sehested, P.L. Hansen, B.S. Clausen, J.R. Rostrup-Nielsen, F. Abild-Pedersen, J.K. Norskov. *Nature* 427 (2004) 426.
[47] S.M. Oxford, J.D. Henao, J.H. Yang, M.C. Kung, H.H. Kung. *Appl. Catal. A.* 339 (2008) 180.
[48] A. Carlsson, A. Puig-Molina, T.V.W Janssens, *J. Phys. Chem. B* 110 (2006) 5286.
[49] B.D. Chandler, S. Kendell, H. Doan, R. Korkosz, L.C. Grabow, C.J. Purcell. *ACS Catal.* 2 (2012) 684.
[50] M.C. Kung, R.J. Davis, H.H. Kung. *J. Phys. Chem. C,* 111 (2007) 11767.
[51] M. Shekhar, J. Wang, W.-S. Lee, M.C. Akatay, E.A. Stach, W.N. Delgass, F.H. Ribeiro. *J. Catal.* 293 (2012) 94.
[52] W.D. Williams, M. Shekhar, W.-S. Lee, V. Kispersky, W.N. Delgass, F.H. Ribeiro, S.M. Kim, E.A. Stach, J.T. Miller, L.F. Allard. *J. Am. Chem. Soc.* 132 (2010) 14018.
[53] J. Lu, P. Serna, C. Aydin, N.D. Browning, B.C. Gates. *J. Am. Chem. Soc.* 133 (2011) 16186.
[54] J.A. Osborn, F.H. Jardine, J.F. Young, G. Wilkinson. *J. Chem. Soc. A* (1966) 1711.
[55] M.A. Bennett, D.L. Milner. *J. Am. Chem. Soc.* 91 (1969) 6983.
[56] J.P. Collman, M. Kubota, F.D. Vastine, J.Y. Sun, J.W. Wang *J. Am. Chem. Soc.* 90 (1968) 5430.

CHAPTER 2:

Gold nanoparticle-catalyzed reduction in a model system: Quantitative determination of reactive heterogeneity of a supported nanoparticle surface

a collaboration between
Michael Nigra, Ilke Arslan, and Alexander Katz

Reprinted from *Journal of Catalysis*, Vol 295, Michael M. Nigra, Ilke Arslan, and Alexander Katz, Gold nanoparticle-catalyzed reduction in a model system: Quantitative determination of reactive heterogeneity of a supported nanoparticle surface, pages 115-121, Copyright (2012), with permission from Elsevier. Available online at: http://dx.doi.org/10.1016/j.jcat.2012.08.001

Abstract

Kinetic poisoning experiments employing organic ligands were conducted using a gold nanoparticle-catalyzed reaction consisting of the reduction of resazurin to resorufin. The kinetic contributions of three distinct types of sites along with the number density of each of these site types during reaction were determined. The calculated number densities of each of the three types of sites, hypothesized to be corners, edges, and terraces, correlates well with atomic-resolution micrographs of the supported gold nanoparticles, obtained using aberration-corrected transmission electron microscopy and with predictions based on geometric models of idealized gold nanoparticles. The most active sites comprising 1% of the surface atoms exhibit at least 30% of the total activity of the catalyst for resazurin reduction. The selective mechanical blocking of surface sites on nanoparticles, particularly undercoordinated sites, paves the way for novel approaches utilizing organic ligands to quantify the activity of different active sites and control catalysis on metal surfaces.

2.1 Introduction

Metal surfaces of a working catalyst have long been known to be heterogeneous in nature and have been hypothesized to consist of several distinct types of active sites for catalysis and adsorption [1] and [2]. These effects contribute to the structure sensitivity of certain chemical reactions as proposed by Boudart *et al*. [3] and [4], and a relevant goal in understanding catalysis employing heterogeneous metal surfaces is the quantification of the number and the catalytic contributions of different active sites present under reaction conditions. As an example, coordinatively unsaturated corner and edge atoms have been shown to be the most active sites on the surface of unsupported metals for some reactions [5]. Early work has shown these types of sites to dissociatively chemisorb CO on a Pt surface [6] and, more recently, in gold cluster-catalyzed reactions, coordinatively unsaturated corner sites have been invoked as the relevant active sites for ammonia synthesis [7], oxygen dissociation [8] and [9], propylene and acrolein oxidation [10], hydrogenolysis [11], CO oxidation [12], [13] and [14], coking [11] and [15], and water–gas shift reactions [16] and [17]. However, the quantification of deconvoluted catalytic rates of different types of sites and elucidation of structural features on a metal surface that could be responsible for these individual rates have remained a largely unresolved challenge. A commonly used method for experimentally determining the contributions of different sites is by poisoning or blocking specific types of sites and observing the changes in reactivity and/or selectivity that result under reaction conditions. Pioneering studies by Kung *et al*. demonstrate through kinetic poisoning experiments employing bromide ion that CO oxidation activity on Au/TiO_2 catalysts could be entirely suppressed by bromide, which preferentially attaches to the most coordinatively unsaturated sites [13], and similar types of kinetic poisoning experiments have been reported in other systems [12]. More recent studies demonstrate that coordinatively unsaturated sites are responsible for coking on supported Pd catalysts through a process that selectively blocks the coordinatively unsaturated sites with an alumina overcoat layer [15].

A lofty goal and largely unmet challenge when using kinetic poisoning experiments has been assessing the number density and activity of the most reactive sites, which are titrated under the most dilute conditions during kinetic poisoning. Here, in this manuscript, we use the specific chemisorption of organic ligands under reaction conditions to, for the first time by poisoning ~1% of the surface metal atoms, determine the individual catalytic contribution of the most

reactive sites. Our approach uses a model gold nanoparticle–catalyzed reaction system consisting of the aqueous-phase reduction of resazurin to resorufin using hydroxylamine as reductant. This model system was chosen specifically because the active site is found on the gold surface of nanoparticles in solution in the absence of a support; thus, it does not require the role of a support or perimeter sites [18], [19], [20] and [21]. Indeed, in order to minimize any possible role of other effects such as support and perimeter sites, we have used an inert support consisting of TMS-capped (trimethylsilyl-capped) silica. This support serves the purpose of anchoring our gold nanoparticles so as to preserve gold nanoparticle size and integrity during kinetic poisoning experiments, while minimizing complications due to possible catalytically relevant interactions between support and metal nanoparticle. Our approach employs triphenylphosphine (TPP) and dodecanethiol (DDT) probe molecules for kinetic poisoning experiments. These ligands are chemisorbed to the gold surface at submonolayer coverages and are chosen to investigate whether ligand binding to our gold nanoparticles also contributes electronic effects as a result of ligand chemisorption on catalysis. TPP synthesizes electron-rich gold [22] and [23], whereas a thiolate chemisorbed layer when using DDT results in a significantly *d*-charge depleted gold surface [23] and [24]. Our hypothesis is that if both chemisorption of TPP and DDT have the same effect on catalysis, then mechanical site blocking of an active site is solely responsible for the observed effects, rather than electronic effects resulting from the chemisorbed organic ligand. Also, as a control for a non-binding ligand, dodecylamine (DDA) is used to demonstrate lack of catalytic response when kinetic poisoning does not occur due to lack of strong ligand chemisorption [25] and [26].

The model reaction system of resazurin reduction to resorufin using hydroxylamine as reductant has been previously investigated using fluorescence microscopy by Chen *et al*. using gold and carbon nanotubes as electron transfer catalysts. Though the molecular-level mechanism of the reduction is complex and not fully understood [27], previously measured kinetics on gold display a Langmuir–Hinshelwood profile, which requires the adsorption of resazurin to the gold surface [18], [19], [20] and [21]. It is reasonable to therefore postulate that this adsorption event benefits from having a coordinatively unsaturated site, and thus kinetics of this reaction could depend on degree of site coordinative unsaturation. Elegant spatial mapping of the active sites on the carbon nanotube using microscopy demonstrated the non-uniformity of the catalytically active surface, in that defect sites and/or carbon nanotube ends (i.e., not the nanotube sidewall) were observed to be the active sites for this reaction. Recent catalytic spatial mapping results using gold nanorods with the reaction of Amplex Red to the same resorufin product demonstrate that defect sites on the surface and ends of the gold nanorods are sites that are most active for this reaction. These sites are known to consist of greater coordinatively unsaturated site density than in the rod center [28]. However, quantification of the numbers of these active sites as a fraction of the total and their activity could not be achieved due to lack of required spatial resolution [18] and [28]. This quantification forms the goal of this manuscript, particularly the quantification of the most active sites.

2.2 Experimental

2.2.1 Synthesis of Au/TMS-SiO_2 catalyst

Gold nanoparticles were synthesized on a silica using a method previously described by Zanella *et al*. [29] In brief, a gold(III) ethylenediamine chloride complex was synthesized [30]

and was impregnated onto silica (Aerosil 200, Degussa) by adding 1 g of silica (pretreated in oven at 110°C) to a 100 mL aqueous solution of a 4 mM gold(III) ethylenediamine complex at 45°C and stirring for 16 h. The solid was then filtered and dried under vacuum. The sample was then treated in pure hydrogen (99.999% UHP, Praxair) at 200 °C (ramp rate, 2 °C/min) for 4 h at a hydrogen flow rate of 75 mL/min. After cooling to room temperature, the silica surface was then capped with trimethylsilyl groups using a previously published procedure [31], using N-methyl-N-(trimethylsilyl)trifluoroacetamide (MSTFA) as a capping agent. In this surface-capping step, 500 mg of the Au/SiO_2 catalyst was added to a solution of 10 g of toluene and 2.5 g of MSTFA and was stirred at room temperature for 2 h. The solid was then filtered and washed with toluene and methanol and dried overnight in air. Afterward, the catalyst was dried in an oven at 120°C for 4 h and was then placed in a darkened vial for storage ($Au/TMS\text{-}SiO_2$).

2.2.2 Titration of Au nanoparticle surface with organic ligands

30 mg of $Au/TMS\text{-}SiO_2$ catalyst was mixed with 10 mL of dichloromethane (HPLC grade) solvent, and the amount of ligand (either DDT, TPP, or DDA) dissolved in dichloromethane needed to achieve the desired fractional monolayer coverage was added. After 1 h, the catalyst was filtered, washed with 50 mL of dichloromethane, and dried overnight.

2.2.3 Resazurin reduction reaction

Five milligrams of organic ligand-bound $Au/TMS\text{-}SiO_2$ was added to a 10 μM resazurin (2:1 isopropanol:DI water solvent) solution. To this solution was added 20 μL of a 0.163 M NH_2OH-DI water solution in the dark. The isopropanol was HPLC grade from EMD, and the DI water was purified using a Barnstead Nanopure system to 18 MΩ. The solution was shaken for 10 s and then left to rest in the dark. An aliquot of 20 μL of the reaction mixture was added to 5 mL of an isopropanol/water mixture (2 isopropanol/1 water by volume), and the fluorescence emission intensity was measured using a Hitachi F-4500 fluorimeter operating at an excitation wavelength of 532 nm. Other fluorimeter settings were slit size: 5.0 nm, PMT voltage: 950 V, and scan rate: 240 nm/min. The resorufin product fluoresces at 588 nm, and the measurement of that emission wavelength allows for a linear correlation between resorufin concentration and fluorescence intensity (*vide infra*). Rates were calculated based on these measurements.

2.2.4 Transmission electron microscopy measurements

Low magnification HAADF-STEM images were recorded using a 200 kV F20 UT Tecnai microscope at the National Center for Electron Microscopy at Lawrence Berkeley National Laboratory. At least 200 particles were measured to obtain a particle size distribution. The atomic-resolution images were acquired on a (probe) aberration-corrected 300 kV FEI Titan instrument at the Environmental Molecular Sciences Laboratory at the Pacific Northwest National Laboratory. The samples were dry-loaded onto a holey-carbon copper grid for both sets of experiments.

2.2.5 UV-Vis spectroscopy measurements

Liquid phase UV-Vis measurements were recorded to characterize the amount of triphenylphosphine remaining in solution after binding to the supported catalyst, upon filtering the slurry containing the catalyst through a 0.7-μm syringe filter. A 1-mL aliquot of the solution was removed and analyzed. Absorption spectra were recorded from 400 nm to 260 nm, with a step size of 0.5 nm and a time per data point of 0.166 s, using a Varian Cary 4000 UV-Vis spectrometer.

Solid-state UV-Vis measurements were taken to observe whether there is gold nanoparticle aggregation upon ligand binding. Samples were measured that had been treated with 0.5 monolayer equivalent of either TPP or DDT. A Teflon reference was used, and scans were taken from 800 nm to 400 nm, with a step size of 0.5 nm and a time per data point of 0.166 s, using a Varian Cary 4000 UV-Vis spectrophotometer.

2.3 Results and discussion

2.3.1 Catalyst characterization and active site titration with organic ligands

An important goal in the understanding of heterogeneous catalysis is quantification of the rate per site and number density of different sites under reaction conditions, for solid catalysts consisting of a distribution of reactive sites. Using the gold nanoparticle-catalyzed reduction of resazurin to resorufin as a model system, our approach relies on kinetic poisoning experiments using submonolayer coverages of organic ligands adsorbed onto the gold nanoparticle catalyst and is shown in Scheme 2.1. The heterogeneous catalyst consists of gold nanoparticles anchored on the surface of TMS-capped silica. These nanoparticles are characterized using HAADF-STEM in Figure 2.1 and Figure 2.2. These data demonstrate a 3.5 nm ± 0.7 nm (3.7 nm based on gold nanoparticle mass-weighted distribution) average size of the supported gold nanoparticles, which does not change as a result of organic ligand chemisorption. This result is further supported by the lack of observed change in the surface-plasmon band before and after ligand chemisorption, when using diffuse-reflectance UV-Vis spectroscopy, as shown in Figure 2.3. Similar data demonstrating lack of change to the supported gold nanoparticle size have also been observed after reduction catalysis and kinetic poisoning experiments. The lack of observed changes to the nanoparticle size during organic ligand chemisorption and catalysis may be facilitated by the anchored nature of the gold nanoparticles, since, previously, adsorption of organic ligands such as thiolates and phosphines onto gold have been shown to lead to nanoparticle aggregation [32], particularly at submonolayer coverages [22].

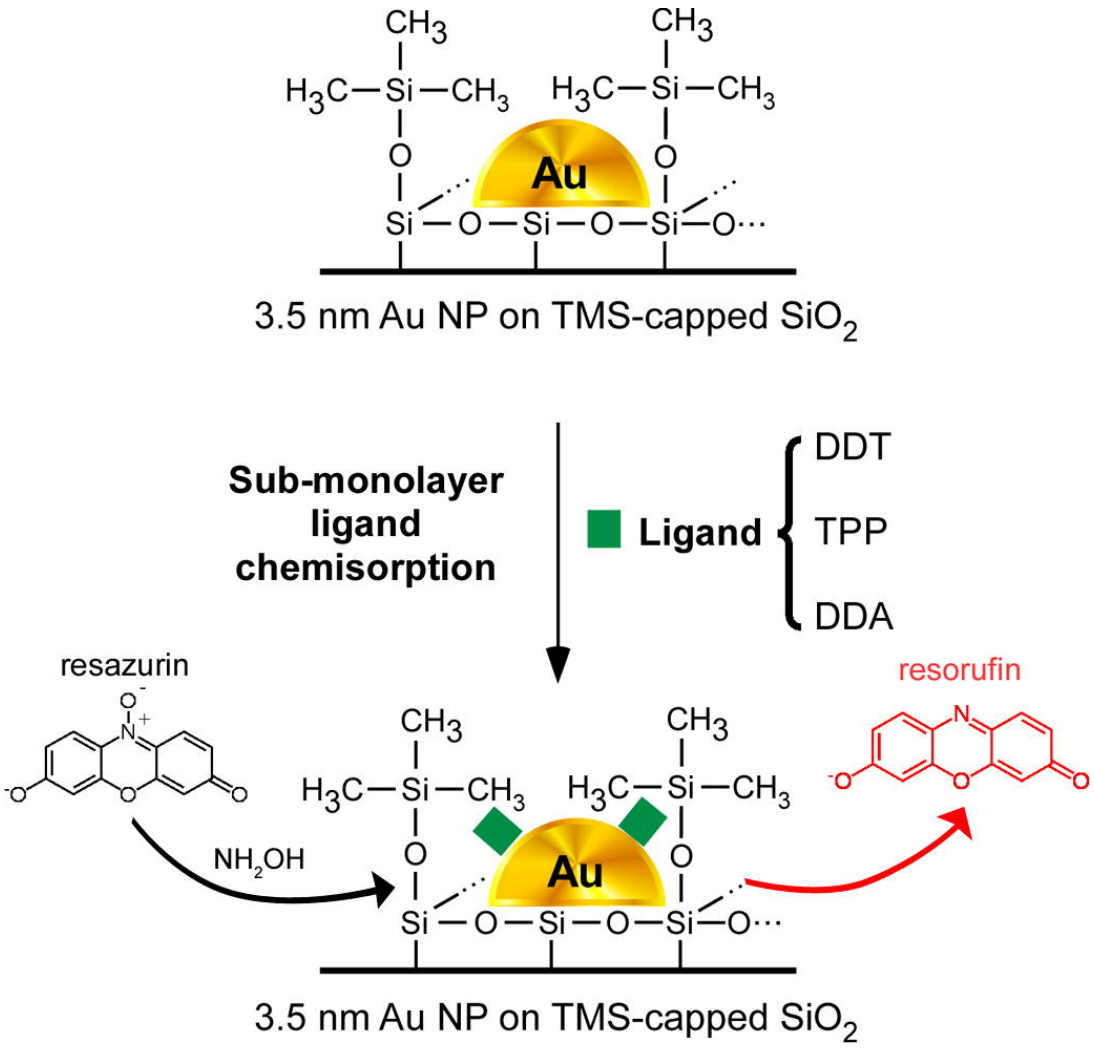

Scheme 1: Kinetic poisoning experiments involving organic ligand binding at submonolayer coverages to gold nanoparticles supported on TMS-capped silica, during resazurin reduction.

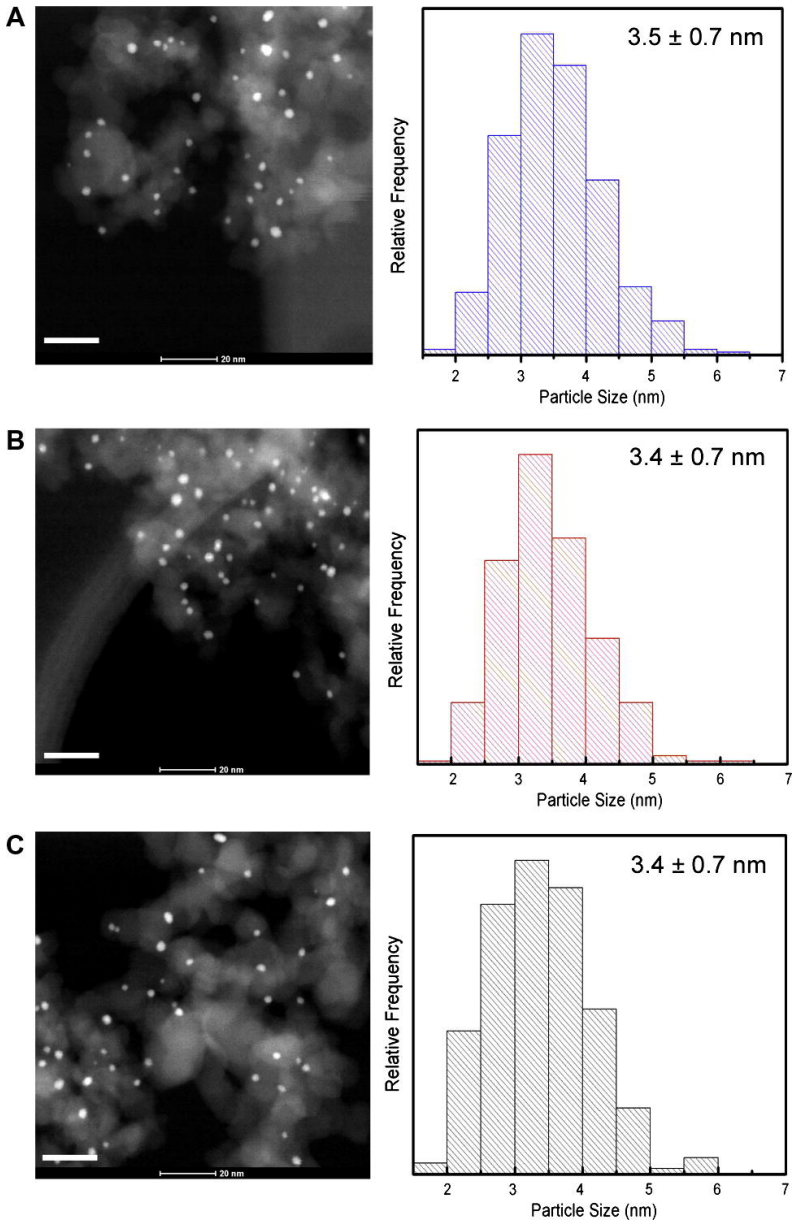

Figure 2.1: Representative HAADF-STEM micrographs of Au nanoparticles on TMS-capped SiO_2. Particle size distributions for each sample are shown beside each micrograph in the right panel. (a) No organic ligand bound to Au nanoparticle surface. (b) 0.5 monolayer equivalents of DDT bound to the Au nanoparticle surface. (c) 0.5 monolayer equivalents of TPP bound to the Au nanoparticle surface.

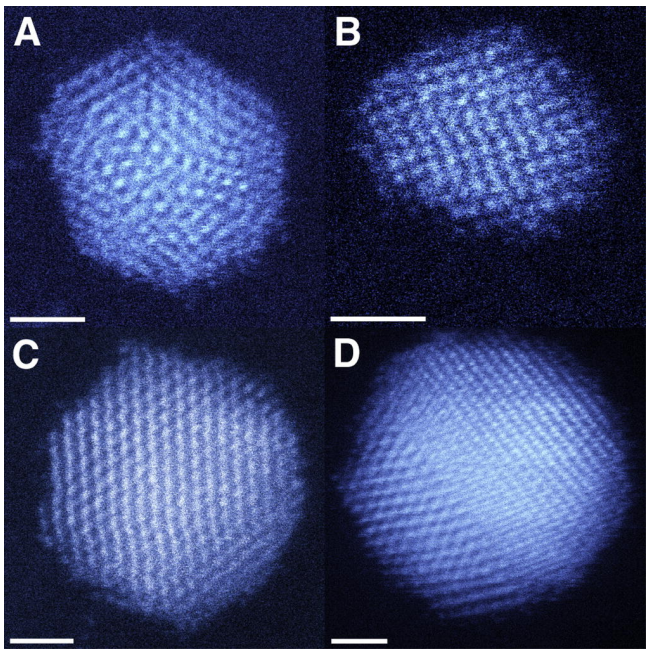

Figure 2.2: (A) through (D) representative aberration-corrected micrographs of Au nanoparticles on TMS-capped SiO_2. The scale bar in each panel represents 1 nm.

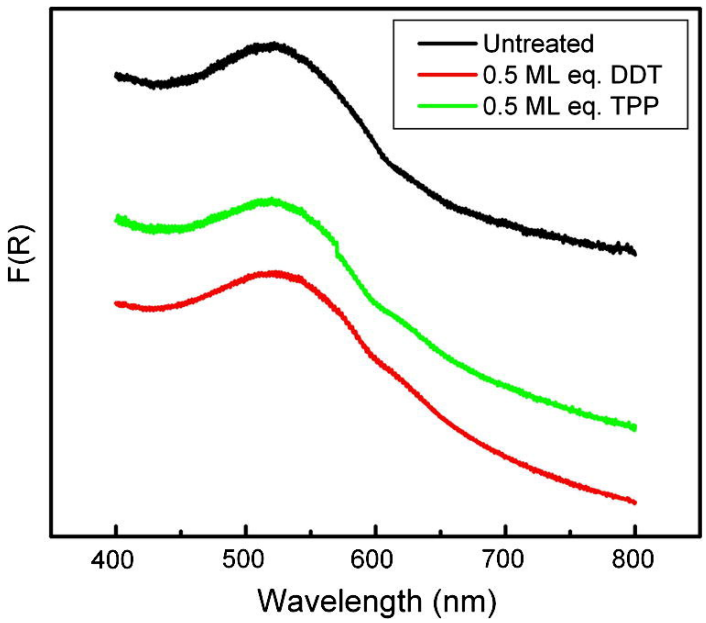

Figure 2.3: Diffuse-reflectance UV-Vis spectra of catalysts before and after organic ligand binding. Virtually no change in the surface-plasmon band spectra is observed upon ligand binding, indicating the absence of gold nanoparticle aggregation.

A degradation reaction was observed when treating TPP with gold nanoparticles on an uncapped (i.e., native silanol containing) silica support. The green curve in Figure 2.4 illustrates the consequences of this reaction by following the near-complete consumption of an amount of TPP corresponding to 2.5 monolayers of coverage, when using gold nanoparticles on an uncapped silica support. This TPP degradation reaction was prevented by capping silanols native to the silica surface with TMS functionality. The red curve in Figure 2.4 demonstrates the consumption of an amount of TPP corresponding to a single monolayer coverage for this case (based on the 3.5 nm diameter size of the supported gold nanoparticles, the known footprint of TPP on gold nanoparticles [33], and the 1.3% gold loading in our materials). Data in Table 2.1 summarize the results of several experiments consisting of treating gold nanoparticles anchored on TMS-capped silica with TPP, as followed spectrophotometrically, and show that a single monolayer of TPP is consumed even when treating such gold nanoparticles with excess TPP. The data above indicate that the measured geometrical area calculated on the basis of TPP chemisorption is consistent with TEM and ICP-OES elemental analysis and that the undesired degradation reaction of TPP in the presence of Au on native silanol-containing silica is circumvented. These results permit the selective placement of organic ligand groups on the metal surface and enable the number counting of blocked sites during kinetic poisoning experiments.

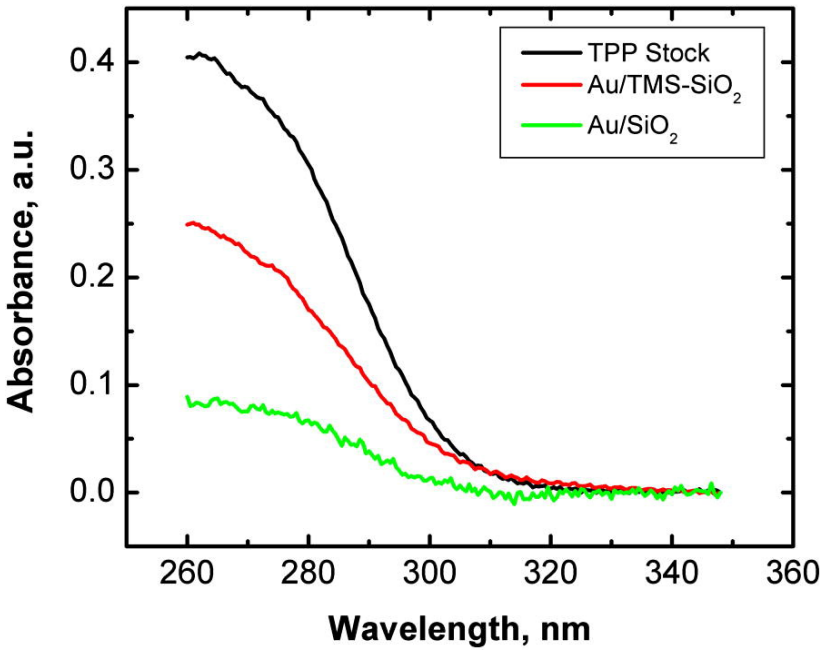

Figure 2.4: Triphenylphosphine binding experiments with gold nanoparticles on (green) silica and (red) TMS-capped silica. Approximately 2.5 monolayer equivalents of TPP were added to each sample. The figure illustrates that much more TPP is consumed on the uncapped support (green) than on the capped support, and this is due to TPP degradation/side reaction. By capping silanols with TMS groups, this overconsumption of TPP is arrested, and a maximum of 1.0 monolayer equivalents of TPP is bound, as expected for chemisorption only (i.e. in the absence of degradation/side reaction) based on the footprint for TPP adsorbed on gold nanoparticles.

Table 2.1: Binding capacity of Au/TMS-SiO_2 catalysts. The catalysts are able to bind as much TPP as corresponding to a single monolayer, with no significant overconsumption or underconsumption.

Sample	Monolayer equivalents of TPP added	Monolayer equivalents of TPP consumed
1	0.50	0.50
2	2.0	0.97
3	2.5	1.08

2.3.2 Kinetic consequences of active site blocking with organic ligands

Figure 2.5 represents the normalized pseudo first-order rate constant of the reduction reaction during kinetic poisoning experiments, which involve submonolayer organic ligand coverages corresponding to 0.005–1 fraction of a chemisorbed monolayer (a representative kinetic first-order rate constant analysis is shown in Supplementary information). Ligand DDA served as a control consisting of a ligand that was not expected to strongly chemisorb to the gold surface under the protic solvent reaction conditions [25] and [26]. This was manifested by virtually no change in the reaction rate upon addition of DDA to the catalyst, as shown in Figure 2.5.

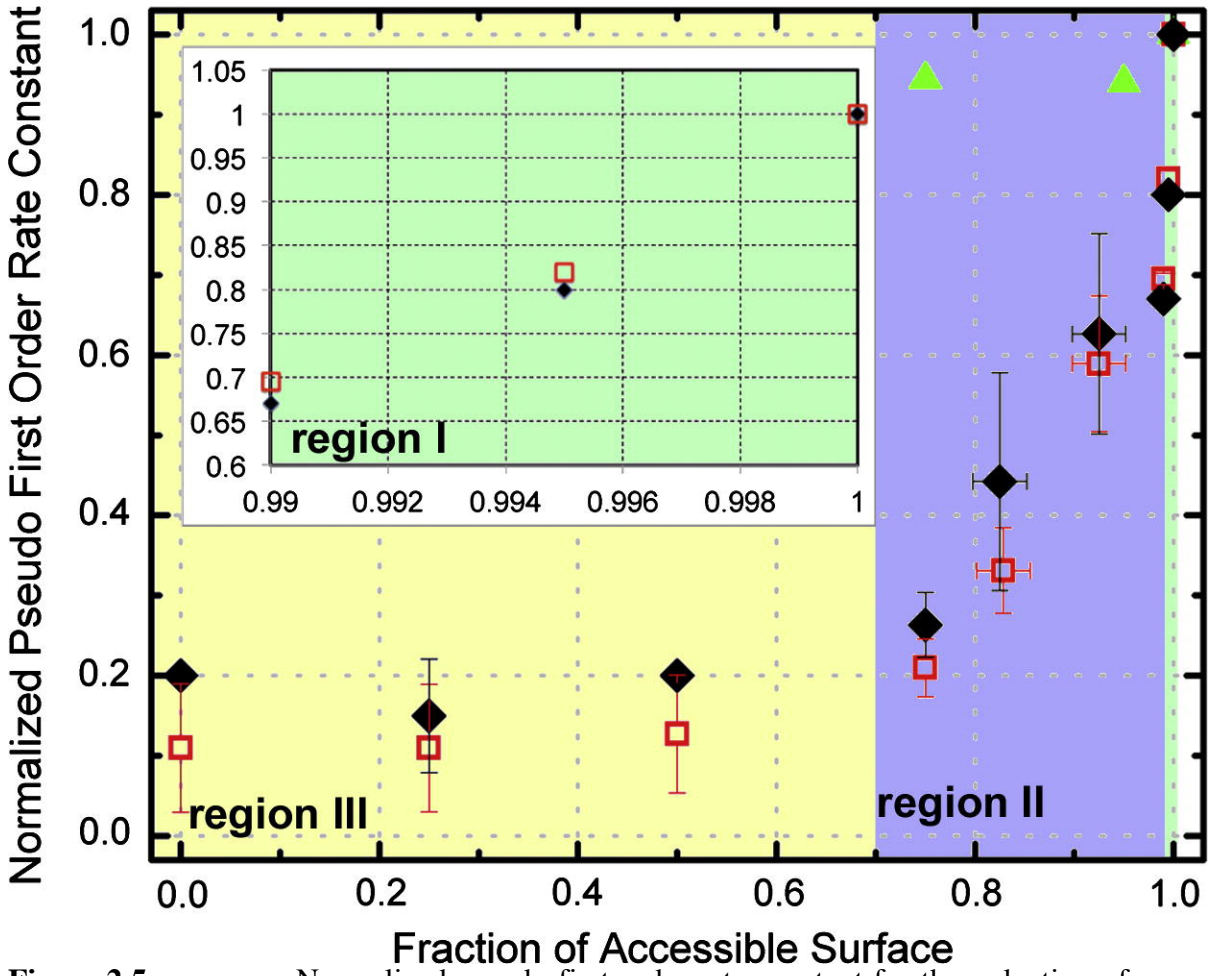

Figure 2.5: Normalized pseudo first-order rate constant for the reduction of resazurin to resorufin on organic ligand-bound Au nanoparticles supported on TMS-capped silica, with varying degrees of accessible gold surface. TPP (♦), DDT (□), and DDA (▲) are used as ligands to block gold surface active sites during the course of kinetic poisoning experiments. (Inset) Represents a zoom into the high fraction of accessible surface region of main figure for TPP (♦) and DDT (□).

The undistinguishable effect on rate when binding either TPP, which results in an electron-deficient (*d*-charge depleted) gold surface [22] and [23], or DDT, which results in an electron-rich gold surface [23], [34] and [35] during kinetic poisoning in Figure 2.5, means that the effect of the organic ligand binding is simply a mechanical site blocking. Otherwise, if these were not the case, electronic contributions to the rate as a result of organic ligand binding would be expected to manifest radically different effects for DDT and TPP on rate, given their different roles for depleting/adding d-orbital occupancy to bound gold surface atoms. Such a result may be due to the large (bulk) size of the gold nanoparticles used in this study (3.5 nm diameter), which change their electronic properties in response to organic ligand adsorption in only a slight fashion as previously measured via XPS [22] relative to smaller sub-nanometer clusters [23]. The lack of observed electronic effect during our kinetic poisoning experiments is consistent with previous observations of lack of electronic effect during kinetic poisoning experiments when using bromide anion, on 2-nm gold nanoparticles supported on TiO_2[13].

A uniform linear decrease in the resazurin reduction rate versus percentage of blockage of gold nanoparticle surface would be consistent with a single type of site responsible for catalytic activity in this system. Yet data in Figure 2.5 clearly show different linear regimes as indicated by the different slopes as a function of organic ligand fractional monolayer coverage. These regimes are shaded in different colors in Figure 2.5 for clarity. The different observed regimes suggest the possibility of multiple distinct types of active sites for catalysis, which differ in activity as indicated by the respective slopes of Figure 2.5 in each regime. The three regimes comprising Figure 2.5 are summarized in Table 2.2 (*vide infra*).

Table 2.2: Relative differences in activity between regions in Figure 2.5

Region of Figure 2.5 and proposed site type	**Catalytic activity nM/s/specific site * 10^{-3}**	**Relative turnover frequency**
I and Corners	41	17
II and Edges	2.5	1
III and Terraces	0	0

The inset data in Figure 2.5 focus on the least amount of gold surface-site blockage corresponding to a maximum of 0.01 fraction of a chemisorbed monolayer of either TPP or DDT and is labeled as region I in Figure 2.5. This amount of blockage resulted in a 30% decrease in rate constant in region I. The abrupt observed decrease in slope in Figure 2.5 at fractional chemisorbed monolayer coverages above 0.01 indicates that the number of most highly active sites present as a fraction of the total gold surface atoms is approximately 1%. Data in Figure 2.5 exhibit a further uniform decrease in the reaction rate within the range of fractional monolayer coverages corresponding to 0.01–0.3 for both TPP and DDT ligands in region II. This indicates the presence of a second type of uniform site, which becomes saturated at a coverage of 0.3 of a monolayer. The remaining region III in Figure 2.5 indicates the presence of a third type of uniform site, which consists of a near-zero slope as a function of TPP/DDT surface coverage up to a single monolayer. These surface sites appear not to contribute to the observed catalyzed rate of reaction. The lack of observed activity in region III sites (at higher fractional monolayer coverages) is similar to previous observations during kinetic poisoning experiments using supported 2 nm Au/TiO_2 catalysts using bromide anion, where at 10% coverage of surface gold with bromide, the remaining sites possessed no catalytic activity [13]. Lastly, there is a residual

catalytic activity of sites at full monolayer coverage, which is manifested in a clear non-zero *y*-intercept in Figure 2.5. This result suggests that there are some sites that cannot be blocked by either TPP or DDT ligands and yet that are accessible to reactants for catalysis.

When using strongly interacting ligands such as either DDT or TPP, we hypothesize that the most coordinatively unsaturated sites will be titrated preferentially during kinetic poisoning experiments. Such an outcome is based on the reasonable supposition that the most coordinatively unsaturated sites will have the strongest binding affinity for the organic ligands. This is supported by previous experimental observations and DFT (density functional theory) calculations, when using inorganic blocking agents for kinetic poisoning experiments [11], [12] and [13]. Based on this, we suggest that region I might correspond to corners, region II might correspond to edges, and region III might correspond to terrace sites above. This assignment is summarized in Table 2.2 and is further supported with geometric models in discussion below.

Furthermore, Figure 2.5 shows a small residual catalytic activity present even when blocking all accessible surface sites, with either TPP or DDT ligand, and this corresponds to roughly 15% of the unblocked activity, based on the *y*-intercept in Figure 2.5. This observation is not isolated or without precedent. Residual catalytic activity upon saturating metal surfaces with a monolayer of organic ligand has been previously observed on alkanethiol-monolayer-covered Pd catalysts for selective hydrogenation of unsaturated epoxides [36] and [37]. We wished to investigate whether the observed residual catalytic activity after binding a monolayer of organic ligands to our gold nanoparticles was due to the same type of catalytic site as responsible for catalysis on an unblocked gold surface. Previous results on gold nanoparticle–catalyzed reduction of resazurin to resorufin demonstrate that this system exhibits Langmuir–Hinshelwood kinetics, with K_m = 4.9 μM [21] and [38]. The residual sites consisting of a gold surface after full monolayer coverage of TPP binding also display Langmuir–Hinshelwood kinetics, as shown by data in Figure 2.6. These saturation kinetics preclude catalysis without resazurin reactant binding as a possible background reaction occurring on the residual sites. Our measured K_m of 5.4 μM in Figure 2.6 is fully consistent with that measured above for an unblocked gold nanoparticle surface, but a direct comparison with prior results is unwarranted given the slightly different particle size of 6 nm used in the previously measured data set [21] and [38]. This suggests the same type of solid site being active on an unblocked gold nanoparticle as on the residual sites after a monolayer of organic ligand binding and further implies that the residual sites consist of region I or II in order to exhibit catalytic activity. When also taking into consideration the activity of residual (sites that are untitratable during kinetic poisoning experiments) sites, there are two possible extreme scenarios: either (i) all of the residual sites are region I sites or (ii) all of the residual sites are region II sites. If all of the residual sites are region I sites, then the total fraction of these sites on the surface is 1.5%, and for the case that the residual sites are all region II sites, then the total fraction of these sites on the surface is 38%, in order to account for the observed residual catalytic activity. It may be that the residual sites use some combination of these extremes consisting of both region I (corner) as well as region II (edge) sites.

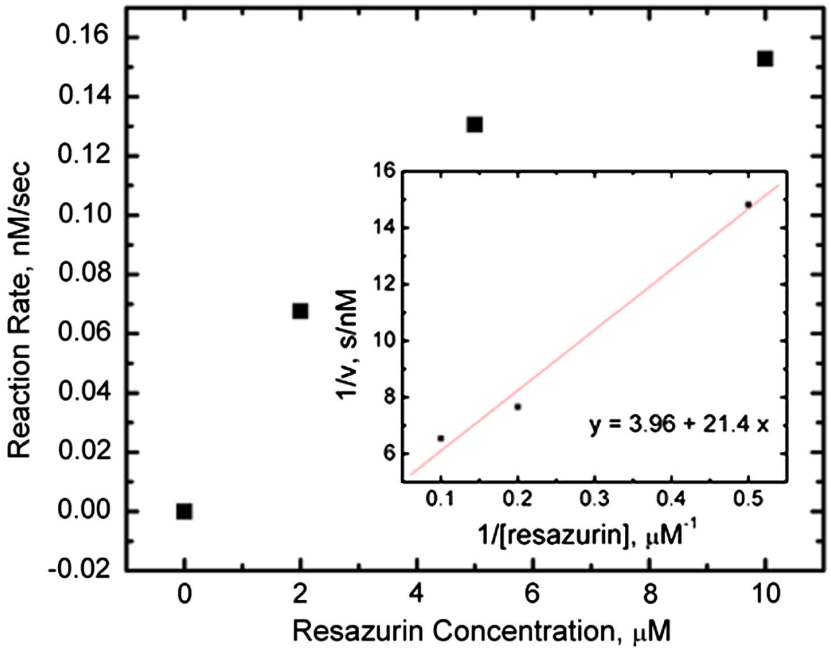

Figure 2.6: Reaction rate as a function of initial resazurin concentration with a 1.0 monolayer equivalent coverage TPP modified catalyst. The shape of the curve is indicative of Langmuir–Hinschelwood kinetic on these sites as proposed in earlier literature results from Chen *et al*. [21].

In order to shed further light on the residual catalytic activity as indicated by the non-zero *y*-intercept in Figure 2.5, we attempt to connect our results to prior results concerning vacancies observed on alkanethiol self-assembled monolayers on Au (1 1 1). These vacancies have been previously shown to comprise 6–10% of a flat single-crystal Au (1 1 1) surface as observed by STM (scanning tunneling microscopy) [39]. STM images show the vacancies to be located at domain boundaries on the Au (1 1 1) surface [40]. Vacancies in the thiol self-assembled monolayers (SAMs) were also observed electrochemically by Rubenstein *et al*. on gold electrodes, where the pinholes in the SAM behave as microelectrode arrays that are buried in a surrounding insulator consisting of alkane chains [41]. Based on the fact that metal nanoparticles are comprised of many different crystal facets and will thus have more boundary regions between these crystal faces than on a Au (1 1 1) surface, we hypothesize that the SAMs that are formed on the gold nanoparticle surface will have more vacancies than observed on Au (1 1 1) samples, given the expected greater number density of facets on the nanoparticle. We postulate that our slight residual activity illustrated in Figure 2.5 may in fact arise from these fraction of pinhole sites, which remain inaccessible to the binding of organic ligands such as the thiols and phosphines used here in this manuscript during kinetic poisoning experiments, and which have been previously alluded to as vacancies in the self-assembled monolayer literature [40] and [41].

To provide an estimate of the expected number density of corner, edge, and terrace sites on our gold nanoparticle surface and to investigate whether this number density is consistent with the number of sites observed for region I, II, and III sites, respectively, during kinetic poisoning experiments, results of geometric calculations are used pertaining to idealized nanoparticles consisting of FCC tetrahedron, FCC cube, FCC octahedron, FCC rhombic dodecahedron, cubo-octahedron, BCC cube, BCC octahedron, and hexagonal bipyramid [42]. The number density of corner, edge, and terrace sites in proportion to total surface atoms was

calculated for each of these idealized geometric models, corresponding to our 3.5-nm gold nanoparticle size (see Supplementary information). Depending on the geometry, the fraction of corner atoms relative to the total surface atoms varies from 0.5% to 8.3%, whereas the fraction of edge atoms varies from 12.5% to 46.7%. These ranges are within the bounds of our measured region I and region II sites above, hypothesized to correspond to corners and edges, respectively.

An estimate of the number density of corner and edge atoms relative to total surface atoms in our gold nanoparticles can be obtained by using aberration-corrected scanning transmission electron microscopy, as shown in Figure 2.7. The atomic-resolution image in Figure 2.7a shows a single facet of the gold nanoparticle (in transmission). The quantification of edge and corner gold atoms is accomplished by counting the columns of atoms along the red lines, as shown in Figure 2.7b. Of the ~238 total surface atoms in Figure 2.7a, the number of edge atoms along the red lines in Figure 2.7b is estimated to be 57, and the number of corner atoms comprising vertices between the red lines in Figure 2.7b is estimated to be 6. This corresponds to approximately 24% of the gold surface atoms being edges and 2.5% being corners in the supported gold nanoparticle. These estimates are within experimental uncertainty of the measured values for the fraction of region I and region II sites on the gold surface of our catalysts, if these sites correspond to corners and edges, respectively. They also fall within the range predicted by the geometric models discussed above.

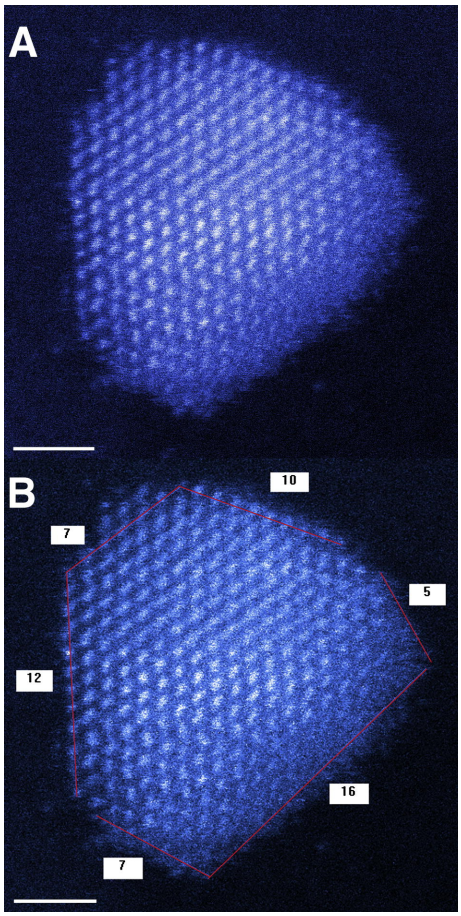

Figure 2.7: (A and B) Aberration-corrected HAADF-STEM images of a representative Au nanoparticle in our catalyst with atomic resolution. (B) The counted number of edge atoms for this particle. The scale bar in each panel represents 1 nm.

In summary, the reasoning above suggests that region I sites in our catalyst are the most active catalytic sites on the gold nanoparticle surface and are responsible for 30% of the observed reduction reaction activity. These are proposed to correspond to corner sites. Region II sites are less active than the corner sites described above and account for approximately 55% of the observed reduction activity as proposed edge sites. The remaining 70% of sites consisting of region III sites are proposed to terraces correspond to terraces, which are observed to be inactive for the reduction reaction. These results deconvolute the reactive heterogeneity on the surface of supported gold nanoparticles for reduction catalysis in this system. These concepts can be successfully applied to elucidate structure-sensitivity trends previously observed in this catalysis system, based on the changing edge atom site densities as a function of gold nanoparticle size (see Supplementary information) [21].

2.4 Conclusions

The contributions of three different types of sites on a gold nanoparticle catalyst have been elucidated and quantified along with number density of each type of active site, using kinetic poisoning experiments involving organic ligands, DDT and TPP, and the reduction of resazurin to resorufin as a model reaction. Comparison with geometric calculations in the literature led to the hypothesis that these different sites are likely the corner, edge, and terrace sites of the gold nanoparticle that are titrated by DDT and TPP in order of increasing coordinative saturation. A turnover frequency-based comparison of the various sites demonstrates that most active sites, likely to be corner atoms on the nanoparticle surface, comprise 1% of the total surface atoms, and exhibit 30% of the total activity. These sites are approximately 17-fold more active for the reduction reaction relative to the next most active site, edges, whereas terrace sites are completely inactive. The observed number densities of corner, edge, and terrace sites correlate well with aberration-corrected transmission electron microscopy of the supported gold nanoparticles, as well as idealized geometric models of the gold nanoparticle surface. The organic ligand-based methods used here to titrate sites during kinetic poisoning experiments suggest new methods of controlling catalysis activity and selectivity by submonolayer coverages of organic ligands.

2.5 Acknowledgements

The authors acknowledge helpful discussions with Prof. Yaron Paz at Technion in Haifa, Israel, and Prof. Matthew Neurock at University of Virginia. We are grateful to the Management and Transfer of Hydrogen via Catalysis Program funded by Chevron Corporation, the National Science Foundation (CBET 0854560), and U.S. Department of Energy under contract DE-SC0005822 for financial support. The authors acknowledge support of the National Center for Electron Microscopy, Lawrence Berkeley Lab, which is supported by the U.S. Department of Energy under contract DE-AC02-05CH11231. This work was supported in part by the Laboratory Directed Research and Development program at the Pacific Northwest National Laboratory (PNNL). The aberration-corrected electron microscopy was performed in the William R. Wiley Environmental Molecular Sciences Laboratory, a U.S. Department of Energy (DOE) national scientific user facility located at PNNL and funded by BER. PNNL is operated by Battelle for the U.S. DOE under contract DE-AC05-76RL01830.

2.6 Supplementary Information

2.6.1 Calculation of number of region II sites from Figure 2.5

The number of edge sites was calculated by the following procedure. The line of best fit through the terrace region is found, and the line of best fit through the edge region is found. The point of intersection represents the fraction of sites that are edge and corner sites.

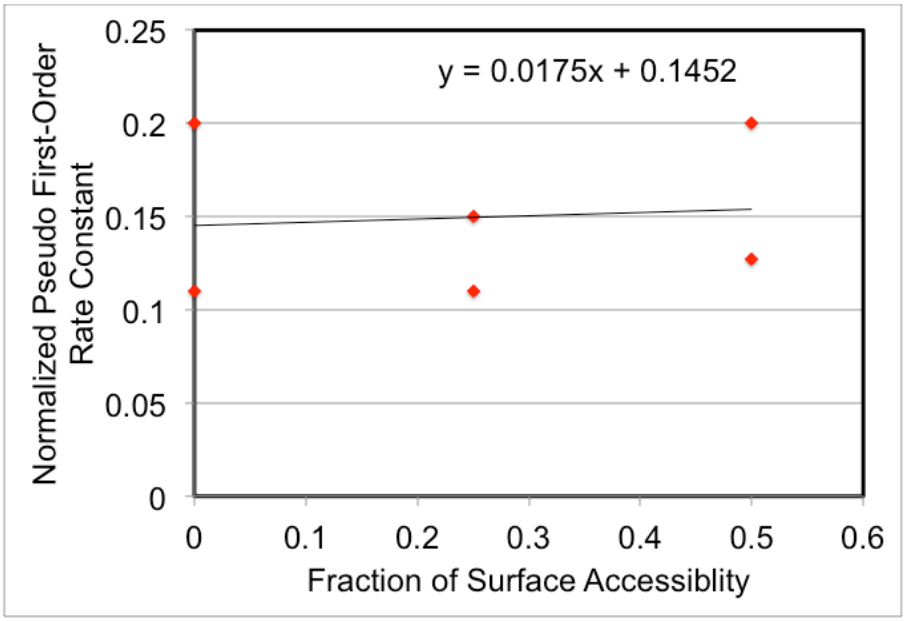

Figure 2.S.1: Linear regression results in the terraces region of Figure 2.5.

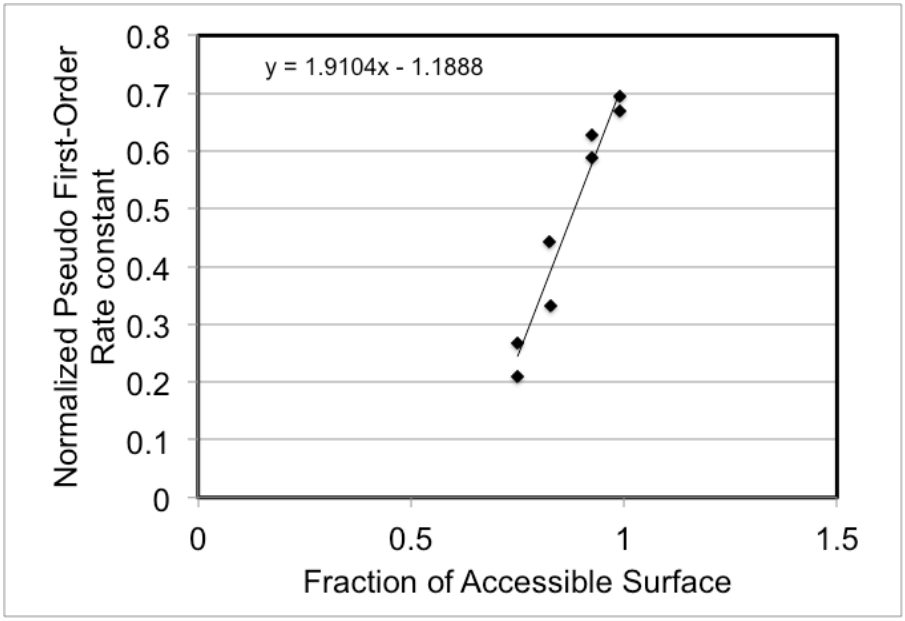

Figure 2.S.2: Linear regression in the region of edge site activity of Figure 2.5.

At the intersection of the two above-mentioned regression lines, the fraction of accessible surface is 0.7. Subtracting the 1% of corner atoms from this yields that 29% of the total surface sites are edge atoms, which account for 55% of the observed activity.

2.6.2 Comparison of activity between region I and region II sites

Linear regression for the corner sites region:

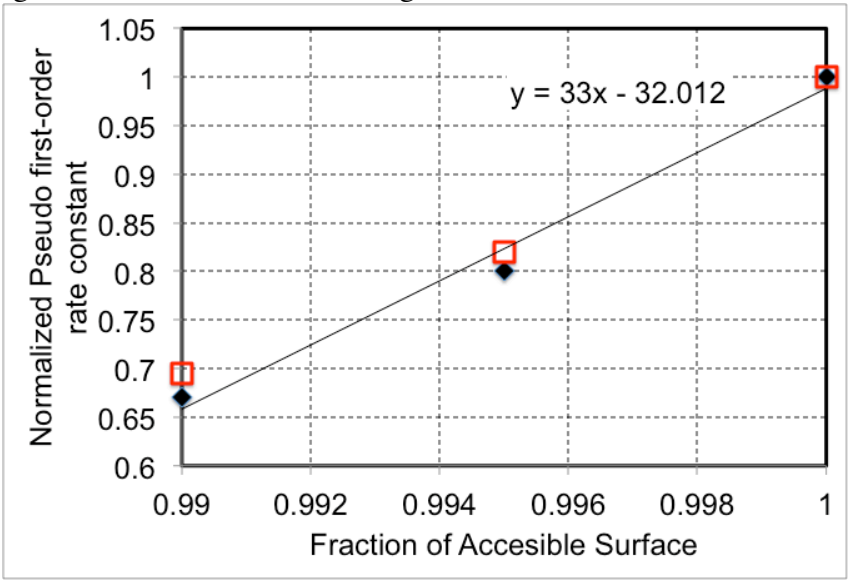

Figure 2.S.3: Linear regression in the region of corner site activity of Figure 2.5.

Dividing the slope of the corner region by the slope of the edges region, the quotient is approximately 17, thus the corner sites are approximately 18 times more active than the edge sites.

2.6.3 Rate constant calculations

To obtain the pseudo-first order rate constant, a plot of ln(1-X), where X is the reaction conversion coming from the measurement of the fluorescence of the reaction solution, versus time is shown below. The slope is related the pseudo first order rate. Dividing the slope by the mass of the catalyst gives the pseudo-first order rate constant on a mass of catalyst basis. Next, this rate constant is divided by the pseudo-first order rate constant of the sample in the absence of organic ligands, to obtain the normalized pseudo-first order rate constant, which is shown in Figure 2.5.

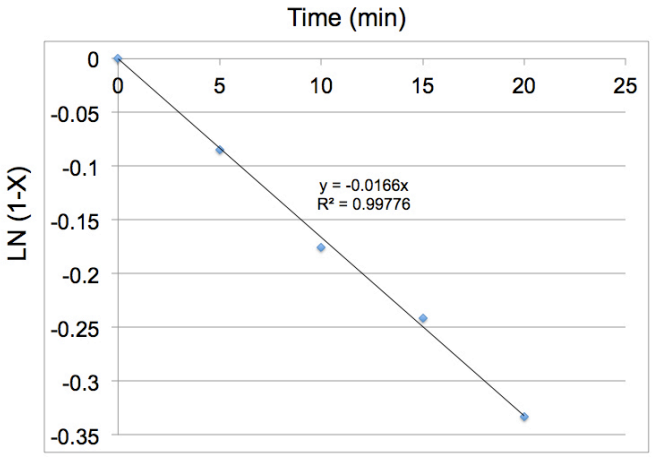

Figure 2.S.4: Plot of LN(1-X) versus time for resazurin reduction reaction where LN represents natural logarithm. The normalized pseudo-first order rate constant is obtained through this graph. In this case k = 9.2E-5 nM/(mg catalyst * min)

2.6.4 Organic ligand coverage calculations

Sample calculation for a 3.5 nm particle

Mass of Au in catalyst:

$$(0.030\text{g catalyst})\left(\frac{1.0\text{g Au}}{100\text{g catalyst}}\right) = 3.0\left(10^{-4}\right)\text{g Au}$$

Density of Au:

r = 19.3 (10^6) g/m^3

Volume of one nanoparticle (3.5 nm in diameter):

$$V = \frac{4\pi\left(1.75\left(10^{-9}\right)\text{m}^3\right)}{3} = 2.24\left(10^{-26}\right)m^3$$

Surface area of one nanoparticle (3.5 nm in diameter)

$$A = 4\pi\left(1.75\left(10^{-9}\right)\text{m}\right)^2 = 3.85\left(10^{-17}\right)m^2$$

Mass of one nanoparticle (3.5 nm in diameter):

$$m = V\rho = 4.33\left(10^{-19}\right)\text{g}$$

Number of particles:

$$\text{number of particles} = \frac{\text{mass of Au}}{m} = \frac{0.0003\text{g}}{4.33\left(10^{-19}\right)\frac{\text{g}}{\text{particle}}} = 6.92\left(10^{14}\right)\text{particles}$$

Total surface area:

$$A_{total} = (\text{number of particles})\,(A) = 2.66\left(10^{-2}\right)m^2$$

Moles of TPP needed assuming a $30(10^{-20})$m^2/TPP footprint[33]:

$$\text{mol TPP} = \frac{A_{total}}{\text{footprint}} = \frac{2.66\,(10)^{-2}\,m^2}{\frac{30(10^{-20})m^2}{\text{molec TPP}}}\left(\frac{1\text{ mol TPP}}{6.02\,(10^{23})\,\text{molec}}\right) = 1.48\left(10^{-7}\right)\text{mol TPP}$$

To obtain the amount needed for fractional monolayers multiply the moles of TPP by the fraction of the monolayer desired.

For DDT a footprint of 21 square angstroms was used and the same footprint was also used for DDA. [43]

2.6.5 Calculation of particle size distribution with mass weighting

Using the particle size distribution measured by HAADF-STEM, the average size was also calculated by a mass averaged method. The detail of the calculation is shown below.

Particle Size	% of total	Mass of 1 particle	Mass of group of particles
1.75	0.4415	5.41589E-20	2.39112E-20
2.25	5.29801	1.15107E-19	6.0984E-19
2.75	18.54305	2.10162E-19	3.89704E-18
3.25	27.15232	3.46901E-19	9.41918E-18
3.75	24.50331	5.32905E-19	1.30579E-17
4.25	14.79029	7.75752E-19	1.14736E-17
4.75	5.73951	1.08302E-18	6.21601E-18
5.25	2.86976	1.46229E-18	4.19642E-18
5.75	0.4415	1.92114E-18	8.48184E-19
6.25	0.22075	2.46715E-18	5.44624E-19
6.75	0	3.1079E-18	0
		Average Mass	5.0E-19
		Average Particle Radius	1.8E-09
		Average Particle Diameter	3.7E-09

2.6.6 Calculation of reaction rate for region I (corner) and region II sites (edge):

Region I
The rate on the unblocked surface is 1.50 nM/(mg cat * s).
30% of the reactivity is from region I, giving 0.45 nM/(mg cat * s).
Dividing by the total gold surface are of the catalyst (can be calculated from information shown earlier and knowing that 1% of the surface area are Type I sites:
0.45 nM/(mg cat * s) * (1 mg cat/ 1.09E-3 m^2 Au total) * (100 m^2 Au total / 1 m^2 type I site Au)
=4.1E+4 nM / m^2 type I site Au / sec

Region II
The rate on the unblocked surface is 1.50 nM/(mg cat * s).
55% of the reactivity is from region II, giving 0.83 nM/(mg cat * s).
Dividing by the total gold surface are of the catalyst (can be calculated from information shown earlier and knowing that 30% of the surface area are Type II sites:
0.85 nM/(mg cat * s) * (1 mg cat/ 1.09E-3 m^2 Au total) * (100 m^2 Au total / 30 m^2 type II site Au)
=2.5E+3 nM / m^2 type I site Au / sec

2.6.7 Application of geometric model of surface atom populations to published data with different particle sizes

We compared rates measured by Chen with Au nanoparticles of different sizes (6.0 nm and 9.1 nm) to the geometric model used by Nørskov *et. al.*[44] to correlate Chen's measured rates with the number of undercoordinated sites. Chen's results show a factor of 2.1 greater rate with the 6.0 nm particles as compared to the 9.1 nm particles (See table 1 in reference).[21] The difference in the number of edge sites between the two particle sizes is also a factor of 2.1 (38 / 18 = 2.1). A magnified region of Nørksov's model is show below for the region of interest. The difference in the populations of the corner sites shown in Figure 5 is less than the line width, and is assumed to be negligible for this analysis.

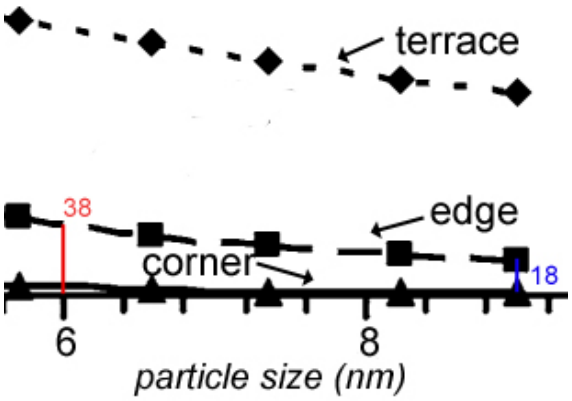

Figure 2.S.5: Data from geometric calculations correlating populations of terrace, edge, and corner sites.[5]

2.6.8 Calculation of number of corner and edge atoms for idealized geometries of particles

Using the results contained in reference 42 in the main manuscript, the number density of corner and edge atoms in proportion to total surface atoms was calculated assuming a 3.7 nm particle size, based on a mass-weighted distribution. The results are shown below for idealized geometries.

Geometry	Corners % of surface	Edges % of surface
Tetrahedron, FCC	0.5	15
Cube, FCC	1.4	12.5
Octahedral, FCC	0.99	22.4
Rhombic Dodecahedron, FCC	8.3	46.7
Cubo-octahedron	4.3	21.4
Cube, BCC	1.8	20.3
Octahedral, BCC	1.2	16
Hexagonal bipyramid	1.4	32.3

The number of edge and corner atoms changes by less than a factor of 12% when considering the narrow particle size distribution instead of the mass-average mean.

2.6.9 Fluorescence calibration curve for resorufin

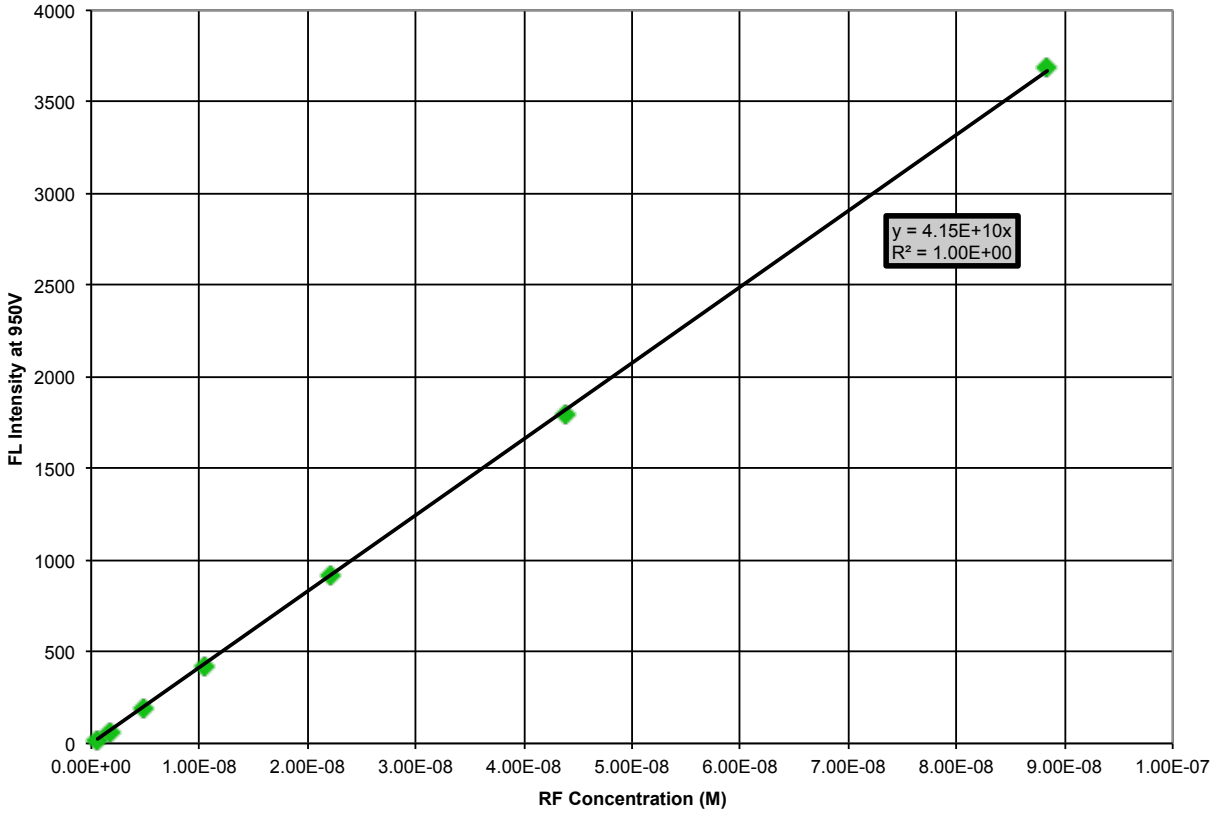

Figure 2.S.6: Resorufin concentration as a function of fluorescence intensity. Resorufin concentration is on the *x*-axis and fluorescence intensity is on the y-axis.

2.7 References

[1] H.S. Taylor, *Proc. Roy. Soc. Lond. A* 108 (1925) 105.

[2] R.A. van Santen, M. Neurock, *Molecular and Heterogeneous Catalysis: A Conceptual and Computational Approach*, VCH-Wiley, Inc., 2006.

[3] M. Boudart, A. Aldag, J.E. Benson, N.A. Dougharty, C.H. Girvin, *J. Catal.* 6 (1966) 92.

[4] M. Boudart, *Adv. Catal.* 20 (1969) 153.

[5] G.A. Somorjai, K.R. McCrea, J. Zhu, *Top. Catal.* 18 (2002) 157.

[6] Y. Iwasawa, R. Mason, M. Textor, G.A. Somorjai, *Chem. Phys. Lett.* 44 (1976) 468.

[7] C.J.H. Jacobsen, S. Dahl, P.L. Hansen, E. Törnqvist, L. Jensen, H. Tøpsoe, D.V. Prip, P.B. Møenshaug, I. Chorkendorff, *J. Mol. Catal. A* 163 (2000) 19.

[8] X. Deng, B.K. Min, A. Guloy, C.M. Friend, *J. Am. Chem. Soc.* 127 (2005) 9265.

[9] B.K. Min, A.R. Alemozafar, M.M. Biener, J. Biener, C.M. Friend, *Top. Catal.* 36 (2005) 77.

[10] B.K. Min, X. Deng, X. Liu, C.M. Friend, A.R. Alemozafar, *ChemCatChem* 1 (2009) 116.

[11] A.K. Rovik, S.K. Klitgaard, S. Dahl, C.H. Christensen, I. Chorkendorff, *Appl. Catal. A* 358 (2009) 269.

[12] B.D. Chandler, S. Kendell, H. Doan, R. Korkosz, L.C. Grabow, C.J. Purcell, *ACS Catal*. 2 (2012) 684–694.
[13] S.M. Oxford, J.D. Henao, J.H. Yang, M.C. Kung, H.H. Kung, *Appl. Catal. A* 339 (2008) 180.
[14] C. Lemire, R. Meyer, S. Shaikhutdinov, H.-J. Freund, *Angew. Chem. Int. Ed.* 43 (2004) 118.
[15] J. Lu, B. Fu, M.C. Kung, G. Xiao, J.W. Elam, H.H. Kung, P. Stair, *Science* 335 (2012) 1205.
[16] W.D. Williams, M. Shekhar, W.S. Lee, V. Kispersky, W.N. Delgass, F.H. Ribeiro, S.M. Kim, E.A. Stach, J.T. Miller, L.F. Allard, *J. Am. Chem. Soc*. 132 (2010) 14018.
[17] M. Shekhar, J. Wang, W.S. Lee, W.D. Williams, S.M. Kim, E.A. Stach, J.T. Miller, W.N. Delgass, F.H. Ribeiro, *J. Am. Chem. Soc*. 134 (2012) 4700.
[18] P. Chen, X. Zhou, H. Shen, N.M. Andoy, E. Choudhary, K.-S. Han, G. Liu, W. Meng, *Chem. Soc. Rev*. 39 (2010) 4560.
[19] W. Xu, J.S. Kong, Y.-T.E. Yeh, P. Chen, *Nat. Mater*. 7 (2008) 992.
[20] W. Xu, J.S. Kong, P. Chen, *Phys. Chem. Chem. Phys*. 11 (2009) 2767.
[21] X. Zhou, W. Xu, G. Liu, D. Panda, P. Chen, *J. Am. Chem. Soc*. 132 (2010) 138.
[22] J.-M. Ha, A. Solovyov, A. Katz, *Langmuir* 25 (2009) 10548.
[23] N. de Silva, J.-M. Ha, A. Solovyov, M.M. Nigra, I. Ogino, S.W. Yeh, K.A. Durkin, A. Katz, *Nat. Chem*. 2 (2010) 1062.
[24] M.J. Hostetler, J.E. Wingate, C.-J. Zhong, J.E. Harris, R.W. Vachet, M.R. Clark, J.D. Londano, S.J. Green, J.J. Stokes, G.D. Wignall, G.L. Glish, M.D. Porter, N.D. Evans, R.W. Murray, *Langmuir* 14 (1998) 17.
[25] D.V. Leff, L. Brandt, J.R. Heath, *Langmuir* 12 (1996) 4723.
[26] S. Bharathi, N. Fishelson, O. Lev, Langmuir 15 (1999) 1929.[27] C.J. Bueno Alejo, C. Fasciani, M. Grenier, J.C. Netto-Ferreira, J.C. Scaiano, *Catal. Sci. Technol*. 1 (2011) 1506.
[28] X. Zhou, N.M. Andoy, G. Liu, E. Choudhary, K.-S. Han, H.S. Shen, P. Chen, *Nat. Nanotechnol*. 7 (2012) 237.
[29] R. Zanella, A. Sandoval, P. Santiago, V.A. Basiuk, J.M. Sangier, *J. Phys. Chem. B* 110 (2006) 8559.
[30] B.P. Block, J.C. Bailar, *J. Am. Chem. Soc*. 73 (1951) 4722.
[31] C. Qi, T. Akita, M. Okumura, K. Kuraoka, M. Haruta, *Appl. Catal. A* 253 (2003) 75.
[32] M.M.Y. Chen, A. Katz, *Langmuir* 18 (2002) 8566.
[33] T. Inasaki, S. Kobaysashi, *Electrochim. Acta* 54 (2009) 4893.
[34] J. Nara, S. Higai, Y. Morikawa, T. Ohno, *J. Chem. Phys*. 120 (2004) 6705.
[35] P. Zhang, T.K. Sham, *Phys. Rev. Lett*. 90 (2003) 245502.
[36] S.T. Marshall, M.K. O'Brien, B. Oetter, A. Corpuz, R.A. Richards, D.K. Schwartz, J.W. Medlin, *Nat. Mater*. 9 (2010) 853.
[37] S.T. Marshall, D.K. Schwartz, J.W. Medlin, *Langmuir* 27 (2011) 6731.
[38] W. Xu, H. Shen, G. Liu, P. Chen, *Nano Res*. 2 (2009) 911.
[39] S. Kwon, J. Choi, H. Lee, J. Noh, *Colloids Surf. A* 313–314 (2008) 324.
[40] G. Poirier, *Chem. Rev*. 97 (1997) 1117.
[41] H.O. Finklea, D.A. Snider, J. Fedyk, E. Sabatani, Y. Gafni, I. Rubinstein, *Langmuir* 9 (1993) 3660.
[42] R. Van Hardeveld, F. Hartog, *Surf. Sci*. 15 (1969) 189–230.

[43] A.C. Templeton, S. Chen, S.M. Gross, R.W. Murray, *Langmuir*, 15 (1999), 66.
[44] T.V.W Janssens, B.S. Clausen, B. Hvolbaek, H. Falsig, C.H. Christensen, T. Bligaard, J.K. Nørskov, *Top. Catal.* 44 (2007), 15.

CHAPTER 3:

Identification of site requirements for reduction of 4-nitrophenol using gold nanoparticle catalysts

a collaboration between
Michael Nigra, Jeong-Myeong Ha, and Alexander Katz

"Identification of site requirements for reduction of 4-nitrophenol using gold nanoparticle catalysts" Michael M. Nigra, Jeong-Myeong Ha, and Alexander Katz, *Catalysis Science and Technology* 2013, Vol. 3, pages 2976-2983. - Reproduced by permission of The Royal Society of Chemistry. Available online at: http://dx.doi.org/10.1039/C3CY00298E

Abstract

The homogeneous *versus* heterogeneous nature of the active site of gold catalysis of the 4-nitrophenol reduction to 4-aminophenol is investigated using poisoning experiments that employ various organic ligands and 4 nm gold nanoparticles as catalysts. DDT (dodecanethiol)-bound gold nanoparticles are unable to catalyze this reaction, whereas nanoparticles capped with calixarene ligands consisting of calix[6]arene phosphine C6P and calix[4]arene thiol MBC are active. Poisoning of residual terrace sites upon addition of 2-naphthalenethiol (2-NT) in these latter two catalysts results in a gold nanoparticle that consists solely of ostensibly similar pinhole defect sites. However, the reaction rate for the catalyst consisting of C6P + 2-NT is 6.5-fold higher relative to the rate for catalyst consisting of MBC + 2-NT. This observation along with lack of activity for the DDT-bound catalyst suggests that pinhole defect sites and the gold nanoparticle surface cannot be the active site for catalysis. Instead, the active site is suggested to be a leached gold species that is present in exceedingly small concentrations (cannot be detected by disappearance of gold nanoparticles from solution during catalysis). Such a supposition is supported by observations of induction time and the interplay between observed induction time and kinetics. It is observed that the composition of the organic ligands in the system controls the kinetics and the induction time. Additionally, there is an absence of an induction time in a solution containing used catalyst, to which reactants are added. In the initial catalysis, it is observed that as the thiol ligand concentration on the surface increases, the induction time increases and the reaction rate decreases. The leached species were unable to be detected *via* changes in the surface-plasmon resonance absorption of the gold nanoparticles in solution before and after catalysis, as well as electron microscopy studies of used nanoparticle catalysts. This suggests that the leached species concentration is low, and their catalytic activity in turn must be quite high.

3.1 Introduction

Gold clusters exhibit extraordinarily rich catalytic activity for a variety of reactions involving oxidation and reduction. [1–4] Identification of the location and the nature of the active site in catalytic systems has been a topic of intense research in both heterogeneous and homogeneous catalysis, [5] and is invaluable in enabling the rational design of active sites for catalysis. A particularly important question that arises is whether the active site for catalysis is either a homogeneous or a heterogeneous site. [5–7] Here, we aim to address this question for a model gold-catalyzed reduction reaction consisting of 4-nitrophenol (4-NP) to 4-aminophenol (4-AP) using sodium borohydride in solution. Our goal is to gain insight into whether the active site for this reaction is located on the surface of a gold nanoparticle or, alternatively, whether it is a leached gold species in solution. There are different methods that one can employ to identify the active sites of a reaction such as poisoning experiments [8–11] as is explored in this contribution. Our approach uses poisoning experiments that poison calixarene-bound gold particles and where virtually all catalytically relevant sites on the gold surface can be blocked *via* binding 2-naphthalenethiol (2-NT) on the surface of the nanoparticles.

The reduction of 4-nitrophenol to 4-aminophenol using sodium borohydride as a reducing agent in the presence of gold nanoparticles as catalysts in solution has been widely studied, though still not fully mechanistically understood. This reduction reaction is also catalyzed by other metal nanoparticles, such as platinum [12,13] and silver, [12,14–16] in addition to gold.

The most suggested mechanism for this reaction is the Langmuir–Hinshelwood mechanism that requires that both a 4-NP and an activated hydrogen species be present on the surface simultaneously to react. [17,18] Another suggested mechanism for this reaction is the Eley–Rideal mechanism where only the activated hydrogen species must be present on the surface of the gold nanoparticle and the 4-NP reacts with the activated hydrogen without binding to the gold surface. [19]

Here, we wished to investigate whether poisoning experiments support the heterogeneous nature of catalysis in the 4-NP reduction to 4-AP using sodium borohydride as reductant. Our study uses gold nanoparticles bound and stabilized by calix[6]arene phosphine (C6P), calix[4]arene thiol (MBC), and dodecanethiol (DDT) ligands, which are shown in Figure 3.1 and which have been synthesized in previous work. [20–22] A unique feature of these calixarene-bound gold nanoparticles in solution, as compared to many other organic ligand-bound gold nanoparticles, is that there is a measurable amount of open binding sites and accessibility of the surface of the nanoparticles. [21,22] The accessibility of the gold surface is assessed by the binding of a 2-naphthalenethiol (2-NT) probe molecule as shown in Figure 3.1. The 2-NT probe is able to bind to the surface of the gold nanoparticle if there are accessible surface sites present because of the strong affinity between gold and thiol groups. [21] The origin of the accessible surface sites on the calixarene-bound gold clusters is due to an inherent flexibility of the bound ligand on the surface. [21,23] This flexibility allows for the exposure of accessible patches of the underlying metal surface in a dynamic fashion while also maintaining passivation and stabilization of the nanoparticle. The sterically bulky calixarene ligand subsequently prevents aggregation which would otherwise ensue in the absence of the ligand layer. In contrast, the DDT ligand, a long chain alkanethiol molecule, packs into very dense and rigid layers on the surface of the gold particles and does not demonstrate any accessibility to the 2-NT probe molecule. [21]

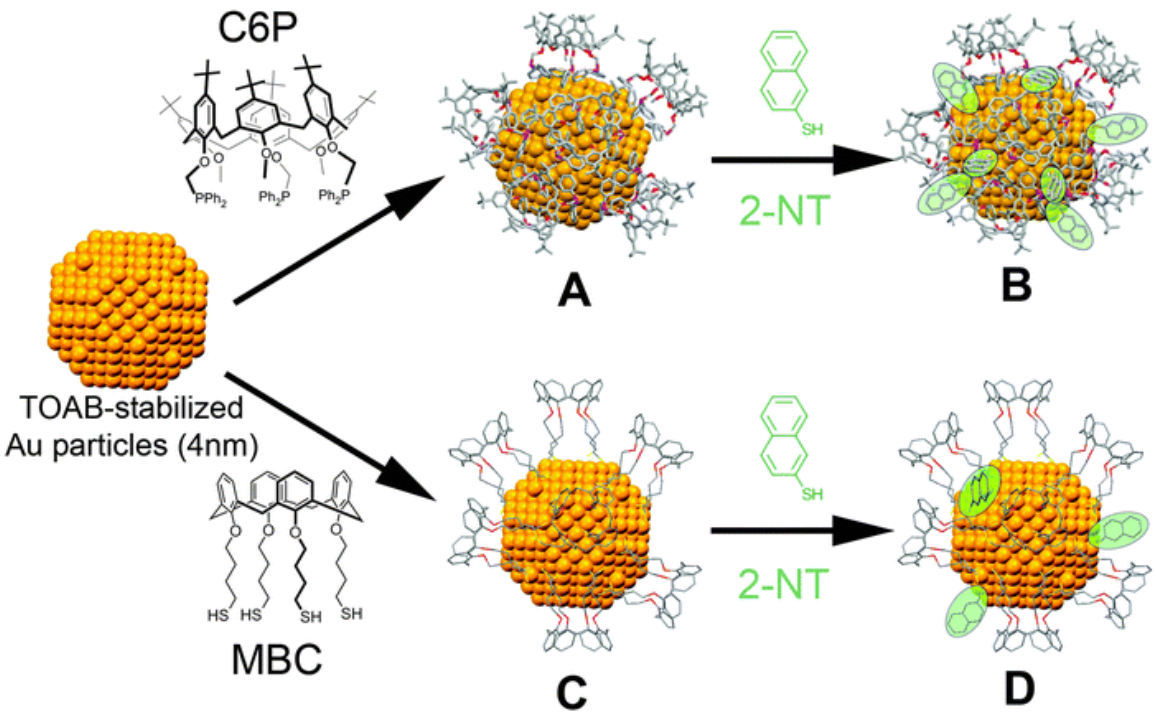

Figure 3.1: Schematic representation of calixarene-bound Au nanoparticle catalysts used in this study. (a) C6P-bound nanoparticles, (b) C6P-bound nanoparticles + 2-NT, (c) MBC-bound nanoparticles, (d) MBC-bound nanoparticles + 2-NT.

The different calixarene ligand-bound gold clusters (C6P and MBC along with the possibility having bound 2-NT) shown in Figure 3.1 along with the DDT bound clusters (not shown in Figure 3.1) set the stage for a comparative synthetic study of catalysis. This comparative study is aimed to assess how each ligand environment on the surface of the gold nanoparticle affects catalysis in a 4-NP to 4-AP reduction reaction. To draw a parallel to biological catalysts, the environment that ligands create around the active site of enzymatic catalysts is known to be of critical importance through electronic effects and by controlling accessibility to the active site. [24,25] In our systems, the environment of the gold catalyst is altered both sterically and electronically with different organic ligands bound to the surface of the gold nanoparticles. [21,22] These ligands vary in both the functional group (thiols and phosphines) bound to the gold nanoparticle as well as the size of the ligand ranging from the smallest DDT ligand to the largest C6P ligand.

The degree of small-molecule substrate accessibility of the gold surface has been previously measured [21] on all three of the gold-nanoparticle systems described above. The trend that is seen in these three systems is that as the steric bulk of the ligand increases, the amount of open binding sites and accessibility of the gold nanoparticle surface increases. This availability ranges from no available binding sites on the DDT-bound gold particles to over 20% of surface atoms (as measured by the footprint of 2-NT on the gold nanoparticle surface) being accessible on the most accessible particles in this study. Additionally, we have demonstrated *via* X-ray photoelectron spectroscopy (XPS) slight differences in the electronic state of gold

nanoparticles, as compared with tetraoctylammonium bromide-stabilized Au nanoparticles. [21] Whereby calixarene phosphine-bound 4 nm gold nanoparticles demonstrate an electronically richer gold surface while thiol-bound gold particles exhibit a charge-depleted gold surface. [26,27] The latter is exemplified in smaller 2.2 nm gold nanoparticles, where we have demonstrated a 0.75 eV greater Au $4f_{7/2}$ binding energy observed with a DDT-bound Au nanoparticle relative to a calixarene phosphine bound gold nanoparticle. [22,28] It has been observed that the electronically rich state of metal nanoparticles is favorable for reduction reactions such as water reduction or metal deposition, [29] showing that the electronic state of the gold nanoparticles in our system can be an important consideration. Metal nanoparticles can be charged in the presence of $NaBH_4$, as the BH_4^- is a strongly electron donating species. [29,30] In the case of 4-NP reduction, it is theorized that a surface-hydrogen species is transferred to the metal by BH_4^-. [18,30] This electron transfer is further thought to be facilitated by an electron-rich metal surface. [18,30] A secondary goal of our study is to investigate further the catalytic ramifications of the different electronic effects imparted by electron donating and electron accepting ligands that are bound to our gold particles in this current study, in the aforementioned 4-NP reduction.

Literature precedent for ligand environmental effects in this particular reaction system has been nicely demonstrated by Liu *et al*. [31] These authors demonstrate ligand effects on a system of gold nanoparticles bound to larger polymer nanospheres. These polymer nanospheres each consist of differently functionalized surfaces, which are functionalized with carboxylic acid, amide, pyridine, or thiol functionalities. Each of these ligands can create different environments when bound to the surface of the gold nanoparticle catalysts. Depending on the ligand environment of the gold catalyst, Liu *et al*. report that the reaction rate changes by a factor of 2.2, with the slowest rate for the thiol-functionalized system and the fastest for the carboxylic acid system. [31] We hypothesize due to the strong electron accepting nature of the bound thiolate groups that the slow catalysis rate using the thiol-functionalized system may be due to the electronically charge-depleted state of the gold surface. [26,27]

3.2 Experimental procedures

3.2.1 Synthesis of tetraoctylammonium bromide (TOAB)-stabilized Au nanoparticles

TOAB-stabilized 4 nm nanoparticles were synthesized using methods previously reported in the literature. [20,21] In brief, 6 mg of $HAuCl_4 \cdot 3H_2O$ (Aldrich) were dissolved in 0.4 mL of deionized water (18 MΩ, Barnstead Nanopure dispenser). Toluene (Fisher, HPLC grade) was added to make a solution with a concentration of 2 mM in Au atoms which produced a 2 phase mixture. TOAB was added, 100 eq. to Au atoms, to this two-phase mixture in order to extract the Au from the aqueous phase to the organic phase. This mixture was stirred for 5 minutes and left unagitated for 25 more minutes. After this time elapsed, the organic phase was transferred to a 25 mL Erlenmeyer flask and stirred vigorously. An aqueous solution of sodium borohydride was added, 10 eq. to Au atoms in 0.4 mL DI water, in one shot to the Au solution all at room temperature. The reaction was continually stirred for 3.5 hours and afterwards the organic phase was removed and stored in a vial.

3.2.2 Synthesis of MBC-modified Au nanoparticles

Modification of the TOAB-stabilized Au nanoparticles was performed following similar procedures to that of Ha *et al*. [20,21] 10 μL of a 2 mM 25,26,27,28-tetrakis(4-mercaptobutyloxy)calix[4]arene (MBC) stock solution in toluene solvent was added to 5 mL of a TOAB-stabilized gold nanoparticle solution that was 200 μM in Au atoms. The solution was shaken for 1 minute and stored in the dark for at least 16 hours before any further measurements.

3.2.3 Synthesis of C6P-modified Au nanoparticles

Modification of the cone-5,11,17,23,29,35-hexa(*tert*-butyl)-37,39,41-tris(diphenylphosphinomethoxy)-38,40,42-trimethoxycalix[6]arene (C6P) stabilized Au nanoparticles was performed following similar procedures to that of Ha *et al*. [21] 20 nmol of C6P in toluene was added to 5 mL of a solution 200 μM in Au atoms. The solution was shaken for 1 minute and stored in dark conditions for at least 16 hours before any further measurements.

3.2.4 Synthesis of DDT-bound Au nanoparticles

Synthesis of DDT-bound Au nanoparticles was based on previously published procedures [21] where approximately 8 mg of $HAuCl_4 \cdot 3H_2O$ is dissolved in 0.4 mL DI water. Dichloromethane (DCM) is added to give a concentration of 2 mM in Au atoms. 4 equivalents of TOAB with respect to Au atoms was added and stirred for 30 minutes. The organic phase of the biphasic mixture was transferred to an Erlenmeyer flask. One equivalent of DDT (Aldrich) was added to this flask and stirred in an ice bath for 30 minutes. Next, a 1 M aqueous solution of $NaBH_4$ with 10 equivalents of $NaBH_4$ to Au atoms was added to the flask and stirred continuously in an ice bath for 3 hours.

3.2.5 Blocking of surface accessibility with 2-NT

Gold surface sites were blocked by adding an amount of 2-NT in toluene solution (0.5 mM 2-NT in toluene) that is equivalent to the binding capacity as measured previously [2] to either a 2 or 4 mL solution of C6P or MBC bound Au nanoparticles (200 μM in Au atoms). The vial was shaken for 1 minute and then left to sit for 30 minutes before additional experiments were run.

3.2.6 4-Nitrophenol reduction catalysis

A 3 mL solution containing 50 μM Au atoms, 100 μM 4-nitrophenol (4-NP), and 18 mM $NaBH_4$ was prepared in a solvent mixture of 67% isopropanol–33% DI water (volume basis). This was performed by addition of the aqueous solution containing $NaBH_4$ to the 4-NP solution in isopropanol, which resulted in a yellow color that was manifested in a shift of the UV-Vis absorbance peak to around 405 nm, corresponding to the formation of the 4-nitrophenolate ion. [32–34] The gold nanoparticle catalyst dissolved in isopropanol was then added to this mixture in a cuvette. The absorbance was measured using a UV-Vis spectrophotometer (Varian Cary-4000) at 405 nm, which corresponds to the wavelength of maximum absorbance of the 4-nitrophenolate ion produced when 4-nitrophenol is in solution in the presence of $NaBH_4$. [32–34] The solution of gold nanoparticles dissolved in isopropanol was then added to this solution of 4-NP and $NaBH_4$. The cuvette was then shaken for approximately 30 seconds. After the cuvette was placed in the spectrophotometer, a scan at 405 nm was recorded every 6 seconds in order to

monitor reaction kinetics *via* disappearance of reactant. $NaBH_4$ produced hydrogen gas that bubbled through the reaction mixture to keep the system well-mixed.[15,33] The concentration of gold atoms was kept at 50 μM in order to enable comparisons with equal number of gold atoms for all systems.

3.3 Results and discussion

We first performed a comparative study of gold-nanoparticle catalysts consisting of different ligands within the set of DDT, C6P, and MBC. Such organic ligand-bound gold nanoparticles were synthesized as previously described by Ha *et al*. [20–22] Literature precedent verifies that the 4-NP to 4-AP reduction does not occur without the presence of a gold (or other noble metal) catalyst. [32–34] It is also well-documented in the literature that this reaction selectively produces one product, 4-aminophenol, which is one of the reasons that this reaction is very widely studied as a model of reactivity on metal nanoparticulate systems. [14,18,32,33] Looking more closely at the catalyzed reaction rates, the kinetics of this reaction can be treated as pseudo-first order reaction kinetics, due to the large excess of sodium borohydride present in solution. [32,34–36] Figure 3.2 shows the first-order rate constant plots as well as the plots of how the 4-NP concentration changes *versus* time. Pseudo-first order rate constants were obtained by using the slopes from the $\ln(1 - X)$ *versus* time plots, where X is the conversion of 4-NP, as illustrated in panels b, c, e, and f of Figure 3.2.

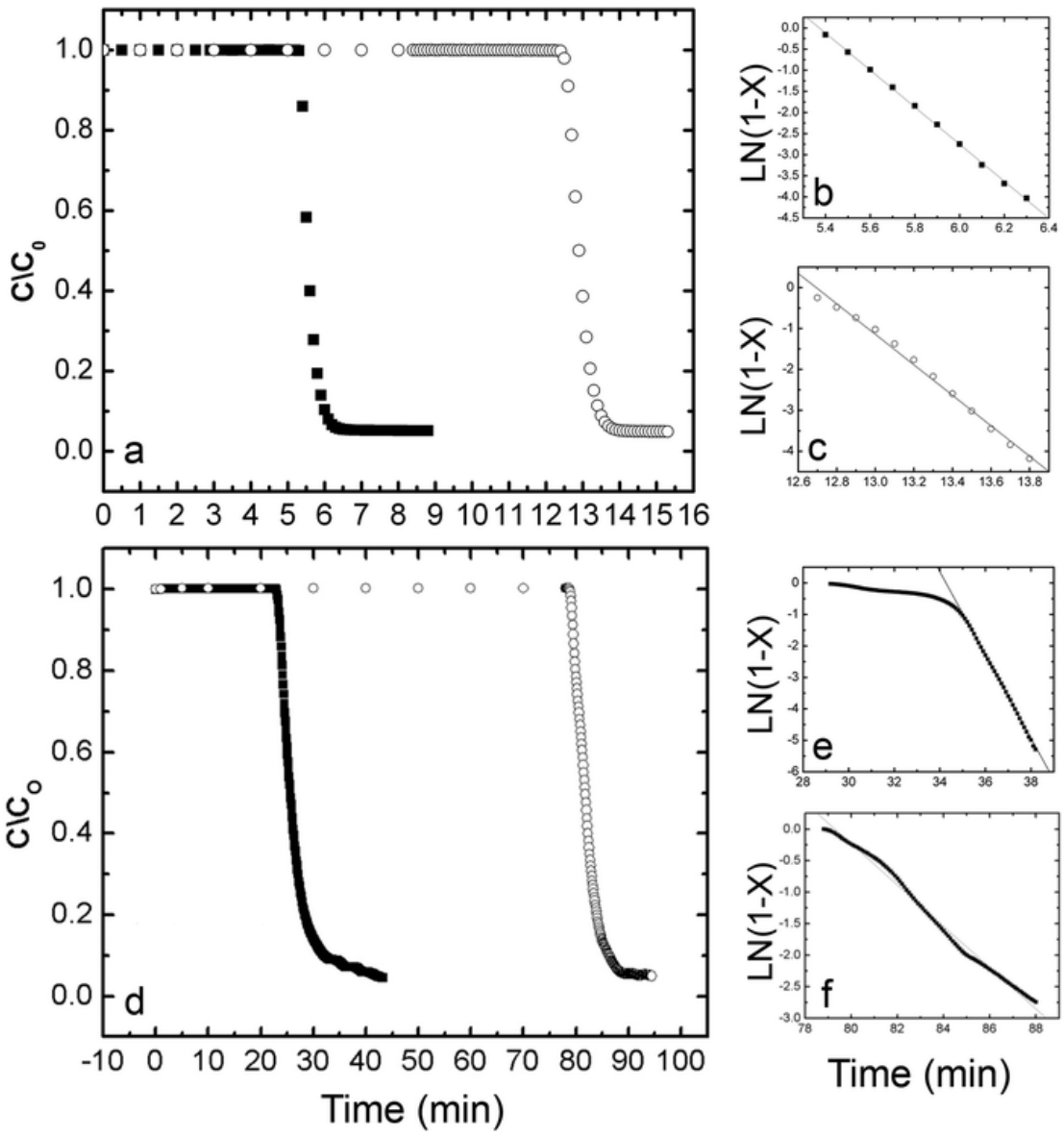

Figure 3.2: Kinetics of 4-NP reduction using calixarene-bound gold nanoparticles. (a) Normalized concentration of 4-nitrophenolate ion at 405 nm *versus* time for Au nanoparticles with only C6P bound (solid squares) and C6P + 2-NT bound (open circles), (b) first order rate constant plot for Au nanoparticles bound with only C6P for 4-nitrophenol reduction, (c) first order rate constant plot for Au nanoparticles bound with C6P + 2-NT for 4-nitrophenol reduction, (d) normalized concentration of 4-nitrophenolate ion at 405 nm *versus* time for Au nanoparticles with only MBC bound (solid squares) and MBC + 2-NT bound (open circles), (e) first order rate constant plot for Au nanoparticles bound with only MBC for 4-nitrophenol reduction, (f) first order rate constant plot for Au nanoparticles bound with MBC + 2-NT for 4-nitrophenol reduction.

Data in Table 3.1 show that DDT-bound gold nanoparticles display no catalytic activity for 4-NP reduction during the 19 hours that the reaction was observed. These DDT-bound gold nanoparticles do not contain any accessible binding sites for 2-NT. [21] The only possible catalytic active sites on such particles are pinhole defects within the DDT monolayer. We have previously shown that similar pinhole defects consist of either edge or corner gold atoms and account for less than 8% of the total gold-surface atoms in similarly sized gold nanoparticles. [8] The observed lack of catalytic activity for 4-NP reduction implies that these pinhole sites are not catalytically active for 4-NP reduction reaction. Such a result contrasts their catalytic activity in other reduction reactions catalyzed by gold, for example the reduction of resazurin to resorufin. [8] This datum is the first hint that the catalytically active site in the 4-NP reduction system may not be on the gold nanoparticle surface, otherwise, the residual pinhole sites would be expected to have some catalytic activity.

Table 3.1: Comparison of reaction rates and induction times for different ligand-bound gold nanoparticle catalysts. The concentration of gold atoms in all of these systems is all at 50 μM in solution. The reaction using DDT particles was monitored for 19 hours with no visible reaction

Ligands bound to Au nanoparticle surface	**Induction time (min)**	**Pseudo-first order reaction rate constant (min^{-1})**
DDT	--	0
C6P	5.4 ± 0.7	4.3 ± 1.2
C6P + 2-NT	11.2 ± 1.1	2.0 ± 1.1
MBC	32 ± 5	0.92 ± 0.23
MBC + 2-NT	67 ± 15	0.31 ± 0.17

If gold terrace sites are active sites for the reaction, we expect enhanced catalytic activity in our systems, consisting of open and accessible binding sites for 2-NT, as measured previously with steady-state fluorescence titration experiments. [21] This is expected due to the increased number of active sites where there is room for the substrates to bind on the gold nanoparticle surface (*i.e.* in regions where 2-NT would bind). As illustrated in Table 3.1 and Figure 3.2, catalytic activity is observed for both the C6P and the MBC-bound gold nanoparticle systems. The C6P-bound gold nanoparticle catalyst is approximately 4.7-fold more active than the MBC-bound catalyst. Such an observation is not entirely consistent with the previously measured difference in accessible surface area (to 2-NT) between these two nanoparticle systems, which would be expected to account for a 1.9-fold difference in rates between the two catalysts, with everything else being equal. Electronic effects of a more electron-rich gold surface when using C6P calixarene phosphine-bound gold nanoparticles could possibly to explain the remaining rate difference as it has been previously hypothesized that reductant activation with gold catalysts occurs more readily with an electron-rich gold surface. [29] Thus, the faster rate of the phosphine-bound gold nanoparticles could be partially explained by their higher electron richness *versus* the thiol-bound gold nanoparticles. However, we have previously shown that when using 4 nm gold nanoparticles as catalysts for reduction, there are virtually no observed electronic effects of organic ligands on catalysis8 as a result of the large size of the nanoparticle. There are larger organic ligand electronic effects for smaller gold clusters compared to 4 nm gold nanoparticles. [21,22] Altogether, the observed rate enhancement between C6P and MBC is

inconsistent with the increased available 2-NT binding sites in the former. This may be due to (i) a leached active site responsible for 4-NP reduction catalysis, which is more influenced by ligand electronic effects and which is a consequence of leaching from the original gold nanoparticle during catalysis conditions, or (ii) some combination of available terrace sites and pinhole defects responsible for catalysis, though DDT-bound catalyst data above suggest a lack of activity due to pinhole defects. We more thoroughly investigate these two possibilities below, with additional comparative studies using 2-NT-bound catalysts.

Both the C6P and MBC nanoparticle catalysts require an induction time period, during which the reaction rate is zero. This induction time period has been previously observed by several other investigators in the literature, as well as for other noble metal nanoparticulate catalysts such as silver and platinum. [14,17,18,32,33,37–40] This finding makes this catalyst system fundamentally different from the gold nanoparticle-catalyzed reduction of resazurin to resorufin [8] that we investigated previously. In another electron-transfer reaction, the reduction of eosin using the same $NaBH_4$ reductant in the presence of a gold nanoparticle catalyst, an induction period is also observed. [41] The authors hypothesize in this last system that the induction time for this reaction, as well as in other electron-transfer reactions originates due to the reducing agent requiring time to inject electrons into the metal. The injected electrons raise the Fermi level of the metal, which changes the redox potential of the catalyst. [41]

Table 3.1 data show that as the amount of thiol on the gold surface increases, the induction time increases in a commensurate fashion. This follows the trend previously described, whereby a more electron-rich gold surface (*i.e.* one with fewer thiolates bound to it) will activate the BH_4^- reductant more easily and will therefore require less induction time. Others have hypothesized this induction period is caused by slow diffusion of reactants to the surface of the gold nanoparticles. [32] However, diffusion limitations for this reaction have been dismissed as a possible origin of the induction time by Ballauff *et al.* who performed an analysis of kinetic data that shows that the apparent first-order rate constant decreases with increasing 4-NP concentrations. Additionally, for constant 4-NP concentrations while changing $NaBH_4$ concentration, the apparent first-order rate constant is constant over the $NaBH_4$ concentrations tested in these experiments. [18] Ballauff *et al.* also provide an analysis of the Damköhler number that reveals that mass transfer in these systems is at least two orders of magnitude faster than the reaction kinetics. [17] Another hypothesis suggests that the induction time is rooted in slow surface restructuring of the gold nanoparticles, [17,18] while, others suggest that the origin of the induction time is due to reduction of the dissolved oxygen present in the reaction solution. [33] Our observations reveal that the induction time is dependent on the ligand(s) present on the gold nanoparticle surface (Table 3.1). If the induction time was only based on the reduction of the dissolved oxygen in the system, then it would be expected that the induction times for all of our systems would be similar (same reaction conditions for each sample run). In summary, we believe that the remaining explanation – related to some sort of surface restructuring – may be responsible for the observed induction time. We investigate this possibility further below.

Further insight into the nature and location of the active site for 4-NP reduction using gold catalysts was gained using poisoning experiments to block sites on the gold nanoparticle surface. These poisoning experiments used 2-NT as the poison to block sites. 2-NT is a good choice as a poison because the number of 2-NT binding sites present on these gold nanoparticles is well known, based on previous titration experiments. [21] Results in Table 3.1 and Figure 3.2 illustrate that when an amount of 2-NT is added that is equal to the number of binding sites on the gold nanoparticle surface (*i.e.* the gold surface is saturated with either thiol or thiol–

phosphine ligands), the reaction still occurs, albeit with a longer induction time and a slightly slower rate than in the case without 2-NT. The difference between the C6P and the C6P + 2-NT rate constants is about a factor of 2, and the difference between the MBC and MBC + 2-NT rate constants is about a factor of 3. Such an observation could still be due to either of the two effects described above: (i) some combination of terrace and pinhole defects being responsible for catalysis *versus* (ii) a leached smaller site being responsible for catalysis. Previously, when performing kinetic poisoning experiments on a different gold reduction catalysis system, a plateau was observed wherein the catalytic activity did not change appreciably upon poisoning terrace sites on the surface. However, there was a residual catalytic activity hypothesized to be due to pinhole defect sites. [8] Alternatively, to support possibility (ii), as the amount of thiol present in the catalyst increases, the reaction rate decreases. Such subtle electronic effects would likely be more pronounced for a leached small site rather than the large 4 nm gold nanoparticle. In addition, as already mentioned above, the lack of residual pinhole catalytic activity in the gold catalyst bound with a monolayer of DDT ligand suggests that possibility (i) above is less likely.

Data in Table 3.1 shows that the rate of the C6P + 2-NT catalyst is nearly 6.5-fold higher compared with the MBC + 2-NT catalyst. Such an outcome cannot be explained by the same pinhole defect sites being responsible for catalysis in the two systems, but instead points to leached species, presumably consisting of small gold complexes/clusters, as being responsible for catalysis. Such a result is consistent with an entire absence of induction time after the initial catalytic run (see Figure 3.S.2), suggesting that leached species remain in solution and are stable upon addition of new reactants to the mixture.

Ballauff *et al*. hypothesize that the origin of the induction time observed in 4-NP reduction systems comes from the restructuring of the nanoparticle surface, as shown by their data in both gold and platinum nanoparticle systems. [17,18] They show that the surface reconstruction has a time scale or reciprocal rate that is related to the pseudo first-order rate constant of the reduction reaction. [18] In a later publication from Ballauff *et al*., [17] a spontaneous reconstruction of the surface atoms is invoked to explain a non-zero *y*-intercept in the absence of all substrates, when the reciprocal induction time is plotted *versus* the concentration of 4-NP. Further investigations illustrate that there is also a substrate-induced surface reconstruction that exhibits a quadratic dependence on the 4-NP surface coverage, meaning that multiple 4-NP molecules are needed to affect changes in the surface structure. [17]

We also observe similar trends between the induction time and the pseudo first order rate constant in Table 3.1, as Ballauff *et al*. [17,18] observed. As our induction time decreases, the rate constant increases. From the additional insights of the poisoning experiments using 2-NT above, we hypothesize that the surface reconstruction previously described may be a surface reaction that leads to leaching of the gold species from the particle surface, giving the gold catalyst its catalytic activity.

We attempted to use the surface-plasmon band of gold to assess just how much leaching may be required for catalysis, when using an MBC + 2-NT as a representative catalyst. Data in Figure 3.3 shows almost no change in the gold surface plasmon band intensity at 520 nm during the induction period and during 4-NP reduction catalysis. This means that the concentration of gold nanoparticles is roughly constant and not changing during these processes, and suggests that very little leached gold is necessary for an active catalyst. Such a result is consistent with high angle annular dark-field scanning transmission electron microscopy (HAADF-STEM) of gold nanoparticle catalyst before and after use, which shows similar particle size distributions in solution as well as similar morphology (see Figure 3.S.3). Recently Corma *et al*. have shown that

small gold clusters can be extraordinarily active (ppm quantities of gold catalyst are sufficient) as catalysts in solution, for ester-assisted hydration of alkynes. [4] Hutchings *et al*. have shown that oxidized Au^{3+} species derived from Au/C catalysts are crucial in the hydrochlorination of acetylene. [1] Our observations above suggest a high activity for leached sites according to mechanism (ii) described above, for gold-catalyzed 4-NP to 4-AP in solution, though at this time, we are unable to more precisely pinpoint details on the leached active site (*i.e*. oxidation state and chemical connectivity).

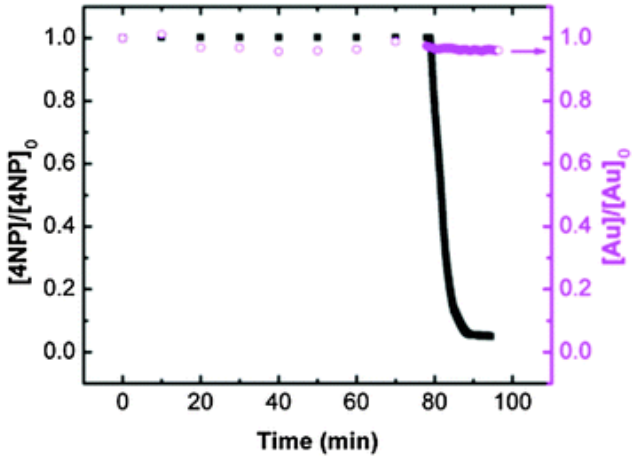

Figure 3.3: Gold nanoparticle concentration (open violet circles) taken at the SPR band of 520 nm as a function of time before and after catalysis for MBC + 2-NT-bound gold nanoparticles. The consumption of 4-nitrophenol is also shown with solid black squares. Very little leaching is necessary for an active catalyst.

3.4 Conclusions

Using comparative studies of different organic ligand-bound gold nanoparticle catalysts, we investigate the nature and location of the active site for the gold-catalyzed reduction of 4-NP to 4-AP. Specifically, we investigate two possible mechanisms wherein (i) pinhole defects coupled with residual terrace sites on the gold nanoparticle surface are the catalyst active site *versus* another mechanism involving (ii) leached small gold species from the nanoparticle surface as being the active site responsible for catalysis. The lack of observed catalytic activity with DDT-capped gold nanoparticles and the 6.5-fold increase in rate when comparing C6P + 2-NT catalyst relative to MBC + 2-NT catalyst all but disqualifies possibility (i) above as a major contributor, since all of these catalysts consist of completely blocked surfaces with only the pinhole sites remaining according to scenario (i) above. The observed organic ligand-dependent rates and induction times for catalysis are instead consistent with surface restructuring on the gold nanoparticle during catalysis and a small minority of leached gold species as being the active site responsible for catalysis. As shown in these gold-catalyzed systems, elucidating the nature of catalytically active sites using organic-ligand poisoning experiments provides a useful method for determining the homogeneous *versus* heterogeneous nature of the active sites on gold catalysts.

3.5 Acknowledgements

We are grateful to the Management and Transfer of Hydrogen *via* Catalysis Program funded by Chevron Corporation for financial support. The authors acknowledge support of the National Center for Electron Microscopy, Lawrence Berkeley Lab, which is supported by the U.S. Department of Energy under Contract # DE-AC02-05CH11231.

3.6 Supplementary information

3.6.1 Calculation of reaction rate constant and induction time

Pseudo-first order reaction rate constants were calculated by plotting ln(1-X) where X is the conversion of 4-NP versus time. The slope of the line of best fit in the plot gives the pseudo-first order rate constant. In some of the MBC samples, there were two negatively sloping regions, with one region having a significantly steeper slope. The most steeply sloped region was used to calculate the rate constant, and the less steep region was included as part of the induction time as shown in Figure 3.S.1.

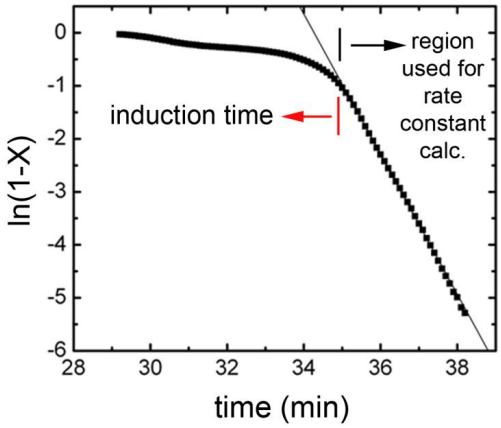

Figure 3.S.1: Kinetics plot of MBC-Au nanoparticle catalyzed reaction illustrating how the reaction rate was calculated and the induction time determined when there were two regions of different slope in the ln(1-X) versus time plots.

3.6.2 Addition of additional 4-nitrophenol to reaction mixture after initial 4-nitrophenol is consumed

Additional 4-NP was added to the reaction solution to achieve approximately the original concentration. The reaction proceeds without an induction time and the 4-NP begins to be consumed as it is added to the reaction mixture. Fig. S2 shows a plot of the relative concentration (referenced to the initial 4-NP concentration) as a function of time. The sharp peaks in the graph occurs after the doses of 4-NP are added to the reaction mixture. The fact that the value of $C/C_0 = 1$ is not observed after each addition can be explained by the fast reaction in the time in between when the 4-NP was added and the time until the first measurement taken after the addition.

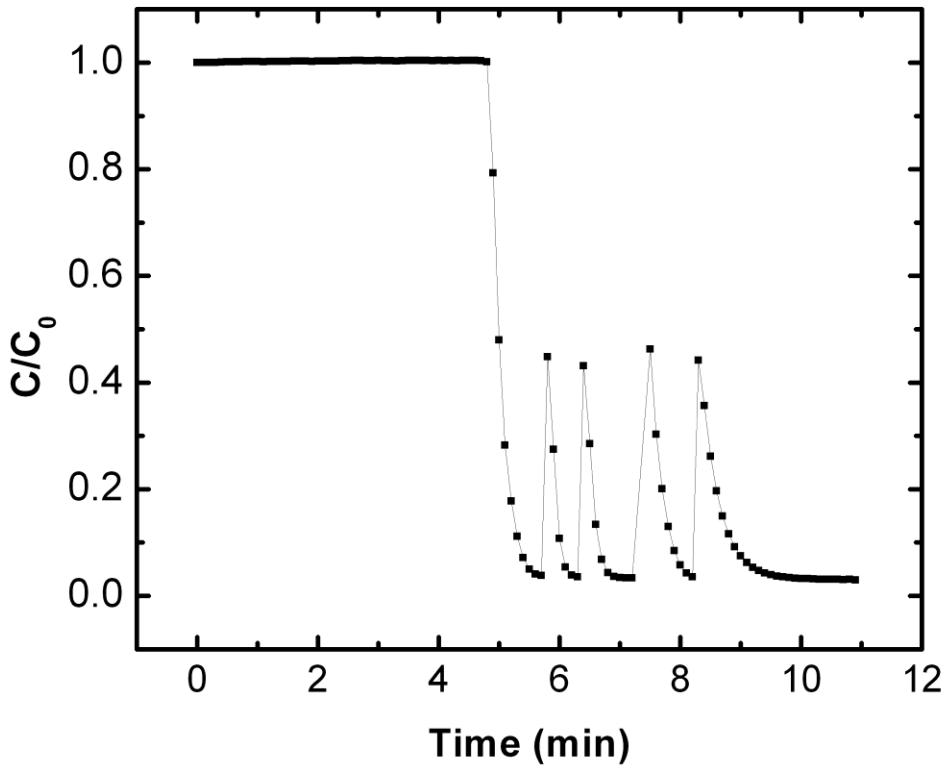

Figure 3.S.2: 4-NP concentration versus time of reaction plot using C6P-bound Au nanoparticles. No induction time is necessary upon adding the additional doses of 4-NP to the solution after the initial amount of 4-NP is consumed.

3.6.3 HAADF-STEM before and after reaction

TEM images were acquired before and after reaction and showed no significant particle morphology or size changes in solution as a result of the reaction. Figure 3.S.3 shows the TEM images as well as the particle size histograms.

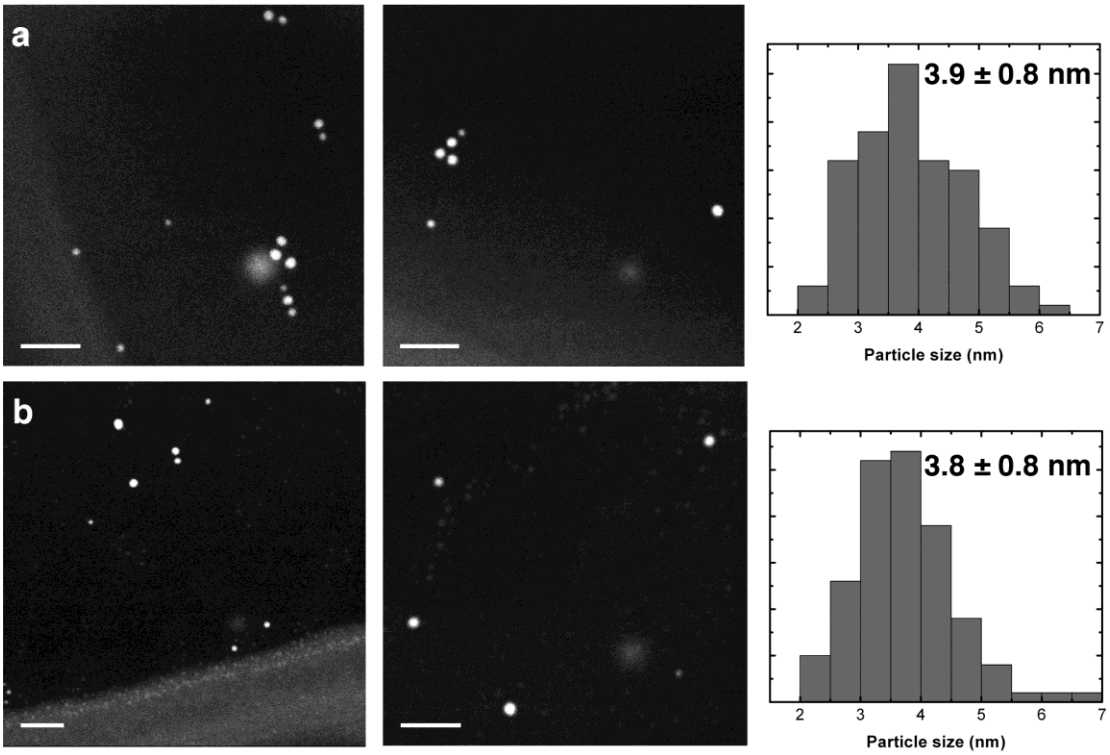

Figure 3.S.3 a) MBC-Au nanoparticles before reaction. (b) MBC-Au particles after reaction. The white scale bar represents 20 nm.

3.6.4 Synthesis of gold nanoparticle catalysts

Gold nanoparticle catalysts were synthesized according to literature procedures. [20,21] to use in catalysis, the gold nanoparticles were exhaustively characterized using previously developed procedures, including accessibility measurements of 2-NT. These nanoparticles showed accessibility that was identical to values previous published in the literature. [20,21]

3.7 References

[1] M. Conte, C.J. Davies, D.J. Morgan, T.E. Davies, D.J. Elias, A.F. Carley, P. Johnston, G.J. Hutchings, *J. Catal.*, 297 (2013), 128.

[2] A.A. Herzing, C.J. Kiely, A.F. Carley, P. Landon, G.J. Hutchings, *Science*, 321 (2008) 1331.

[3] T. Takei, T. Akita, I. Nakamura, T. Fujitani, M. Okumura, K. Okazaki, J. Huang, T. Ishida, M. Haruta, *Adv. Catal.*, 55 (2012) 1.

[4] J. Oliver-Meseguer, J.R. Cabrero-Antonino, I. Domínguez, A. Leyva-Pérez, A. Corma, *Science*, 338 (2012)1452.
[5] J.E. Mondloch, E. Bayram, R.G. Finke, *J. Mol. Catal. A*, 355 (2012) 1.
[6] E. Bayram, M. Zahmakiran, S. Özakar, R.G. Finke, *Langmuir*, 26 (2010) 12455.
[7] E. Bayram, R.G. Finke, *ACS Catal.*, 2 (2012) 1967.
[8] M.M. Nigra, I. Arslan, A. Katz, *J. Catal.*, 295 (2012) 115.
[9] S.M. Oxford, J.D. Henao, J.H. Yang, M.C. Kung, H.H. Kung, *Appl. Catal. A*, 339 (2008) 180.
[10] B.D. Chandler, S. Kendell, H. Doan, R. Korkosz, L.C. Grabow, C.J. Purcell, *ACS Catal.*, 2 (2012) 684.
[11] M. Shekhar, J. Wang, W.-S. Lee, W.D. Williams, S.M. Kim, E.A. Stach, J.T. Miller, W.N. Delgass, F.H. Ribeiro, *J. Am. Chem. Soc.*, 134 (2012) 4700.
[12] K. Esumi, R. Isono ,T. Yoshimura, *Langmuir*, 20 (2004) 237.
[13] F. Coccia, L. Tonucci, D. Bosco, M. Bressan, N. d'Alessandro, *Green Chem.*, 2012, 14, 1073.
[14] N. Pradhan, A. Pal, T. Pal, *Colloids Surf. A*, 196 (2002) 247.
[15] S. Saha, A. Pal, S. Kundu, S. Basu, T. Pal, *Langmuir*, 26 (2010) 2885.
[16] Y. Lu, Y. Mei, M. Drechsler, M. Ballauff, *Angew. Chem. Int. Ed.*, 45 (2006) 813.
[17] S. Wunder, Y. Lu, M. Albrecht, M. Ballauff, *ACS Catal.*, 1 (2011) 908.
[18] S. Wunder, F. Polzer, Y. Lu, Y. Mei, M. Ballauff, *J. Phys. Chem. C*, 114 (2010) 8814.
[19] Y. Khalavka, J. Becker, C. Sönnichsen, *J. Am. Chem. Soc.*, 131 (2009) 1871.
[20] J.-M. Ha, A. Katz, A.B. Drapailo. V.I. Kalchenko, *J. Phys. Chem. C*, 113 (2009) 1137.
[21] J.-M. Ha, A. Solovyov, A. Katz, *Langmuir*, 25 (2009) 10548.
[22] N. de Silva, J.-M. Ha, A. Solovyov, M.M. Nigra, I. Ogino, S.W. Yeh, K.A. Durkin, A. Katz, *Nat. Chem.*, 2 (2010) 1062.
[23] J.-M. Ha, A. Solovyov, A. Katz, *J. Phys. Chem. C,* 114 (2010) 16060.
[24] H. Beinert, *JBIC*, 5 (2000) 2.
[25] L. Quintanar, J. Yoon, C. P. Aznar, A.E. Palmer, K.K. Andersson, R.D. Britt, E.I. Solomon, *J. Am. Chem. Soc.*, 127 (2005) 13832.
[26] P. Zhang, T.K. Sham, *Phys. Rev. Lett.*, 90 (2003) 245502.
[27] J. Nara, S. Higai and Y. Morikawa, *J. Chem. Phys.*, 120 (2004) 6705.
[28] M.J. Hostetler, J.E. Wingate, C.-J. Zhong, J.E. Harris, R.W. Vachet, M.R. Clark, J.D. Londono, S.J. Green, J.J. Stokes, G.D. Wignall, G.L. Glish, M.D. Porter, N.D. Evans, R.W. Murray, *Langmuir*, 14 (1998) 17.
[29] A. Henglein, *J. Phys. Chem.*, 97 (1993) 5457.
[30] H. Zhang, X. Li, G. Chen, *J. Mater. Chem.*, 19 (2009) 8223.
[31] W. Liu, X. Yang, L. Xie, *J. Colloid Interf. Sci.*, 313 (2007) 494.
[32] R. Fenger, E. Fertitta, H. Kirmse, A.F. Thünemann, K. Rademann, *Phys. Chem. Chem. Phys.*, 14 (2012) 9343.
[33] S. Panigrahi, S. Basu, S. Praharaj, S. Pande, S. Jana, A. Pal, S.K. Ghosh, T. Pal, *J. Phys. Chem. C*, 111 (2007) 4596.
[34] Y. Deng, Y. Cai, Z. Sun, J. Liu, Chong Liu, J. Wei, W. Li, Chang Liu, Y. Wang, D. Zhao, *J. Am. Chem. Soc.*, 132 (2010) 8466.
[35] K. Kuroda, T. Ishida, M. Haruta, *J. Mol. Catal. A*, 298 (2009) 7.
[36] Y. Zhang, S. Liu, W. Lu, L. Wang, J. Tian, X. Sun, *Catal. Sci. Technol.*, 1 (2011) 1142.

[37] Y. Mei, G. Sharma, Y. Lu, M. Ballauff, M. Drechsler, T. Irrgang, R. Kempe, *Langmuir*, 21 (2005) 12229.
[38] J. Zheng, Q. Zhang, J. Chen, Y. Xia, *Nano Lett*., 10 (2010) 30.
[39] M.A. Mahmoud, M.A. El-Sayed, *Nano Lett*., 11 (2011) 946.
[40] Y. Gao, X. Ding, Z. Zheng, X. Chen, Y. Peng, *Chem. Commun*., (2007), 3720.
[41] G. Weng, M.A. Mahmoud, M.A. El-Sayed, *J. Phys. Chem. C*, 116 (2012) 24171.

CHAPTER 4:

A bioinspired approach for controlling accessibility in calix[4]arene-bound metal cluster catalysts

a collaboration between
Namal de Silva, Jeong-Myeong Ha, Andrew Solovyov, Michael Nigra, Isao Ogino, Sheila Yeh, Kathleen Durkin, and Alexander Katz

"A bioinspired approach for controlling accessibility in calix[4]arene-bound metal cluster catalysts." Namal de Silva, Jeong-Myeong Ha, Andrew Solovyov, Michael M. Nigra, Isao Ogino, Sheila W. Yeh, Kathleen A. Durkin, and Alexander Katz, *Nature Chemistry* 2010, Vol. 2, pages 1062-1068. - Reproduced by permission of Nature Publishing Group. Available online at: http://dx.doi.org/10.1038/nchem.860

Abstract

In enzymes, the electronic and steric environments of active centres, and therefore their activity in biological processes, are controlled by the surrounding amino acids. In a similar manner, organic ligands have been used for the 'passivation' of metal clusters, that is, inhibition of their aggregation and control of their environment. However, the ability of enzymes to maintain large degrees of accessibility has remained difficult to mimic in synthetic systems in which little room, if any, is typically left to bind to other species. Here, using calix[4]arene macrocycles bearing phosphines as crude mimics of the rigid backbones of proteins, we demonstrate the synthesis of gold clusters and the control of their accessibility through an interplay between the sizes of the calixarene ligands and metal cores. For 0.9-nm cores, 25% of all the gold atoms within the cluster bind to the chemisorption probe 2-naphthalenethiol. This accessibility dramatically decreases with 1.1-nm and 4-nm gold cores.

4.1 Introduction

Nature routinely uses amino-acid residues to tune the electronic and steric environment surrounding metal-cluster active sites [1] in proteins. Enzymes accomplish this while also providing accessibility for small-molecule reactants to bind to the active site— the first step in the catalytic cycle. For instance, the Fe–S cluster active site in the enzyme aconitase is able to coordinate isocitrate substrate in the presence of high local concentrations of potentially inhibiting carboxylates and basic functional groups on the protein backbone. [2] Similarly, the enzyme laccase consists of four anionic carboxylate-containing residues within a distance of 12 Å of the cationic multi-copper active site. The enzyme maintains coordinative unsaturation by preventing direct electrostatic interaction between these anionic residues and the active site. This, also, is thought to be crucial for controlling the binding affinity of water to the active site. [3]

As yet unanswered is the question of how enzymes are able to maintain coordinative unsaturation at active sites in the presence of inhibitors on the protein backbone, and in such close proximity. The established view of the protein backbone is that it consists of a series of conjoined, rigid, nanoscale segments. [4] Based on this, we hypothesized that these rigid segments could form a cage structure to surround each metal-cluster active site with an effective mesh size large enough to be penetrable to small molecules but not to other rigid protein segments. Accessibility in this hypothetical mechanism relies critically on the metal-cluster active site being smaller than the rigid segment length, as schematically illustrated in Figure 4.1a,b. Our goal is to translate this mechanism to the realm of synthetic metal clusters, using calix[4]arene macrocycles as crude mimics of rigid protein backbone segments.

In synthetic metal-cluster catalysts, ligand functionalization has the important function of preventing their aggregation while facilitating, in principle, the same electronic and steric control of the metal active site as in proteins. [5] Gold cluster catalysis, in particular, has recently become a rapidly expanding field with great potential. [6,7] but the tendency of cluster active sites to aggregate has been a major limitation. [8] Cluster catalysts have previously been functionalized with organic ligands such as cucurbituril, [9] b-cyclodextrin, [10–12] dendron, [13] dendrimer, [14] and polymer [15] ligands. Progress in this area relies on controlling catalysis by tuning the electronic properties of the metal surface, which may be achieved using such organic ligands.

In a related approach, [1] the redox potential of Fe–S clusters in proteins had been tuned within a range of 0.5 eV by tuning the microenvironment of their organic ligands. In addition,

platinum metal clusters on alumina have been functionalized using cinchoni- dine as a ligand, leading to an enhancement by a factor of over 20 in the rate of a-ketoester hydrogenation. [16]

Using organic ligands to ultimately control the electronic and catalytic properties of a metal-cluster active site requires the design and synthesis of specific ligands for the metal surfaces. The ligands must have precisely positioned functional groups through which their interaction with the metal surfaces can be precisely controlled, and must allow accurate measurement of the surface accessibility of the resulting metal cluster–ligands systems.

Recently, we have demonstrated [17] that achiral gold nanoparticles can be converted into gold nanoparticles with a chiral surface plasmon band (shown by circular dichroism spectroscopy) through adsorption of a chiral calixarene–amine ligand onto their surfaces. We also synthesized [18] 4-nm gold nanoparticles bound with calix[6]arene triphosphine ligands, and found that they featured enhanced stability against aggregation, increased metal electron density, and accessible metal surfaces that served as small- molecule binding sites. However, the proportion of accessible gold atoms in these nanoparticles is still only a small fraction of the total. Increasing the accessibility of functionalized metal clusters and nanoparticles remains critical for catalysis as well as other applications that rely on the binding of molecules to metal surfaces.

In this manuscript, we use a bioinspired approach for the design and synthesis of organic ligand-bound gold clusters with significantly enhanced surface accessibility. This approach relies on the synthesis of a subnanometre gold core in **{Au–1}–2a** (schematically illustrated in Figure 4.1c), which is smaller in size than the bulky calix[4]arene ligand bound on its surface, as well as slightly larger gold clusters **{Au–2}–2b** and **{Au–3}–2c**. Cluster characterization using high-angle annular dark-field scanning transmission electron microscopy (HAADF-STEM) and X-ray photoelectron spectroscopy (XPS) demonstrates that the Au(I)–calixarene precursor complex structure controls the ensuing calixarene-bound gold cluster size. The accessibility of the gold clusters is determined through steady-state fluorescence measurements with the probe molecule 2-naphthalenethiol (2NT) (Figure 4.1d,e). These specifically demonstrate **{Au–1}–2a** to have the largest level of accessibility on a per-metal atom basis yet reported for an organically functionalized metal cluster in solution. This accessibility is schematically illustrated in Fig. 1d, which shows accessible binding sites in **{Au–1}–2a** saturated with 2NT.

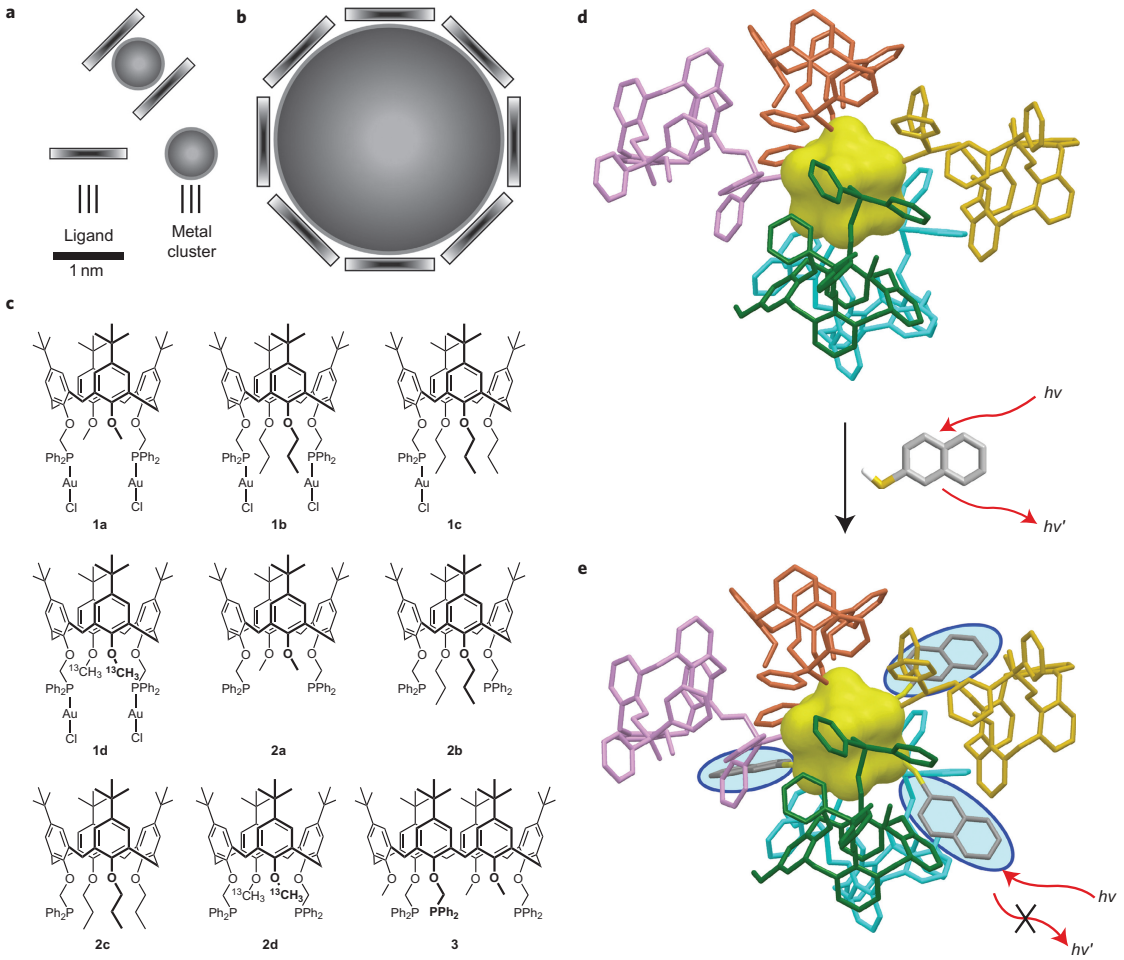

Figure 4.1: Illustration of comparative synthetic approach adopted to control the accessibility of gold clusters through bulky calix[4]arene ligands. (a,b), Schematic of subnanometer gold core (note black scale bar) (a) and 4-nm gold nanoparticle (b), both of which are bound with bulky organic ligands, represented by the darkened rectangles. The cluster in (a) consists of accessible sites on the length scale of a small molecule, which are slightly smaller than the bulky organic ligands and cover a significant fraction of the total cluster surface area. (c), Relevant calixarene–phosphine ligands and related Au(I) precursor complexes (**1a–d**). (d), Schematic of calixarene-bound cluster **{Au–1}–2a** consisting of a 0.9-nm Au_{11} metal core and five bound calixarene ligands. Two of these calixarene ligands (**2a**) are bound in a bidentate fashion (brick red and light turquoise), and three are bound in a monodentate fashion (dark yellow, dark green and light purple). The monodentate ligands consist of bound phosphine and unbound phosphine-oxide substituents. (e), Schematic of cluster in d after treatment with the 2NT chemisorption probe, which fluoresces when free in solution and is represented by grey (C), yellow (S) and white (H). 2NT bound to the gold surface of **{Au–1}–2a** is highlighted with light blue transparent ovals edged with dark blue. The fluorescence quenching of 2NT when chemisorbed on the gold cluster surface permits quantification of the amount of accessible binding sites. Calixarene upper-rim tert-butyl substituents and hydrogens have been omitted for clarity in d and e.

4.2 Results and Discussion

Au(I) complexes tert-butyl-calix[4]arene-$(OR)_{4-x}(OCH_2PPh_2AuCl)_x$ (x = 2, distal phosphorylation pattern, R = CH_3 (**1a**) C_3H_7–n (**1b**); x = 1, R = C_3H_7–n (**1c**)) were synthesized using previously reported procedures for similar substitution reactions, [19,20] and consist of a purely cone conformer as determined using ^{31}P and ^{1}H nuclear magnetic resonance (NMR) spectroscopies in $CDCl_3$. Preference for the cone conformer for **1a** is in stark contrast to the case for **2a**, in which all three conformers are present in $CDCl_3$ solution (molar ratio of partial cone to 1,3-alternative to cone for **2a** was measured to be 32:20:48 using ^{1}H NMR spectroscopy at -57°C). Complexes **1a**, **1b** and **1c** were characterized using single-crystal X-ray diffraction (Figure 4.2; selected bond lengths and angles are given in Supplementary Table 4.S.2). Comparison of the solid-state structures of **1a** and **1b** highlights a significant difference in the gold atom organization with respect to the calixarene lower-rim oxygen plane. Both gold atoms are located on the same side of this plane in the structure of **1a**. Consistent with σ (C–H)–π interactions [21] between the phenyl groups of both coordinated PPh_2 and the methoxy lower-rim substituents, the distances between the aromatic rings (centroid) and the carbon atoms of the methoxy substituents in the structure of **1a** are both 3.5 Å. In contrast, in the structure of **1b**, the unfavourable sterics between the gold and lower-rim propoxy groups prevent both gold atoms from being on the same side of the calixarene lower-rim oxygen plane. The steric role of the propoxy groups in defining the organization of $AuPPh_2Cl$ substituents, described above, may be further elucidated through molecular modelling of **1b** using density functional theory (DFT) at the B3LYP/LACV3P*+ level. These calculations demonstrate that the crystal structure conformation of **1b** is at least 2.4 kcal mol [21] lower in electronic energy than the lowest energy conformer in which the two $AuPPh_2Cl$ units are on the same face of the plane defined by the calixarene lower-rim oxygens. Therefore, for **1b**, >99% of the population of conformers should be in the form observed in the crystal structure as a result of these intramolecular steric considerations.

Gold clusters were synthesized via $NaBH_4$ reduction of Au(I)– phosphine calix[4]arene complexes **1a–c** dispersed in ethanol, under dilute conditions because of the low solubility of the reducing species and the complex during the reduction reaction. Similar procedures have been used previously for the synthesis of Au_{11} clusters. [22] Solvents such as dichloromethane, benzene and tetrahydrofuran completely solubilize at least one of the components and subsequently fail to produce a uniform distribution of small gold clusters after reduction. The UV–visible spectrum of **{Au–1}–2a** in CH_2Cl_2 solution consists of a band near 415 nm, which falls within the region characteristic of bands for small Au_n clusters (where $n \approx 11$). [23–31] Also characteristic of such Au_n clusters are the HAADF-STEM data [29,30,32] (Figure 4.2), which reveal a core diameter of 0.9 ± 0.1 nm for **{Au–1}–2a**. Electrospray ionization (ESI) mass spectrometry of **{Au–1}–2a** showed a complex pattern of multiple peaks, from which $[Au_{11}L_2Cl_3]^{2+}$ (L = calixarene phosphine ligand) could be identified as a doubly charged molecular ion. This fragment, however, appears only under ESI conditions, because the incorporation of Na (below 0.38 mol% via XPS) and Cl (below 0.05 mol% via elemental analysis) in **{Au–1}–2a** can be ruled out. Both elemental analysis and XPS demonstrate a gold-to-phosphine molar ratio of near unity (or, equivalently, a gold-to-calixarene molar ratio of approximately two), leading to an extraordinarily low gold mass fraction of 21% for **{Au–1}–2a**. This appears to be one of the lowest metal-to-ligand mass ratios measured for a gold cluster. Elemental analysis for a Au_{11} core in **{Au–1}–2a** requires five calixarene ligands. Spatial

constraints require several of the **2a** calixarene ligands to bind to the metal core in **{Au–1}–2a** in a monodentate fashion. Such a decreased ligand denticity in **{Au–1}–2a** (that is, the number of atoms of the ligand that coordinate to the metal) is consistent with similar observations of decreased denticity in gold nanoparticle systems consisting of excess ligand (relative to the minimum amount required for surface saturation where the adsorbed calixarene ligand lies flat and is bound with maximum denticity to the gold surface). [18] $^{31}P\{^{1}H\}$ NMR spectroscopy of **{Au–1}–2a** shows two resonances centred at δ = 23.7 ppm and 24.6 ppm at -60°C in CD_2Cl_2. These resonances are different from the distinct δ = 22.5 ppm resonance observed for unreduced **1a** at -60°C in CD_2Cl_2. The 24.6 ppm downfield resonance in the $^{31}P\{^{1}H\}$ NMR spectrum is assigned to phosphine oxide, and XPS quantifies the phosphine-to-phosphine-oxide ratio at 2.25 ± 0.36 in **{Au–1}–2a**. As proposed previously for Rh_6-based clusters in which one end of a bisphosphine ligand remains uncomplexed, [33] the P atoms on the monodentate **2a** ligands that are not bound to the gold core in **{Au–1}–2a** have a phosphine oxide functionality.

The structure proposed as a model of **{Au–1}–2a** is shown in Figure 4.1c, and consists of a Au_{11} core with two **2a** bidentate bound ligands and three other ligands bound in a monodentate fashion. HAADF-STEM analysis of **{Au–2}–2b** and **{Au–3}–2c** reveals significantly larger core diameters of 1.1 ± 0.2 nm and 1.9 ± 0.5 nm, respectively (Figure 4.2). The presence of a clearly identifiable surface plasmon resonance absorption band in the UV–visible spectrum of **{Au–3}–2c** in CH_2Cl_2 solution, near 520 nm, further confirms the presence of larger nanoparticles in **{Au–3}–2c** that are absent in **{Au–1}–2a** and **{Au–2}–2b**. The data above suggest a correlation between small cluster size and the ability of the precursor ligand **2a** to chelate to a subnanometre gold surface during cluster nucleation and growth. This is facilitated by having both phosphine groups able to coordinate to gold on the same face of the calixarene lower rim, and is only possible for complex **1a** of the three investigated (*vide supra*).

Au $4f_{7/2}$ XPS data (all XPS experiments were performed unsupported) are summarized in Table 4.1 and shed further light on the interactions between gold and bound calix[4]arene phosphine ligands in the clusters. The Au $4f_{7/2}$ binding energies for **{Au–2}– 2b** and **{Au–3}–2c** are at least 0.35 eV smaller than the corresponding value for bulk gold (84.0 eV), and for **{Au–3}–2c** the binding energy is 0.75 eV lower than for similarly sized thiolate-bound gold clusters, which consist of depleted gold *d*-charge. [34] This confirms the role of the corresponding calixarene phosphines as electron donor ligands to the gold cluster metal cores, which is further corroborated by recent single-crystal X-ray diffraction studies of Ir_4 cluster assemblies consisting of ligands **2a–c**, [35] as well as XPS characterization of larger 4-nm gold nanoparticles modified with a calix[6]arene phosphine ligand (entry **{Au–4}–3** in Table 4.1). [18] However, within the systematic trend of decreasing particle sizes in Table 4.1, the measured Au $4f_{7/2}$ binding energy monotonically increases in the series **{Au–4}–3**, **{Au–4}–2c**, **{Au–2}–2b**, **{Au–1}–2a**. In addition, there is a similar trend of increasing full-width at half-maximum (FWHM) of the Au $4f_{7/2}$ peak for the same series of calixarene-bound gold clusters. Differential charging effects can be ruled out as a possible explanation for this FWHM trend, as the P 2*p* peak width involving these clusters remains unchanged. [36]

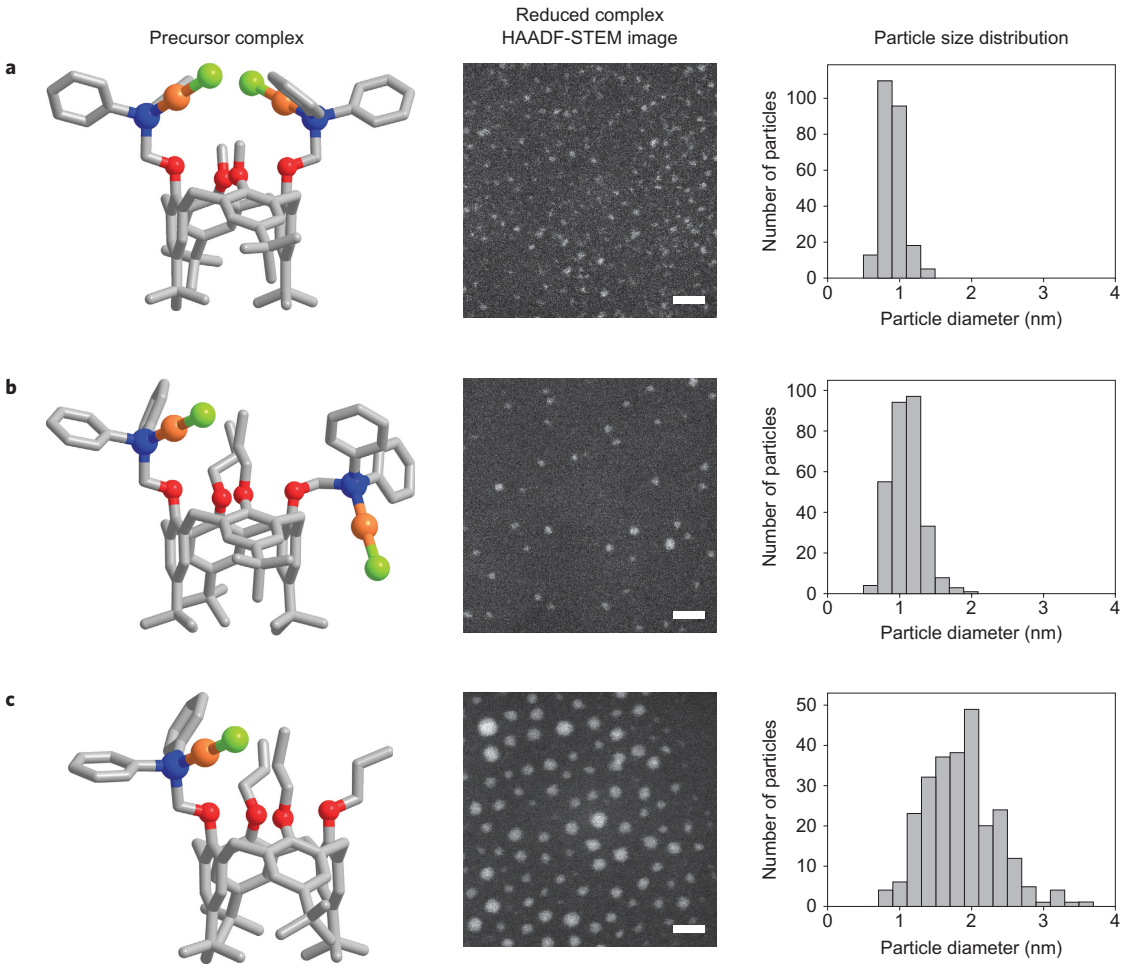

Figure 4.2: Structure of molecular precursors, and images and particle size distributions of gold clusters. (a–c), Precursor Au(I) complex structures (left column) of **1a** (a), **1b** (b) and **1c** (c) as determined by single-crystal X-ray diffraction (grey, C; red, O; blue, P; orange, Au; green, Cl), with hydrogens omitted for clarity. HAADF-STEM images (middle column) of reduced Au(I) precursor complexes consisting of **{Au–1}–2a** (0.9 ± 0.1 nm, 242 particles) (a), **{Au–2}–2b** (1.1 ± 0.2 nm, 295 particles) (b) and **{Au–3}–2c** (1.9 ± 0.5 nm, 257 particles) (c). Scale bar, 5 nm. Particle size distributions (right column) for all HAADF-STEM data collected for **{Au–1}–2a** (a), **{Au–2}–2b** (b) and **{Au–3}–2c** (c). The smallest methoxy substituents in **1a** facilitate CH–π interactions between methyl groups and phenyl substituents and the proximal organization of two gold atoms on the same face of the calixarene lower-rim plane (defined by the red phenolic oxygens). This enables chelation of ligand **2a** to the subnanometre gold core in **{Au–1}–2a**, which is synthesized upon **1a** reduction. The slightly larger propoxy substituents in **1b** are unable to accomplish this and lead to an organization in which the two gold atoms are on different sides of the calixarene lower-rim plane. Upon reduction of **1b**, this leads to larger gold clusters in **{Au–2}–2b**. The monodentate ligand **2c** leads to the largest nanoparticles upon reduction of complex **1c**.

Table 4.1: Summary of characterization data for gold cluster bound with lower-rim calixarene-phosphine ligands.

Gold cluster	Ligand	Diameter (nm[*])	Au/P[†]	Au (wt %[†])	Au 4*f* BE (FWHM) (eV[§])	Total Au 2NT bound[•] Surface Au 2NT bound[¶] (%)
{Au-1}-2a	**2a**	0.9 ± 0.1	1.11 ± 0.11	21‡	84.15 (1.64)	25.0 (25.0)
{Au-2}-2b	**2b**	1.1 ± 0.2	1.78 ± 0.09	38	83.65 (1.23)	6.3 (8.0)
{Au-3}-2c	**2c**	1.9 ± 0.5	3.25 ± 0.15	40	83.55 (1.11)	1.2 (2.1)
{Au-4}-2a	**2a**	4.1 ± 0.9	N/D	N/D	N/D	0.0 (0.0)
{Au-4}-2c	**2c**	4.1 ± 0.9	N/D	N/D	N/D	0.0 (0.0)
{Au-4}-3	**3**	4.1 ± 0.9[#]	N/D	N/D	83.85 (1.09)[#]	1.4 (4.8)[#]

[*] Based on HAADF-STEM. [†] Based on XPS. [‡]Verified using ICP analysis. [§]Binding energy (BE) and FWHM measured using XPS. [•]Fraction of total gold atoms bound to 2NT chemisorption probe, based on steady-state fluorescence measurement assuming a stoichiometry of one Au atom bound per chemisorbed 2NT. [¶]Fraction of surface gold atoms bound to 2NT chemisorption probe based on date in footnote [•]. [#]Data taken from ref. 18.

Taken together, these data suggest a final-state hole-shielding effect resulting from extra atomic relaxation, which tends to increase the binding energy for smaller gold clusters and acts in opposition to the surface ligand effect of the calixarene phosphine as an electron donor. [37,38] It should be noted that because XPS experiments are conducted on unsupported calixarene-bound gold nanoparticles, the final-state effect in this case must be due to the interaction between the bound phosphine as surface ligand and the gold core. From the perspective of XPS, the uniqueness of this system in comparison to others that use electron-withdrawing ligands such as thiols [34,37,39,40] arises from the fact that the effect of the surface ligand and the final-state effect can be separated because of their opposing influences on the Au $4f_{7/2}$ peak binding energy. Indeed, the two effects almost cancel one another out in **{Au–1}–2a**, which has a Au $4f_{7/2}$ binding energy only slightly (0.15 eV) above the value for bulk gold.

The amount of accessible surface in all three gold clusters can be measured using the chemisorption probe 2NT, as this probe has been used previously to measure accessible areas in calixarene-bound gold nanoparticles. [18] The data in Figure 4.3a reveal a percentage of total gold atoms that are coordinated to 2NT in **{Au–1}–2a** of 25%. This is 18 times higher than the previously reported highest value, measured for **{Au–4}–3** (ref. 18). Control experiments with similarly sized Au_{11} clusters consisting of neutral $Au_{11}(PPh_3)_7(SCN)_3$ (ref. 41; also shown in Figure 4.3a) and cationic $[Au_{11}(PPh_3)_8Cl_2]PF_6$ (ref. 42) clusters demonstrate an entire lack of 2NT binding, which is consistent with there being no exchange of thiols for phosphine in other Au_{11}-based clusters at temperatures below 40ºC (ref. 32). In addition, 4-nm gold nanoparticles bound with either **2a** or **2c** (entries **{Au–4}–2a** and **{Au–4}–2c** in Table 4.1) demonstrate no accessibility to 2NT binding. Controls consisting of varying longer equilibration times of 2NT

with calixarene-bound gold clusters before steady-state fluorescence measurement have similar 2NT binding results.

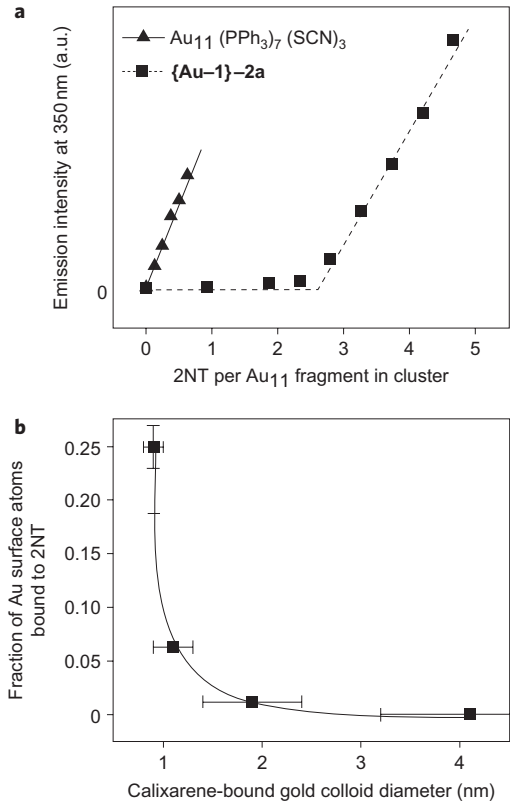

Figure 4.3: Determination of gold cluster accessibility through the steady-state fluorescence of the 2NT probe molecule. (a), Fluorescence emission intensity of 2NT on **{Au–1}–2a** (squares) and $Au_{11}(PPh_3)_7(SCN)_3$ (triangles) clusters. Each solution contains 5 mM of Au_{11} fragments in dichloromethane and is excited at 283 nm. Emission intensity is subtracted from dichloromethane solvent background. Despite having similarly sized Au cores $Au_{11}(PPh_3)_7(SCN)_3$ lacks accessibility and **{Au–1}–2a** manifests itself as a functional cluster that binds 2NT to accessible binding sites. (b), Fraction of gold surface atoms that are bound with 2NT (lower bound) versus cluster diameter as measured using HAADF-STEM for gold clusters of various sizes that are bound with lower-rim substituted cone calix[4]arene phosphine ligands. The dependence of accessibility on gold core size is consistent with the synthesis of accessible binding sites according to the mechanism shown in Figure 4.1a,b. The error bars show the size distribution of the diameter of each type of gold cluster (see Figure 4.2, right panels): **{Au–1}–2a**, 0.9 ± 0.1 nm; **{Au–2}–2b**, 1.1 ± 0.2 nm; **{Au–3}–2c**, 1.9 ± 0.5 nm.

An additional control is undertaken to rule out the presence of free calixarene ligand in solution upon 2NT binding, because the exchange of thiols for phosphine in $Au_{11}(PPh_3)Cl_3$ has been previously reported to lead to phosphine ligand in solution albeit at elevated temperatures. [32] This control uses ^{13}C-labelled **2d** as a sensitive probe of free ligand in solution because of its

distinct methoxy carbon resonances at 60.6, 59.6 and 57.9 ppm, which correspond to a mixture of conformers in $CDCl_3$ solution, as discussed above for unlabeled **1a**. The synthesis and reduction of the Au(I) complex **1d** results in a ^{13}C-labelled gold cluster **{Au–1}–2d**, which is similar in all respects to **{Au–1}–2a** except for the presence of the ^{13}C- methoxy label. Consistent with the cone conformer for bound calixarene–phosphine ligands, the ^{13}C NMR spectrum of **{Au–1}–2d** exhibits no methoxy resonances below 60 ppm. Treatment of **{Au–1}–2d** with a fivefold excess of 2NT (relative to the amount necessary for saturation of accessible binding sites) results in a 0.1 ppm downfield shift in the major methoxy resonance using ^{13}C NMR spectroscopy, which is consistent with a *d*-charge depletion of gold upon 2NT binding. [43] There is a lack of upfield methoxy resonances below 60 ppm even after 1 week. This result effectively rules out the possibility of **1d** in solution after 2NT binding, and also the release of the corresponding phosphine oxide ligand in solution after 2NT binding, which has upfield methoxy resonances that are similar to those of **1d**. Additional controls demonstrate no 2NT binding for molecular complexes **1a**, **1b** and **1c**, excluding the possibility of apparent binding due to possible traces of unreduced complex in solution.

The data in Table 4.1 summarize the percentage of bound gold atoms after 2NT chemisorption, and demonstrate that the fraction of bound surface atoms decreases monotonically with increasing particle size in the order **{Au–1}–2a** > **{Au–2}–2b** > **{Au–3}–2c** > **{Au–4}–2c** (same as **{Au–4}–2a**). The trend in the 2NT binding data above cannot be explained by surface area-to-volume considerations given the surface atom basis data in Table 4.1 (ref. 44), and the trend (for example, accessibility in **{Au–3}–2c** versus **{Au–4}–2c**) also cannot be explained on the basis of the radius of curvature, which has previously been reported to account for 1.4-fold increases in the available surface area for 1.6- nm gold clusters when compared with bulk gold surfaces. [45] Considering the footprint of the 2NT probe (> 24.4 $Å^2$), [18] the actual quantity of gold atoms within these accessible gaps must be significantly more than the fraction of surface atoms bound to 2NT in Table 4.1. Accessibility decreases by less than 20% in **{Au–1}–2a** after storage in the dark at room temperature for 6 months, and all clusters reported here are air- and water-stable. All results discussed above have been reproduced on at least three different synthesis batches.

Figure 4.3b graphically summarizes the accessibility data, and shows a sharp increase in the fraction of accessible gold surface atoms for calixarene-bound gold clusters that correspond in size to the calix[4]arene phosphine ligand. The mechanism for this enhanced accessibility is proposed to arise due to a ligand-packing problem on the surface of a small gold core. Few accessible spaces are created on larger particles because of close-packing of calix[4]- arene ligands on the surface. However, on a gold core that is smaller than the size of a calix[4]arene ligand, the ligands must pack on the surface in such a way that significant gaps are left between them, due to the impossibility of binding a non-integer number of ligands. These gaps are slightly smaller than the size of the calixarene ligand, but are the right size for a small organic molecule and rep- resent a significant fraction of the metal-core surface area. This packing scenario is schematically shown in Figure 4. 1a,b in a comparative fashion for large and small metal core sizes. Such a mechanism provides a general understanding of how accessibility can be controlled in metal clusters that are bound with organic ligands, and is expected to find broad utility in catalysis and other applications that rely on binding molecules to metal cluster surfaces.

4.3 Conclusions

The design and synthesis of organic ligand-bound gold clusters using a bioinspired approach is demonstrated, in which calix[4]arene phosphine ligands serve as crude macrocyclic mimics of rigid protein backbone segments. The resulting electron-rich clusters show that using an organic ligand is a versatile approach to modify- ing the electronic properties of the metal. This is demonstrated by the 0.75 eV reduction in Au $4f_{7/2}$ binding energy for the calixarene phosphine-bound 1.9-nm gold clusters described here when com- pared with similarly sized thiolate-bound gold clusters. [34] Furthermore, the calixarene-bound clusters demonstrate high levels of accessibility, with up to 25% of the total gold atoms binding chemisorption probe 2NT in cluster **{Au–1}–2a**, which is in contrast to a complete lack of accessibility observed in similarly sized Au_{11}-phosphine clusters as well as larger gold nanoparticles. The observed abrupt increase in accessibility when the metal-core diameter is smaller than the calixarene ligand size suggests a new and general mechanism of accessibility in organic ligand-bound metal clusters. This mechanism is expected to find broad utility in catalysis and other applications that rely on creating accessibility for binding molecules to metal clusters functionalized with organic ligands.

4.4 Experimental methods

4.4.1 Synthesis of gold precursors **1a–d**

Ligand **2a** (or either **2b** or **2d**) (0.3 mmol) was reacted with two equivalents of $Au(SMe_2)Cl$ in 20 ml of CH_2Cl_2 for 20 min at room temperature in the dark. The cloudy mixture was filtered to obtain a clear solution, and was then evaporated to yield a white powder. Crystals of **1a** (or either **1b** or **1d**) were obtained by slow evaporation in 50:50 hexane:CH_2Cl_2. **1c** was synthesized following a similar procedure, starting with ligand **2c**, but using 1 equiv. $Au(SMe_2)Cl$. All complexes were white powders that yielded optically clear colourless solutions when dissolved in dichloromethane.

4.4.2 Synthesis of gold colloid **{Au–1}–2a**

$NaBH_4$ (50 mg, or 3.9 equiv. with respect to Au atoms) was added to a suspension of 0.166 mmol (255 mg) of gold precursor complex **1a** in 80 ml of anhydrous ethanol. The disappearance of the starting precursor gold complex from the reaction mixture was monitored by means of thin-layer chromatography in dichloromethane. The resulting mixture was stirred for 40 min at room temperature, filtered and evaporated *in vacuo*. The gold cluster product was washed with ~150 ml of degassed (pH 7) water, and dried under vacuum and subsequently washed with ~10 ml hexane and then again dried under vacuum. This synthesized 130 mg of final **{Au–1}–2a**.

4.4.3 Synthesis of gold colloid **{Au–2}–2b**

$NaBH_4$ (18 mg, or 3.6 equiv. with respect to Au atoms) was added to a suspension of 0.066 mmol (105 mg) of gold precursor complex **1b** in 30 ml of anhydrous ethanol. The remaining procedures were identical to the synthesis of **{Au–1}–2a**, except that the volume of solvent used for washing was adjusted proportionally to the number of moles of calixarene in the

synthesis relative to **{Au–1}–2a**.

4.4.4 Synthesis of gold colloid **{Au–3}–2c**

$NaBH_4$ (6 mg, or 3.8 equiv. with respect to Au atoms) was added to a suspension of 0.041 mmol (50 mg) of gold precursor complex **1c** in 20 ml of anhydrous ethanol. The remaining procedures were identical to the synthesis of **{Au–1}–2a**, except that only water was used as a solvent for washing, and the amount of water was adjusted proportionally to the number of moles of calixarene in the synthesis relative to **{Au–1}–2a**.

4.4.5 Postsynthetic modification of gold nanoparticles with **2a** and **2c**

Gold nanoparticles were synthesized from tetraoctylammonium bromide (20 equiv. relative to gold atoms) stabilized $HAuCl_4$/dichloromethane solution to yield 4-nm gold nanoparticles as previously described. Based on a previously reported molecular footprints of calix[4]arenes on gold nanoparticles [46], 1.25- and 2- monolayer equivalents of calix[4]arene **2a** or **2c** were added to the 4-nm gold nanoparticle solution containing 200 mM gold atoms in 5 ml of dichloromethane, producing **2a**- and **2c**-bound 4-nm gold nanoparticles.

4.4.6 Fluorescence of 2NT bound to gold nanoparticles

The fluorescence of 2NT adsorbed on gold clusters was measured with a steady-state fluorimeter (F-4500, Hitachi) operating at 950 V and with 5 nm of excitation/emission slit width. The solvent used for fluorescence studies was dichloromethane, and the excitation wavelength was 283 nm. A stock solution of 2NT (500 mM in dichloromethane) was added to 5 ml of gold nanoparticle solution, which was shaken for 2 min and equilibrated thereafter for a period of 3 min before each fluorescence measurement.

4.4.7. Characterization of gold clusters

UV–visible spectroscopy of gold clusters was performed with a UV–visible spectrometer (Varian Cary-400). Transmission electron micrographs of gold clusters were observed with 200 kV FEI monochromated F20 UT Tecnai (National Center for Electron Microscopy, Lawrence Berkeley National Laboratory). XPS of gold clusters was carried out by depositing gold clusters onto a silicon wafer using double-sided tape. XPS analysis was performed using a Ulvac-Phi Quantera scanning X-ray microprobe operating with a spectral resolution of 1.05 eV. The energy scale of the spectrometer was calibrated using Ag photoemission peaks in accordance with standard practice. XPS results were corrected using the C 1*s* peak at 284.6 eV.

4.4.8 DFT calculations

Quantum-mechanical calculations on the **1b** system at B3LYP/LACV3P*+ indicate that the conformer found in the crystal structure was lower in energy than other possible conformers. To explore the **1b** conformational space, we built two alternative conformers for **1b** based on the **1a** crystal structure, by extending the **1a** *O*-methyl substituents into *O*-propyl groups. In doing so, we introduced the possibility of different conformations for the new propyl moieties. In

alternative **1b** conformation I, we arranged the propyl moities in a *trans–trans* arrangement (*tt*) with the C–O–C–C and O–C–C–C dihedrals set to be 1808. In alternative **1b** conformation II, these angles were in a *gauche–gauche* (*gg*) arrangement at 260 and 608, respectively. In both of these **1b** conformers, the AuCl moities were left as found in the 1b crystal structure. The *tt* and *gg O*-propyl conformers were chosen as reasonable alternative structures for **1b**, which minimized van der Waals contacts with the remainder of the structure. DFT optimizations were performed in Jaguar 7.5 (ref. 47). The results suggest that the crystal structure conformation of **1b** is at least 2.45 kcal mol^{-1} lower in electronic energy than alternative conformation I (*tt*) and 8.3 kcal mol^{-1} lower in electronic energy than alternative conformation II (*gg*). Because the 'anti' conformation has a degeneracy of two, the population of conformers should be 99.2% in this form. There has been some evidence in the literature that the B3LYP functional may not be optimal for thermodynamic calculations including transition metals, [48] so we followed these B3LYP calculations with M05 [49] functional calculations in Gaussian03, Revision E01 (Gaussian, Inc.) using an LANL2DZ basis set on the Au with 6-31G(*d*) on all other elements. These electronic energy data from these calculations also support the result that the anti form is in fact the lowest energy conformer.

4.5 Acknowledgements

The authors are grateful to Chevron Corporation for financial support of this research. The authors acknowledge the technical assistance of R. Nichiporuk in the Mass Spectrometry Facility and National Institutes of Health grant no. 10RR022393-01 for the acquisition of the Q-Tof mass spectrometer. The authors also thank F.J. Hollander and A. Dipasquale for assistance with the characterization of **1a**, **1b** and **1c** by means of single-crystal X-ray diffraction. The authors acknowledge the support of the National Center for Electron Microscopy, Lawrence Berkeley Lab, supported by the U.S. Department of Energy under contract no. DE-AC02-05CH11231.

4.6 Supplementary information

4.6.1 NMR Spectra

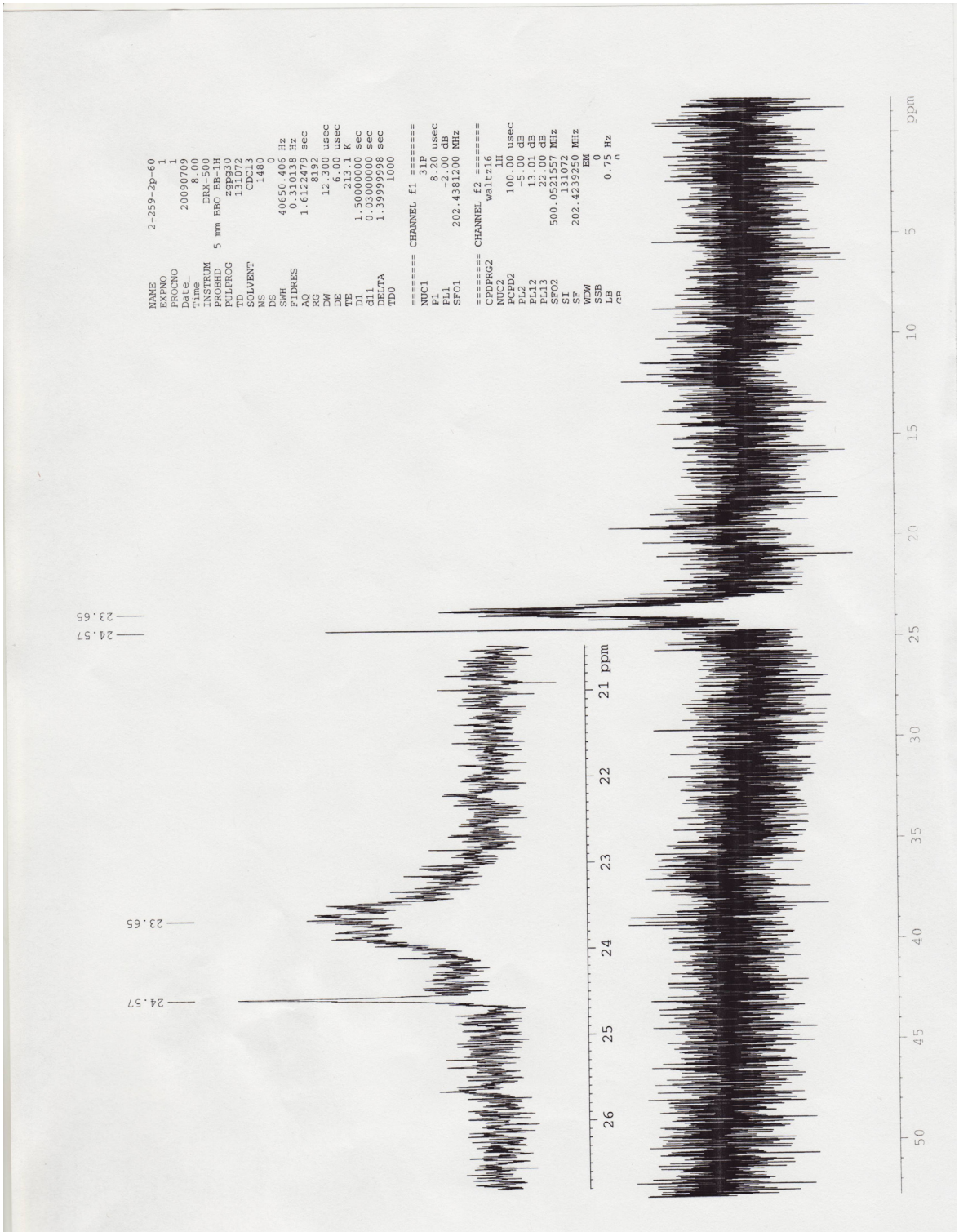

Figure 4.S.1: ^{31}P NMR spectrum of **{Au-1}-2a** at -60°C

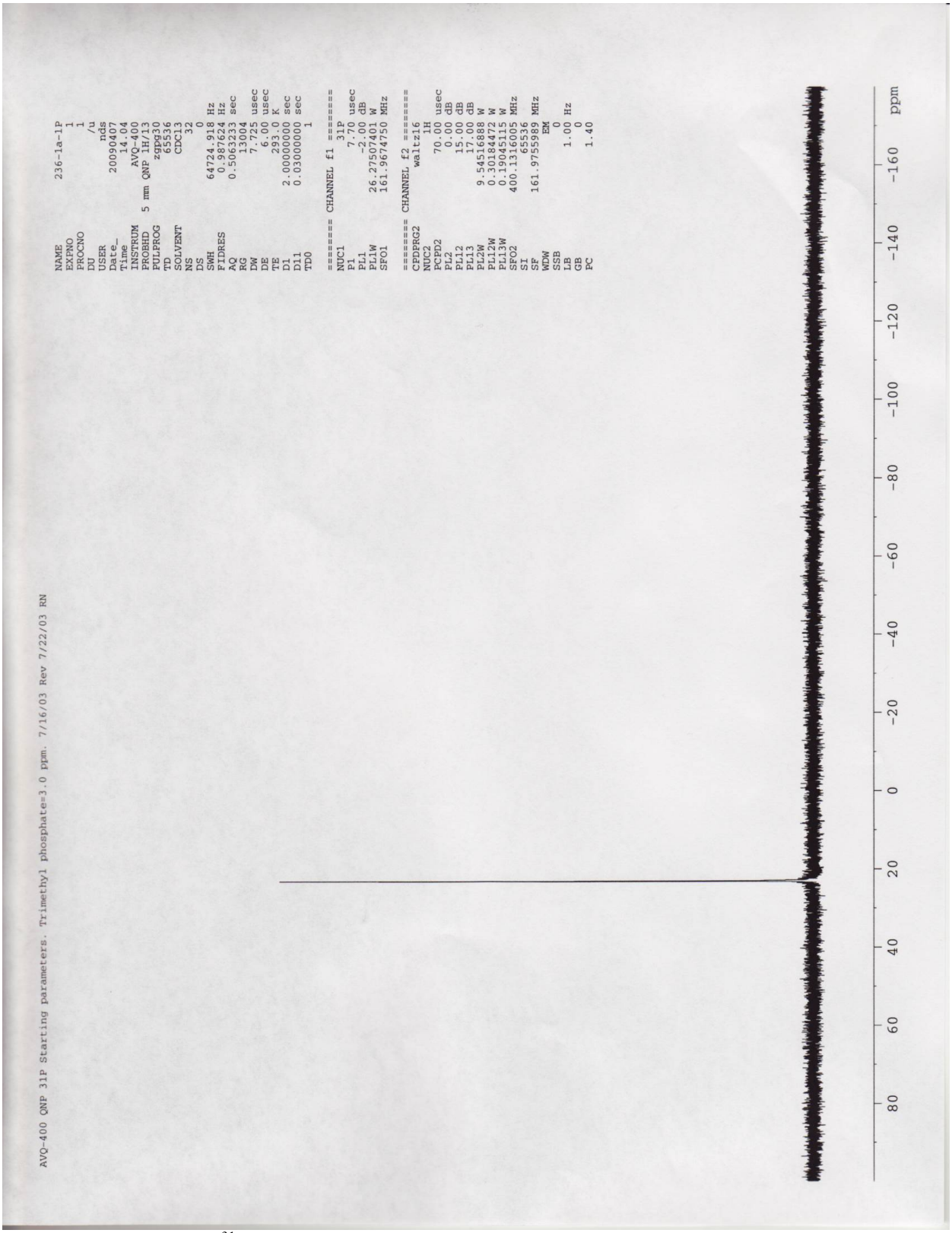

Figure 4.S.2: ^{31}P NMR spectrum of **1a** at room temperature

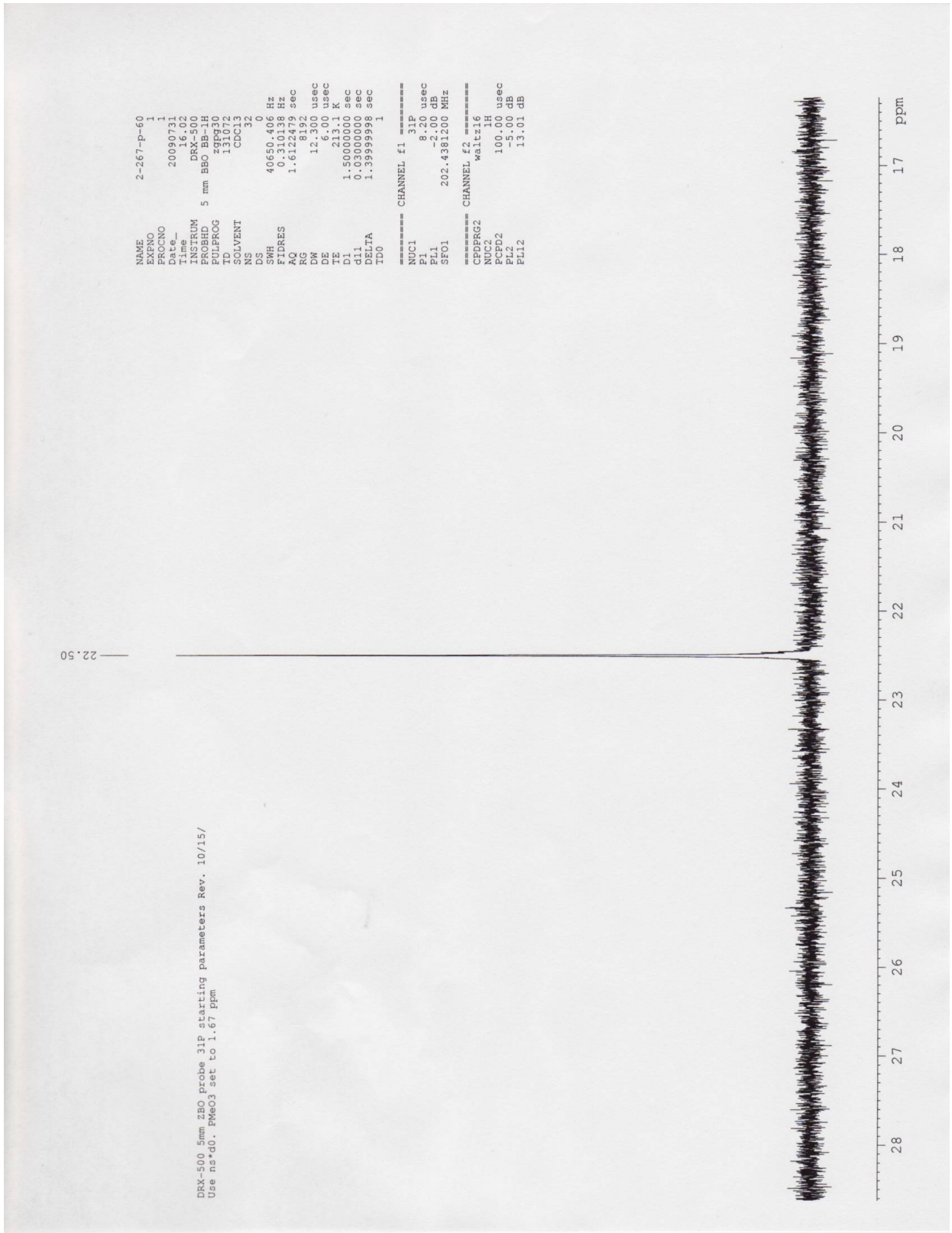

Figure 4.S.3: ^{31}P NMR spectrum of **1a** at -60°C

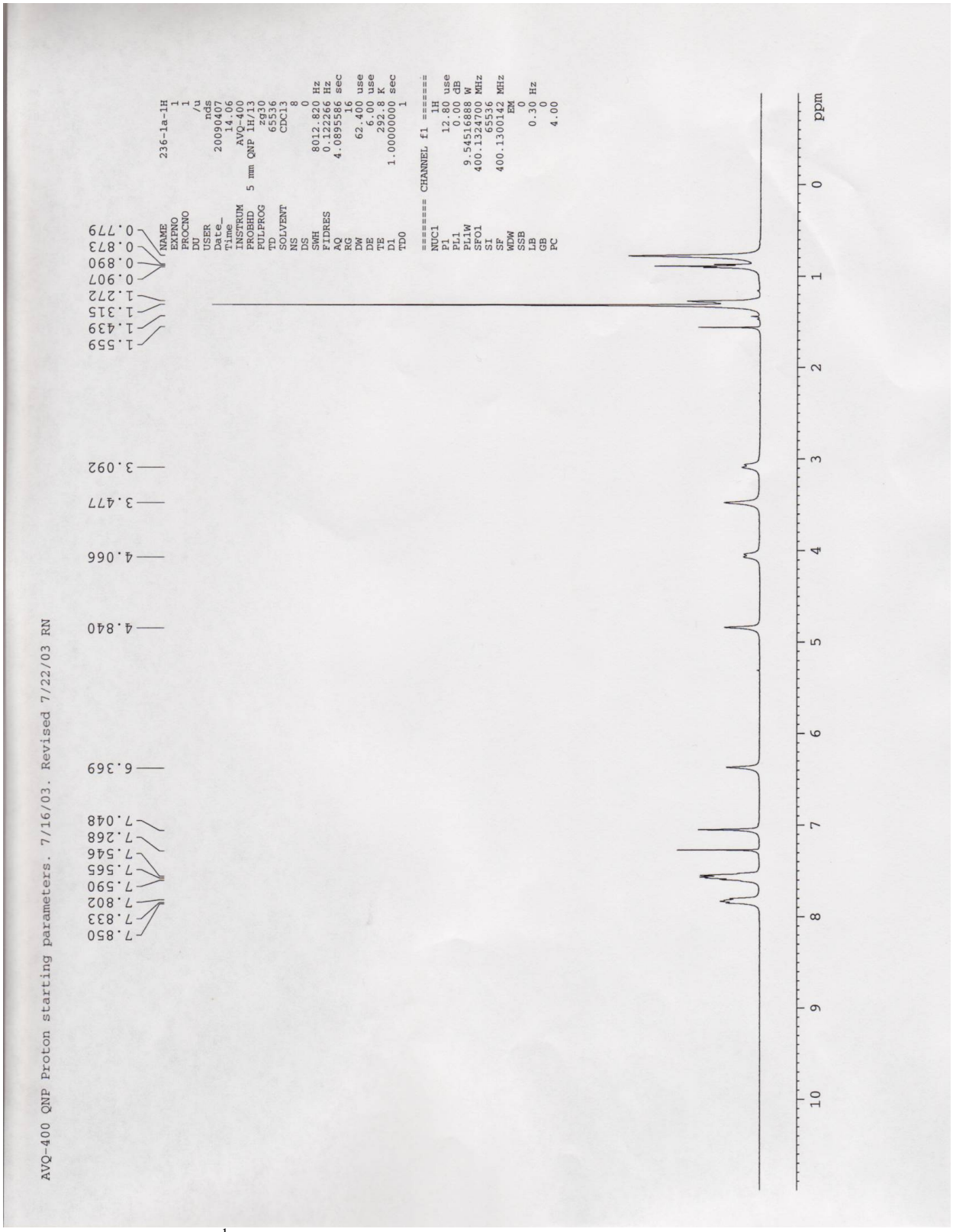

Figure 4.S.4: ^{1}H NMR spectrum of **1a** at room temperature

Figure 4.S.5: ^{31}P NMR spectrum of **1b** at room temperature

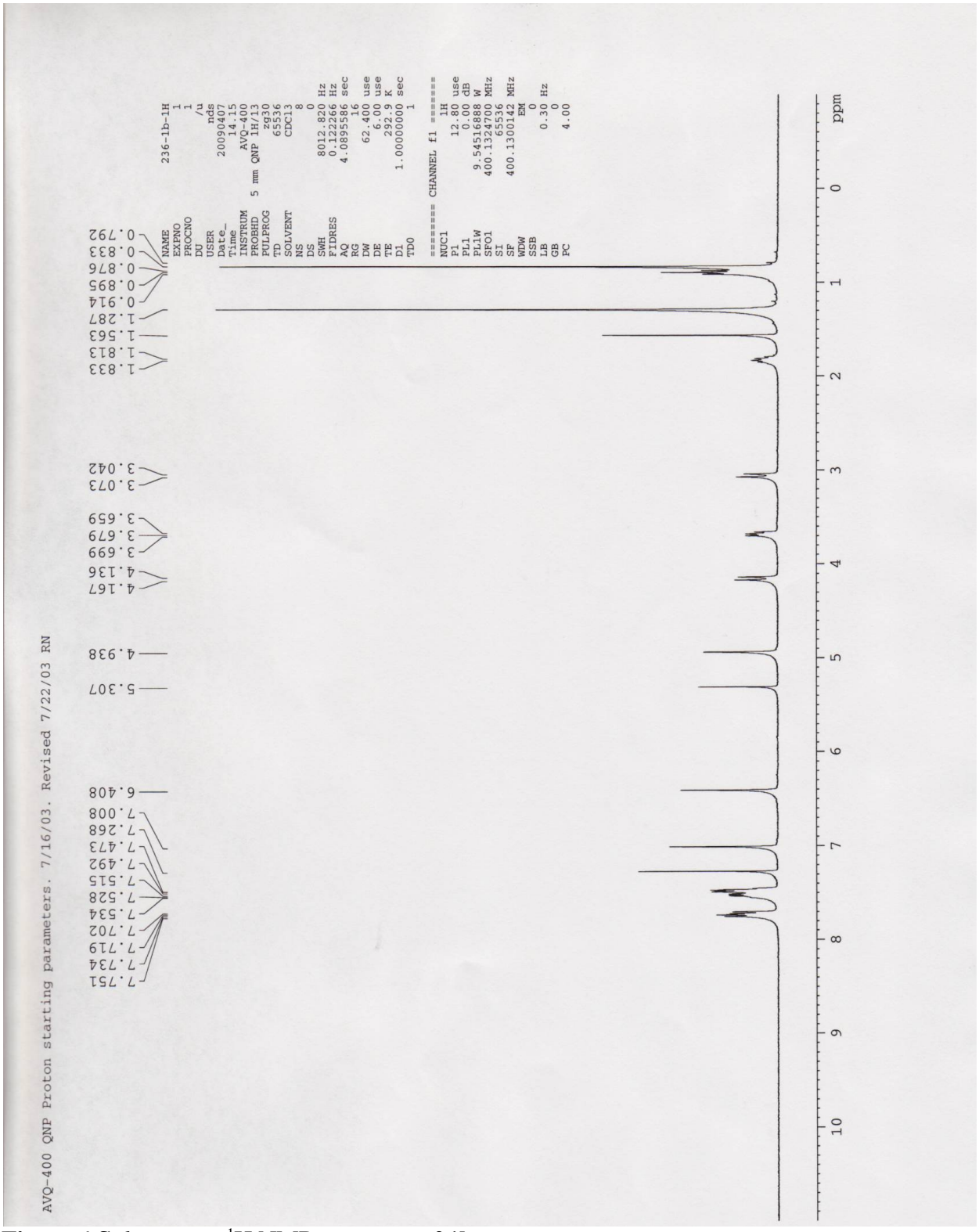

Figure 4.S.6: ^{1}H NMR spectrum of **1b** at room temperature

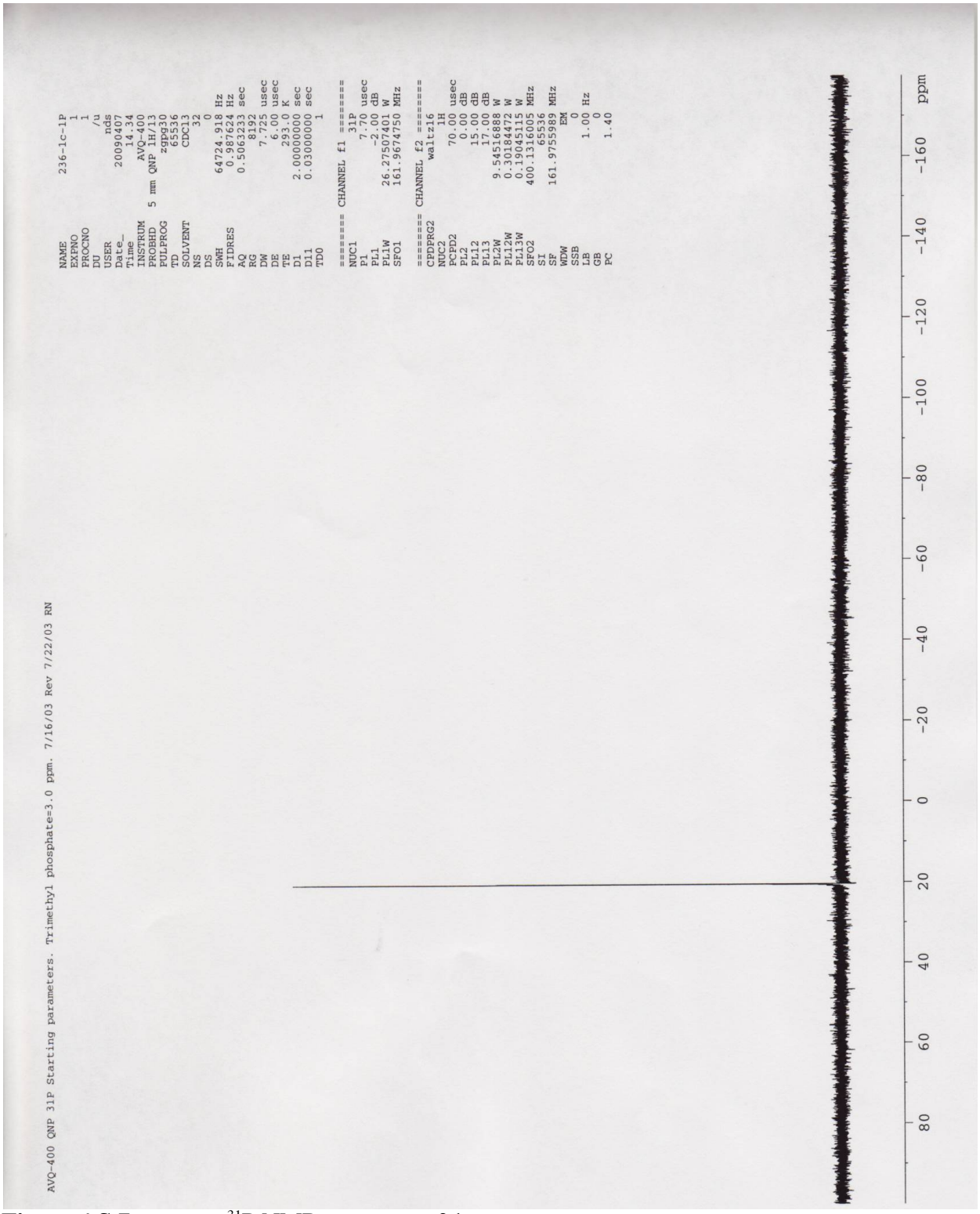

Figure 4.S.7: ^{31}P NMR spectrum of **1c** at room temperature

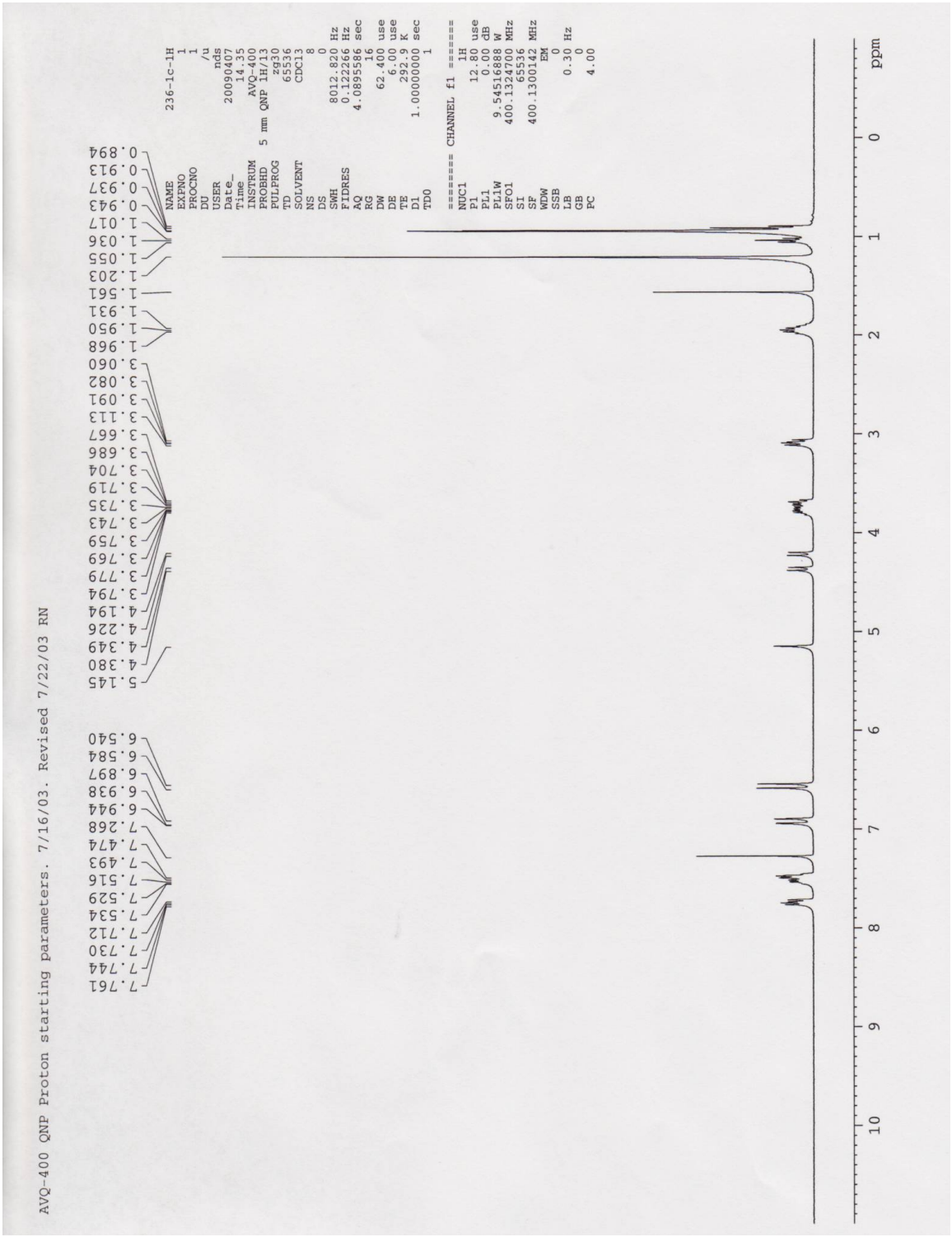

Figure 4.S.8: ^{1}H NMR spectrum of **1c** at room temperature

4.6.2: Mass spectra

4.6.2.1 Mass spectrum of **{Au-1}-2a**

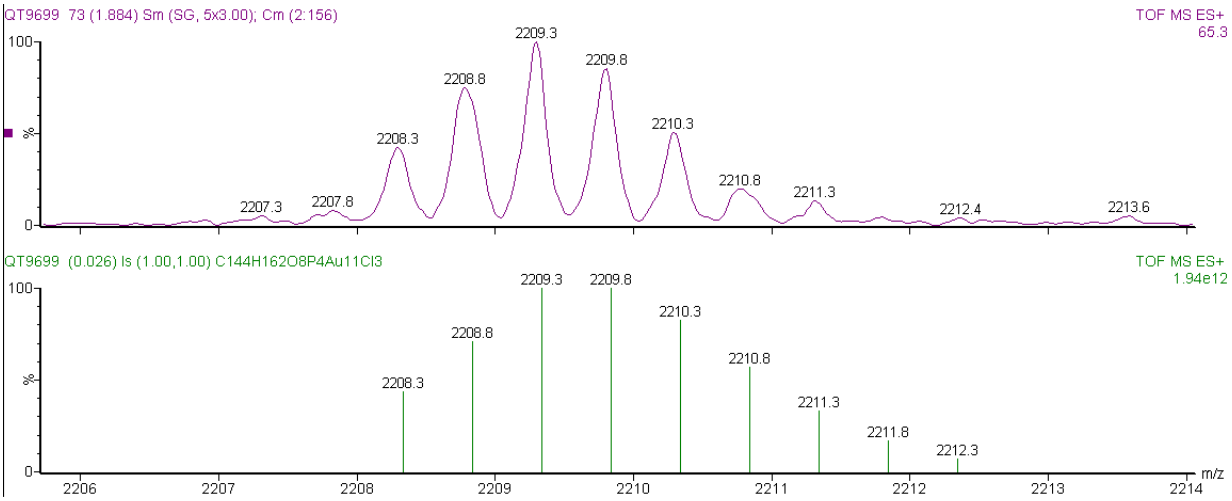

Figure 4.S.9: ESI mass spectrum showing a molecular ion fragment in **1a-red** (top) and theoretical simulation of $[Au_{11}L_2Cl_3]^{2+}$. L= *ter*t-butyl-calix[4]-$(OMe)_2(OCH_2PPh_2)_2$ (bottom).

4.6.2.2 Mass spectrum of **1a**, **1b**, **1c**

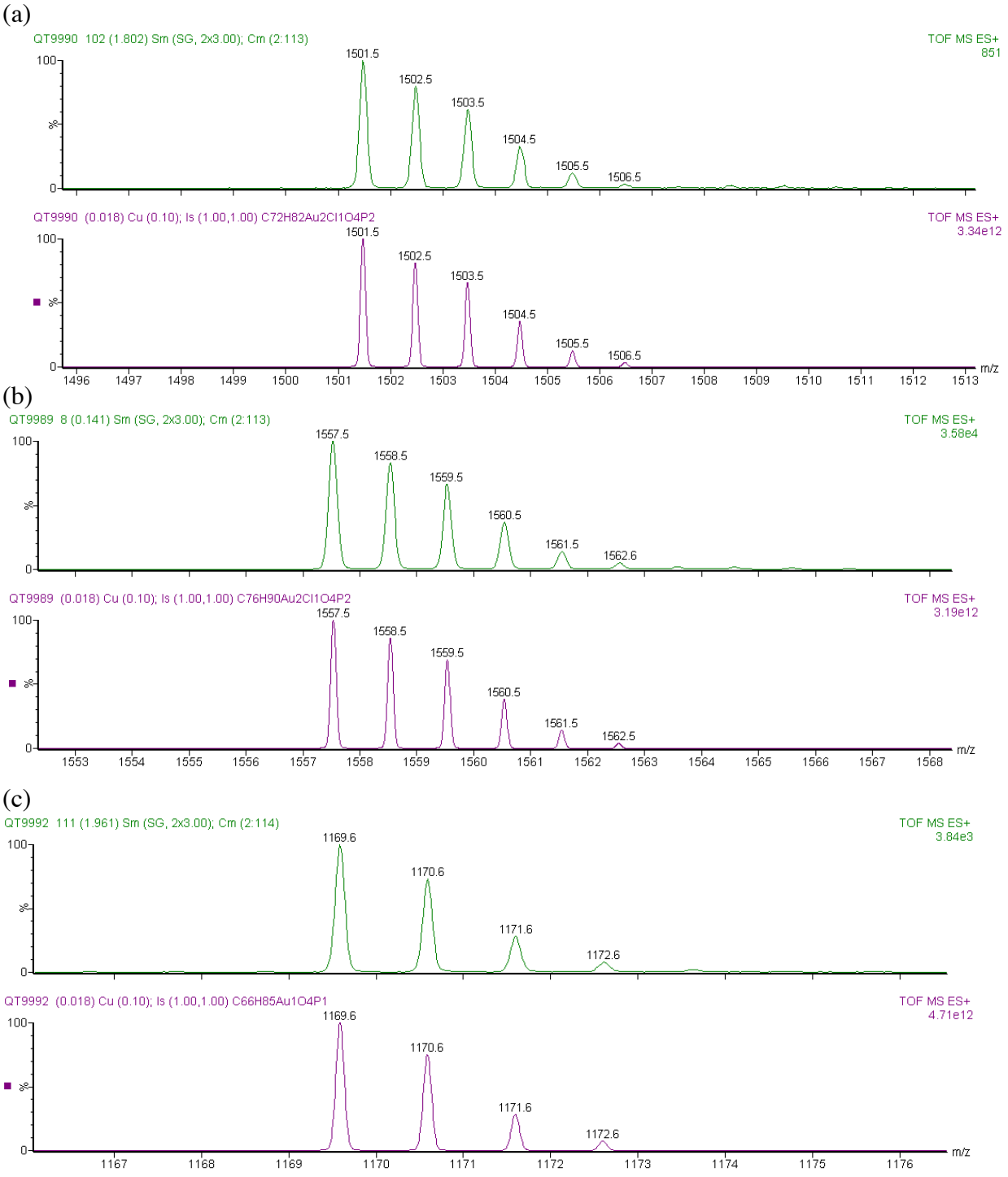

Figure 4.S.10: ESI mass spectra (top) and theoretical simulations (bottom) of $[M\text{-}Cl]^+$ molecular ions of precursors, (a) **1a**, (b) **1b**,and (c) **1c**.

4.6.3 UV-Vis spectra of reduced gold clusters

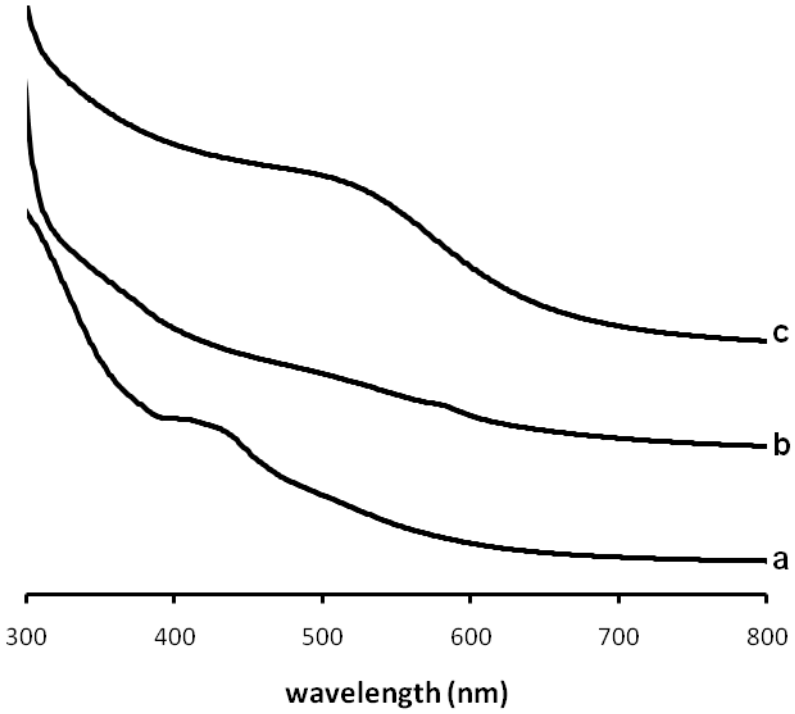

Figure 4.S.11: UV-Visible spectra of (a) **{Au-1}-2a**, (b) **{Au-2}-2b**, and (c) **{Au-3}-2c** in CH_2Cl_2.

4.6.4 Single crystal structures of Au precursors

Table 4.S.1: Single crystal structures of Au precursors

	1a	**1b**	**1c**	**2b**
chemical formula	$C_{79.50}H_{100}Au_2Cl_2O_4P_2$	$C_{76}H_{90}Au_2Cl_2O_4P_2$	$C_{66}H_{85}AuClO_4P$	$C_{76}H_{90}O_4P_2$
formula weight	1646.45	1594.25	1205.73	1129.42
space group	I2/*a*	$P2_1/c$	$P2_1/c$	$P\bar{1}$
color	colorless	colorless	colorless	colorless
a (Å)	19.590(4)	14.6239(10)	19.695(10)	13.9923(5)
b (Å)	22.495(4)	25.8803(18)	14.974(7)	15.1673(5)
c (Å)	20.590(4)	21.5065(15)	20.876(10)	17.3281(6)
α (°)	90	90	90	83.2070(10)
β (°)	105.26(3)	108.7620(10)	96.290(6)	81.5680(10)
γ (°)	90	90	90	63.9150(10)
V (Å^3)	8753(3)	7707.1(9)	6120(5)	3261.19(19)
temperature (K)	163(2)	273(2)	153(2)	100(2)
Z	4	4	4	2
$R[F^2>2\sigma(F^2)]$	0.028	0.049	0.049	0.058
$wR(F^2)$	0.031	0.148	0.118	0.172
G.O.F.	1.34	0.78	1.02	1.54

Table 4.S.2: Selected bonding lengths, angles, and torsion angles

	Bonding	Length (Å)	Angle	Angle (degree)
1a	Au1—Cl2	2.277	O1—C23—P1	107.7
	P1—Au1	2.226	C23—P1—Au1	114.9
	C23—P1	1.829	P1—Au1—Cl2	174.16
	O1—C23	1.428	Au1—P1—C23—O1	-56.2
1b	Au1—Cl1	2.2876	P1—Au1—Cl1	176.96
	Au2—Cl2	2.272	P2—Au2—Cl2	177.61
	Au1—P1	2.2229	C45—P1—Au1	116.1
	Au2—P2	2.2240	C61—P2—Au2	113.7
	P1—C45	1.838	O1—C45—P1	114.7
	P2—C68	1.825	O3—C61—P2	107.8
	O1—C45	1.427	Au1—P1—C45—O1	51.9
	O3—C61	1.432	Au2—P2—C61—O3	-63.7

	Bonding	Length (Å)	Angle	Angle (degree)
1a	Au1—Cl2	2.277	O1—C23—P1	107.7
	P1—Au1	2.226	C23—P1—Au1	114.9
	C23—P1	1.829	P1—Au1—Cl2	174.16
	O1—C23	1.428	Au1—P1—C23—O1	-56.2
1b	Au1—Cl1	2.2876	P1—Au1—Cl1	176.96
	Au2—Cl2	2.272	P2—Au2—Cl2	177.61
	Au1—P1	2.2229	C45—P1—Au1	116.1
	Au2—P2	2.2240	C61—P2—Au2	113.7
	P1—C45	1.838	O1—C45—P1	114.7
	P2—C68	1.825	O3—C61—P2	107.8
	O1—C45	1.427	Au1—P1—C45—O1	51.9
	O3—C61	1.432	Au2—P2—C61—O3	-63.7

While **1a** crystal exhibits complete 2-fold axis with an asymmetric unit of half of **1a** molecule, **1b**'s Au-Cl groups are asymmetrically located with an asymmetric unit of whole a **1b** molecule. Au1-Cl1 in **1b** was located close to the phenyl ring containing C1 with a torsion angle of 51.9° for Au1-P1-C45-O1, which is contrast to torsion angles of -56.2°, -63.7°, and -58.9° for Au-P-C- O of **1a**, **1b**'s other P-Au-Cl group, and **1c** (Table S2). The torsion angle measurement demonstrates that P-Au-Cl groups of **1a**, **1b**, and **1c** are similarly located but only P1-Au1-Cl1 of **1b** is located in different way. Except the possible intramolecular interaction with a calixarene cavity's phenyl ring, all the other surrounding moieties are far from Au1 atom. For the possible Au-arene intramolecular interaction, the shortest intramolecular distances between aromatic carbons and Au1 are 3.509 Å (Au1-C1), 4.304 Å (Au1-C2), 4.653 Å (Au1-C3), 4.367 Å (Au1-C4), 3.662 Å (Au1-C5), and 3.213 Å (Au1-C6). These distances are much longer than those of a rare example of Au-η^6-arene interaction, 3.118 – 3.246 Å.[1] Although Au1-C6 distance is close to that of Au-arene interaction, Au-arene interaction cannot be expected in **1b** because the other Au- C distances and the Au-phenyl distance are too long to be confined by Au-arene interaction. There is no other close contact between Au1 and its surroundings: thus, Au1-Cl1 in **1b** must be located by the crowded propoxy groups and not affected by any other distinct inter- or intra-molecular interaction.

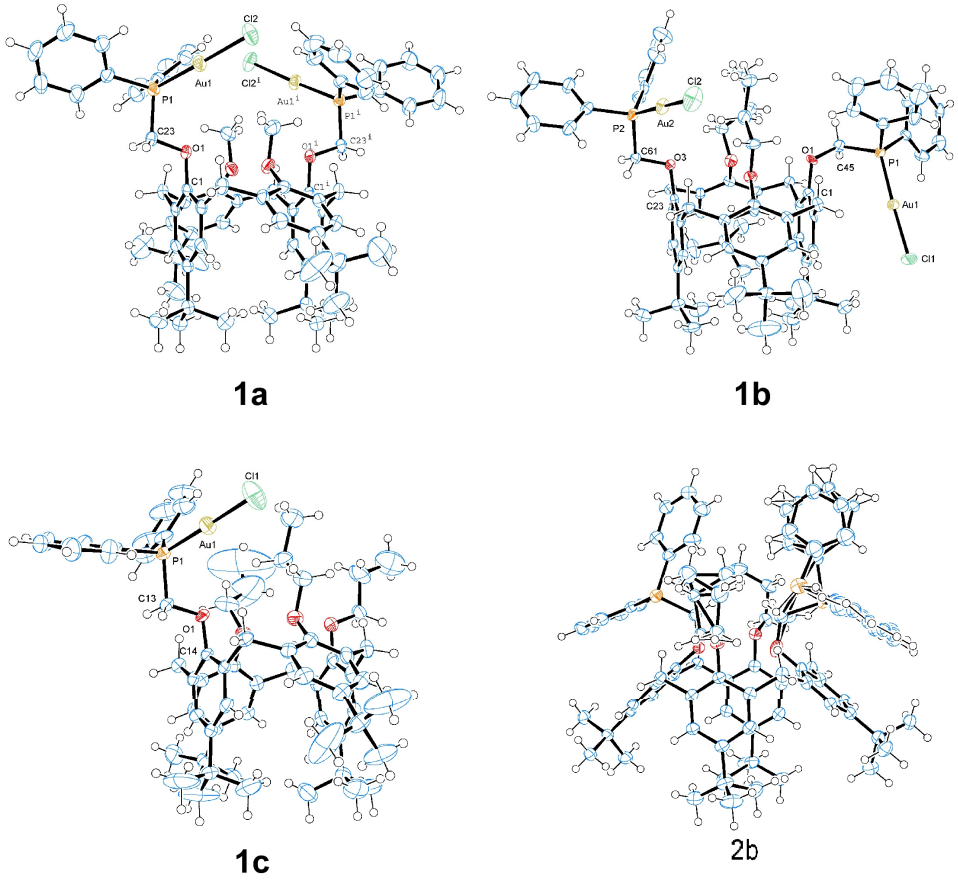

Figure 4.S.12: Single crystal structures of **1a**, **1b**, **1c**, and **2b**. The solvent molecules in **1a** and **1b** are removed. Each thermal ellipsoid, except hydrogen atoms, represents 50% of possibility.

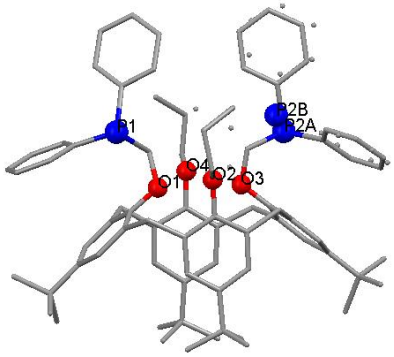

Figure 4.S.13: Single crystal X-ray crystallographic structure of *tert*-butyl-calix[4]-$(OR)_2(OCH_2PPh_2)_2$ (R = $C_3H_{7\text{-}n}$). Despite the disorder in one of the phosphine groups (i.e.,P2A, 77%, P2B, 23%) both phosphine groups are organized above the lower rim oxygen plane.

4.6.5 HAADF-STEM images of gold clusters

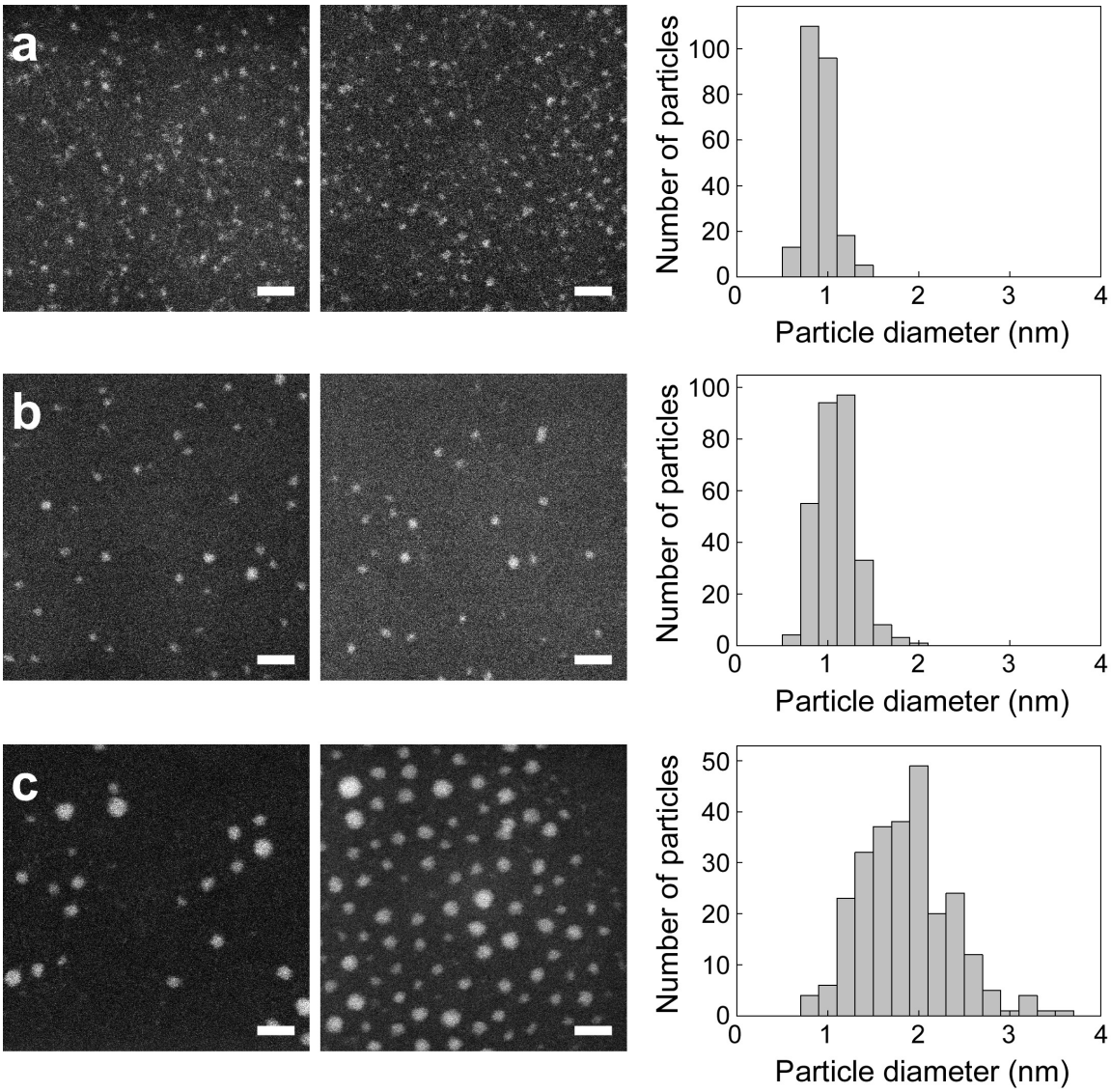

Figure 4.S.14: HAADF-STEM images of (a) **{Au-1}-2a** (0.9 ± 0.1 nm, 242 particles), (b) **{Au-2}-2b** (1.1 ± 0.2 nm, 295 particles), and (c) **{Au-3}-2c** (1.9 ± 0.5 nm, 257 particles). The scale bar represents 5 nm.

4.6.6 Fluorescence of 2NT on gold clusters

The fluorescence emission of 2NT (2-naphthalenethiol) on gold clusters, such as **1a**, **1b**, and **1c**, is observed to measure the accessible surface to which 2NT is bound. During 2NT's binding to the gold clusters, UV-Vis spectra of the clusters did not significantly change except for incorporation of 2NT absorption at 270 – 300 nm. This demonstrates that the gold clusters remain stable after 2NT adsorption (Figure 4.S.20a). On clusters of **1a**, **1b**, and **1c**, the fluorescence of 2NT quenches up to a certain saturation threshold and then increases with increasing concentration of 2NT added (Figure 4.S.20b). Based on observing 21 wt% Au in the elemental analysis of **{Au-1}-2a**, 2.8 ± 0.7 2NT molecules are revealed to be bound to each **{Au-1}-2a** cluster. Based on 38 and 40 wt% gold to be present in **{Au-2}-2b** and **{Au-3}-2c** clusters, respectively (Table 4.S.3), 2.9 ± 0.3 and 3.0 ± 0.5 2NT molecules are bound to each **{Au-2}-2b** and **{Au-3}-2c**, respectively. This calculation for **{Au-2}-2b** and **{Au-3}-2c** assumes 46 and 241 gold atoms for **{Au-2}-2b** and **{Au-3}-2c**, respectively, which is made on the basis of STEM data in Figure 4.2. It must be noted that the quenching concentrations of **{Au-2}-2b** and **{Au-3}-2c** red must be larger than the values above because the organic fractions of both **{Au-2}-2b** and **{Au-3}-2c** are ignored in calculating 2NT's quenching concentration. In addition, **{Au-3}-2c** contains some unreacted **1c** precursors. This does not influence the absolute critical amount of 2NT quenched in fluorescence experiments with **{Au-3}-2c**, because control experiments demonstrate that precursor **1c** does not quench 2NT fluorescence. Because of the existence of some unreacted **1c**, 2NT's actual quenching concentration of 1c-red must be much larger than the calculated value above.

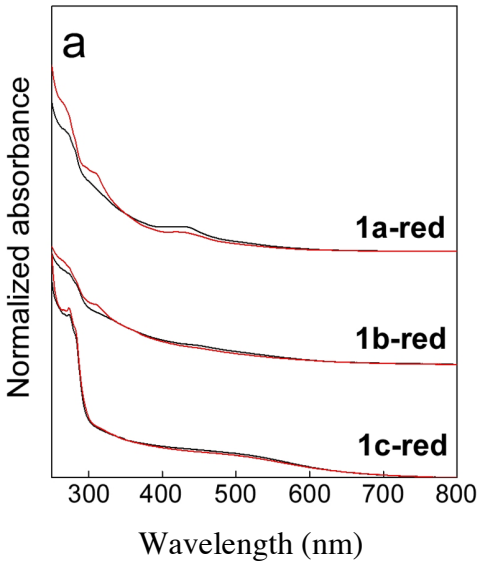

Figure 4.S.15: (a) UV-Vis spectra of clusters before (black) and after (red) 5 μM of 2NT addition to **{Au-1}-2a**, **{Au-2}-2b** and **{Au-3}-2c**. The spectra are normalized at 350 nm.

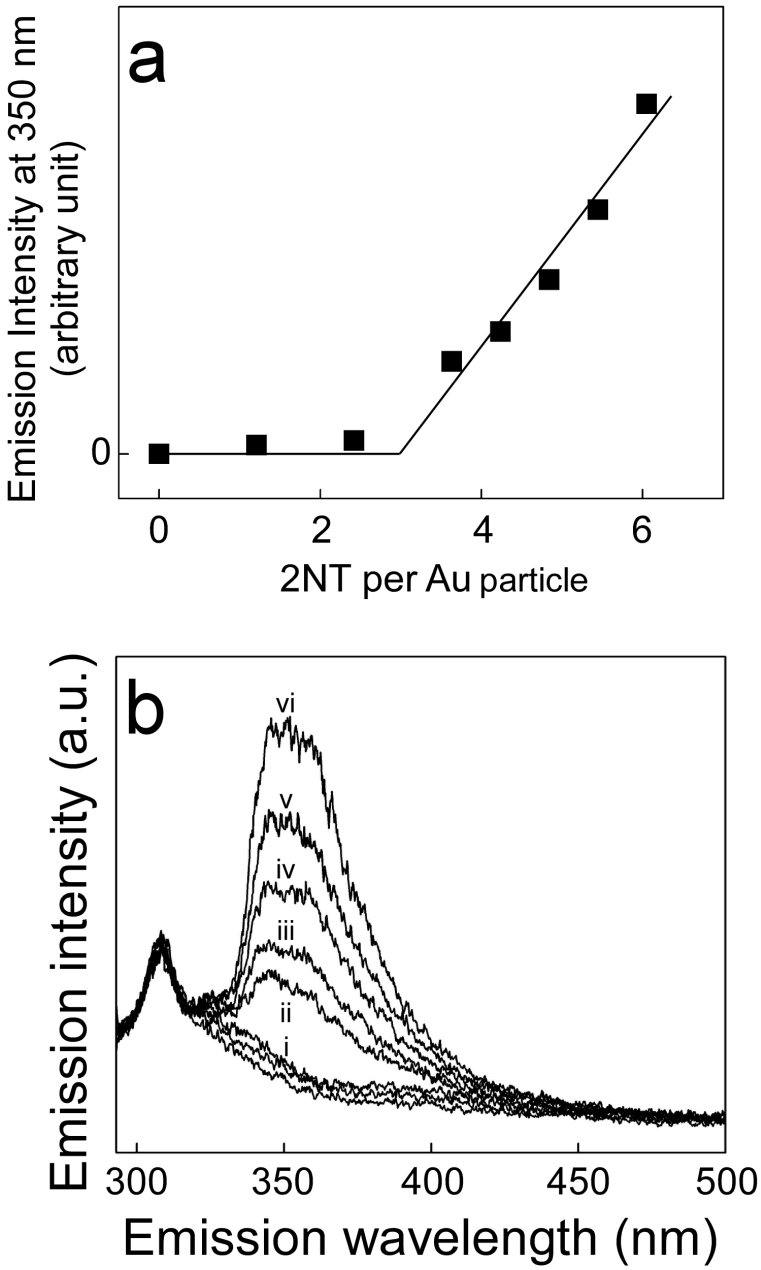

Figure 4.S.16: Fluorescence emission intensity and (b) emission spectra of 2NT on **{Au-2}-2b.** 2NT per Au nanoparticle is 2.421 (i), 3.63 (ii), 4.24 (iii), 4.84 (iv), 5.45 (v), and 6.05 (vi), respectively. Each solution contains 4.35 μM of Au nanoparticles in dichloromethane and excited at 283 nm. The nanoparticle concentration is calculated assuming the Au nanoparticle powder consists of 38 wt% gold (based on XPS result) and each nanoparticle consists of 46 gold atoms (based on TEM images).

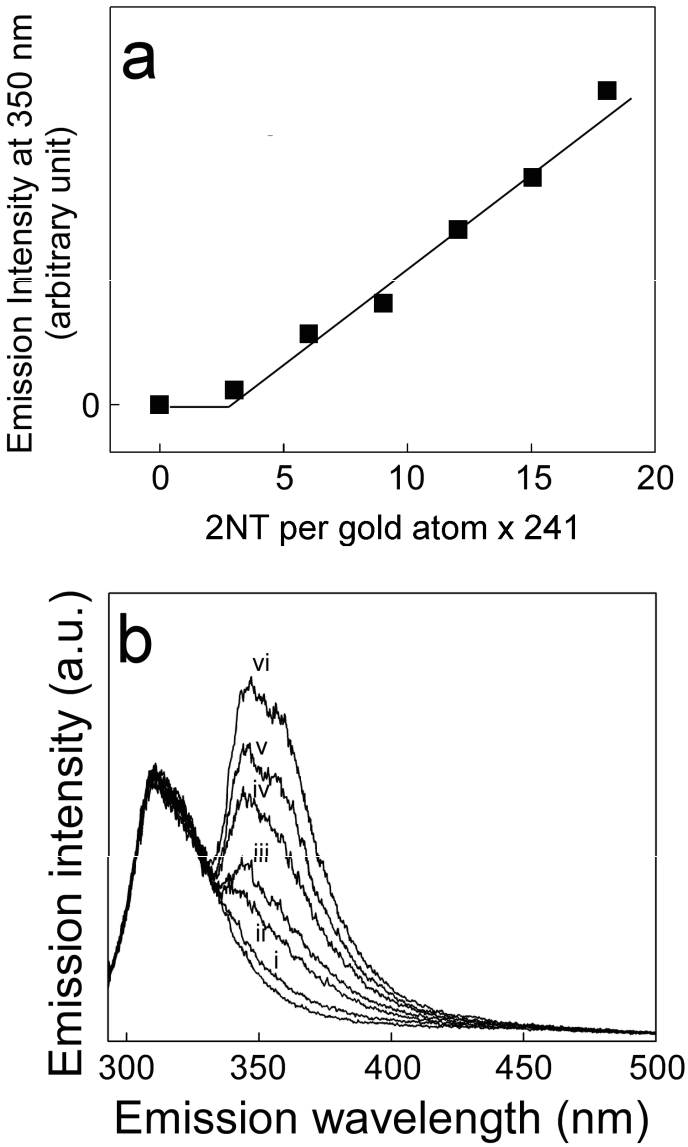

Figure 4.S.17: Fluorescence emission intensity and (b) emission spectra of 2NT on **{Au-3}-2c**. 2NT per Au nanoparticle is 3.03 (i), 6.03 (ii), 9.05 (iii), 12.1 (iv), 15.1 (v), and 18.1 (vi), respectively. Each solution contains 0.83 μM of Au nanoparticles in dichloromethane and excited at 283 nm. The nanoparticle concentration is calculated assuming the Au nanoparticle powder consists of 40 wt% gold (based on XPS result) and each nanoparticle consists of 241 Au atoms (based on TEM images).

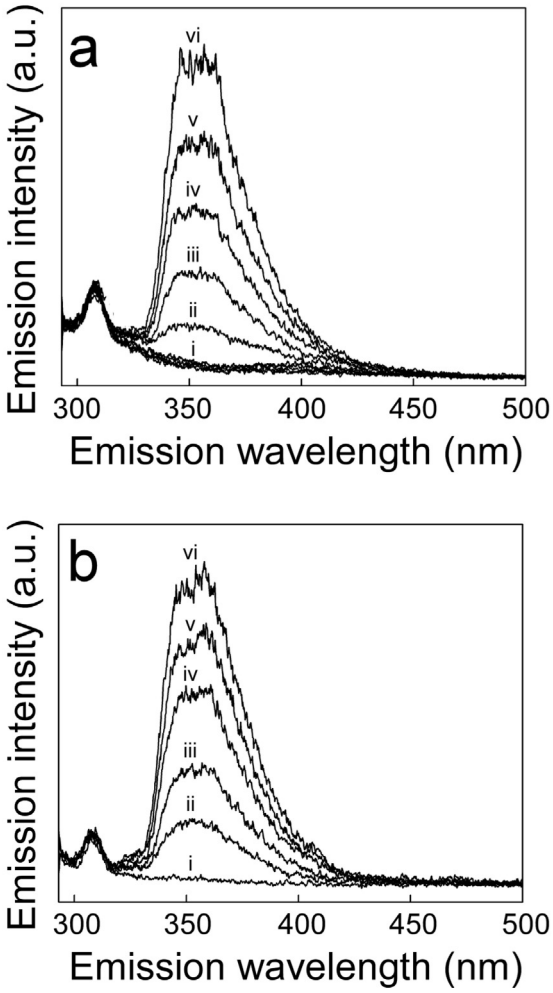

Figure 4.S.18: Fluorescence emission spectra of 2NT on (a) **{Au-1}-2a** and (b) $Au_{11}(PPh_3)_7(SCN)_3$. 2NT per Au_{11} fragment is 2.74 (i), 3.29 (ii), 3.83 (iii), 4.38 (iv), 4.93 (v), and 5.48 (vi) in (a), and 0 (i), 0.125 (ii), 0.25 (iii), 0.375 (iv), 0.5 (v), and 0.625 (vi) in (b), respectively. Each solution is assumed to contain 5 μM of Au_{11} fragments in dichloromethane and excited at 283 nm.

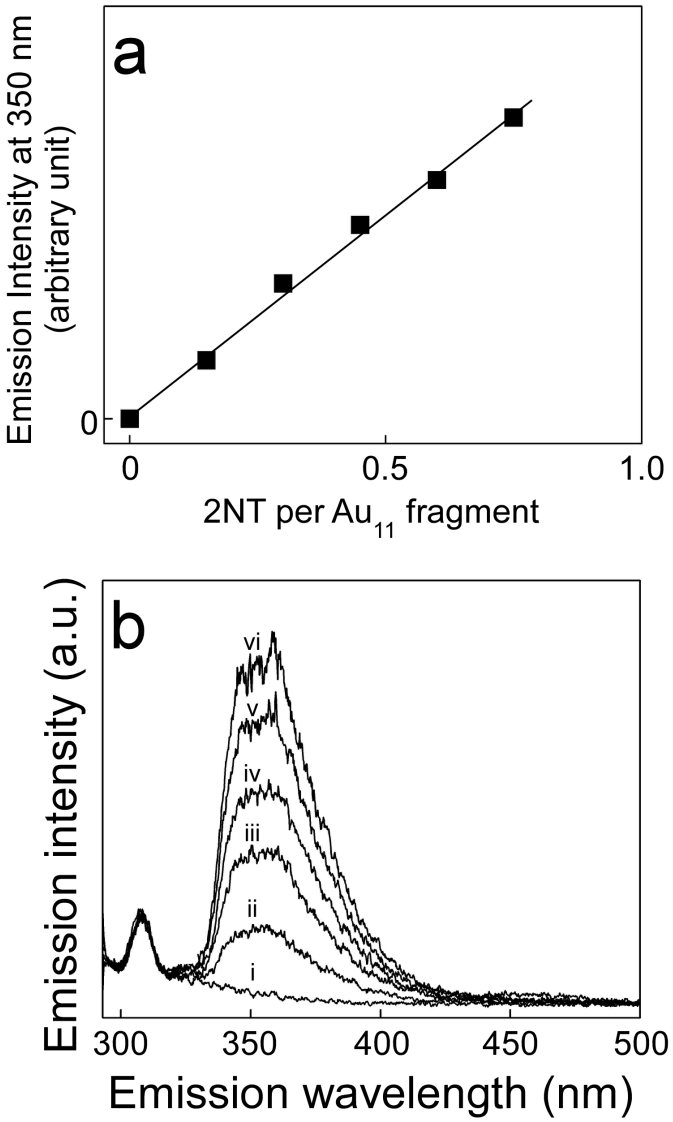

Figure 4.S.19: (a) Fluorescence emission intensity and (b) emission spectra of 2NT on $[Au_{11}(PPh_3)_8Cl_2]PF_6$. 2NT per Au_{11} fragment is 0 (i), 0.15 (ii), 0.3 (iii), 0.45 (iv), 0.6 (v), and 0.75 (vi), respectively. Each solution contains 5 μM of Au_{11} fragments in dichloromethane and excited at 283 nm.

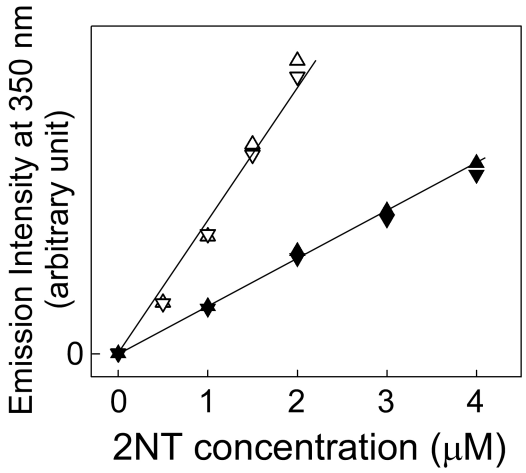

Figure 4.S.20: Fluorescence emission intensity of 2NT treated with **2a**- and **2c**-bound 4-nm gold nanoparticles (▲: 1.25-monolayer equivalent **2a**-bound nanoparticles, ▼: 2-monolayer equivalent **2a**-bound nanoparticles, Δ: 1.25-monolayer equivalent **2c**-bound nanoparticles, ∇: 2- monolayer equivalent **2c**-bound nanoparticles). The lack of an observed quenching at low 2NT concentrations means there is no 2NT binding (i.e. accessible surface area) in **2a**- and **2c**-bound 4-nm gold nanoparticles. This is relevant to understanding the importance of small gold core size in explaining the mechanism of observed accessibility for **{Au-1}-2a** and **{Au-3}-2c**.

4.6.7 X-ray photoelectron spectroscopy

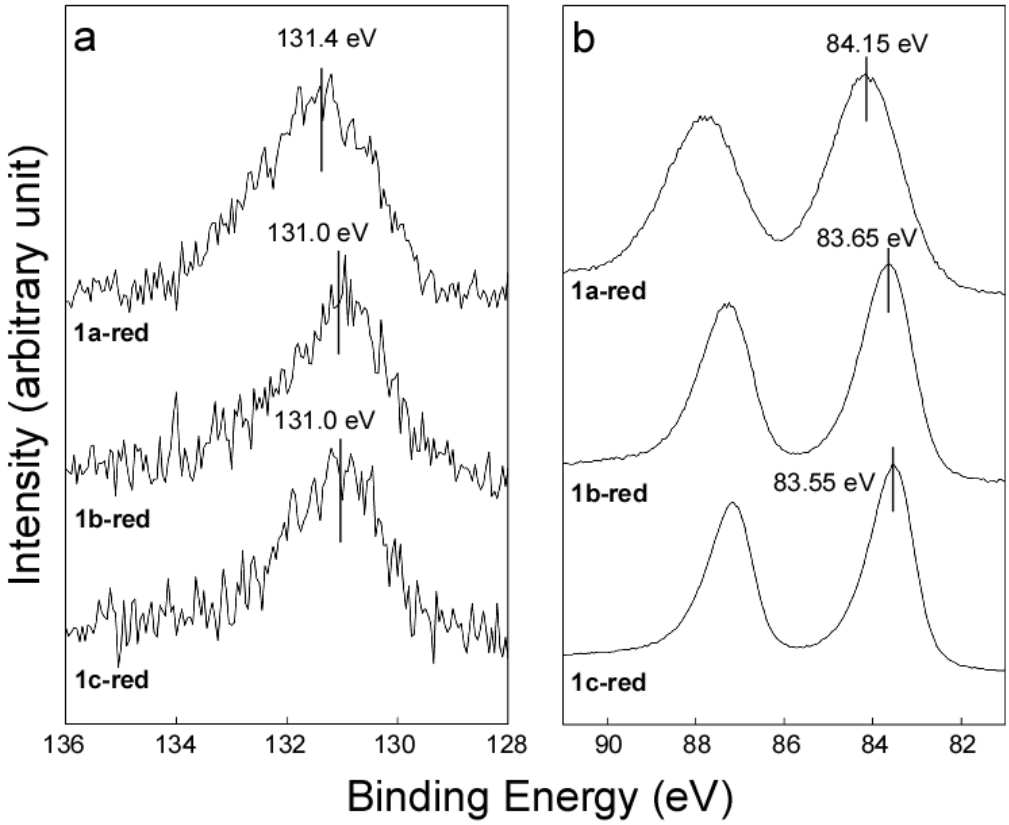

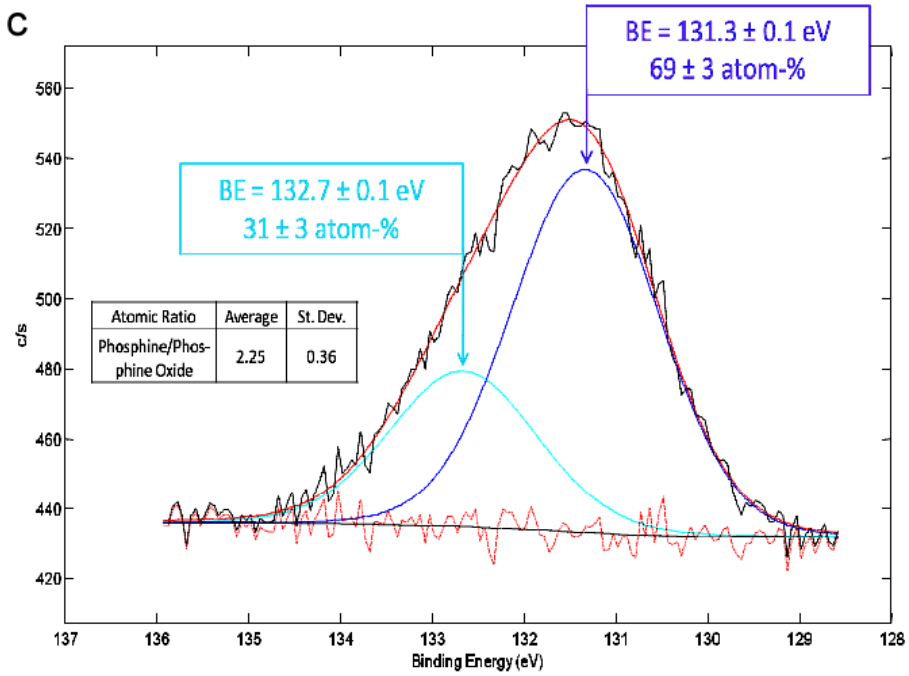

Figure 4.S.21: a) P 2*p* and (b) Au 4*f* XPS results of **{Au-1}-2a**, **{Au-2}-2b**, and **{Au-3}-2c**. Deconvolution of **{Au-1}-2a** results in (a) is shown in (c). Binding energy is corrected by C 1*s* at 284.6 eV.

4.6.8 Elemental analysis of **{Au-1}-2a**

Table 4.S.3: Elemental analysis of clusters based on ICP analysis

%C	%H	%P	%O[a]	Au%	%Cl
54.39	5.46	3.58	14.97	21.39	0.21

[a] O elemental analysis above is calculated on the basis of 100% minus all other elemental compositions.

4.6.9 Conformation of calixarene

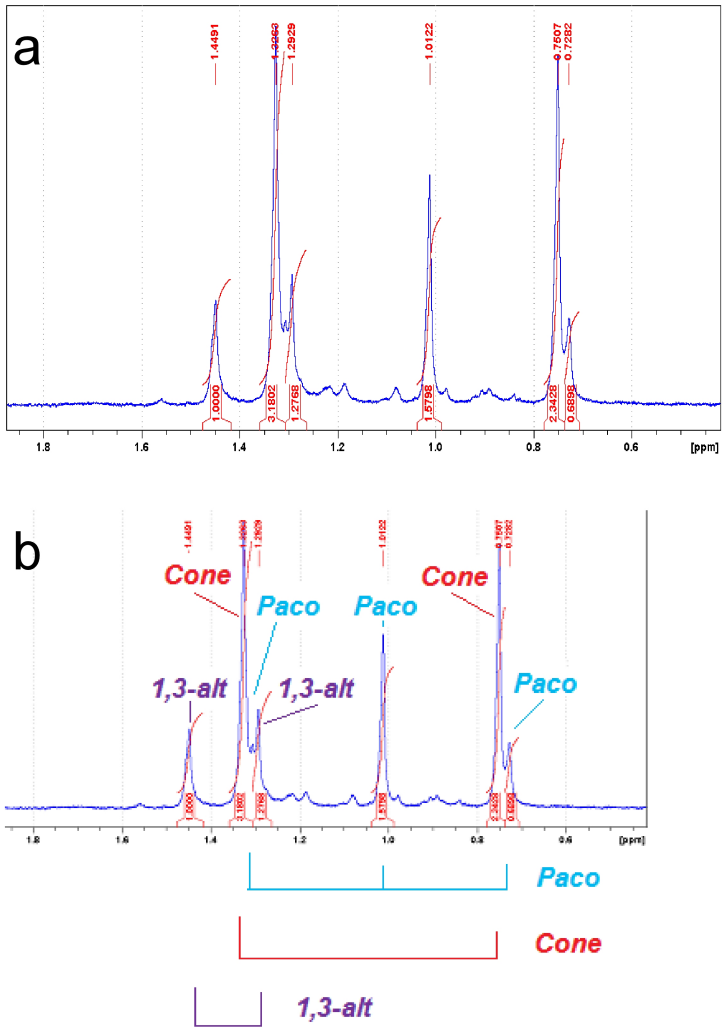

Figure 4.S.22: a) ^{1}H NMR of aliphatic region of calixarene at –57 ^{o}C ($CDCl_3$, DRX-500 MHz) with (b) assignment of conformers.

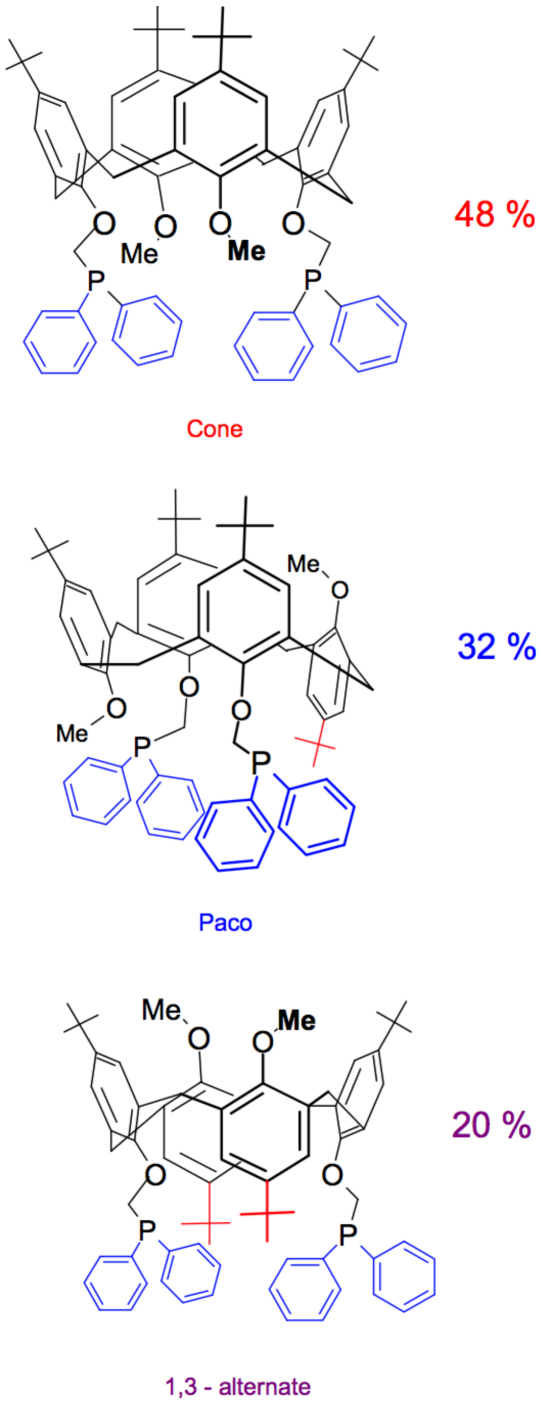

Figure 4.S.23: Distribution of conformers calculated from data in Figure 4.S.21(b)

4.6.10 Molecular mechanics graphic of **{Au-1}-2a**

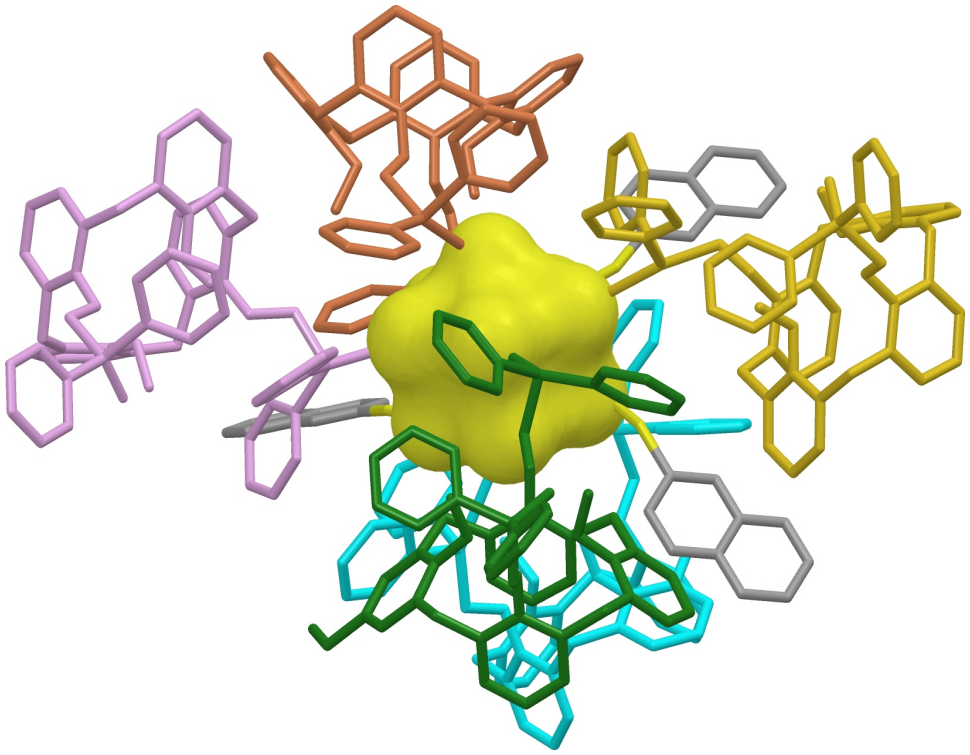

Figure 4.S.24: Molecular mechanics representation of **{Au-1}-2a** based on manuscript data. Calixarenes were manually placed on the gold surface in such a fashion as to minimize VDW conflicts. Then the system was subject to minimization with the OPLS force field in Maestro 9.5, Macromodel 9.7 (2009 Schrodinger, LLC) with bonds to the Au atoms constrained. Substituents consisting of *tert*-butyl and hydrogen were included in the calculation but are undisplayed for clarity.

4.6.11 Calculations of fraction of surface gold atoms bound with 2NT

Accessible gold surface areas during 2NT titration are estimated as follows. Full shell theory is used to estimate the percentage of surface gold atoms relative to total gold atoms (see Corma et al. Table 12.1 on page 395 in Nanoparticles and Catalysis (Wiley VCH Verlag, 2008, Weinheim, Didier Astruc (editor)), except in **{Au-1}-2a**, where this percentage was assumed to be 100%. Values not given in the table were estimated via logarithmic interpolation. For this purpose, the following gold total atom numbers were used: 2460 for 4 nm gold colloid, 46 for **{Au-2}-2b**, and 241 for **{Au-3}-2c**.

4.6.12 References for section 4.6

[1] F.-B. Xu, Q.-S. Li, L.-Z. Wu, X.-B. Leng, Z.-L. Li, X.-S. Zeng, Y.-L. Chow, Z.-Z. Zhang, *Organometallics*, 22 (2003) 633.

4.7 References for Chapter 4

[1] H. Beinert, *J. Biol. Inorg. Chem.*, 5 (2000) 2.
[2] A.H. Robbins, C.D. Stout, *Proc. Natl Acad. Sci. USA*, 86 (1989) 3639.
[3] L. Quintanar, J. Yoon, C. P. Aznar, A. E. Palmer, K. K. Andersson, R. D. Britt, E. I. Solomon, *J. Am. Chem. Soc.*, 127 (2005) 13832.
[4] J.R. Banavar, A. Maritan, *Annu. Rev. Biophys. Biomol. Struct.*, 36 (2007) 261.
[5] Z. Xu, F.-S. Xiao, S.K. Purnell, O. Alexeev, S. Kawi, S.E. Deutsch, B.C. Gates, *Nature,* 372 (1994) 346.
[6] A. Corma, H. Garcia, *Chem. Soc. Rev.,* 37 (2008) 2096.
[7] A.S.K. Hashmi, G. J. Hutchings, *Angew. Chem. Int. Ed.*, 45 (2006) 7896.
[8] T.V. Choundhary, D.W. Goodman, *Top. Catal.*, 21 (2002) 25.
[9] A. Corma, H. Garcia, P. Montes-Navajas, A. Primo, J.J. Calvino, S. Trasobares, *Chem. Eur. J.*, 13 (2007) 6359.
[10] A. Nowicki, Y. Zhang, B. Léger, J.-P. Rolland, H. Bricout, E. Monflier, A. Roucoux, *Chem. Commun.*, 3 (2006) 296.
[11] A. Denicourt-Nowicki, A. Ponchel, E. Monflier, A. Roucoux, *Dalton Trans.*, 48 (2007) 5714.
[12] A. Denicourt-Nowicki, A. Roucoux, F. Wyrwalski, *Chem. Eur. J.*, 14 (2008) 8090.
[13] K.R. Gopidas, J.K. Whitesell, M.A. Fox, *J. Am. Chem. Soc.* 125 (2003) 6491.
[14] R.M. Crooks, M. Zhao, L. Sun, V. Chechik, L.K. Yeung, *Acc. Chem. Res.*, 34 (2001) 181.
[15] N. Toshima, *Macromol. Symp.*, 156 (2000) 45.
[16] A. Baiker, *J. Mol. Catal. A*, 115 (1997) 473.
[17] J.-M. Ha, A. Solovyov, A. Katz, *Langmuir,* 25 (2009) 153.
[18] J.-M. Ha, A. Solovyov, A. Katz, *Langmuir*, 25 (2009) 10548.
[19] W. Xu, R.J. Puddephatt, L. Manojlovic-Muir, K.W. Muir, C.S.J. Frampton, *J. Incl. Phenom.*, 19 (1994) 277.
[20] C.B. Dieleman, D. Matt, A. Harriman, *Eur. J. Inorg. Chem.*, (2000) 831, and references therein.
[21] R. Ungaro, A. Pochini, G.D. Andreetti, P. Domiano, *J. Chem. Soc. Perkin Trans. II*, (1985) 197.
[22] P.A. Bartlett, B. Bauer, S.J. Singer, *J. Am. Chem. Soc.*, 100 (1978) 5085.
[23] V.G. Albano, P.L. Bellon, M. Manassero, M. Sansoni, *Chem. Commun.*, (1970) 1210.
[24] F.A. Vollenbroek, J.J. Bour, J.W.A. van der Velden, *Rec. Trav. Chim. Pays-Bas*, 99 (1980) 137.
[25] J.M.M. Smith, J.J. Bour, F.A. Vollenbroek, P.T. Beurskens, *J. Cryst. Spec. Rec.*, 13 (1983) 355.
[26] D. Safer, B. Lizann, J.S. Leigh, *J. Inorg. Biochem.*, 26 (1986) 77.
[27] Y. Yang, S. Chen, *Nano Lett.*, 3 (2003) 75.
[28] K. Nunokawa, S. Onaka, T. Yamaguchi, T. Ito, S. Watase, M. Nakamoto, *Bull. Chem. Soc. Jpn*, 76 (2003) 1601.
[29] G.H. Woehrle, M.G. Warner, J.E. Hutchison, *J. Phys. Chem. B*, 106 (2002) 9979.
[30] Y. Yanagimoto, Y. Negishi, H. Fujihara, T. Tsukuda, *J. Phys. Chem. B*, 110 (2006) 11611.
[31] K.P. Hall, D.M.P Mingos, *Prog. Inorg. Chem.*, 32 (1984) 237, and references therein.
[32] G.H. Woehrle, J.E. Hutchison, *Inorg. Chem.*, 44 (2005) 6149.

[33] S.P. Tunik, A.V. Vlasov, N.I. Gorshkov, G.L. Starova, A.B. Nikol'skii, M.I. Rybinskaya, A.S. Batsanov, Yu.T. Struchkov, J. Organomet. Chem. 433 (1992) 189.
[34] M.J. Hostetler, J.E. Wingate, C.-J. Zhong, J.E. Harris, R.W. Vachet, M.R. Clark, J.D. Londono, S.J. Green, J.J. Stokes, G.D. Wignall, G.L. Glish, M.D. Porter, N.D. Evans, R.W. Murray, *Langmuir*, 14 (1998) 17.
[35] N. de Silva, A. Solovyov, A. Katz, *Dalton Trans.*, 39 (2010) 2194.
[36] L.D. Menard, S.-P. Gao, H. Xu, R.D. Twesten, A.S. Harper, Y. Song, G. Wang, A.D. Douglas, J.C. Yang, A.I. Frenkel, R.G. Nuzzo, R.W. Murray, *J. Phys. Chem. B*, 110 (2006) 12874.
[37] C.C. Chusuei, X. Lai, K. Luo, D.W. Goodman, *Top. Catal.* 14 (2001) 71.
[38] M.G. Mason, *Phys. Rev. B*, 27 (1983) 748.
[39] L.D. Menard, H. Xu, S.-P. Gao, R.D. Twesten, A.S. Harper, Y. Song, G. Wang, A.D. Douglas, J.C. Yang, A.I. Frenkel, R.W. Murray, *J. Phys. Chem. B*, 110 (2006) 14564.
[40] G.M Veith, A.R. Lupini, N.J. Dudney, *J. Phys. Chem. C*, 113 (2009) 269.
[41] F. Cariati, L. Naldini, *Inorg. Chim. Acta*, 5 (1971) 172.
[42] F.A. Vollenbroek, J.J. Bour, J.M. Trooster, J.W.A. van der Veldon, *Chem. Commun.,* (1978) 907.
[43] P. Zhang, T.K. Sham, *Phys. Rev. Lett.*, 90 (2003) 245502.
[44] A. Corma, H. Garcia, *Supported Gold Nanoparticles as Oxidation Catalysts in Nanoparticles and Catalysis*, Wiley VCH Verlag, (2008) 389–426.
[45] P. D. Jadzinsky, G. Calero, C.J. Ackerson, D.A. Bushnell, R.D. Kornberg, *Science,* 318 (2007) 430–433.
[46] J.-M. Ha, A. Katz, A.B. Drapailo, V.I. Kalchenko, *J. Phys. Chem. C*, 113 (2009) 1137.
[47] Jaguar, version 7.5, MacroModel, version 9.6, Schrodinger, New York (2008).
[48] Y. Zhao, D.G. Truhlar, *Acc. Chem. Res.*, 41 (2008) 157.
[49] Y. Zhao, N.E. Schultz, D.G. Truhlar, *J. Chem. Phys.* 123 (2005) 161103.

CHAPTER 5:

Accessible gold clusters using calix[4]arene N-heterocyclic carbene and phosphine ligands

a collaboration between
Michael Nigra, Alexander J. Yeh, Alexander Okrut, Antonio G. DiPasquale, Sheila W. Yeh, Andrew Solovyov and Alexander Katz

"Accessible gold clusters using calix[4]arene N-heterocyclic carbene and phosphine ligands"
Michael M. Nigra, Alexander J. Yeh, Alexander Okrut, Antonio G. DiPasquale, Sheila W. Yeh, Andrew Solovyov and Alexander Katz, *Dalton Transactions* 2013, Vol. 42, pages 12762-12771.
- Reproduced by permission of The Royal Society of Chemistry.
Available online at: http://dx.doi.org/ 10.1039/C3DT50804H

Abstract

We investigate the synthesis of accessible calix[4]arene-bound gold clusters consisting of open "coordinatively unsaturated" active sites, using a comparative approach that relies on calix[4]arene ligands with various upper- and lower-rim substituents. In contrast with a reported Au(I)-*tert*-butyl-calixarene phosphine complex, which exhibits a single cone conformer in solution, the H upper-rim analog exhibits multiple conformers in solution. This contrasts with observations of the *tert*-butyl upper-rim analog, which exhibits a single cone conformer in solution under similar conditions. In the solid state, as determined by single-crystal X-ray diffraction, both H and *tert*-butyl upper-rim analogs exhibit exclusively cone conformer. A detailed structural analysis of these two solid-state structures highlights a CH–π interaction involving a methoxy lower-rim substituent and phenyl substituent on P as the key feature that enforces a tight configuration of Au(I) atoms on the same side of the calix[4]arene lower-rim plane. We hypothesize that such a configuration promotes chelation of the ligand to a gold surface and facilitates the synthesis of small Au_{11}-sized clusters after reduction of both complexes. The new cluster, like the one reported with the *tert*-butyl analog, has an extraordinary 25% of surface atoms that are open and accessible to a 2-NT (2-naphthalenethiol) probe in solution. We also investigated the effect of calix[4]arene lower-rim substituents that coordinate to the metal, by using N-heterocyclic carbene (NHC) functional groups rather than phosphines. Four small (<1.6 nm diameter) calix[4]arene NHC-bound gold clusters were synthesized, including three using novel calix[4]arene NHC ligands. The smallest calix[4]arene NHC-bound Au cluster consisted of a 1.2 nm gold core, and its number density of accessible and open surface sites was measured. This required development of a new titration method for open sites on gold clusters, using a SAMSA fluorescein dye molecule, which excites and emits at lower energy relative to the previously used 2-NT probe. The number density of open sites on the new calix[4]arene NHC-bound gold cluster measured by the SAMSA fluorescein probe strongly supports the generality of a mechanical model of accessibility, which does not depend on the functional group involved in binding to the gold surface and rather depends on the relative radii of curvature of bound ligands and the gold cluster core.

5.1 Introduction

Metalloenzymes are thought to stabilize metal clusters in an accessible and open "coordinatively unsaturated" state, which ultimately enables control of selective adsorption and catalysis at the metal cluster site, using organic ligands that are permanently bound to the cluster during catalysis. [1–3] Based on established biophysical models of proteins, [4] we have hypothesized that the structural features that allow enzymes to achieve such stable, accessible and open sites on a metal cluster involve a mechanical construct, in which the peptide backbone serves as a series of conjoined rigid and sterically bulky segments. The assembly consisting of these segments is restricted in its ability to coordinate to the metal cluster in a coordinatively saturated configuration, thereby leaving behind open sites, as a result of both the rigidity and steric bulk of each segment. [4]

We have recently translated this hypothetical construct of open-site accessibility to the realm of synthetic metal clusters. [5] We used the construct that is schematically represented in Scheme 5.1 in order to do this, which reduces to a requirement of the ligand radius of curvature needing to be larger than that of the cluster core, in order to facilitate open sites on the metal

surface. Our approach relied on *tert*-butyl-calix[4]arene phosphine **T1** (Figure 5.1) as a bulky ligand on a gold cluster surface, in which the calix[4]arene conformation is held rigidly as cone and served as a crude mimic of a rigid protein backbone segment. Upon reduction of the Au(I)–calix[4]arene complex **T1G** in dilute ethanol solution, [5] a Au_{11} cluster was obtained. Accessible sites on the gold surface were titrated and the number density of open sites was quantified using steady-state fluorescence measurements with 2-NT (2-naphthalenethiol) as a probe molecule. The extraordinary feature of this cluster is that it consists of 2.7 open sites per cluster, on average, as assessed by 2-NT probe molecule binding on the gold core, [5] making it the most accessible metal cluster reported in solution reported to date. Other cone-conformer calix[4]arene phosphine ligands were also used to synthesize gold cores that were enveloped within a semipermeable monolayer consisting of the calix[4]arene ligands. The calix[4]arene served the role of preventing cluster aggregation as a surface-passivating layer, while facilitating accessibility to the underlying metal core. Our initial data demonstrate that the degree of monolayer permeability and gold core accessibility when using this approach crucially rely on the rigid organic ligand being significantly larger than the size of the metal-cluster core, in order to facilitate accessible open sites on the metal surface, which are smaller than the size of the organic ligand. This data supported the mechanism of accessibility described above and shown in Scheme 5.1.

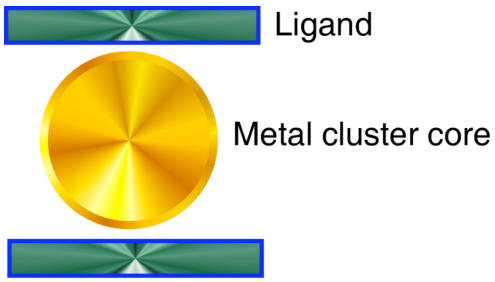

Scheme 5.1: Schematic of a metal cluster where the bulky organic ligands are commensurate with the size of the metal cluster core. This leads to a stable cluster consisting of accessible and open "coordinatively unsaturated" binding sites.

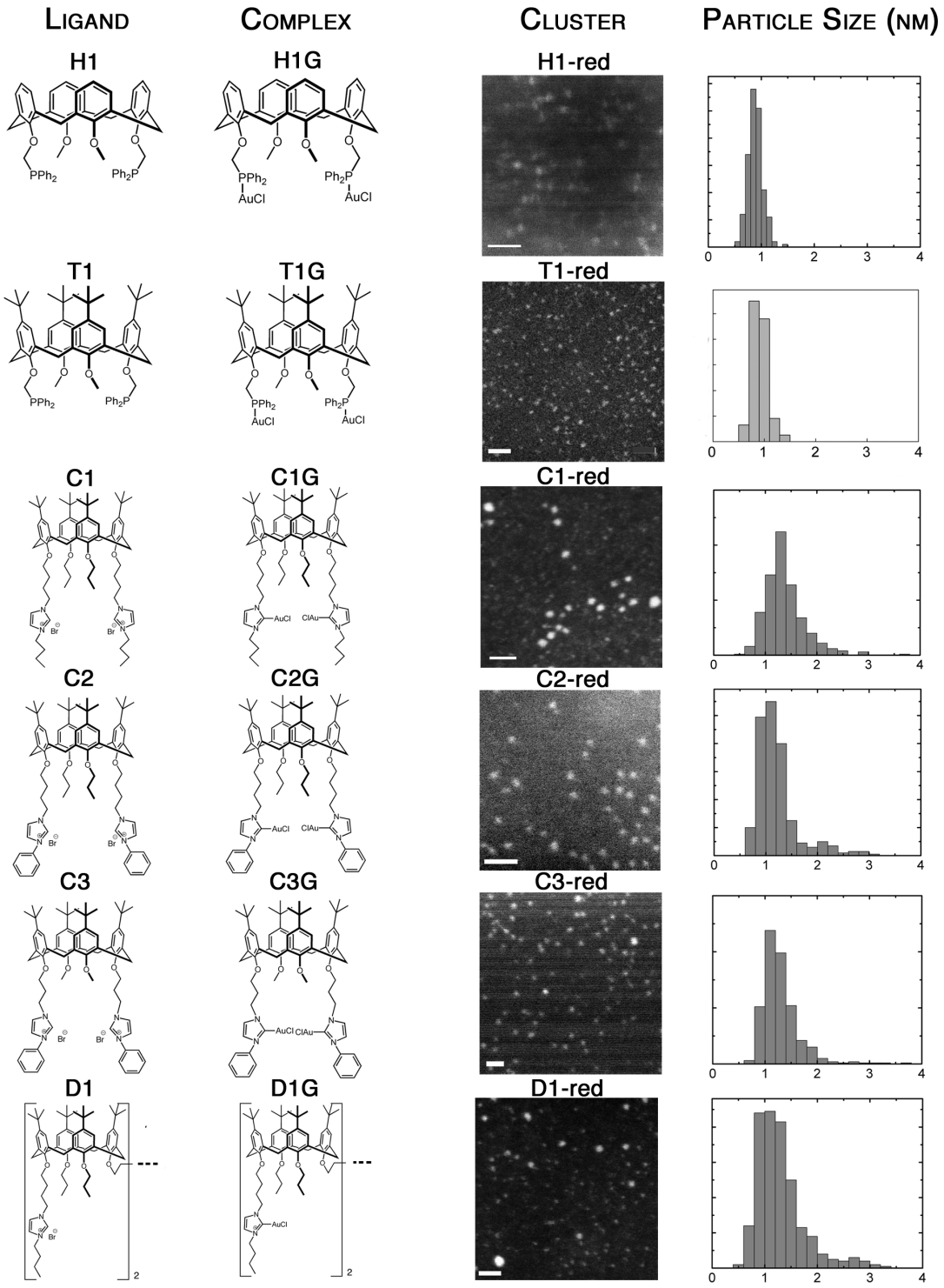

Figure 5.1: Calix[4]arene ligands, Au(I) complexes using calix[4]arene ligands, and HAADF-STEM images of gold clusters resulting from the reduction of Au(I) complexes with particle-size distributions. The micrograph scale bar represents 5 nm. Labels for the corresponding ligands, complexes, and clusters are on top of schematics and data.

Towards the goal of understanding and expanding on the synthesis of gold clusters consisting of stable and accessible surface sites, in this study, we describe accessible gold clusters bound with calix[4]arene ligands that are conformationally mobile as Au(I) complexes in solution prior to reduction, using H rather than *tert*-butyl upper-rim substituents on the calix[4]arene, as well as calix[4]arene ligands that consist of NHC (N-heterocyclic carbene) rather than phosphine lower-rim substituents. [5] The latter NHC-bound gold clusters leverage on the elegant research of Tilley *et al*., who were the first to synthesize NHC-bound gold nanoparticles, with the synthesis of 6.5 nm gold nanoparticles, which formed an ordered supramolecular assembly consisting of interdigitated C_{14}-alkyl substituents on the ligand. [6] Our new calix[4]arene phosphine ligand consists of **H1** (Figure 5.1), which is compared and contrasted with previous results when using *tert*-butyl upper-rim analog ligand **T1**. We also use four calix[4]arene NHC ligands for gold-cluster synthesis. The latter consist of known ligand **C1** as well as new calix[4]arene carbene ligands **C2**, **C3**, and **D1**. Ligands and corresponding Au(I) complexes before reduction are characterized using ^{1}H, ^{13}C, and ^{31}P (where applicable) NMR spectroscopy. Using these ligands and complexes, we investigate the effect of changes in ligand conformational mobility as well as lower-rim substituent (*i.e*. NHC *versus* phosphine) on synthesis of small clusters (less than 1.6 nm in diameter), which consist of stable and open "coordinatively unsaturated" sites. This ultimately informs whether the same mechanism of accessibility in metal clusters, represented schematically in Scheme 5.1, also holds more generally when changing the nature of substituents that coordinate to the metal, within the calix[4]arene ligand.

Similar procedures are used here for synthesis of gold clusters using calix[4]arene ligands as described previously, [5] and cluster characterization after reduction is performed using high-angle annular dark-field scanning transmission electron microscopy (HAADF-STEM), UV-Vis spectroscopy, thermal gravimetric analysis (TGA), accessibility measurements using steady-state fluorescence, X-ray photoelectron spectroscopy (XPS), and electrospray-ionization time-of-flight (ESI-TOF) mass spectrometry.

Our overarching goal is to use molecular precursors in the form of calix[4]arene–gold(I) complexes to synthesize small gold clusters, and, by doing so, investigate how the conformation of the calix[4]arene ligand as well as the identity of lower-rim calix[4]arene substituents that coordinate to metal affect physical and optical properties of the resulting clusters, as well as surface-atom accessibility of resulting open "coordinatively unsaturated" sites on gold clusters.

5.2 Synthesis and characterization of imidazolium calix[4]arene salts

Molecules **3–5** in Scheme 5.2 are used as key precursors for imidazolium calix[4]arene salt synthesis. Typically, in the past, harsh conditions have been required for synthesizing these precursors by treating dialkylcalix[4]arene with dibromopropane [7,8] in the presence of a weak base, such as either cesium carbonate or potassium carbonate. These harsh synthetic conditions consisted of 2–3 days of reflux in acetonitrile and were required in order to attain the target bromocalix[4]arene in moderate yields of around 50%. We chose not to pursue this approach due to the harshness of these conditions. Another reported approach involved using a strong base consisting of sodium hydride, and treating it with dipropoxycalix[4]arene and dibromopropane at 80 °C in DMF for 48 h, which was reported to give 51.8% yield of **4** in the cone conformation. [9] These reported low yields of **4** can be partially rationalized by elimination-type side reactions of bromo intermediates and the formation of oligomers, which are formed upon heating in the

presence of a strong base. In our hands, when reproducing this published approach, [9] we obtained a complex mixture of poorly separable products *via* column chromatography.

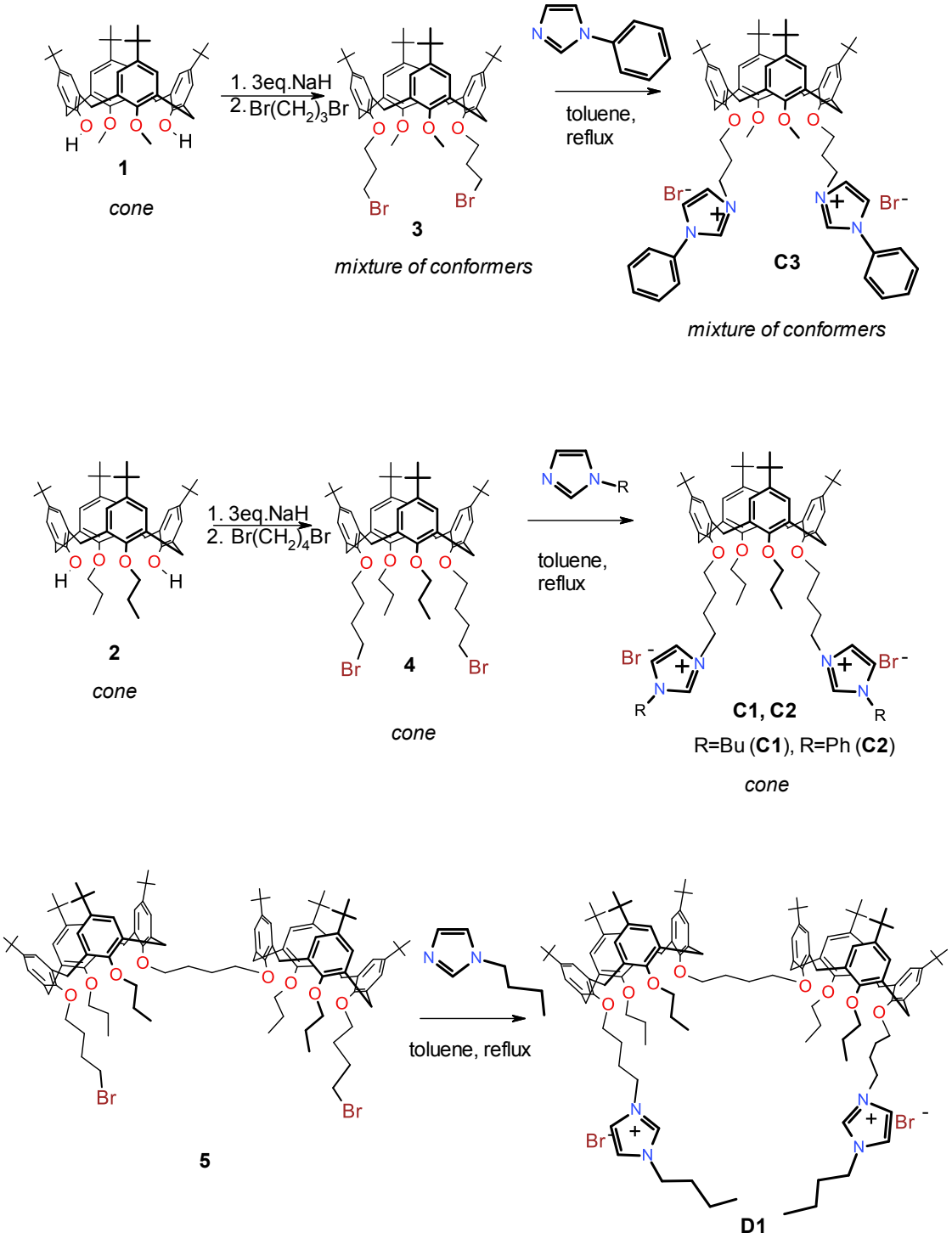

Scheme 5.2: Synthesis of calix[4]arene imidazolium bromide salts for synthesis of ligands **C1**, **C2**, **C3**, and **D1**.

In this contribution, we report a new synthetic approach consisting of the mildest conditions reported to date for the required calix[4]arenes, consisting of bromoalkyl groups substituted on the lower rim. The approach is described in Scheme 5.2, and involves reactions at room temperature, which lead to easy separation of the target product, with minimal waste generated in the process. It also provides access to new dimeric calix[4]arene structures as we demonstrate below. This approach involves treating dialkoxycalix[4]arene with 3 equivalents of NaH for two hours at room temperature, so as to form the corresponding sodium salts. At this time, 2.5 equivalents of dibromoalkane are added to the reaction mixture, and are stirred at room temperature for an additional one hour. Purification of the crude product **4** was performed using chromatography (*n*-hexane and chloroform mixture), which allowed isolation of two chromatographically close products. In addition to the formation of monomeric dibromide **4**, this method enabled the synthesis of dimeric butyl-bridged calix[4]arene-dibromide **5**. ^{1}H NMR spectra of the calix[4]arene dimer showed two close doublets consisting of axial CH_2 bridges and a complex number of aromatic resonances. ESI-MS (+) spectra consist of a strong dimeric peak that can be attributed to [**5** + Na]$^{+}$. Increasing the concentration of base and the reaction time favors the formation of the dimer **5** relative to **4**. The maximum isolated yield of the dimer **5** was 47%, which was achieved by using 8 equivalents of base and a total reaction time of 4 h. Published procedures for synthesis of related compounds, such as calix[4]tubes [10] and double-calix[4]arenes [11–14] as representative examples, required multiple days under reflux conditions and/or high pressure, in order to achieve a similar yield. Both monomer and dimer calix[4]arenes exist as cone conformers as verified by ^{1}H NMR spectroscopy.

The alkylbromination of dimethoxycalix[4]arene **1** results in only monomer product, with no apparent dimer formation. The presence of only monomer product has been confirmed by the appearance of a single peak at 918 in the ESI-MS (+) spectrum and a single distinct chromatographic spot during TLC (thin-layer chromatography). This synthetic result can be explained by the high degree of conformational mobility of methoxycalix[4]arenes *versus* propoxycalix[4]arenes, which may retard the kinetics of calix[4]arene dimer formation due to rotational mobility of aromatic rings. Evidence for such mobility is present in the ^{1}H NMR spectrum of methoxycalix[4]arene **3**, which consists of several broad resonances, indicating different conformers at room temperature in $CDCl_3$. In addition, the ^{13}C NMR spectrum of **3** has a distinct resonance at 37.96 ppm, which is characteristic of bridging carbons having an *anti*-orientation of the aromatic rings. [15] Such evidence is lacking in the corresponding propoxycalix[4]arenes **4** and **5**.

Quaternization of bromocalix[4]arenes **3–5** is performed using a 20-fold excess of 1-alkyl-imidazole in dry toluene at reflux for 18 h. The progress of this reaction was monitored using TLC, and after 18 h, no starting bromide was detected. Crystallization from toluene produced well-defined crystals. ^{1}H NMR spectroscopy of dipropoxy-functionalized imidazolium salts **C1** and **C2** demonstrated cone conformation for both compounds, as evidenced by the presence of a single AX spin system corresponding to the methylene hydrogen atoms. The methoxycalix[4]arene analog **C3** is flexible at room temperature, and its ^{1}H NMR spectrum consists of broad resonances, which indicate several different conformers at room temperature (see Section 5.9). Decreasing the temperature to 223 K led to a sharpening of all resonances, and formation of a well-defined AX spin system with the cone conformer as the major conformer, at 3.18 ppm and 4.21 ppm in the ^{1}H NMR spectrum.

5.3 Synthesis and characterization of calix[4]arene phosphine H1

Phosphorylation of dimethoxycalix[4]arene **6b** with diphenyl-phosphorylmethyltosylate in the presence of NaH was accomplished according to published procedures, [16] as shown in Scheme 5.3. In contrast to the *tert*-butyl analog, which adopts a cone conformation at room temperature in chloroform, [15] calix[4]arene **7b** exists as a mixture of cone and partial-cone conformers, under similar conditions. This mixture of conformers is manifested by the presence of multiple AX methylene-bridge spin systems, and two phosphorous resonances at 21.76 ppm and 21.90 ppm *via* ^{31}P NMR spectroscopy. The cone conformer of **7b** has a single AX spin system corresponding to methylene hydrogens at 3.07 ppm and 4.48 ppm. The partial cone conformer of **7b** has two AX spin systems, corresponding to methyl hydrogens at 2.98 ppm and 4.15 ppm, and 3.62 ppm and 4.07 ppm. Integration of the ^{1}H NMR spectrum of **7b** at room temperature in $CDCl_3$ shows both conformers exist in a 59 : 41 cone : partial cone ratio. Two-dimensional COSY NMR experiments allowed us to assign the different AX spin pairs corresponding to the different conformers (see Supplemental information). Reduction of phosphoryl groups *via* treatment with phenylsilane in toluene at 110 °C for 18 h led to the formation of calix[4]arene phosphine **H1** as a mixture of two conformers, a cone and partial-cone conformer. The ratio of these two conformers is 64 : 36 (cone : partial cone) at 273 K in a deuterated toluene (toluene-d_8) solution, and can be proven by the existence of two sets of resonances of methylene hydrogens in the ^{1}H NMR spectrum. This result is also supported by two ^{31}P NMR resonances for **H1** in $CDCl_3$ solution at the same temperature, at –20.67 ppm and –20.25 ppm. Reducing the temperature of the NMR solution in toluene-d_8 to 213 K shifts equilibrium towards the partial cone conformer, increasing its content to 42% in the mixture of conformers. Heating the same solution to 323 K increases rotational flexibility. This is manifested by (i) the disappearance of partial-cone resonances and (ii) a single broad cone resonance (indicative of motion), in toluene-d_8 solution (see Supplemental Information).

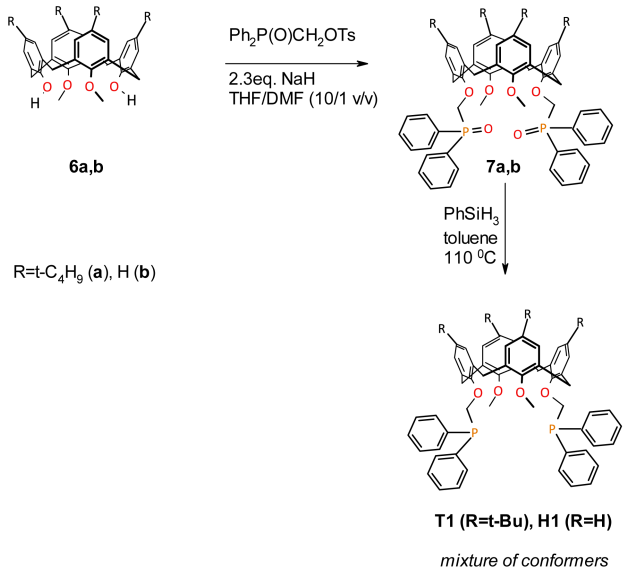

Scheme 5.3: Synthesis of calix[4]arene phosphines **H1** and **T1**.

5.4 Synthesis and characterization of Au(I)–calix[4]arene phosphine complex H1G

The synthesis of **H1G** follows previously published procedures for the *tert*-butyl calix[4]arene analog **T1G**, [5] and is depicted in Scheme 5.4. In contrast to **T1G**, which existed exclusively within the cone conformer as shown by ^{1}H NMR spectroscopic data in Figure 5.2A (though uncomplexed ligand **T1** was observed to be a mixture of conformers in solution under identical conditions), two conformers were observed for **H1G**, consisting of cone and partial cone conformers, in both deuterated chloroform and toluene solution. ^{1}H NMR spectroscopic data in Figure 5.2 allows an estimate of the ratio of cone : partial-cone conformers. This ratio is 0.75 for **H1G** in $CDCl_3$ according to integration data in Figure 5.2C. The higher population of the cone conformer for **H1G** relative to **H1** strongly suggests that both conformers are in equilibrium with one another, as otherwise, the conformer population would not be expected to change upon metal complexation. These two conformers are manifested by asymmetry in the ^{31}P NMR resonance, indicating multiple P environments in Figure 5.2D, which was measured at room temperature in $CDCl_3$ (similar observations were made in toluene-d_8). In stark contrast, previously published data on the synthesis of **T1G** show the presence of only a single cone conformer with one resonance in the ^{31}P NMR spectrum at 22.91 ppm, which is shown in Figure 5.2B. [5] This data suggests that the bulky *tert*-butyl upper-rim substituents in **T1G** create a greater energetic barrier for methoxy-group inversion through the calix[4]arene annulus, relative to the H upper-rim substituents in **H1G**. The data demonstrate that upper-rim substituents play a crucial role in limiting solution-phase conformational mobility, by virtue of their steric bulk.

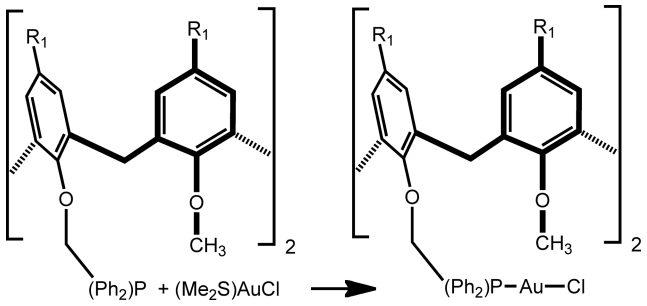

Scheme 5.4: Synthesis of Au(I) phosphine complexes from calix[4]arene phosphine ligands **H1** and **T1**. For **H1** and **H1G**, R_1 = H and for **T1** and **T1G**, R_1 = *tert*-butyl

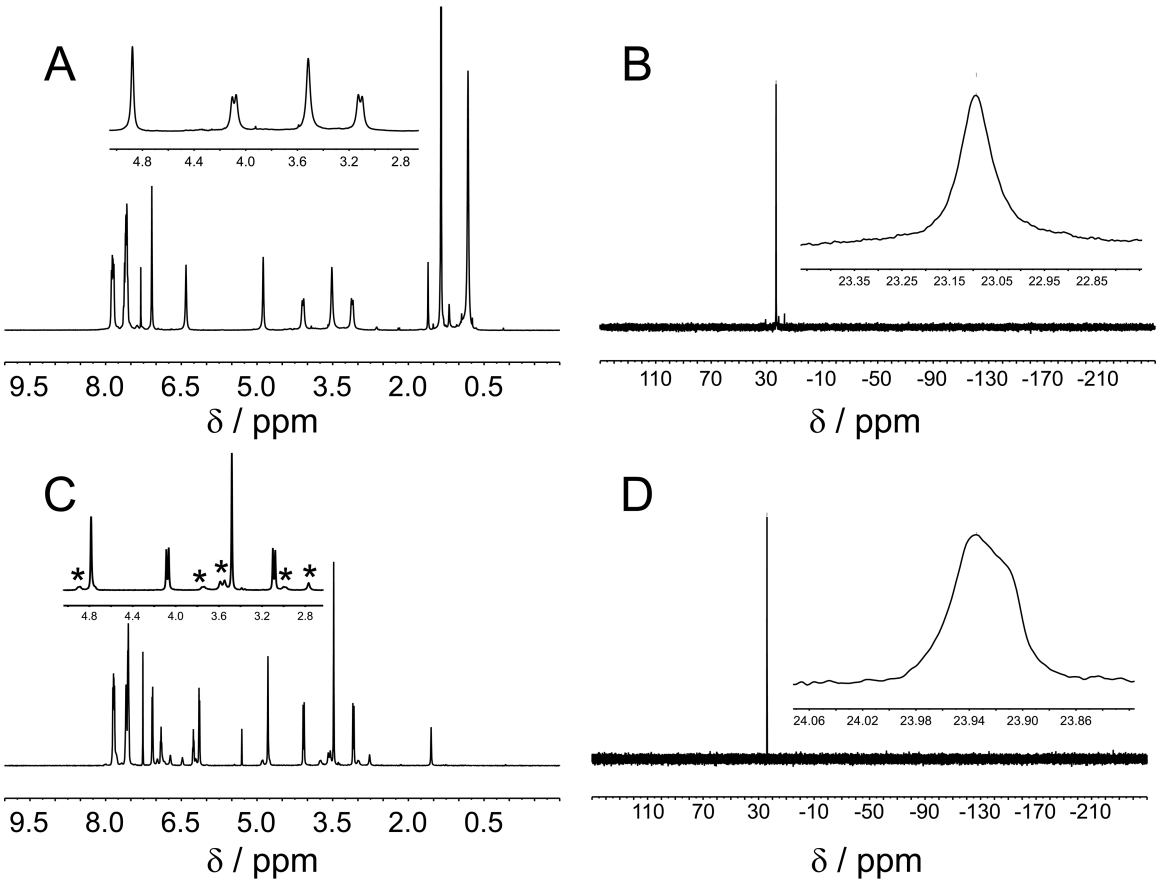

Figure 5.2: A) ^{1}H NMR and B) ^{31}P NMR spectra of **T1G** show the existence of only cone conformer in $CDCl_3$ solution at a temperature of 20°C. C) ^{1}H NMR and D) ^{31}P NMR spectra of **H1G** show the existence of both the cone conformer as well as the partial cone conformer in $CDCl_3$ solution at a temperature of 20 °C. The inlays in A) and C) show details of the ^{1}H NMR spectra with (*) indicating resonances that result from the presence of the partial cone conformer. The insets in B) and D) show the ^{31}P NMR resonances in detail. The presence of a partial cone conformer in **H1G** is indicated by a broad shoulder in the ^{31}P NMR spectrum.

H1G crystallizes in the primitive, monoclinic space group $P2_1/c$ with $Z = 8$; therefore, there are two crystallographically unique molecules, in the form of a pair of enantiomers, that form the asymmetric unit. [17] Structural agreement between the two independent molecules after inversion of one of them is quite remarkable, which can be seen in the root mean square (RMS) overlay of the two molecules (see Figure 5.S.30). [18] Other than slight rotation in one of the phenyl groups in one of the lower Ph_2PAuCl substituents, the molecules are superimposable enantiomers in the solid state, although the molecule itself is achiral. [19] Normally, this would be an indicator for missed crystallographic symmetry, but ADDSYM checks find no additional symmetry beyond that of the indicated space group. [20] As a consequence, we will only refer to one of the two independent molecules when making comparisons with its *tert*-butyl analog, **T1G**, reported previously.

H1G crystallizes in a similar fashion as **T1G** with both Ph_2PAuCl substituents on the same face of the plane defined by the calix[4]arene lower-rim oxygens. An RMS optimized overlay of the two analogs using all common non-hydrogen atoms as optimization points is shown in Figure 5.3a, and reveals slight structural differences. The most noticeable difference is seen in one of the sets of angles between the mean planes of phenyl rings on opposite sides of the calix[4]arene. While both molecules exhibit flattened cone geometry of the calix[4]arene (in a perfect cone, the angle created between the planes of phenyl rings on opposite sides of the calix[4]arene would be the same non-zero angle for adjacent sides), the extent of the flattening differs between the two analogous structures. The lower-rim substituent attached parallel rings (angle between the mean plane of C14–C19 and its symmetry equivalent is less than 1°) in the solid-state structure of **T1G** open up to over 22° in the structure of **H1G**. The difference in the other set of non-attached rings containing the methoxy groups (inset of Figure 5.3a) is less pronounced with an angle of 105° in the structure of **T1G** decreasing slightly to 100° in the structure of **H1G**. The overall increase in the flattening of the cone in the structure of **H1G** may be a result of a stronger σ (C–H)–π interaction [21] between the phenyl group of a coordinated PPh_2 and one of the methoxy lower-rim substituents. While the distances between the aromatic rings (centroid) and the carbon atoms of the methoxy substituents in the structure of **T1G** are both 3.5 Å, this distance decreases to 3.3 Å in **H1G** in one interacting paired set (consisting of a methoxy lower-rim substituent C–H and phenyl group of a coordinated PPh_2) but increases to over 3.9 Å in the non-interacting set involving the other methoxy substituent, as indicated by dashed lines in Figure 5.3b. This asymmetry between the two potential σ (C–H)–π interactions in the structure of **H1G** is likely a sterics issue, as the 22° opening of the calix[4]arene results in the distance between P atoms to be decreased by 0.6 Å in the structure of **H1G** relative to that in **T1G**. That is to say, the long-range P–P distance decreases from 8.12 Å in the structure of **T1G** to 7.54 Å in the structure of **H1G**. Steric crowding in the lower-rim substituent pocket could be preventing the one methoxy group from getting any closer than 3.9 Å to the phenyl group centroid in Figure 5.3b. The long-range Au–Au distance of 7.32 Å in the structure of **T1G** actually increases by 0.45 Å to 7.77 Å in the structure of **H1G**, due to rotation of one of the Ph_2PAuCl substituents about the P–CH_2 bond, again, potentially a result of both the stronger σ (C–H)–π interaction and steric effects in the pocket, but certainly to minimize void space. [22]

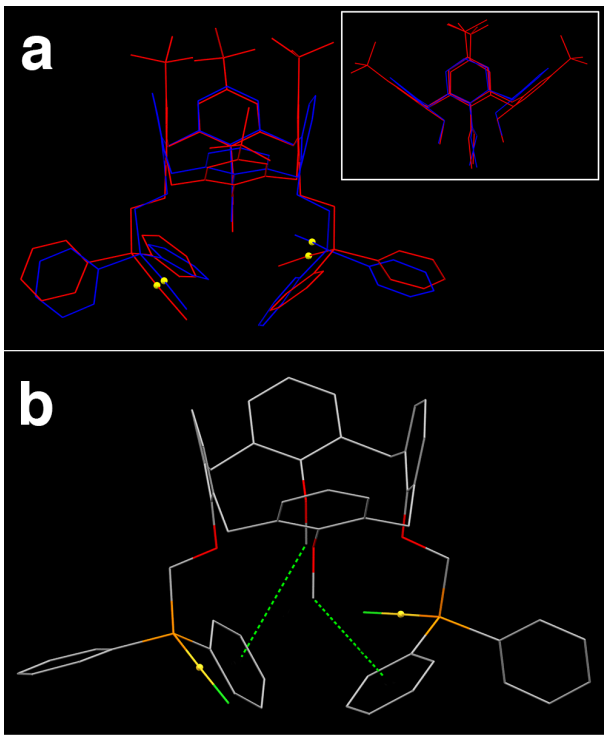

Figure 5.3: a) RMS optimized overlay of **T1G** (red) and one molecule from **H1G** (blue). Au atoms highlighted as yellow spheres. Inset: RMS overlay rotated by 90° and truncated at the phosphorous atom of the $AuPPh_2Cl$ substituent. b) One molecule from **H1G** showing the σ (C–H)–π interactions (green dashed line). Front distance is 3.3 Å and rear distance is 3.9 Å.

Previously, we discussed the importance of the σ (C–H)–π interactions in a comparative study of various calix[4]arene phosphine Au(I) complexes. We concluded that this interaction was responsible for keeping the two phosphine ligands within a configuration that could chelate to a gold surface, and that such chelation may be crucial for the synthesis of the smallest calixarene-bound gold clusters. [5] In **T1G**, these σ (C–H)–π interactions were invoked on the basis of the 3.5 Å distance in the single crystal X-ray structure between the centroid of the aromatic ring and the carbon atoms of the methoxy groups on the lower rim of the calix[4]arene. Based upon observing similar σ (C–H)–π interactions, gold atom organization, and conformation for **H1G** as for **T1G** previously reported, we anticipate that reduction of **H1G** may also lead to Au_{11} clusters, as reported previously for **T1G**.

5.5 Synthesis and characterization of Au(I)–calix[4]arene NHC complexes

The synthesis of Au(I)–calix[4]arene NHC complexes was performed in accordance with Scheme 5.5. In brief, the calix[4]arene imidazolium bromide salt was reacted with silver oxide in dichloromethane solvent, to form a calix[4]arene silver carbene intermediate complex. [23] This silver carbene intermediate was then reacted with an equivalent of Au(I)-dimethylsulfide chloride in dichloromethane solution, to form the corresponding gold carbene complex. The resulting solution was filtered through celite, and the complex was purified *via* column

chromatography (5 : 1 dichloromethane–ethyl acetate), until a white powder was isolated. These purified complexes **C1G**, **C2G**, **C3G**, and **D1G** were characterized *via* ^{1}H NMR spectroscopy (see section 5.9). Our design objective was to use a similar approach as reported previously with calix[4]arene phosphine ligands, [5] except now using calix[4]arene-NHC ligands. We were hoping to use similar σ (C–H)–π interactions involving methoxy substituents and the π system of the PPh_2 moieties (now envisioned to involve instead the N-heterocyclic carbene) to enforce a tight cone conformation, which previously resulted in Au_{11}-sized clusters having a narrow particle-size distribution, when using the Au(I)–calix[4]arene complex **T1G**. However, unlike **T1G**, gold complexation to the ligand did not significantly change the distribution of mixture of conformers for all new NHC complexes investigated here (**C1-3G**, and **D1G**). For example, the broad resonances due to the inversion of the $–OCH_3$ groups observed with methoxycalix[4]arene ligand **C3** are still present in **C3G**, which is in stark contrast to the exclusivity of the cone conformer in **T1G**.

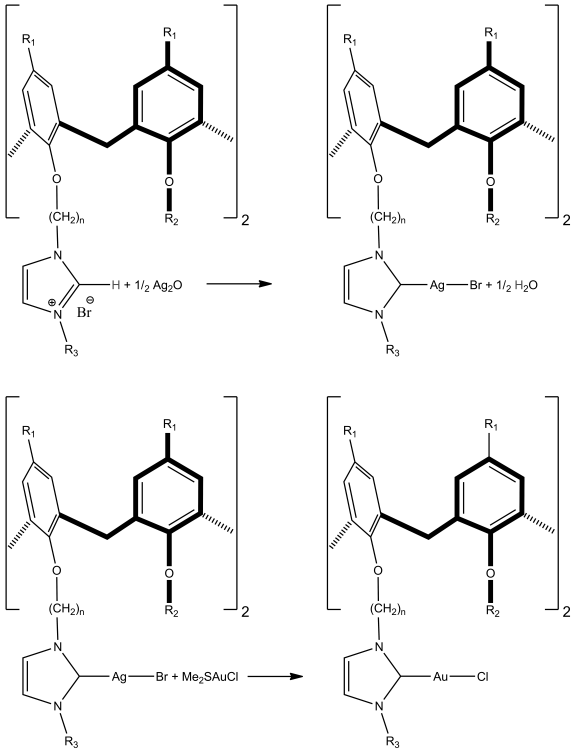

C1G: R_1 = tert-butyl, R_2 = proplyl, R_3 = butyl, n = 4
C2G: R_1 = tert-butyl, R_2 = proplyl, R_3 = phenyl, n = 4
C3G: R_1 = tert-butyl, R_2 = methyl, R_3 = phenyl, n = 3
D1G: R_1 = tert-butyl, R_2 = proplyl, R_3 = butyl, n = 4

Scheme 5.5: Synthesis of Au(I) carbene complexes from calix[4]arene imidizolium bromide salts **C1**, **C2**, **C3**, and **D1**.

5.6 Synthesis and characterization of reduced gold clusters

Following literature precedent, [5,24–32] gold clusters were synthesized *via* $NaBH_4$ reduction of Au(I)–calix[4]arene complexes **H1G**, **C1G**, **C2G**, **C3G**, and **D1G** dispersed in ethanol. The conditions using this procedure are intentionally kept dilute during reduction

because of the low ethanol solubility of $NaBH_4$ and the Au(I)–calix[4]arene complex. Figure 5.1 shows HAADF-STEM images of the reduced metal complexes for each ligand. Cluster **H1-red** corresponds to the same sharp size distribution that is centered at around 0.9 nm in cluster diameter, as previously reported for the Au_{11} cluster **T1-red**, which consists of a *tert*-butyl-upper-rim substituent. [5]

The UV-visible spectrum of **H1-red** in dichloromethane solution consists of a characteristic plateau band that is centered at 415 nm, which is shown in Figure 5.4a. This band was also observed in **T1-red** and is representative of bands for small Au_n clusters where $n \sim 11$–13. [24–29,32] UV-visible spectra in Figure 5.4 show an entire absence of absorbance in the region around 520 nm (where gold nanoparticles larger than ~3 nm would absorb due to the surface-plasmon resonance absorption band) for all reduced clusters. This is consistent with the size distribution histograms measured using HAADF-STEM in Figure 5.1.

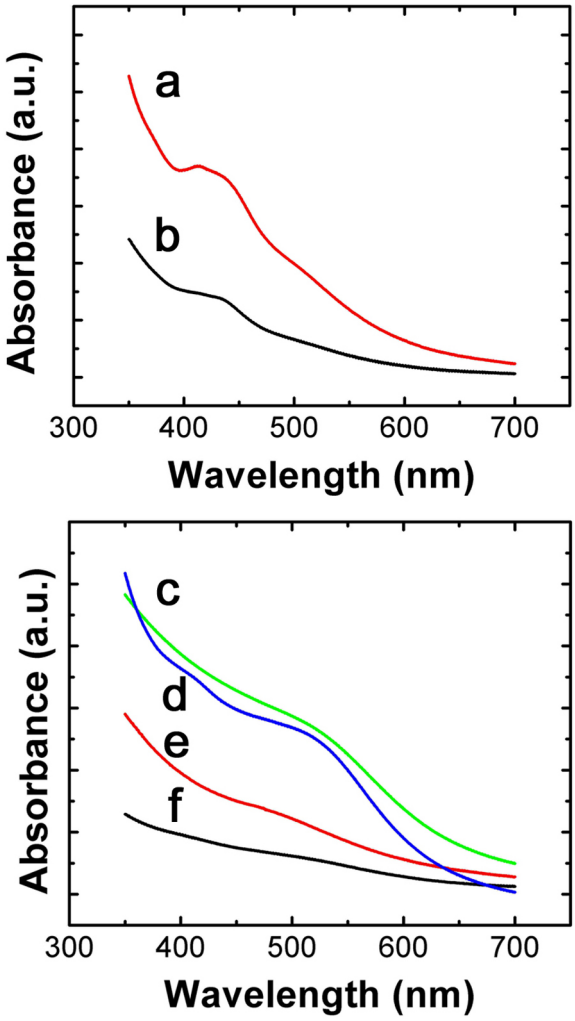

Figure 5.4: UV-Vis spectra for calix[4]arene phosphine (top panel) and carbene (bottom panel) bound gold clusters. The spectra correspond to the following clusters: a (red) **H1-red**, b (black) **T1-red**, c (green) **C3-red**, d (blue – labeled below curve) **D1-red**, e (red) **C2-red**, f (black) **C1-red**. The solvent used for all of measurements with dichloromethane and the temperature was 25°C for all measurements.

The calix[4]arene carbene-bound clusters (**C1-red**, **C2-red**, **C3-red**, and **D1-red**) show slightly larger gold-core cluster sizes compared with cluster **H1-red**, ranging in average diameter from 1.2–1.6 nm. These clusters do not have the characteristic plateau band in the range between 400 and 450 nm, as **H1-red** and **T1-red** do, and microscopy results in Figure 5.1 show these clusters to be larger than Au_{11}. Clusters **C3-red** and **D1-red** have a shoulder in their respective UV-visible spectra at higher wavelengths approaching 500 nm, which is consistent with previously reported larger gold clusters that are bound with calix[4]arene phosphine ligands (average diameters of 1.1 and 1.9 nm).5 This shoulder around 500 nm may be due to a surface-plasmon resonance for the larger nanoparticles; however, we deem this possibility as less likely, due to the following reason. **C1-red** has a similar distribution of particle sizes above 2 nm, relative to **C3-red** and **D1-red**, and lacks such a 500 nm shoulder. Interestingly, **D1-red** also has a small feature at around 400 nm, in the region of the Au_{11} clusters, and microscopy shows this cluster to consist of smaller clusters in addition to larger clusters, which leads to a slightly wider particle-size distribution for **D1-red**.

TGA characterization with the results shown in Table 5.1, can be used to quantify the relative amounts of combustible organics to non-combustible inorganic species (*i.e*. Au and P). [33] For cluster **H1-red**, this ratio is the same as measured for the corresponding complex **H1** prior to reduction. This result suggests that the elemental composition of **H1** and **H1-red** should be nearly equal (*i.e*. the phosphorous to gold ratio should be close to unity).

Table 5.1: Characterization summary of calixarene-bound Au clusters

Gold Cluster	***Ligand***	***Diameter (nm)[a]***	***Au wt. %***
H1-red	H1	0.9 ± 0.1	32 % [b]
T1-red	T1	0.9 ± 0.1	21 % [c]
C1-red	C1	1.6 ± 0.3	33 % [b]
C2-red	C2	1.2 ± 0.4	29 % [b]
C3-red	C3	1.3 ± 0.4	36 % [b]
D1-red	D1	1.3 ± 0.5	21 % [b]

[a] Measured by HAADF-STEM, [b] Measured by TGA, [c] Measured by ICP[5]

Electrospray ionization mass spectrometry (ESI-MS (+)) of **H1-red** reveals a complex pattern of multiple peaks, from which $[Au_{11}L_4Cl]^{2+}$ (L = **H1** ligand where one of the phosphines is a phosphine oxide whereas the other one remains bound to the metal and unchanged as phosphine – as observed previously for monodentate ligands in **T1-red** [5]) could be identified as a doubly charged molecular ion. As with **T1-red**, this fragment appears only under ESI conditions, because the incorporation of Cl in **H1-red** can be ruled out on the basis of XPS results (no evidence of Cl incorporation in **H1-red** *via* XPS). XPS quantifies the phosphine : gold ratio in **H1-red** as 1.1 ± 0.1. The majority of the gold species in **H1-red** have a Au $4f_{7/2}$ binding energy that is similar to the value reported previously for **T1-red**. The state of the P for **T1-red** was previously described as a mixture of phosphine-oxide and phosphine phosphorous, with approximately 30% of the P present as phosphine oxide. A similar distribution of phosphorous species is observed *via* XPS for **H1-red**.

The accessibility of the synthesized gold clusters with calix[4]arene phosphine ligands is measured by using a previously developed procedure that relies on the quenching of steady-state fluorescence intensity upon binding 2-NT as a molecule probe to the gold surface. These measurements show **H1-red** to be the most accessible cluster, and 2-NT titration data for this cluster are shown in Figure 5.5. These results indicate a comparable amount of accessibility for **H1-red** as previously reported for **T1-red**, which is 25.5% of total gold atoms accessible in **H1-red** and 25.0% of total gold atoms accessible in **T1-red**. This correlates well with the HAADF-STEM data and UV-Vis data, which indicate that both of the clusters are very similar in size. This correlation between small cluster size in **T1-red** and **H1-red**, and extraordinarily large density of open "coordinatively unsaturated" sites within the cluster supports the mechanical nature of the mechanism of accessibility, schematically represented in Scheme 5.1. Altogether, our proposed model for **H1-red** closely follows the same one previously proposed for **T1-red**. This comprises a Au_{11} cluster to which five calix[4]arene ligands derived from **H1** are bound to the metal core, with three of these bound in a mono-dentate fashion (rather than a bidentate configuration involving both phosphines on the calix[4]arene ligand).

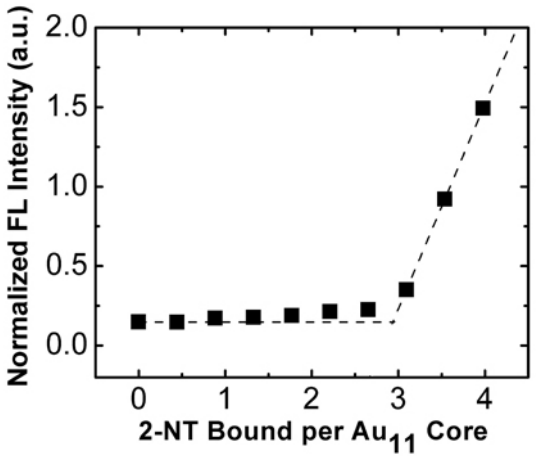

Figure 5.5: Normalized fluorescence emission intensity during titration of **H1-red** with 2-NT. Each solution contains 0.35 mg **H1-red** in 3 mL of dichloromethane and is excited at 283 nm. Temperature for these measurements was 25°C for all measurements. **H1-red** shows a similar binding capacity for 2-NT relative to **T1-red**.

The accessibility of the calix[4]arene-NHC bound Au clusters could not be accurately assessed *via* 2-NT titration due to high background fluorescence of the NHC-bound gold clusters. This background fluorescence problem is not present with **H1-red** and **T1-red**, and required development of a new fluorescent probe titration method, in order to determine the accessibility of a NHC-bound Au cluster. The probe used for this purpose was SAMSA (5-((2-(and-3)-*S*-(acetylmercapto)succinoyl)amino)) fluorescein, which has been shown previously to bind to Au nanoparticles, presumably through the thiol functional group (which can be exposed *via* thioester hydrolysis). [34,35] We first demonstrate that this new probe can be used to measure accessibility in a cluster that has a known number density of open sites, consisting of **T1-red**. Titration data of **T1-red** with SAMSA fluorescein demonstrate a similar number of open sites as when using 2-NT for titration, corresponding to 25% of surface-gold atoms being open

and accessible for probe molecule binding, for both probes. The major difference between the two probes is that while the fluorescence of 2-NT bound to the gold surface is quenched relative to unbound 2-NT in solution, the fluorescence intensity of the SAMSA fluorescein probe is greater (by a factor of 2.6 fold) when bound to the gold surface relative to its intensity in solution as an unbound species. Similar increases in the steady-state fluorescence intensity have been previously observed when binding both pyrene thioesters and pyrene thiocarbonates to a gold surface. [36] Both of these latter two pyrene-based probes as well as the SAMSA fluorescein share the common trait of not having the fluorescent part of the molecule conjugated directly to the functional group involved in binding (coordination) to the gold surface. This is in contrast to 2-NT, where the sulfur atom is directly substituted on the fluorescent naphthalenic ring and is the functional group that is involved in coordination to the gold surface.

With **T1-red** showing the same degree of open-site accessibility when using the SAMSA fluorescein as well as 2-NT steady-state fluorescence assays, we applied the SAMSA fluorescein probe to the smallest calix[4]arene NHC-bound gold cluster, consisting of **C2-red**, in anticipation that this cluster may show the greatest amount of accessibility according to the mechanical model of Scheme 5.1. The accessibility of **C2-red** was quantified using the SAMSA fluorescein probe for varying amounts of **C2-red**, and the amount of SAMSA fluorescein required to saturate the open surface sites for varying concentrations of **C2-red** is shown in Figure 5.6. The slope of the line in Figure 5.6 provides a quantification of the number density of open sites in cluster **C2-red**, and corresponds to 7.1% of surface gold atoms being open and accessible for probe molecule binding. This result is placed comparatively within the context of previous accessibility results on calix[4]arene phosphine-bound gold clusters, in Figure 5.7. The new result involving calix[4]arene NHC-bound **C2-red** in Figure 5.6 indicates a similar accessibility as previously observed for 1.1 nm-sized calix[4]arene phosphine-bound gold clusters.5 This result reaffirms the generality of the accessibility mechanism shown in Figure 5.1, by demonstrating that this accessibility does not depend on the nature of the functional group that coordinates with the gold surface (*i.e.* similar accessibility is observed when using either a phosphine or a NHC functional group).

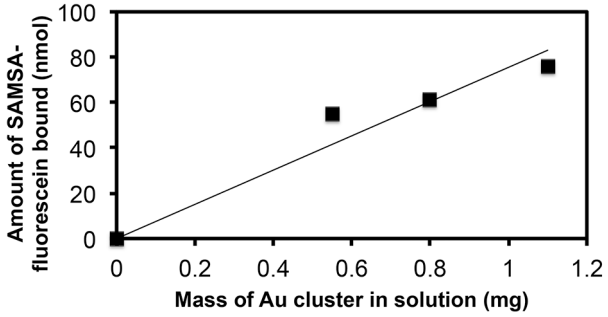

Figure 5.6: Titration of **C2-red** with SAMSA-fluorescein probe molecule. The amount of probe bound scales linearly with the mass of the **C2-red** in solution. The solvent used was isopropanol and the total solution volume was 3 mL. Temperature of the titrations was 25°C for all measurements.

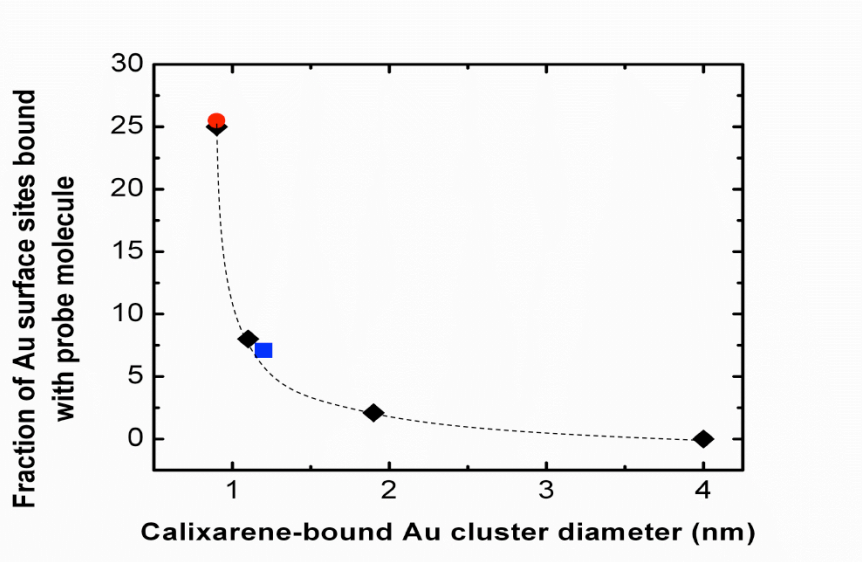

Figure 5.7: Accessibility of the calix[4]arene bound metal core as function of particle diameter. *Tert*-butyl upper rim calix[4]arene phosphine bound gold particles[5] (◆), **H1-red** (●), and **C2-red** (■)

5.7 Conclusions

The design and synthesis of stable and accessible metal clusters consisting of open "coordinatively unsaturated" binding sites using bulky calix[4]arene ligands is demonstrated. These new calix[4]arene-bound gold clusters use a H-calix[4]arene phosphine ligand as well as four different calix[4]arene NHC ligands. Small clusters with calix[4]arene NHC ligands bound to the gold surface were synthesized with average particle sizes ranging from 1.2 to 1.6 nm, and the smallest of these clusters exhibits similar accessibility (*i.e*. open site density) as a similarly sized gold cluster bound with a calix[4]arene phosphine. This key result emphasizes the generality of the accessibility mechanism and the fact that this does not depend on the functional group coordinating to the gold surface. In the case of a H-calix[4]arene phosphine ligand-bound Au cluster, similar physical and optical properties and 2-NT accessibility were observed as in a calix[4]arene phosphine bound cluster, consisting of **T1-red** with *tert*-butyl groups on the upper rim of the calix[4]arene. However, a key comparison of **H1-red** to **T1-red** is that the gold complex precursor of **H1-red** is not exclusively in cone conformation in solution, though it is in the solid state, and yet still leads to similar particles by the methods of characterization used in this paper. This demonstrates that some degree of conformational flexibility within a Au(I)–calix[4]arene complex can still lead to a highly accessible calix[4]arene-bound cluster, consisting of a high density of open "coordinatively unsaturated" sites.

5.8 Acknowledgements

We are grateful to the Management and Transfer of Hydrogen *via* Catalysis Program funded by Chevron Corporation for financial support. We also grateful for Dr Rita Nichiporuk for assistance with ESI-MS experiments. The authors acknowledge support of the National Center for Electron Microscopy, Lawrence Berkeley Lab, which is supported by the U.S.

Department of Energy under Contract #DE-AC02-05CH11231. AGD would like to acknowledge the NIH for a Shared Instrument Grant (S10-RR027172) to fund the purchase of the microsource X-ray diffractometer used in this research.

5.9 Supplementary information

5.9.1 Synthesis of calixarene ligands with NMR and ESI-MS characterization

5.9.1.1 Experimental

All compounds were handled under a dry nitrogen atmosphere. Solvents were dried and distilled by standard methods. Sodium hydride 60% in oil was purchased from Aldrich. *t*-butylcalix[4]arene, dibromoalkanes, 1-R-imidazoles and phenylsilane were purchased from Aldrich. Calixarenes **2**[1], **1**[2], Ph_2POCH_2OTs[3], **6a**[7], **6b**[4], **7a,b**[5,6], **T1**[8], **H1**[5,6] were synthesized using published procedures. ^1H, ^{13}C, ^{31}P NMR spectra were recorded either on a Bruker DRX-500, AVQ-400, AV-300, AV-600 instrument at UC Berkeley NMR facility. The ^1H NMR data are referenced to residual solvent resonance and ^{31}P NMR data are referenced relative to dimethylphosphate. Analytical thin-layer chromatography was performed on precoated silica gel plates (Selecto), and silica gel (Selecto 60) was used for column chromatography. MS spectra were recorded at the UC Berkeley Mass Spectrometry Facility.

5.9.1.2 General procedure of Bromoalkylation of dialkylcalix[4]arenes **1**,**2**

A solution of dialkylcalixarenes **1,2** (1.58 mmol) in 30 ml of DMF were reacted with NaH (4.74 mmol). The resulting solution was stirred for 2 h at r.t. After a cloudy solution formed, di-bromoalkane (4.74 mmol) was added dropwise and stirring was continued for 1h at r.t. The reaction mixture was poured into 100 ml of ice water and extracted with 100 ml of DCM. DCM layer was washed with water and dried over Na_2SO_4. Evaporation gave a white solid that was purified using column chromatography.

5.9.1.3 5,11,17,23-Tetra-tert-butyl-25,27-Dibromopropoxy-26,28-dimethoxy-calix[4]arene (**3**)

Column chromatography with n-hexane-chloroform (1:0.6) and washing with methanol afforded white solid: yield 41%; ^1H NMR ($CDCl_3$) δ 7.24, 7.15, 7.11, 6.94, 6.61, 6.47 (six br s, 8H, ArH), 4.34, 4.10, 3.95, 3.89, 3.77, 3.66, 2.99, 2.45 (eight br m, 26H, $ArCH_2Ar$+OMe+OCH_2+ CH_2Br+CH_2), 1.00, 1.30, 1.41 (three br s, 36H, C_4H_9-*t*); ^{31}C NMR ($CDCl_3$) δ ; 145.36, 144.27, 135.86, 135.38, 132.51, 131.87, 127.34, 126.07, 125.70, 125.43, 125.11, 124.33, 37.96, 34.15, 33.67, 31.73, 31.37, 31.15, 30.80, 30.72; +ESI MS m/z 918 $[M]^+$, 839 $[M\text{-}HBr]^+$.

5.9.1.4 Dibromo-calix[4]arene-dimer (**5**)

Column chromatography with n-hexane-chloroform (1:0.25) and washing with methanol afforded white solid: yield 47%; ^1H NMR ($CDCl_3$) δ 6.78-6.83 (br m, 16H, ArH), 4.41, 4.43 (two d, 4H+4H, ^2J = 13Hz, $ArCH_2Ar$), 3.96 (m, 4H, OCH_2), 3.87(m, 12H, OCH_2), 3.46 (m, 4H,

CH_2Br), 3.15 (d, 8H, ^2J = 13Hz, $ArCH_2Ar$), 2.06-2.16 (br m, 20H, CH_2), 1.08, 1.09, 1.12 (three s, 72H, C_4H_9-*t*), 1.04 (t, 12H, CH_3); ^{31}C NMR ($CDCl_3$) δ 153.70, 153.42, 153.38, 144.45, 144.30, 133.95, 133.81, 133.68, 125.02, 124.93, 76.97, 75.20, 74.13, 34.69, 33.85, 33.57, 31.50, 31.47, 31.13, 31.05, 29.70, 29.04, 26.63, 23.45, 10.41; ; +ESI HR MS calcd for $C_{112}H_{156}O_8Br_2Na_1$ 1810.0059, found 1810.0095.

5.9.1.5 General procedure of calixarene imidazolium bromides **C2**, **C3**, **D1** synthesis

The starting bromocalixarenes **3,4,5** were vacuumed in high vacuum for 3h. The residue was flushed two times with dry argon. A mixture of bromocalixarenes **3,4,5 (**0.59 mmol) and 1-Alkyl-imidazol (11.8 mmol) was heated at 110 ^{0}C in minimal amount (3-5 ml) of freshly distilled over Na toluene. The reaction was monitored by TLC. After disappearance of high R_f spot of bromocalixarene on TLC plate (hexane/chloroform mixture as an eluent) in 18h, a reaction mixture was evaporated and dried in high vacuum for 24h. The residue was treated with n-hexane (for reactions with 1-Butylimidazol) or n-hexane-benzene mixture (10:0.5) (for reaction with Phenylimidazol). After 24h, organic solution was separated and white solid formed was crystallized from toluene. The same general procedure was used for synthesis of **C1**.

5.9.1.6 5,11,17,23-Tetra-tert-butyl-25,27-Dipropoxy-26,28-Bis[1-Phenyl-3-propoxy-imidazolium]calix[4]arene dibromide (**C2**).

Crystallization from toluene afforded white crystals: yield 73%; ^1H NMR ($CDCl_3$) δ 11.05 (s, 2H, NCHN), 7.85 (s, 2H, CHN), 7.81 (d, 4H, ^3J = 7.5 Hz, ArH-Im), 7.67 (s, 2H, CHN), 7.50 (m, 6H, ArH-Im), 7.11 (s, 4H, ArH), 6.49 (s, 4H, ArH), 4.83 (t, 4H, ^3J = 8.0 Hz, Im-CH_2), 4.38 (d, 4H, ^2J = 12.5 Hz, $ArCH_2Ar$), 4.08 (t, 4H, ^3J = 8.0 Hz, OCH_2), 3.74 (t, 4H, ^3J = 6.5 Hz, OCH_2), 3.15 (d, 4H, ^2J = 12.5 Hz, $ArCH_2Ar$), 2.38 (m, 4H, CH_2), 2.19 (m, 4H, CH_2), 1.95 (m, 4H, CH_2), 1.34 (s, 18H, C_4H_9-*t*), 1.10 (t, 6H, ^3J = 7.5 Hz, $CH_2C\mathbf{H}_3$), 0.85 (s, 18H, C_4H_9-*t*); ^{31}C NMR ($CDCl_3$) δ 154.12, 152.38, 145.15, 144.00, 135.57, 134.72, 132.00, 130.46, 130.01, 125.52, 124.47, 123.29, 122.03, 120.38, 77.65, 73.91, 50.49, 34.10, 33.60, 31.74, 31.18, 31.05, 27.40, 26.81, 23.83, 11.01; +ESI HR MS calcd for $C_{76}H_{98}O_4N_4Br_1$ 1209.6766, found 1209.6765.

5.9.1.7 5,11,17,23-Tetra-tert-butyl-25,27-Dimethoxy-26,28-Bis[1-Phenyl-3-propoxy-imidazolium]calix[4]arene dibromide (**C3**).

Crystallization from toluene afforded white crystals: yield 69%; ^1H NMR ($CDCl_3$) δ 11.11 (s, 2H, NCHN), 8.11 (br s, 2H, ArH), 7.82 (m, 6H, ArH), 7.43-7.54 (br m, 6H, ArH), 7.37 (m, 1H, ArH), 7.26 (m, 1H, ArH), 7.15 (m, 2H, ArH), 7.06 (br s, 4H, ArH), 6.50 (br s, 4H, ArH), 4.94 (br s, 4H, CH_2), 3.88, 4.01, 4.17 (three br s, 10H, CH2+OCH3), 3.16 (br s, 4H, CH_2), 2.65 (br s, 4H, CH_2), 1.27 (s, 18H, C_4H_9-*t*), 0.87 (br s, 18H, C_4H_9-*t*); ^{31}C NMR ($CDCl_3$) δ 152.99, 145.14, 144.67, 137.83, 135.89, 134.94, 134.50, 131.88, 130.45, 130.08, 129.87, 128.99, 128.18, 127.49, 125.25, 123.95, 121.95, 121.87, 121.78, 121.47, 121.00, 48.66, 34.06, 33.59, 31.65, 31.10; +ESI HR MS calcd for $C_{70}H_{86}O_4N_4Br_1$ 1125.5827, found 1125.5829.

5.9.1.8 *t*-Butyl-Calix[4]arene-dimer-n-Butyldiimidazolium dibromide (**D1**).

Crystallization from *n*-hexane mixture afforded white solid: yield 58%; ^{1}H NMR ($CDCl_3$) δ 10.85 (s, 1H, NCHN), 7.50 (s, 1H, NCHN), 7.08 (m, 3H, ArH), 6.93 (s, 1H, ArH), 6.83 (s, 8H, ArH), 6.75, 6.77 (two s, 8H, ArH), 4.35-4.43 (br m, 16H, CH_2N+$ArCH_2Ar$), 3.96 (m, 8H, OCH_2), 3.82 (m, 8H, OCH_2), 3.12, 3.15 (two d, ^{2}J = 13.5 Hz, 8H, $ArCH_2Ar$), 1.41, 1.78, 1.93, 2.06 (four m, 28H, CH_2), 1.06, 1.13 (two s, 36H+36H, C_4H_9-*t*), 0.95-1.05 (br m, 18H, CH3); ^{31}C NMR ($CDCl_3$) δ 153.70, 153.12, 152.86, 144.59, 144.52, 144.46, 137.54, 133.99, 133.78, 133.43, 133.28, 125.12, 125.05, 124.91, 122.02, 121.53, 74.93, 73.40, 49.92, 49.87, 46.81, 33.87, 33.80, 33.08, 32.20, 31.50, 31.40, 31.13, 27.42, 26.91, 26.80, 23.45, 19.74, 19.51, 13.51, 10.61; +ESI HR MS calcd for $C_{126}H_{180}O_8N_4$ 1877.3790, found 1877.3822.

5.9.1.9 25,27-Bis[Diphenylphosphorylmethoxy]-26,28-Dimetoxy-calix[4]arene (**7b**)

Column chromatography with chloroform-ethylacetate (1:1) afforded white solid: yield 63%; ^{1}H NMR (C_6D_6) δ 7.82 (m, 10H, ArH), 7.71 (m, 5H ArH), 7.47, 7.51 (two d, ^{3}J = 8.4, 7.2, Hz, 2H, ArH), 6.90-7.08 (br m, 37H, ArH), 6.64 (t, 2H, ^{3}J = 7.8 Hz, ArH), 6.49 (d, 1H, ^{3}J = 7.8 Hz, ArH), 6.45 (d, 1H, ^{3}J = 7.2, Hz, ArH), 6.38 (m, 6H, ArH), 4.48 (d, 4H, ^{2}J = 13.2 Hz, $ArCH_2Ar$), 4.26, 4.27 (two s, 8H, CH_2P), 4.15 (d, 2H, ^{2}J = 13.2 Hz, $ArCH_2Ar$), 4.07 (d, 2H, ^{2}J = 12.6 Hz, $ArCH_2Ar$), 3.62 (d, 2H, ^{2}J = 12.6 Hz, $ArCH_2Ar$), 3.47 (s, 6H, OCH_3-cone), 3.83 (s, 3H, OCH_3-alt), 3.07 (d, 4H, ^{2}J = 13.2 Hz, $ArCH_2Ar$), 2.98 (d, 2H, ^{2}J = 13.8 Hz, $ArCH_2Ar$), 2.59 (s, 3H, OCH_3-alt); ^{13}C NMR ($CDCl_3$) δ 158.69, 156.30, 136.75, 132.78, 132.60, 132.22, 131.51, 131.45, 131.35, 131.29, 130.65, 129.96, 129.21, 128.87, 128.82, 128.74, 128.66, 128.15, 127.49, 122.91, 122.47, 122.30, 73.61, 73.05, 60.52, 30.40; ^{31}P NMR (C_6D_6) δ 21.76, 21.90; +ESI HR MS calcd for $C_{56}H_{50}O_6Na1P2$ 903.2975, found 903.2982.

5.9.1.10 25,27-Bis[Diphenylphosphinomethoxy]-26,28-Dimetoxy-calix[4]arene (**H1**)

Flash column chromatography with DCM distilled afforded white solid: yield 79%; ^{1}H NMR ($CDCl_3$) δ 6.85-7.70 (br m, 56H, ArH), 6.48 (t, 2H, ^{3}J = 7.8 Hz, ArH), 6.27 (m, 3H, ArH), 6.22 (m, 3H, ArH), 4.58 (s, 8H, CH_2P), 4.27 (d, 4H, ^{2}J = 13.2 Hz, $ArCH_2Ar$), 3.95 (d, 2H, ^{2}J = 12.6 Hz, $ArCH_2Ar$), 3.73 (m, 2H, $ArCH_2Ar$), 3.66 (s, 3H, OCH_3-alt), 3.60 (d, 2H, ^{2}J = 12.6 Hz, $ArCH_2Ar$), 3.53 (s, 6H, OCH_3-cone), 3.14 (d, 4H, ^{2}J = 13.2 Hz, $ArCH_2Ar$), 3.08 (d, 2H, ^{2}J = 12.6 Hz, $ArCH_2Ar$), 2.65 (s, 3H, OCH3-alt)"; ^{31}C NMR ($CDCl_3$) δ 158.76, 136.96, 136.47, 133.92, 133.15, 133.03, 132.81, 132.56, 130.34, 128.95, 128.75, 128.66, 128.53, 128.49, 127.75, 127.67, 127.37, 60.70, 30.94; ^{31}P NMR (C_6D_6) d -20.67, -20.25; +ESI HR MS calcd for $C_{56}H_{51}O_4P2$ 849.3257, found 849.3280.

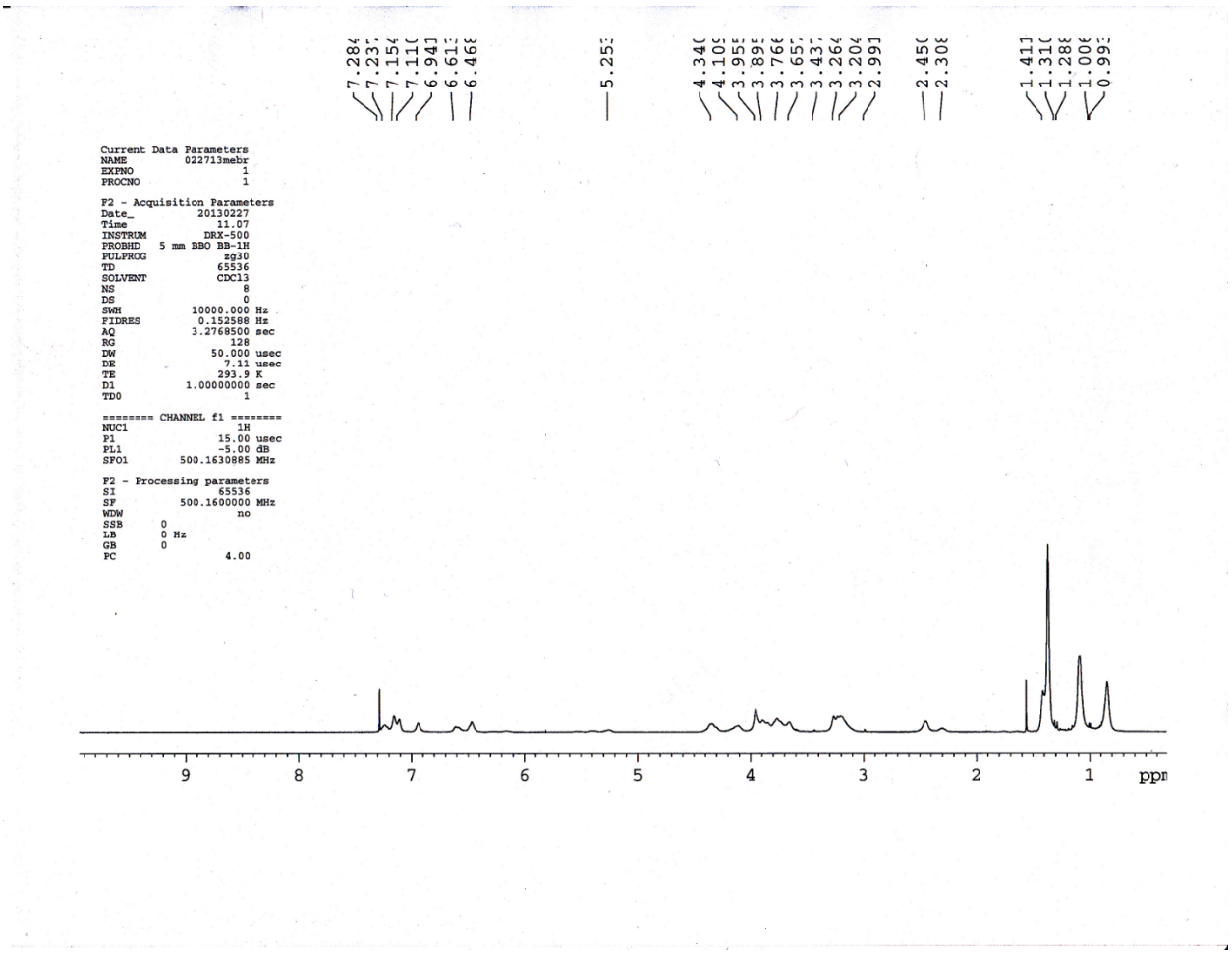

Figure 5.S.1: ^{1}H NMR spectra of **3** ($CDCl_3$)

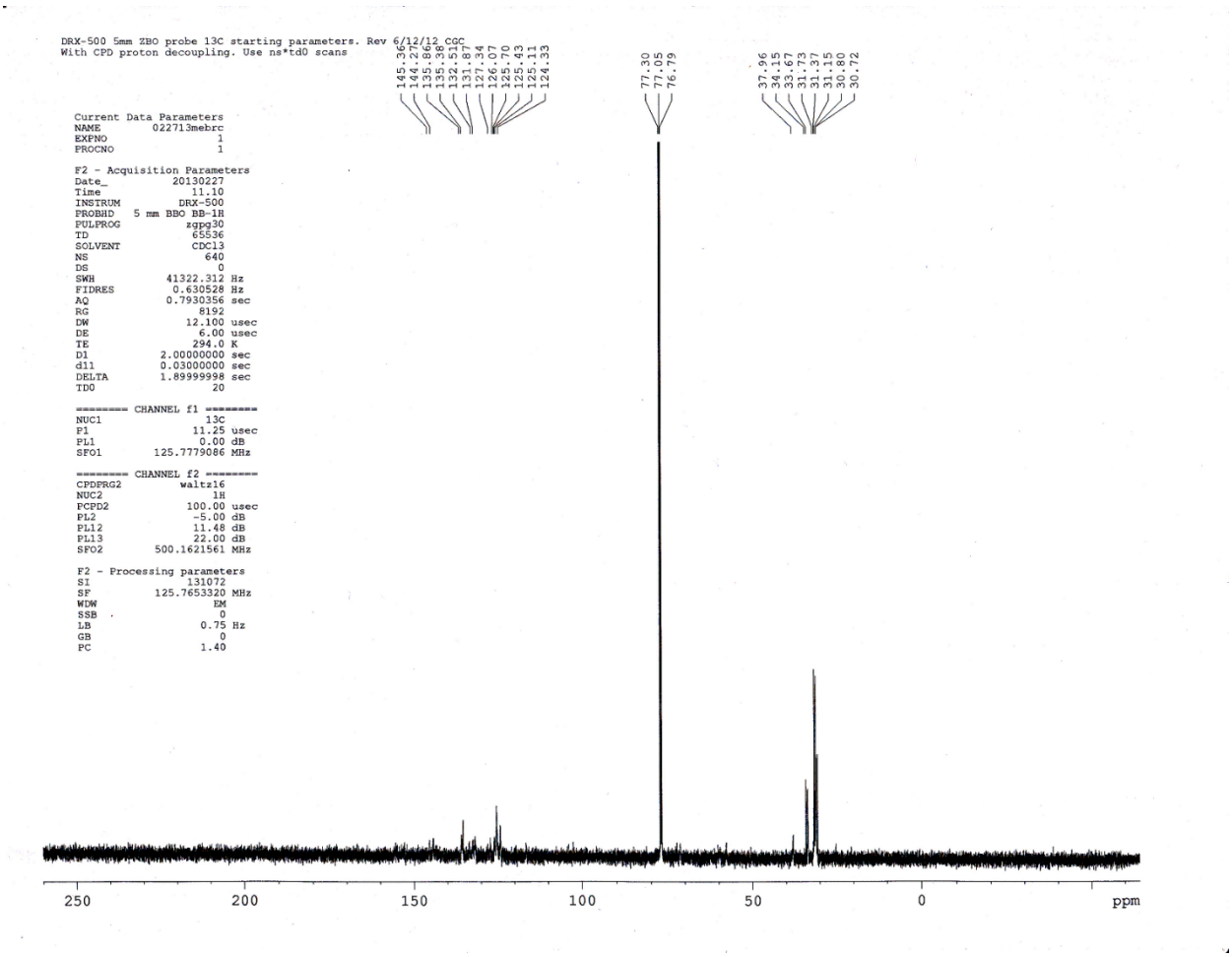

Figure 5.S.2: ^{13}C NMR spectra of **3** ($CDCl_3$)

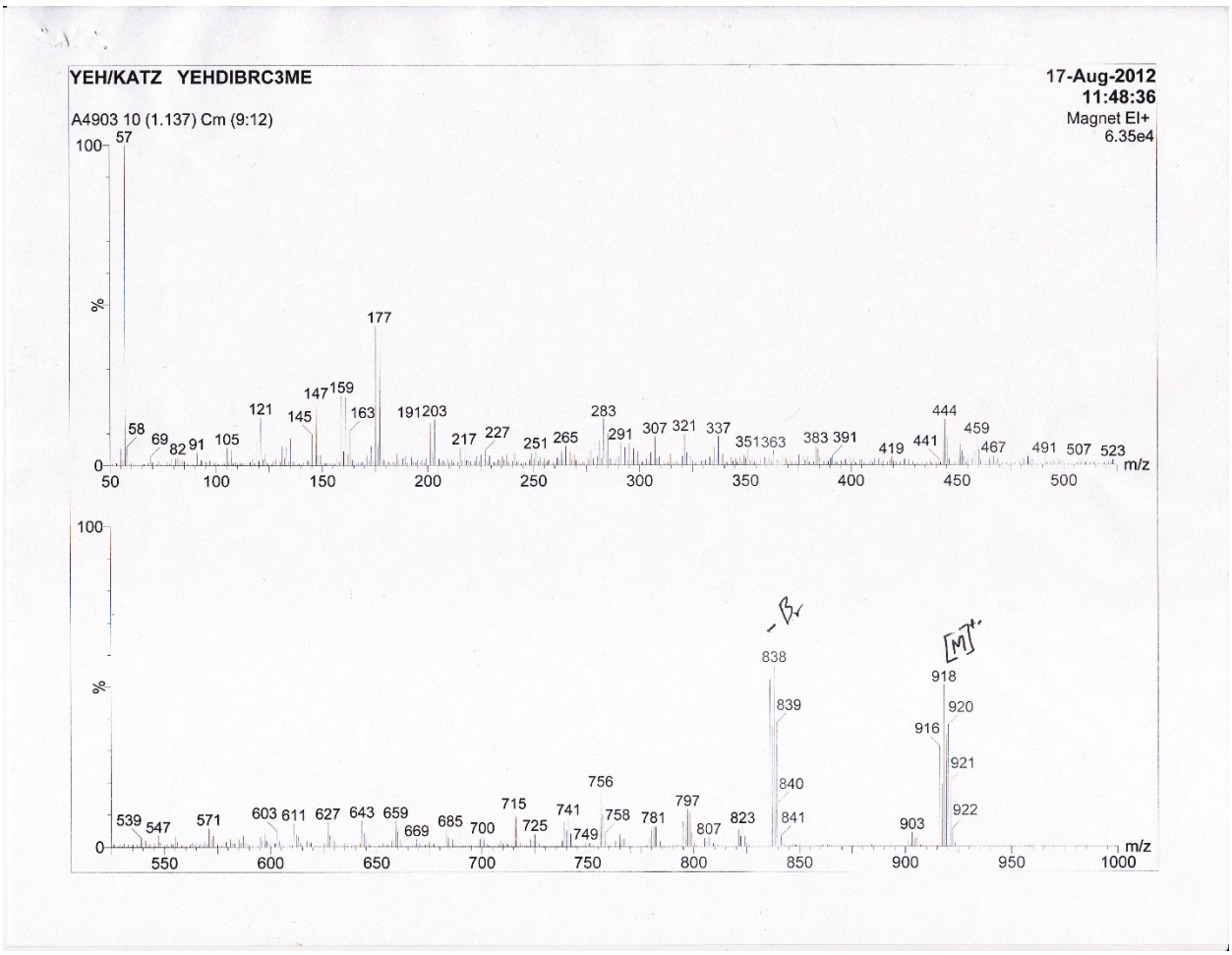

Figure 5.S.3: +ESI MS spectra of **3**

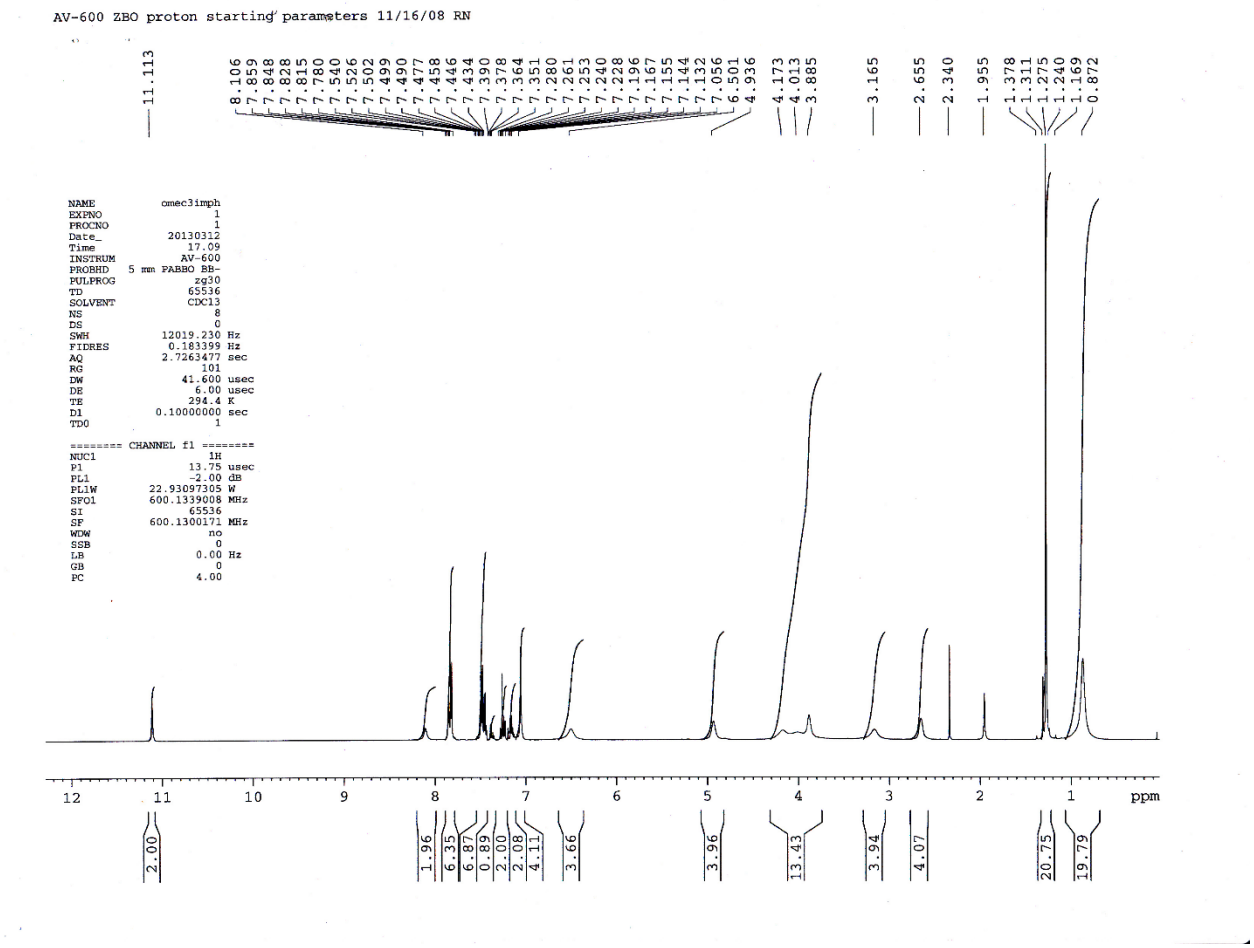

Figure 5.S.4: ^{1}H NMR spectra of **C3** ($CDCl_3$)

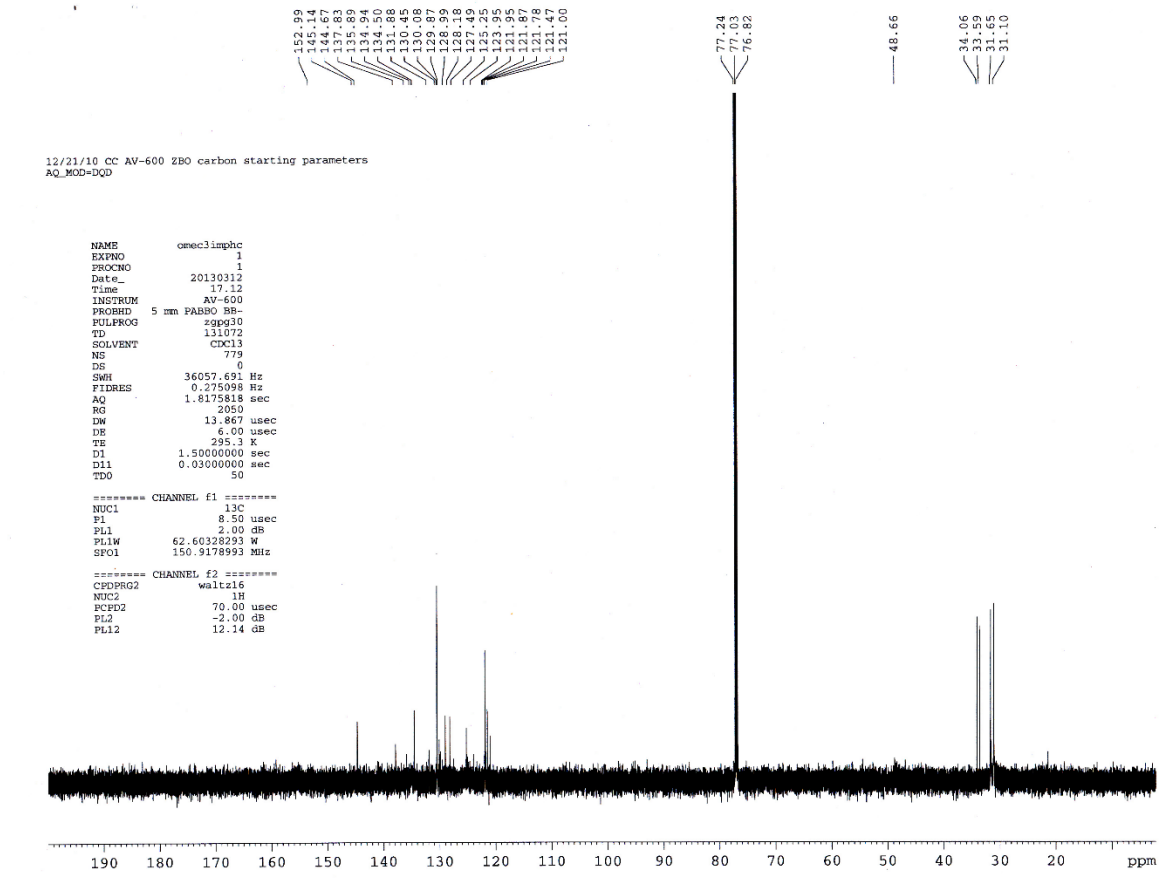

Figure 5.S.5: ^{13}C NMR spectra of **C3** ($CDCl_3$)

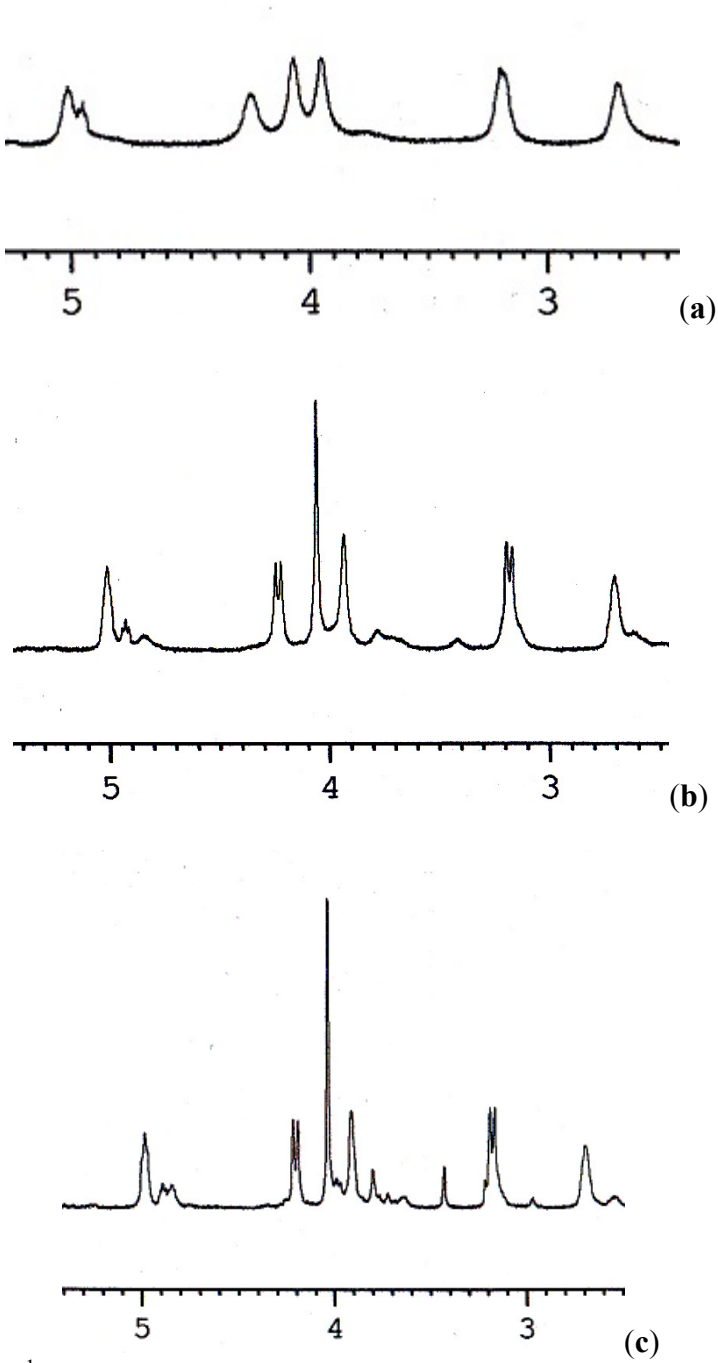

Figure 5.S.6: ^{1}H NMR spectra of **C3** (methylene bridges region) ($CDCl_3$) at 273K (**a**), 253K (**b**), 223K(**c**)

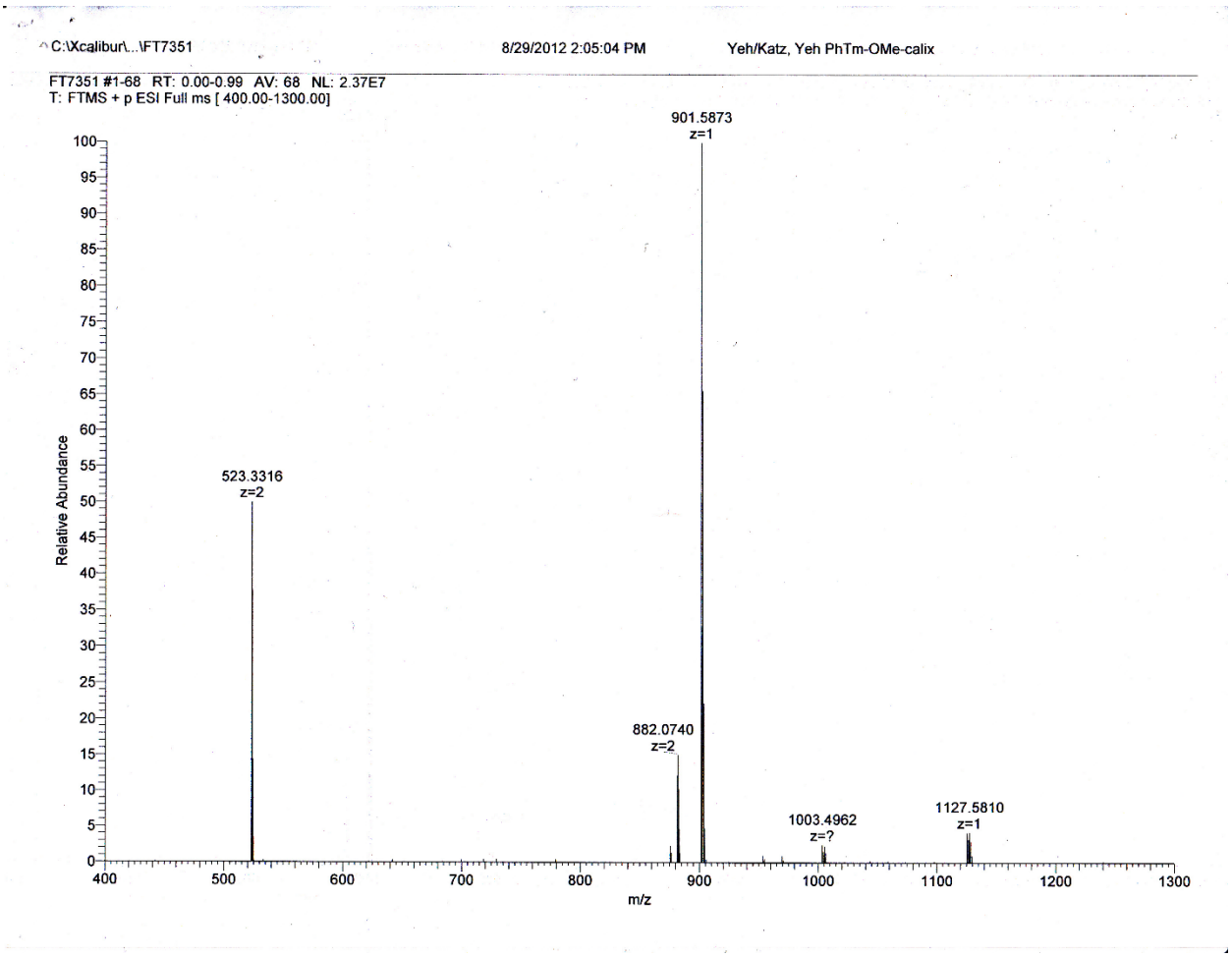

Figure 5.S.7: +ESI MS spectra of **C3**

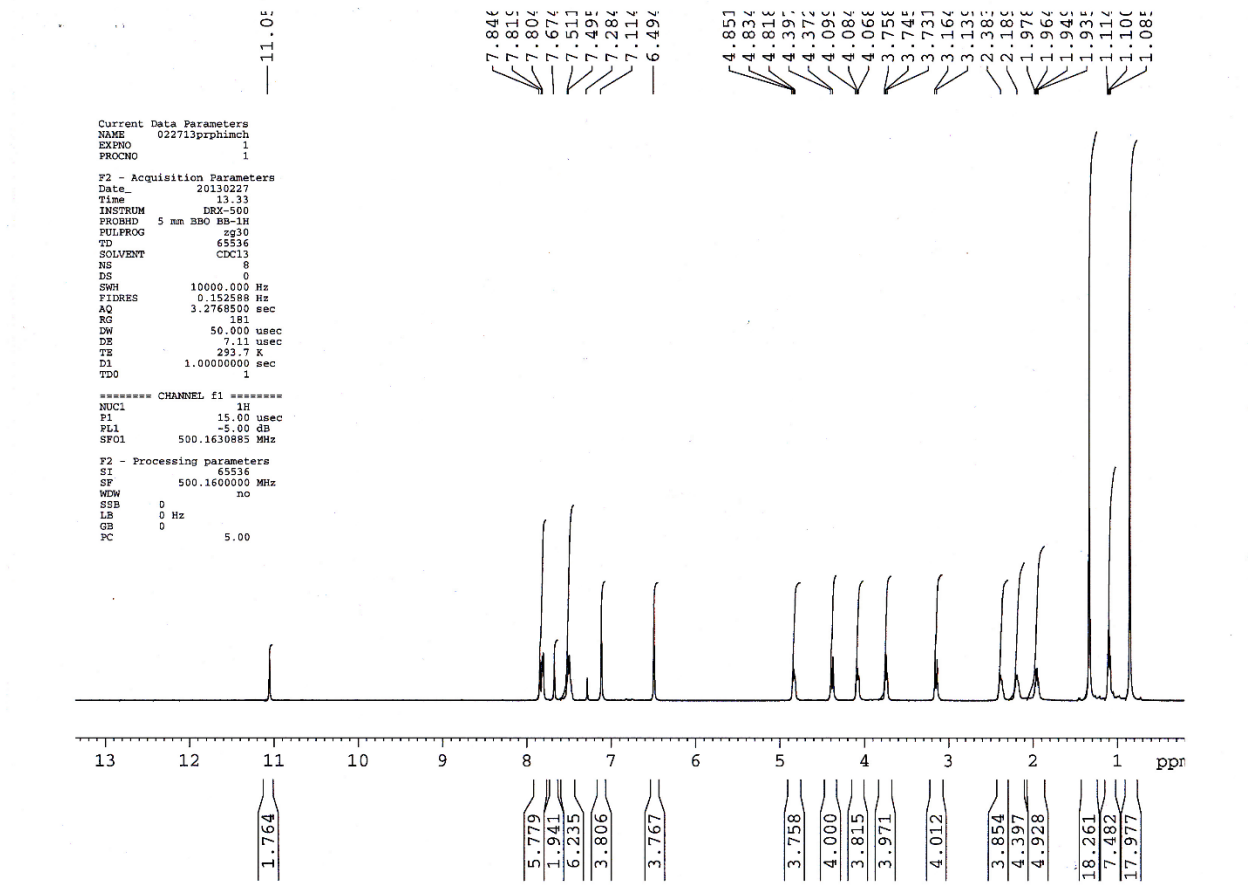

Figure 5.S.8: ^{1}H NMR spectra of **C2** ($CDCl_3$)

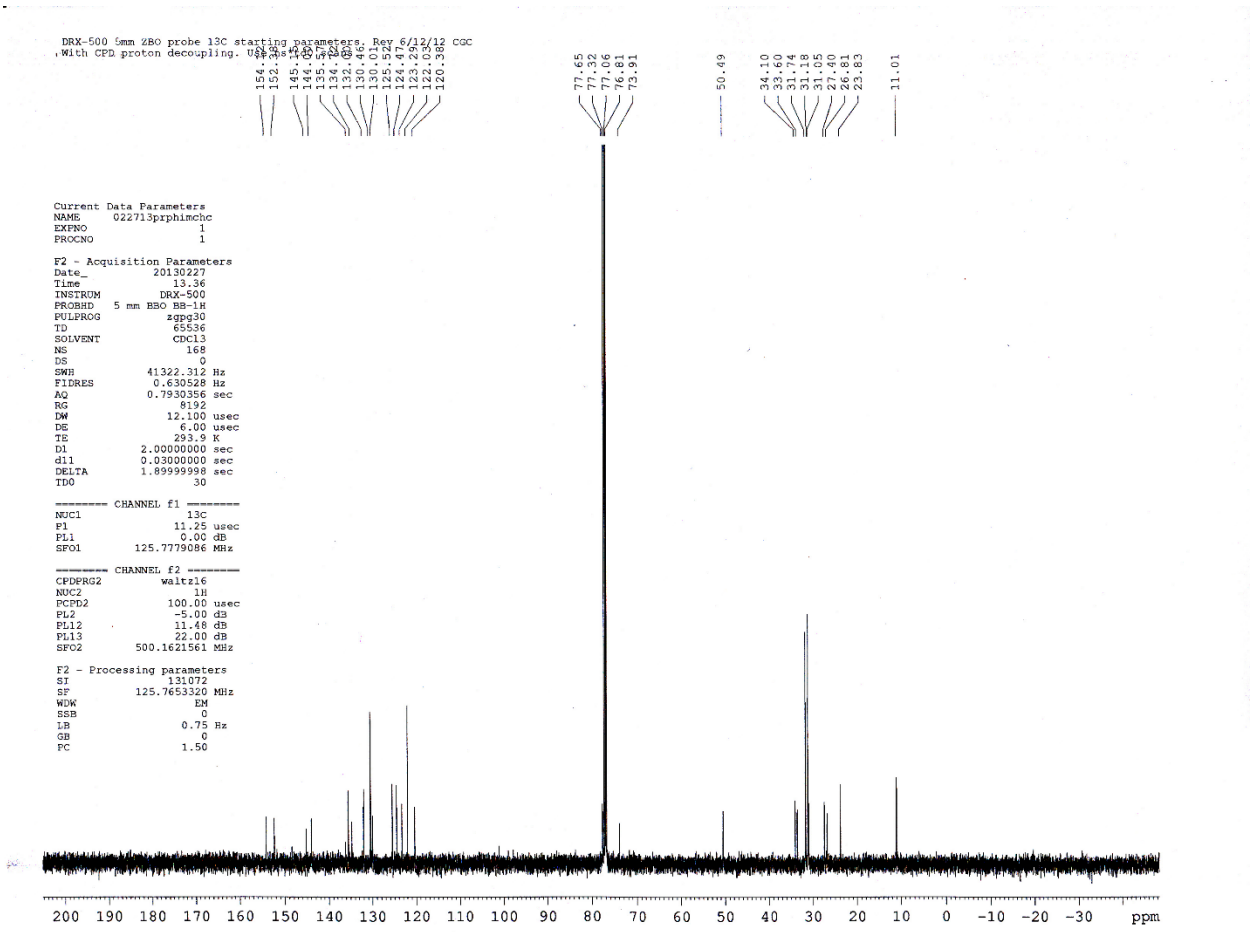

Figure 5.S.9: ^{13}C NMR spectra of **C2** ($CDCl_3$)

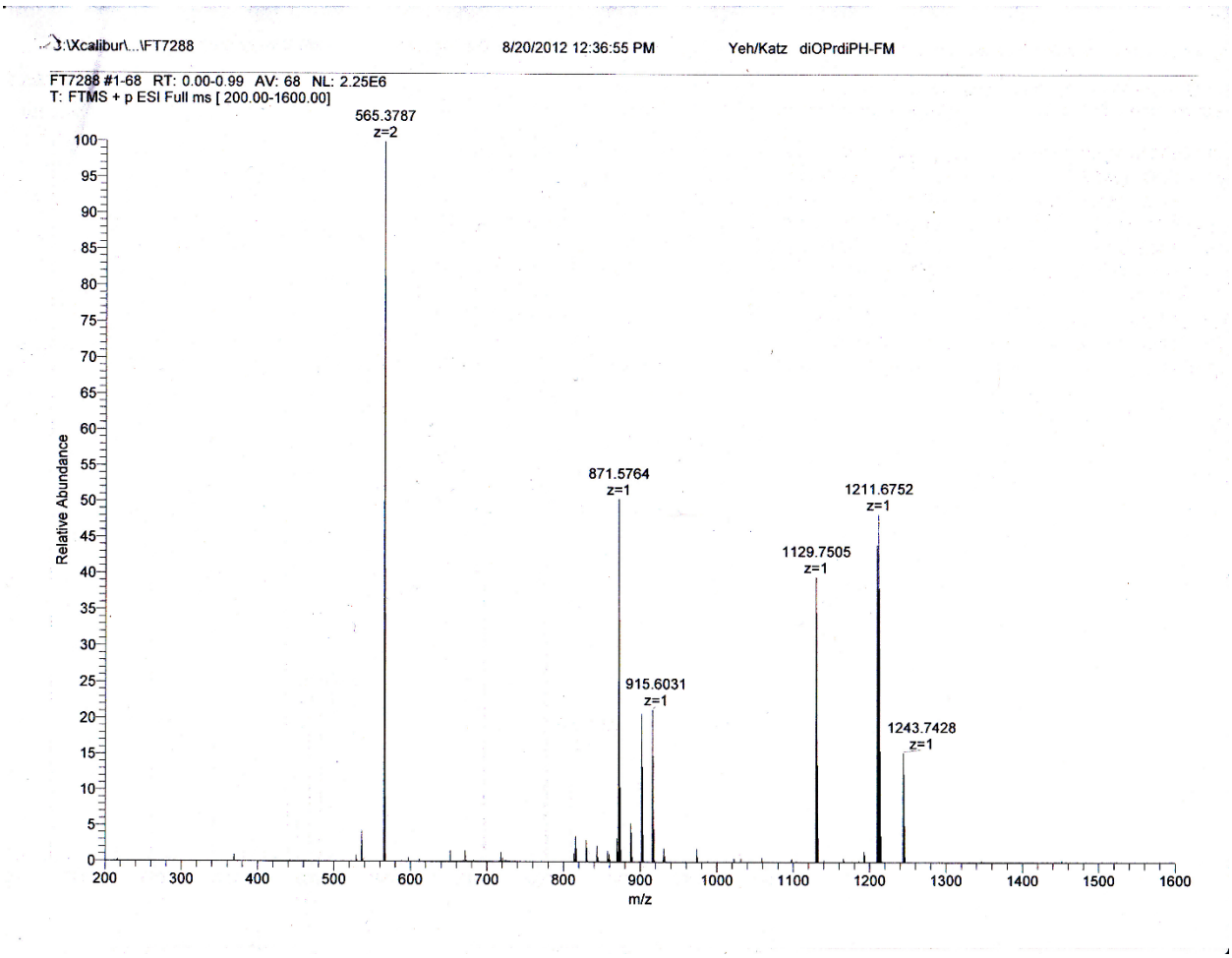

Figure 5.S.10: +ESI MS spectra of **C2**

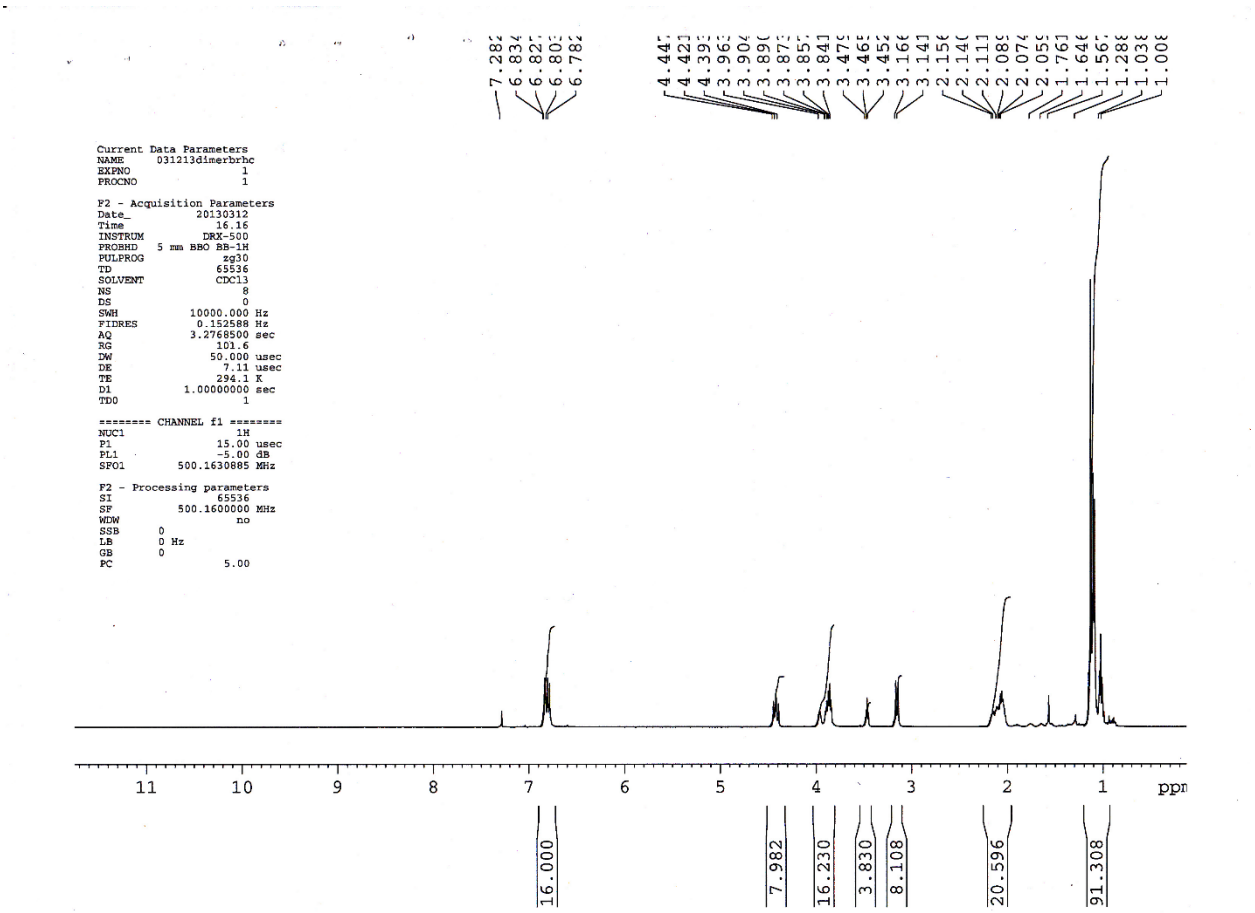

Figure 5.S.11: ^{1}H NMR spectra of **5** ($CDCl_3$)

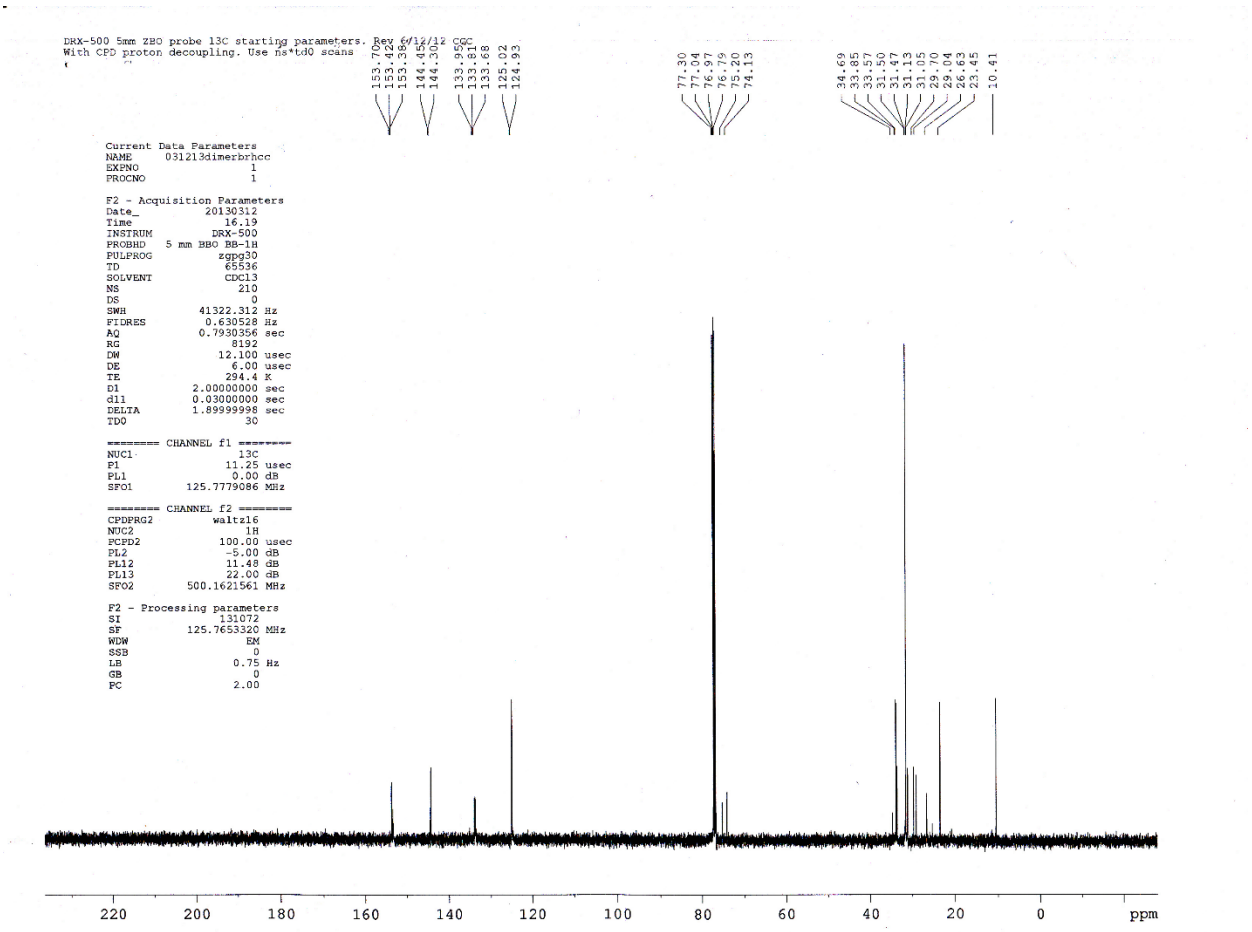

Figure 5.S.12: ^{13}C NMR spectra of **5** ($CDCl_3$)

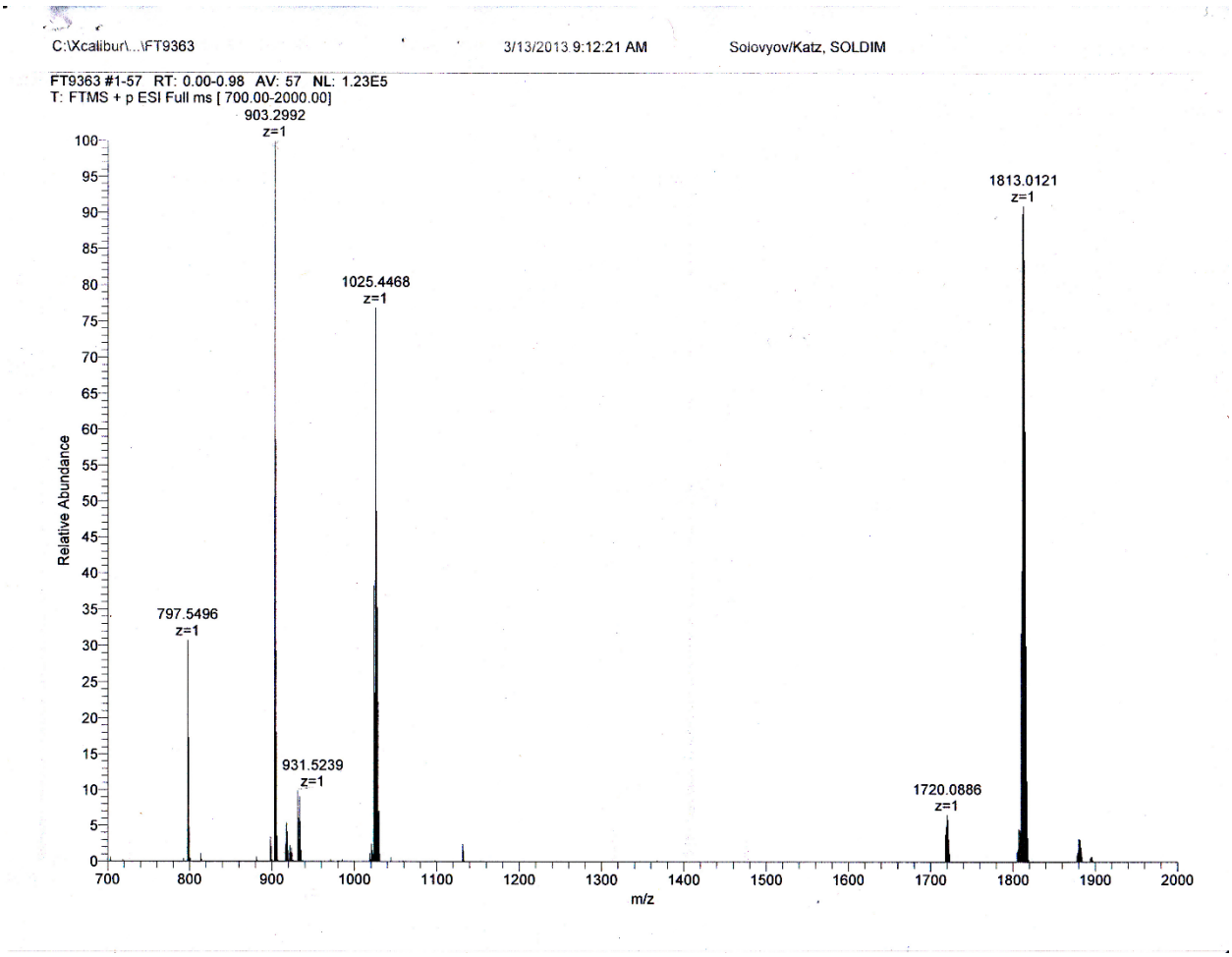

Figure 5.S.13: +ESI MS spectra of **5**

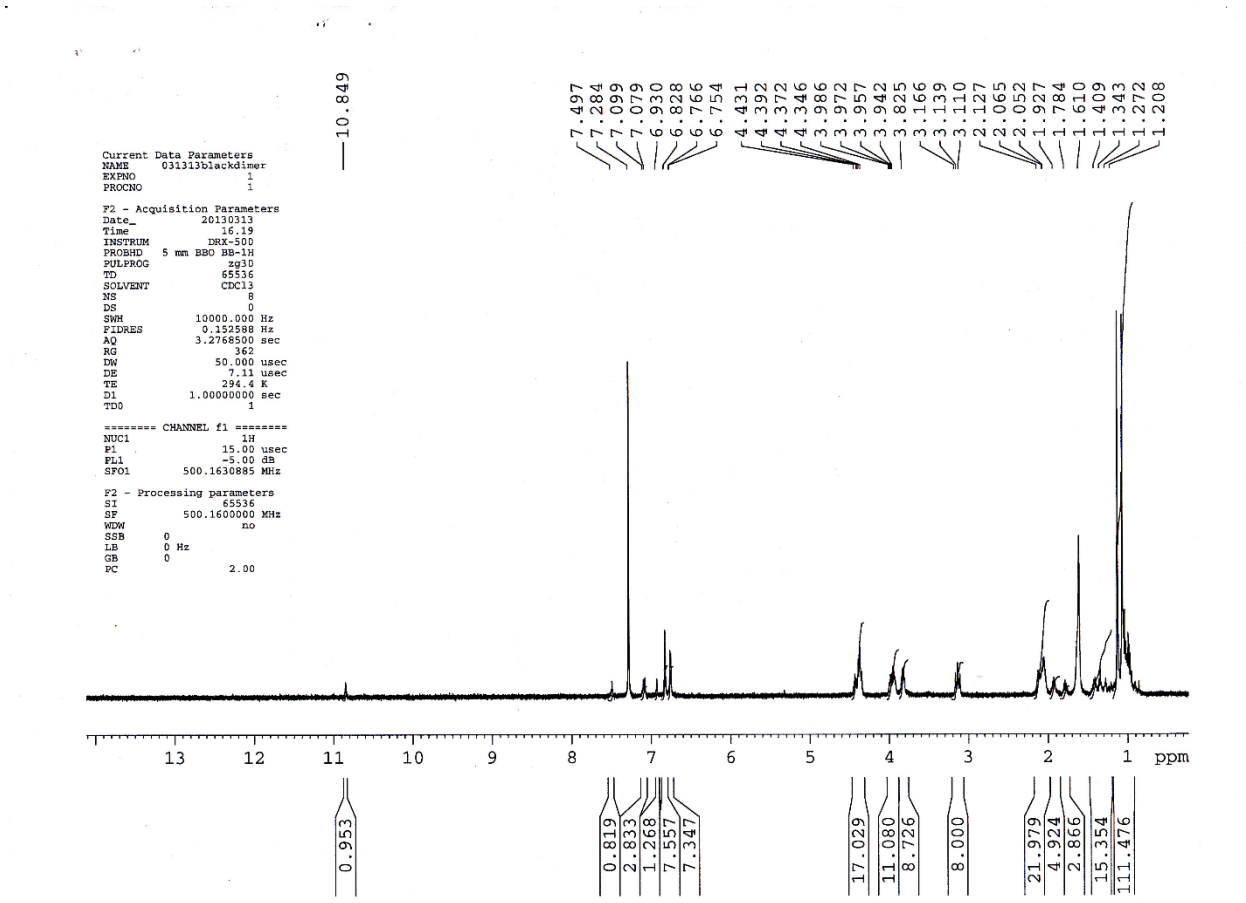

Figure 5.S.14: ^{1}H NMR spectra of **D1** ($CDCl_3$)

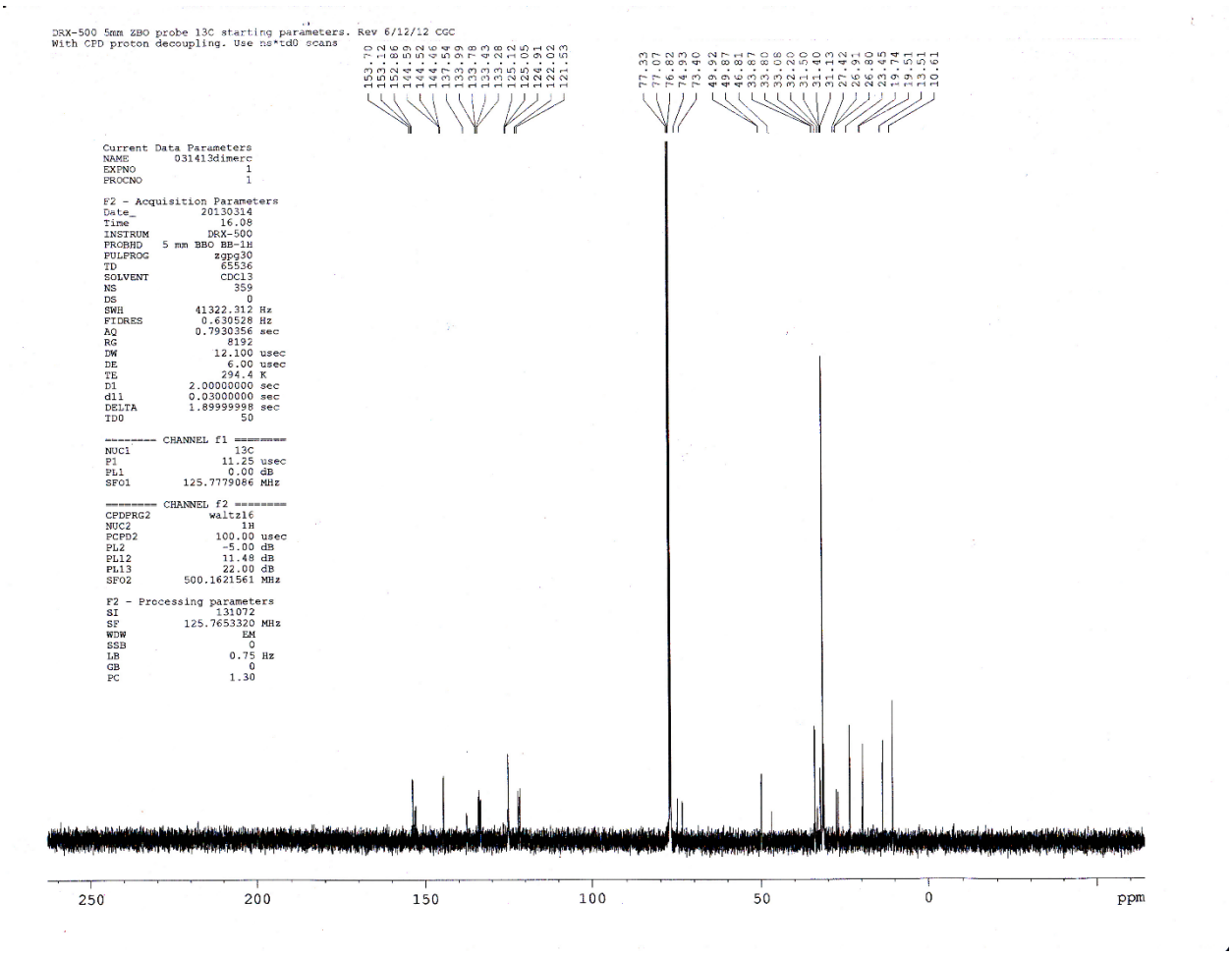

Figure 5.S.15: ^{13}C NMR spectra of **D1** ($CDCl_3$)

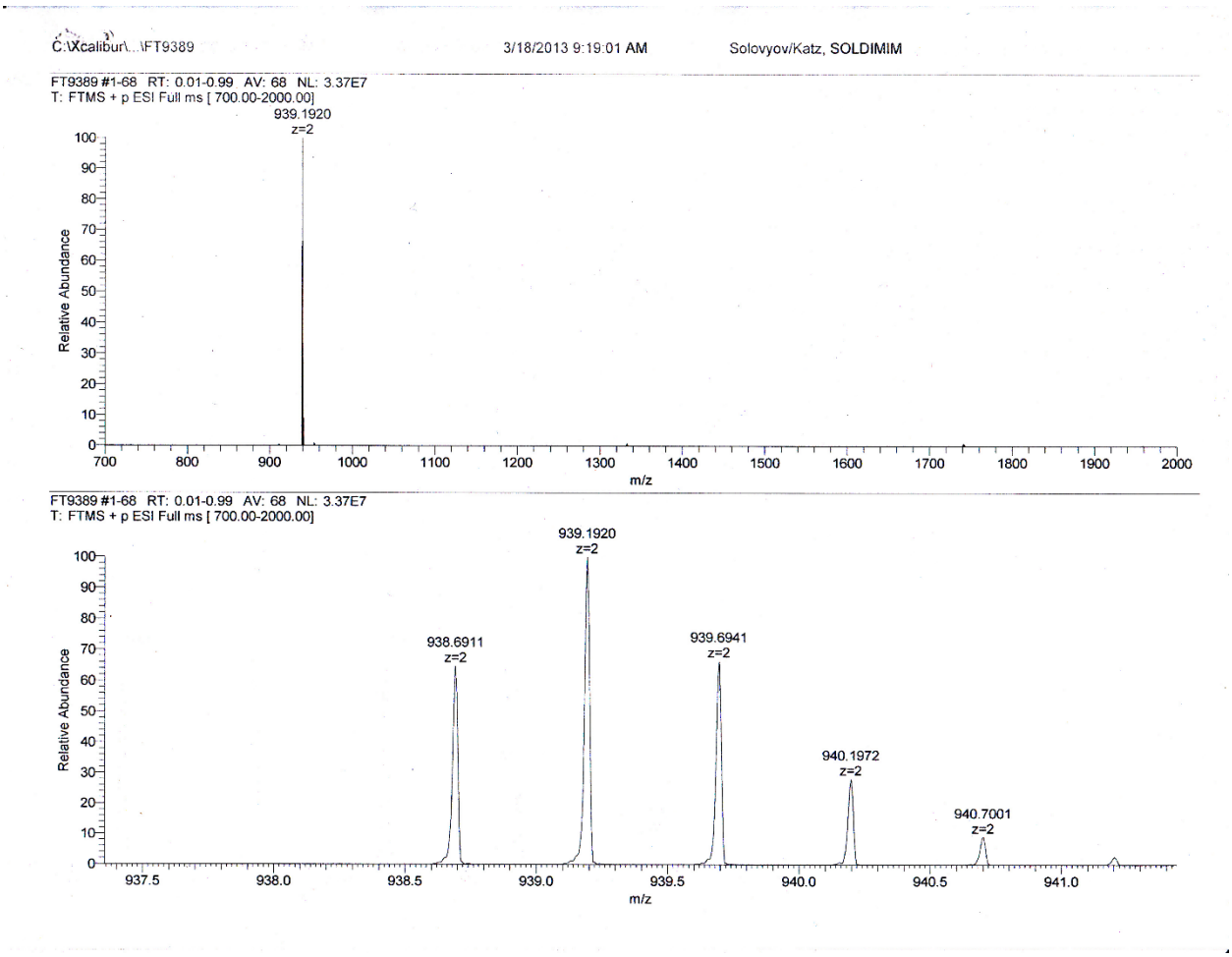

Figure 5.S.16: +ESI MS spectra of **D1**

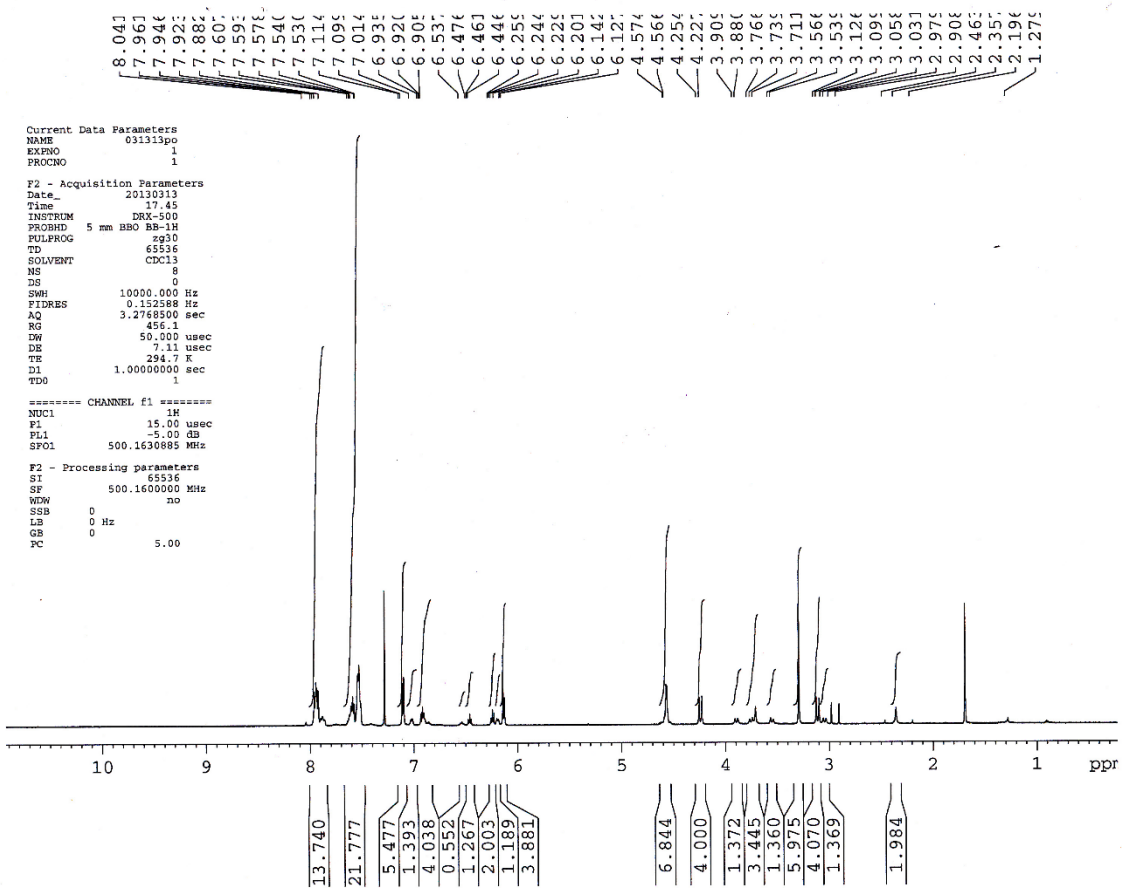

Figure 5.S.17: ^{1}H NMR spectra of **7b** ($CDCl_3$)

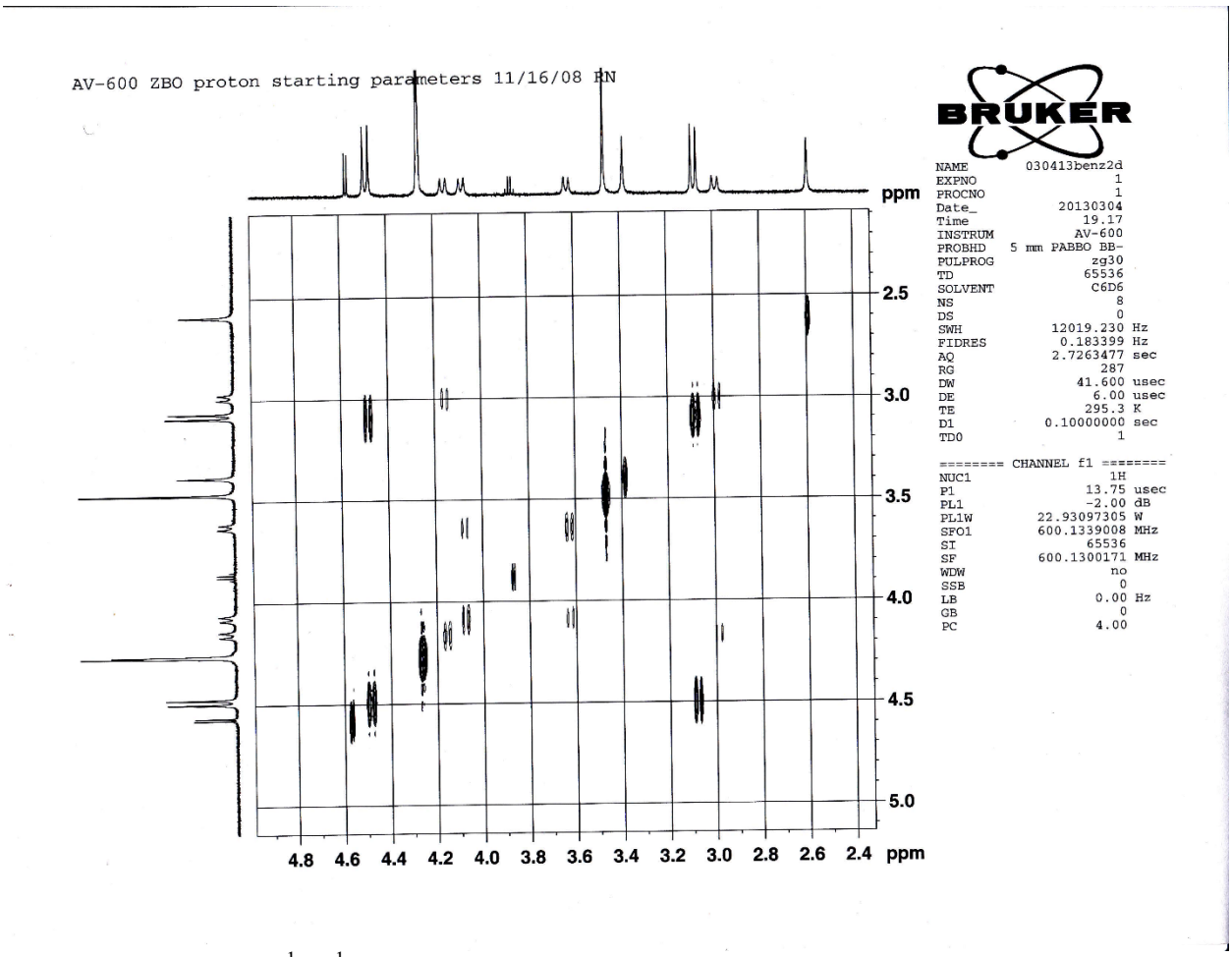

Figure 5.S.18: ^{1}H-^{1}H 2D COSY NMR spectra of **7b** (methylene region) (C_6D_6)

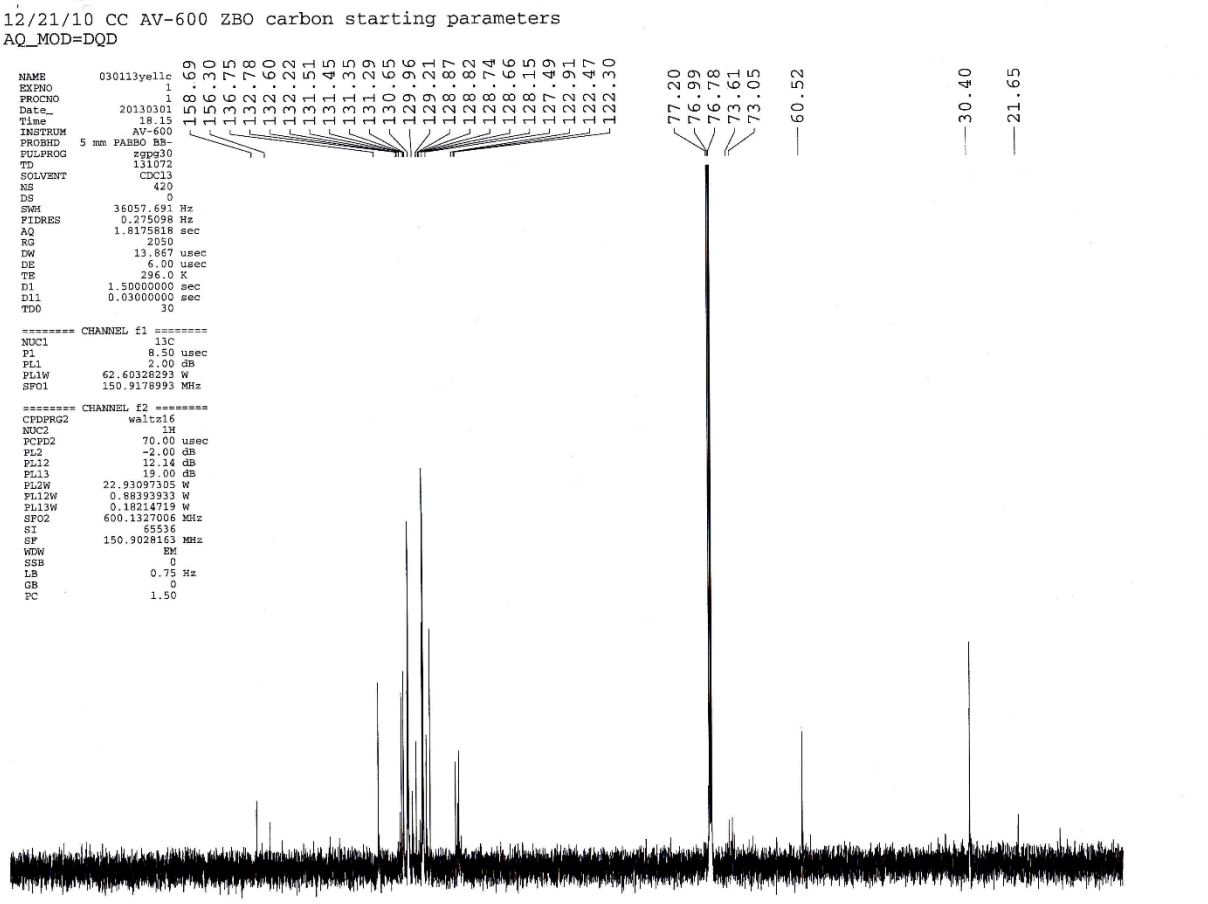

Figure 5.S.19: ^{13}C NMR spectra of **7b** ($CDCl_3$)

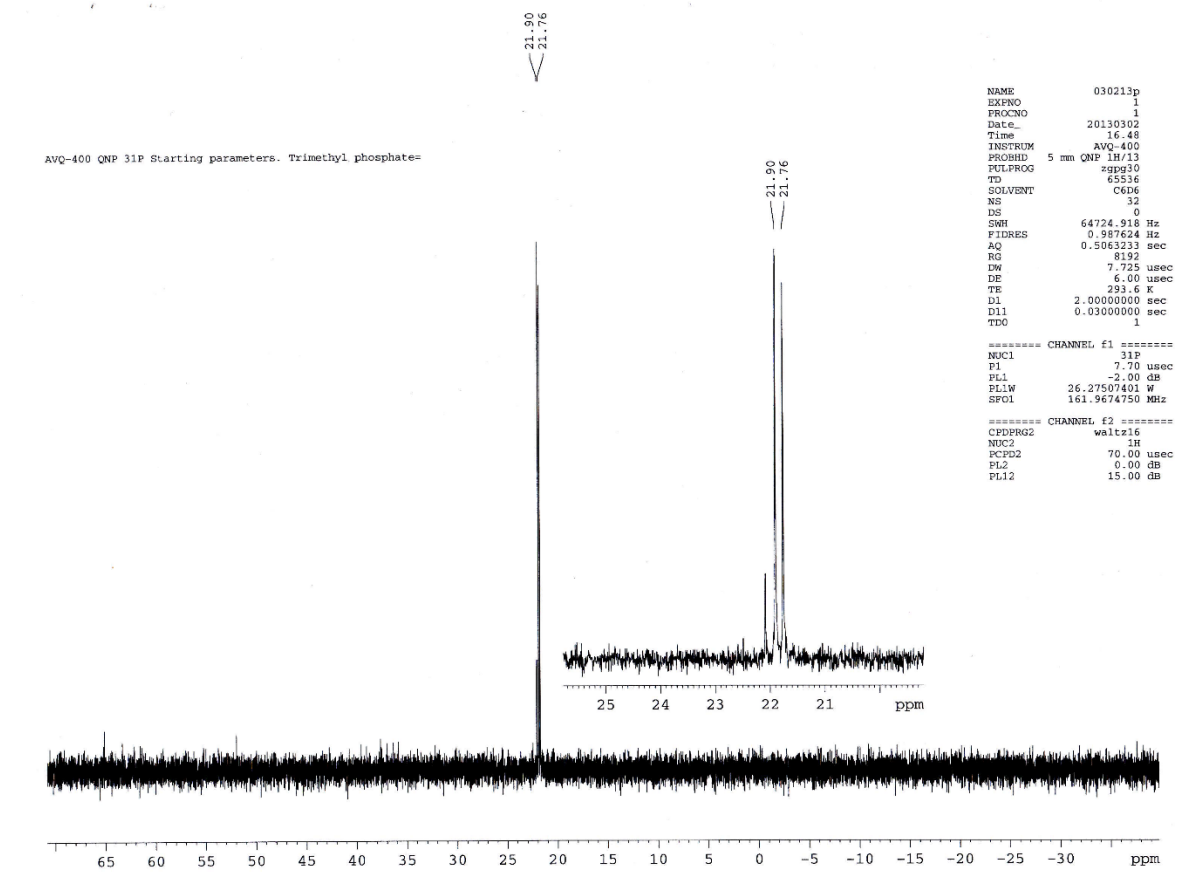

Figure 5.S.20: ^{31}P NMR spectra of **7b** (C_6D_6)

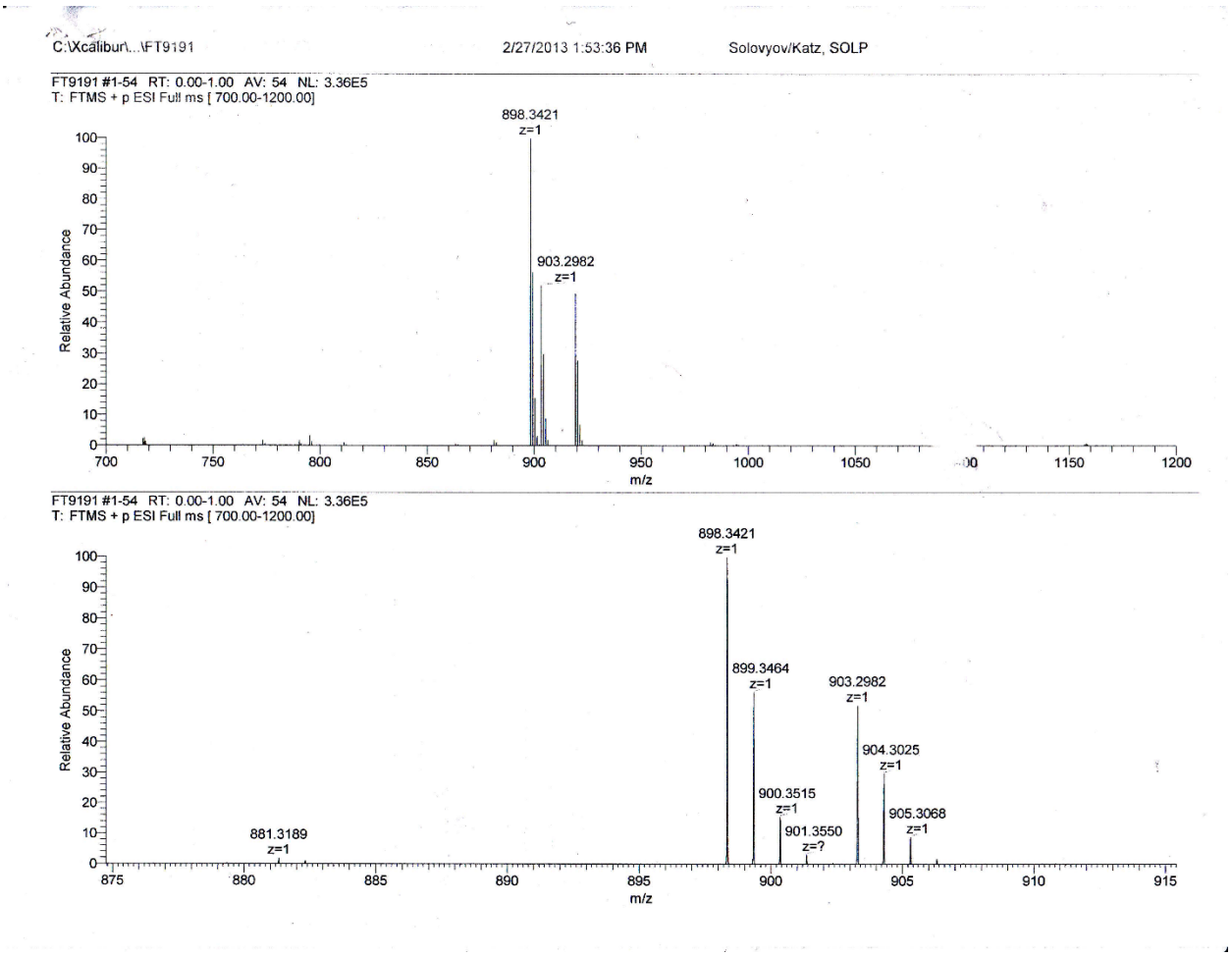

Figure 5.S.21: +ESI MS spectra of **7b**

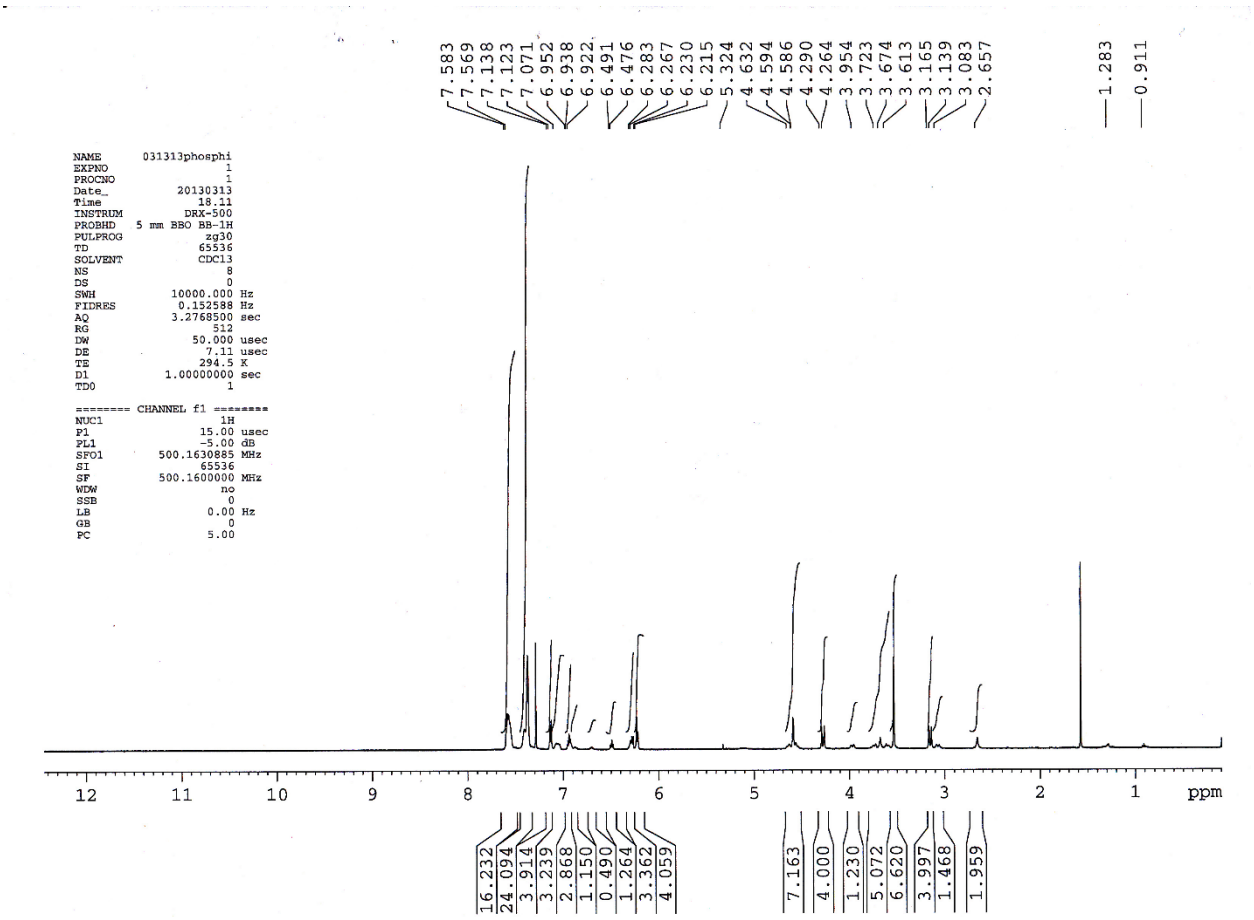

Figure 5.S.22: ^{1}H NMR spectra of **H1** ($CDCl_3$)

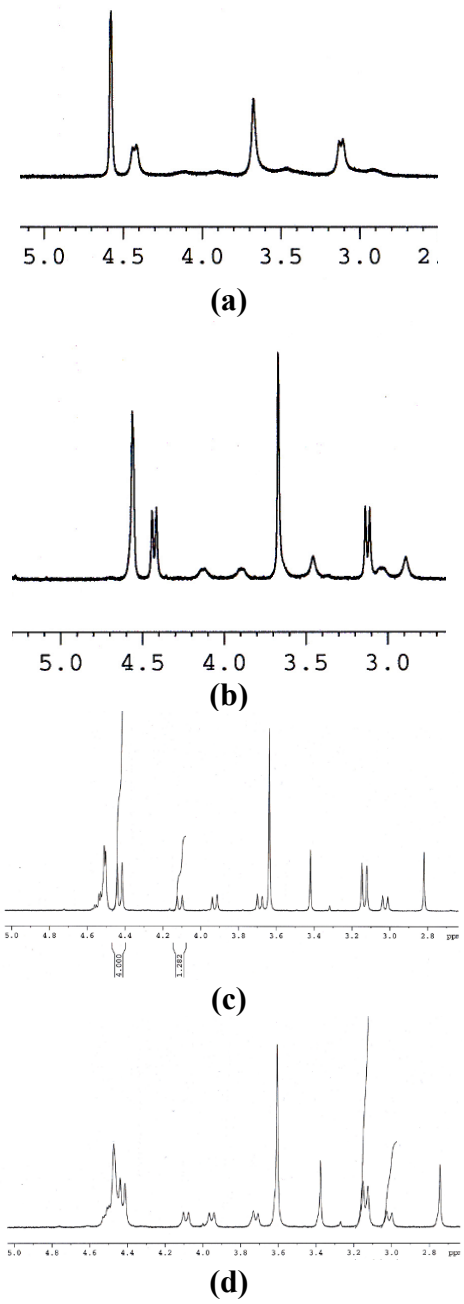

Figure 5.S.23: ^{1}H NMR spectra of **H1** (methylene bridges region) (toluene-d_8) at 323K (**a**), 303K (**b**), 253K(**c**), 213K (**d**)

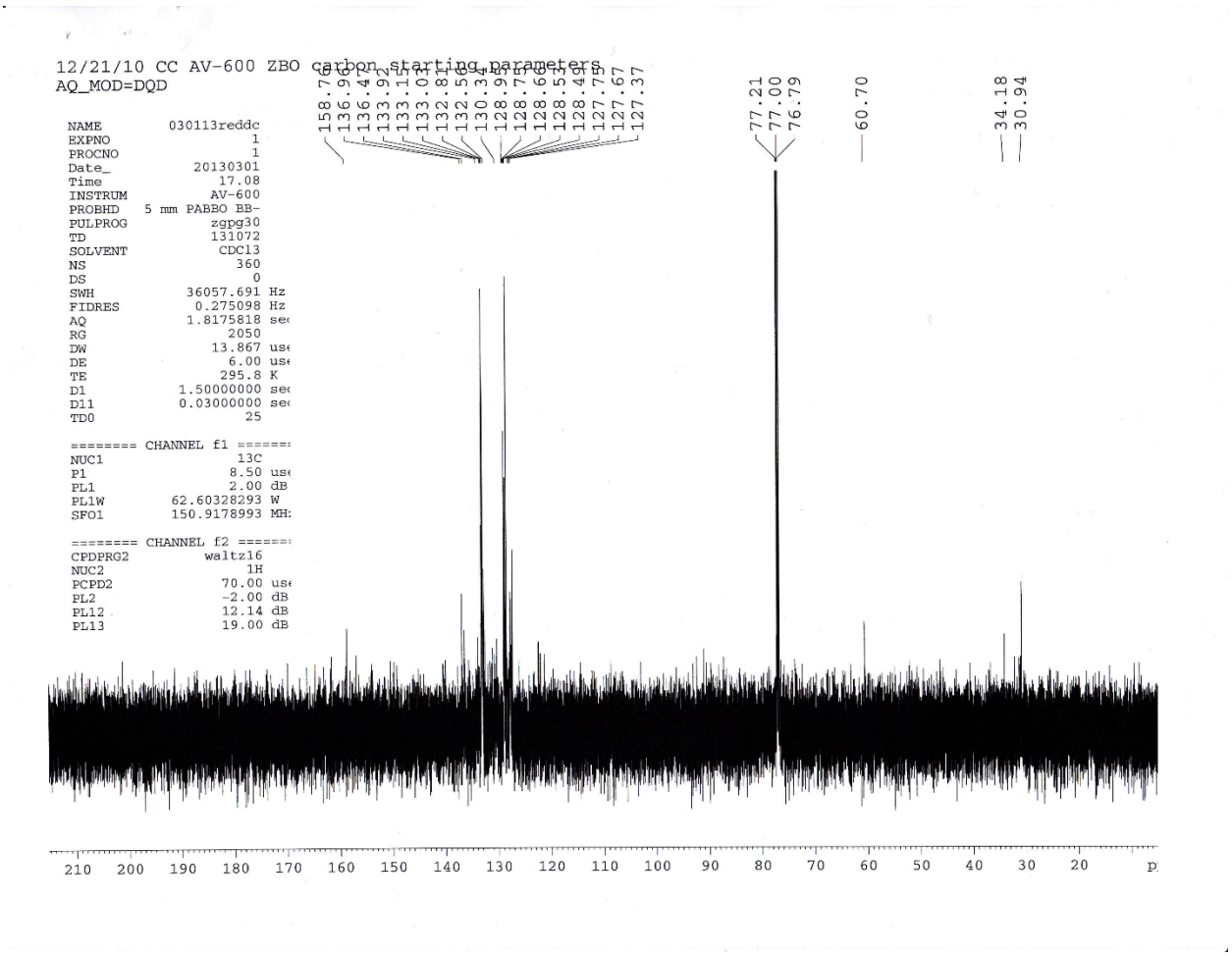

Figure 5.S.24: ^{13}C NMR spectra of **H1** ($CDCl_3$)

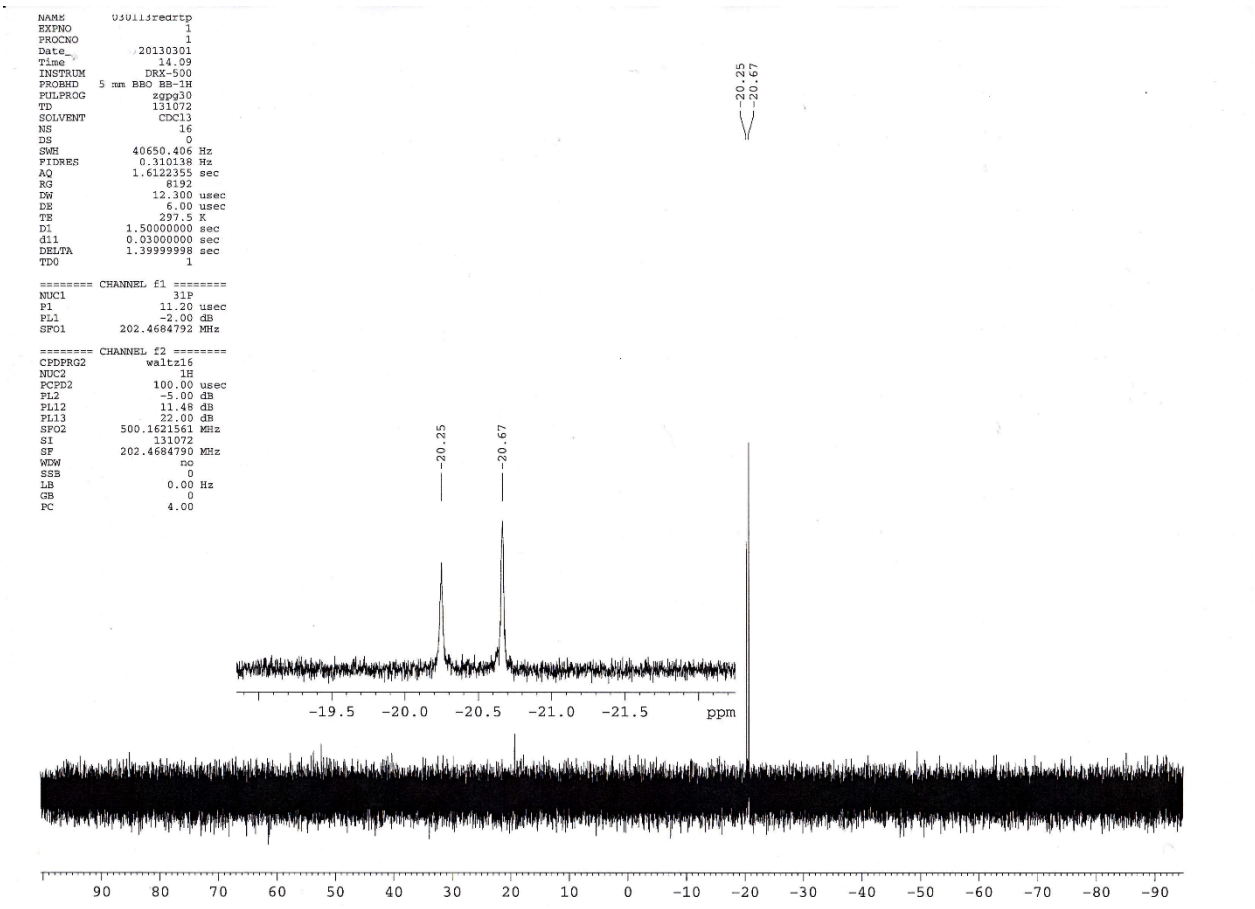

Figure 5.S.25: ^{31}P NMR spectra of **H1** ($CDCl_3$)

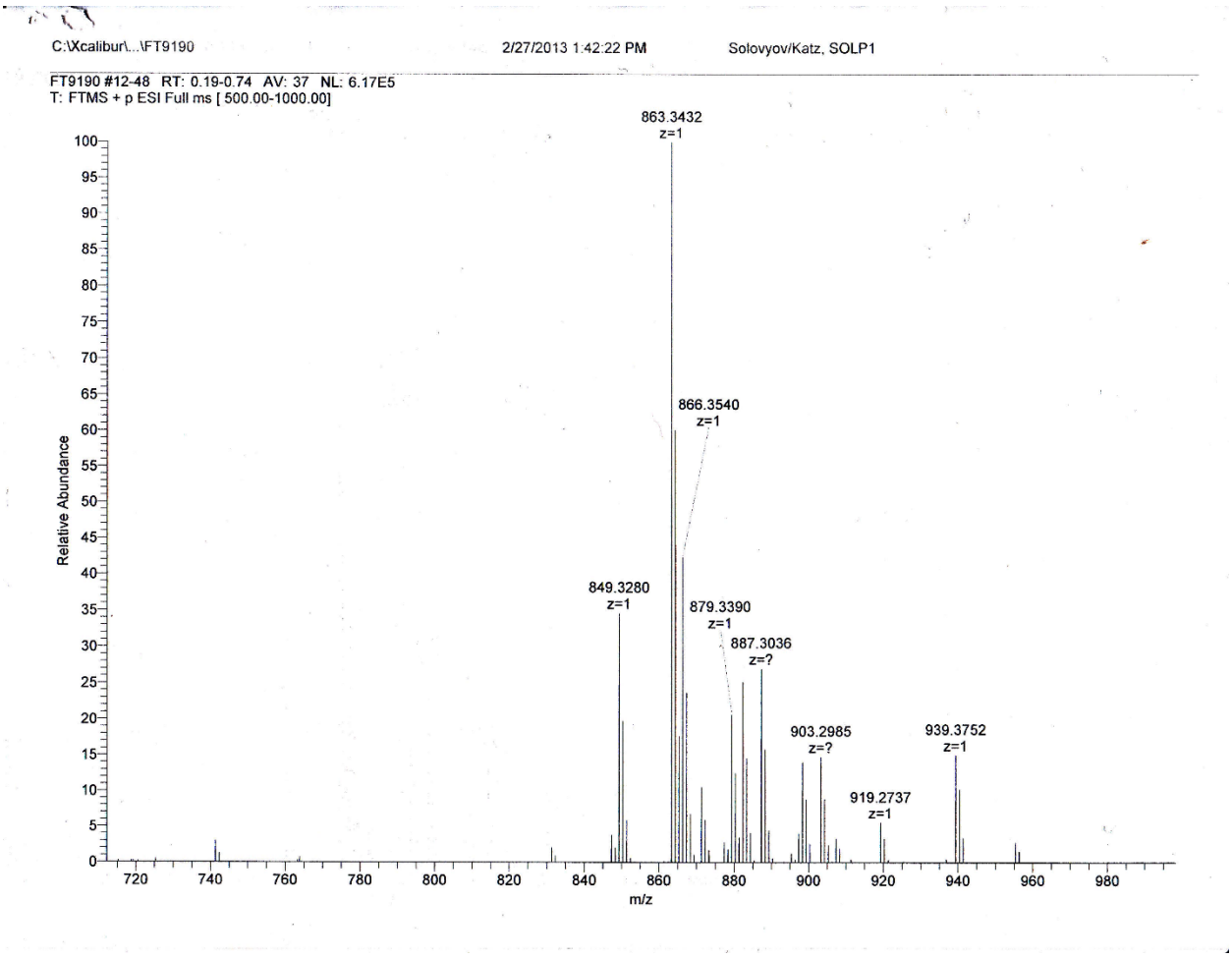

Figure 5.S.26: +ESI MS spectra of **H1**

5.9.2: Synthesis of Au-calixarene complexes with NMR and ESI-MS characterization

5.9.2.1 Synthesis and characterization of **H1G**

300 mg (0.35 mmol) ligand were dissolved in 10 mL dichloromethane and 210 mg (0.71 mmol). Me_2SAuCl were added in the dark. The mixture was stirred in the dark for 45 min. The solution was then filtered through celite and the solvent was evaporated. The obtained product was filtered a second time through celite and the solvent was evaporated. The product was purified via column chromatography (Selecto , dichloromethane : ethylacetate = 2 : 1). ^{1}H NMR (600 MHz, toluene-d_8) δ 7.47 (m, 8H, C_6H_5P), 7.10 (m, 12H, C_6H_5P), 6.91 (m, 6H, ArH), 6.31 (m, 6H, ArH), 4.33 (s, 4H, CH_2P), 4.09 (d, 4H, ^{2}J=13.2 Hz, $ArCH_2Ar$), 3.67 (s, 6H, OCH_3), 2.99 (d, 4H, ^{2}J=13.2 Hz, $ArCH_2Ar$); ^{31}P NMR (toluene-d_8) δ 24.22, 24.44; HR MS TOF $C_{56}H_{50}Au_2Cl_2O_4P_2Na^+$ m/z calculated: 1335.1785, observed: 1335.1819 Single crystals were obtained through slow evaporation of a acetonitrile:DCM solution (4:1) of **H1G**.

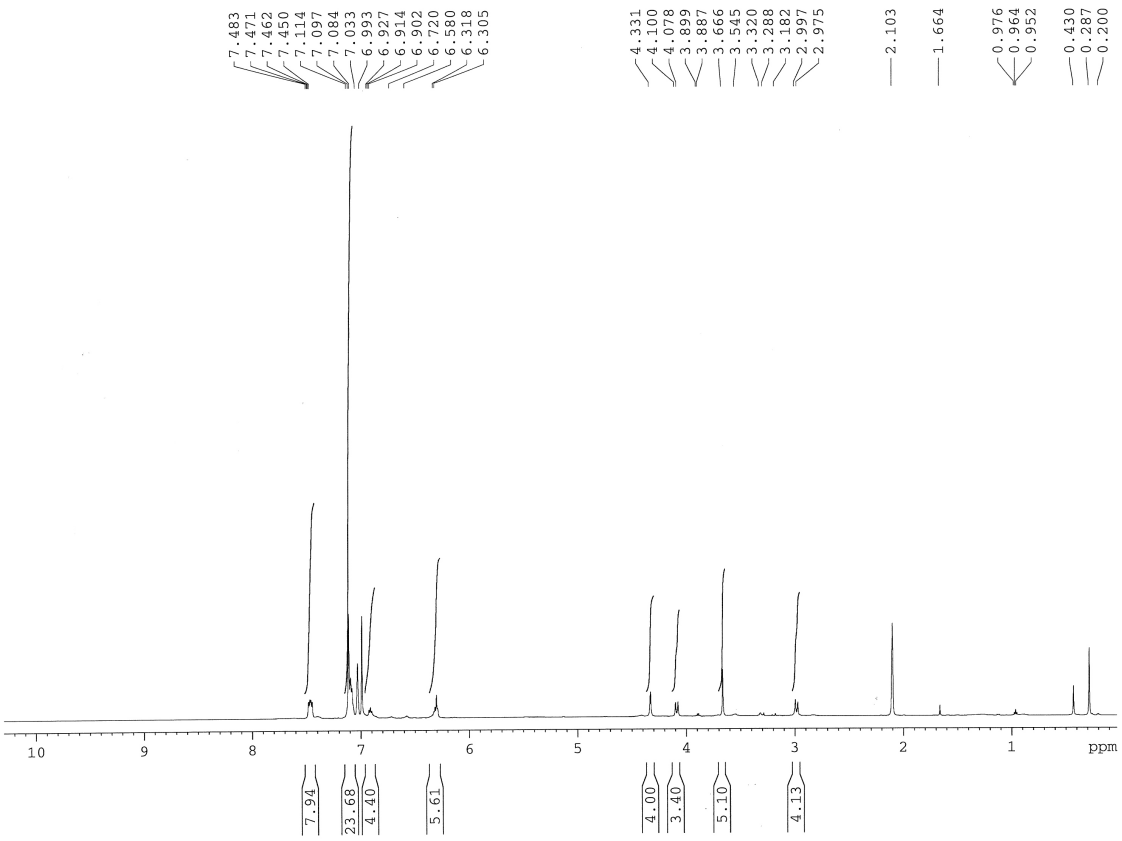

Figure 5.S.27: ^{1}H NMR of **H1G** in toluene-d_8 solvent

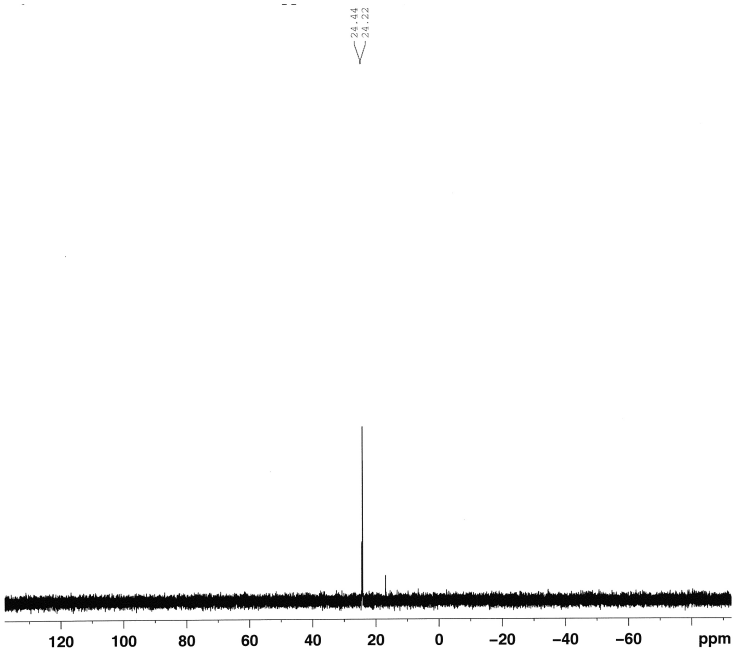

Figure 5.S.28: ^{31}P NMR of **H1G** in toluene-d_8 solvent

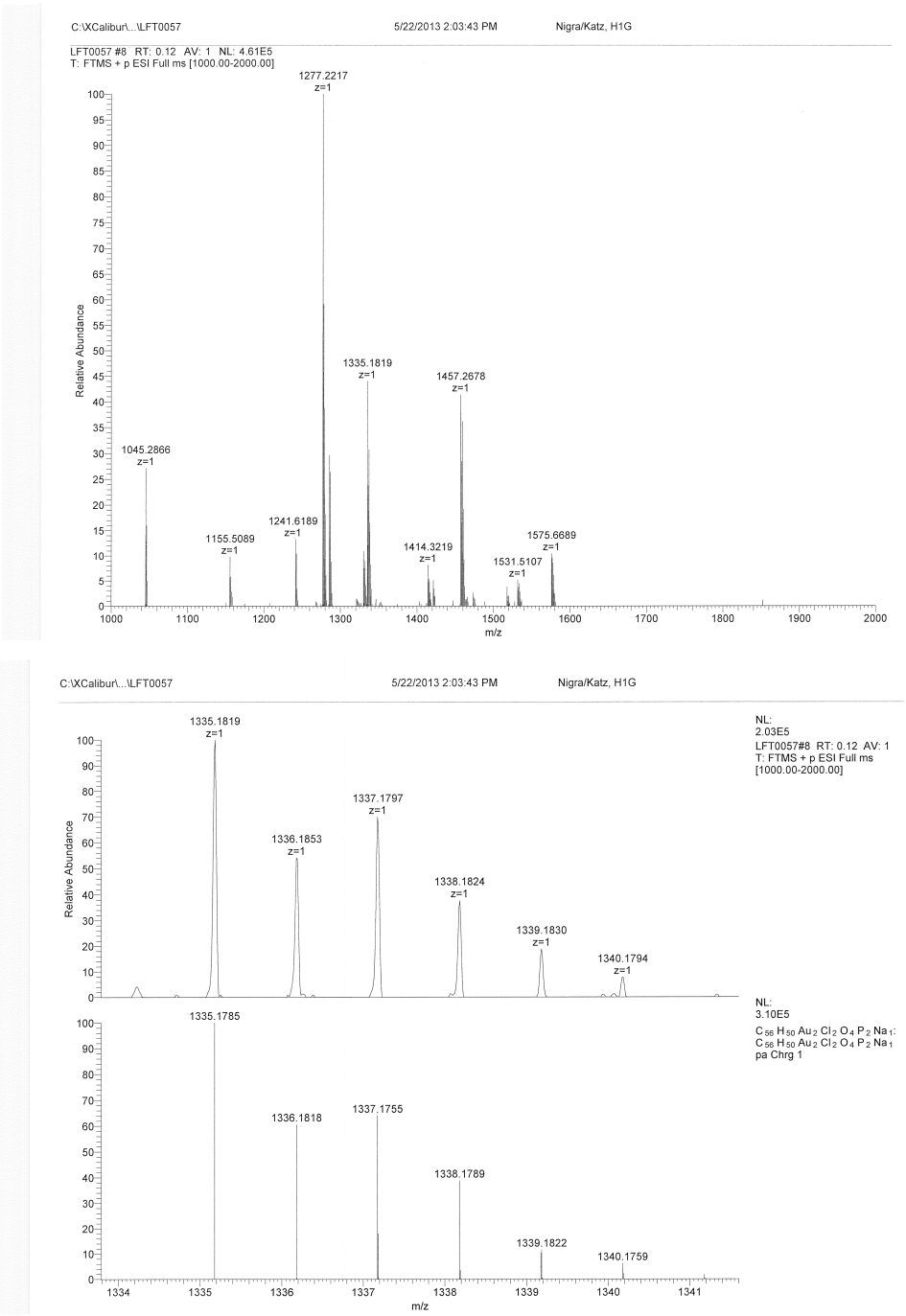

Figure 5.S.29: ESI-MS (+) of **H1G.** Full range spectrum (top), relevant region zoom (middle) simulated spectrum (bottom)

Single-crystal X-ray measurements were completed at the UC Berkeley College of Chemistry X-ray crystallography facility. CCDC #952001 contains the supplementary crystallographic data **H1G**. These data can be obtained free of charge from The Cambridge Crystallographic Data Centre via www.ccdc.cam.ac.uk/data_request/cif Figure 5.S.30 illustrates the 2 molecules of **H1G** located in the unit cell in overlay of the two molecules.

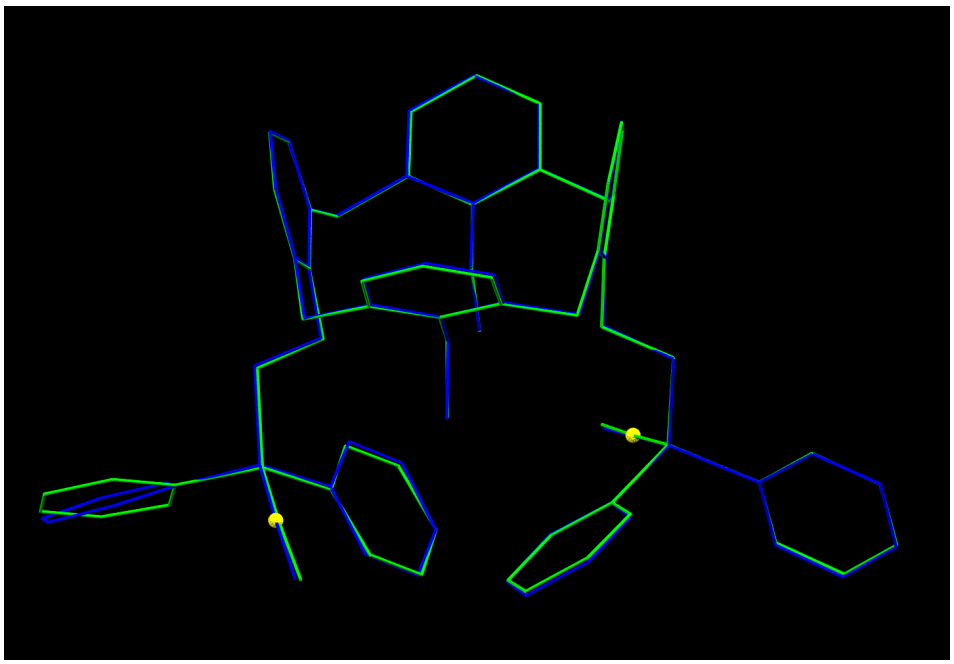

Figure 5.S.30: RMS optimized overlay of the two independent molecules (green = molecule 1; blue = inverted molecule 2) from the X-ray crystal structure of **H1G**. Au atoms highlighted as yellow spheres.

5.9.2.2 Synthesis and characterization of **T1G**

The synthesis and characterization rigorously followed the procedures developed by Katz *et al*. in *Nature Chemistry*, 2010, 2, 1062-1068. Characterization data was identical to the data published.

5.9.2.3 Synthesis and characterization of **C1G**

100 mg (0.08 mmol) ligand were dissolved in 10 mL dichloromethane and 40 mg (0.17 mmol) Ag_2O were added in the dark. The solution was stirred for 15 h and was subsequently filtered through celite. 47 mg (0.16 mmol) Me_2SAuCl were added to the obtained colorless solution. The mixture was stirred in the dark for 1 h. The solution was then filtered through celite and the solvent was evaporated. The obtained product was purified via column chromatography (Selecto , dichloromethane : ethylacetate = 5 : 1). The product is a white powder. ^{1}H NMR (400 MHz, $CDCl_3$) δ 7.04 (s, 2H, ImH), 6.97 (s, 2H, ImH), 6.89 (m, 4H, ArH), 6.67 (m, 4H, ArH), 4.35 (d, 4H, ^{2}J=12.4 Hz, $ArCH_2Ar$), 4.28 (t, 4H, ^{3}J=7.6 Hz, NCH_2), 4.17 (t, 4H, ^{3}J=7.2 Hz, OCH_2), 3.94 (t, 4H, ^{3}J=7.6 Hz, NCH_2), 3.76 (t, 4H, ^{3}J=7.2 Hz, OCH_2), 3.13 (d, 4H, ^{2}J=12.4 Hz, $ArCH_2Ar$), 2.13 (m, 4H, CH_2), 1.97 (m, 8H, CH_2), 1.84 (m, 4H, CH_2), 1.37 (m, 4H, CH_2), 1.16 (s, 18H, t-C_4H_9), 1.05 (m, 6H, CH_3), 1.00 (s, 18H, t-C_4H_9), 0.96 (m, 6H, CH_3); HR MS TOF $C_{72}H_{104}Au_2Cl_2N_4O_4Na^+$, calculated: 1575.6658, actual: 1575.6695

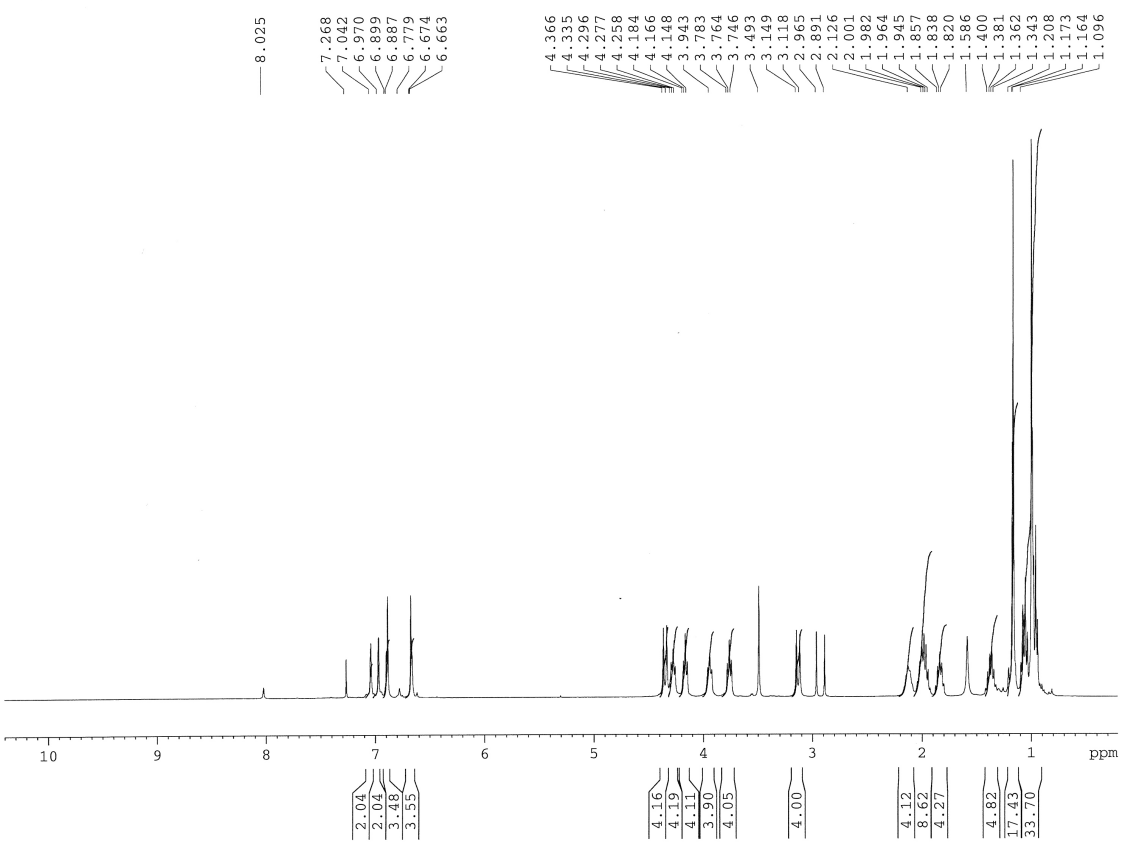

Figure 5.S.31: ^{1}H NMR of **C1G** ($CDCl_3$)

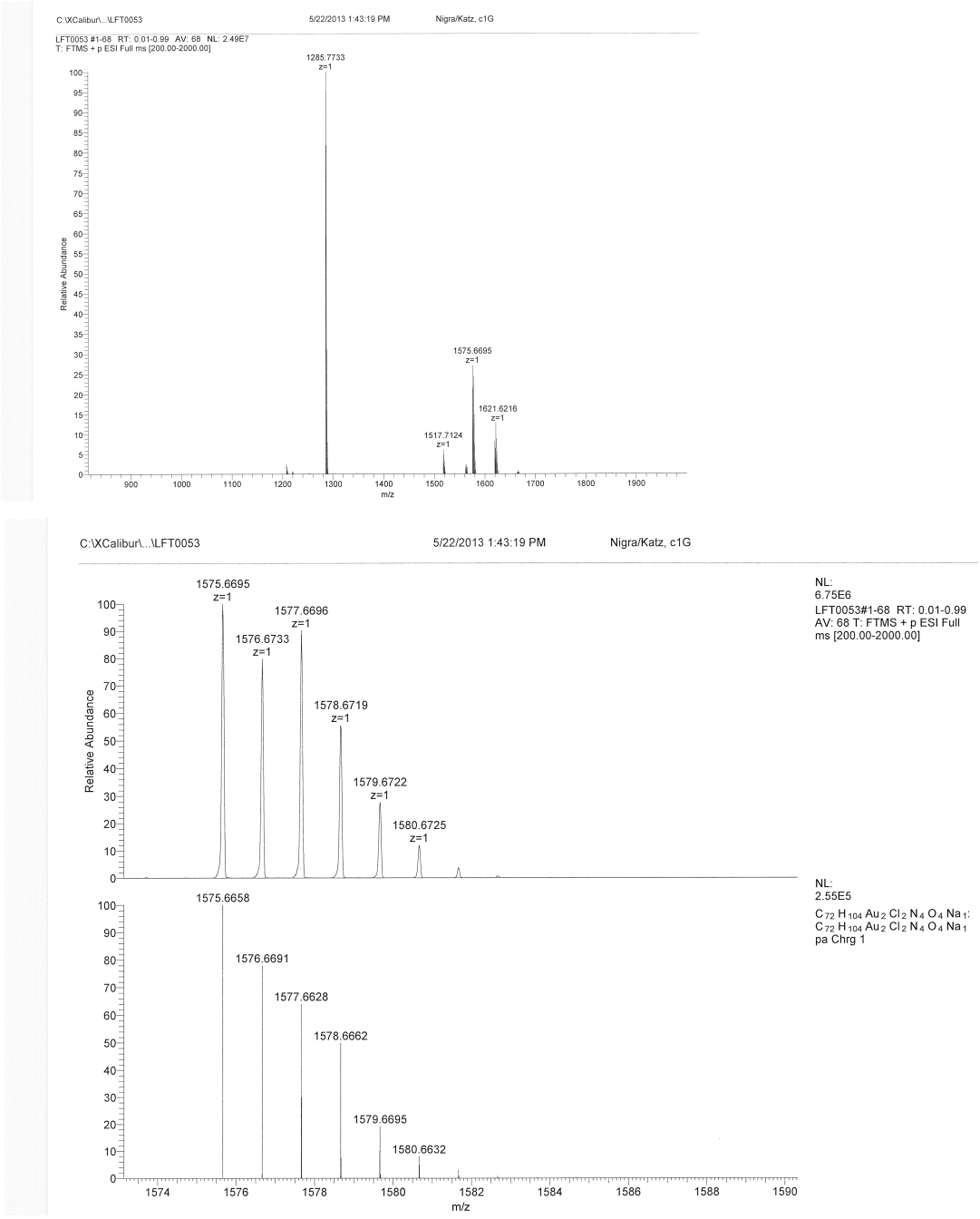

Figure 5.S.32 ESI-MS (+) of **C1G**. Full range spectrum (top), relevant region zoom (middle) simulated spectrum (bottom)

5.9.2.4 Synthesis and characterization of **C2G:**

125 mg (0.097 mmol) ligand **C2** were dissolved in 10 mL dichloromethane and 40 mg (0.17 mmol) Ag_2O were added in the dark. The solution was stirred for 15 h and was subsequently filtered through celite. 57 mg (0.19 mmol) Me_2SAuCl were added to the obtained

colorless solution. The mixture was stirred in the dark for 1 h. The solution was then filtered through celite and the solvent was evaporated. The obtained product was purified via column chromatography (Selecto , dichloromethane : ethylacetate = 5 : 1). The product is a white powder.

^{1}H NMR (400 MHz, $CDCl_3$) δ 7.65 (m, 4H, C_6H_5), 7.45 (m, 6H, C_6H_5), 7.26 (s, 2H, ImH), 7.20 (m, 2H, ImH), 7.00 (s, 4H, ArH), 6.60 (s, 4H, ArH), 4.50 (m, 4H+4H, $ArCH_2Ar$+NCH_2), 4.10 (m, 4H, OCH_2), 3.75 (m, 4H, OCH_2), 3.20 (d, 4H, ^{2}J=12.4 Hz, $ArCH_2Ar$), 2.25 (m, 4H, CH_2), 2.15 (m, 4H, CH_2), 1.95 (m, 4H, CH_2), 1.25 (s, 18H, t-C_4H_9), 1.10 (t, 6H, ^{3}J=7.2 Hz, CH_3), 0.95 (s, 18H, t-C_4H_9); HR MS TOF $C_{76}H_{96}Au_2Cl_1N_4O_4$, calculated: 1557.6646, actual: 1577.6646.

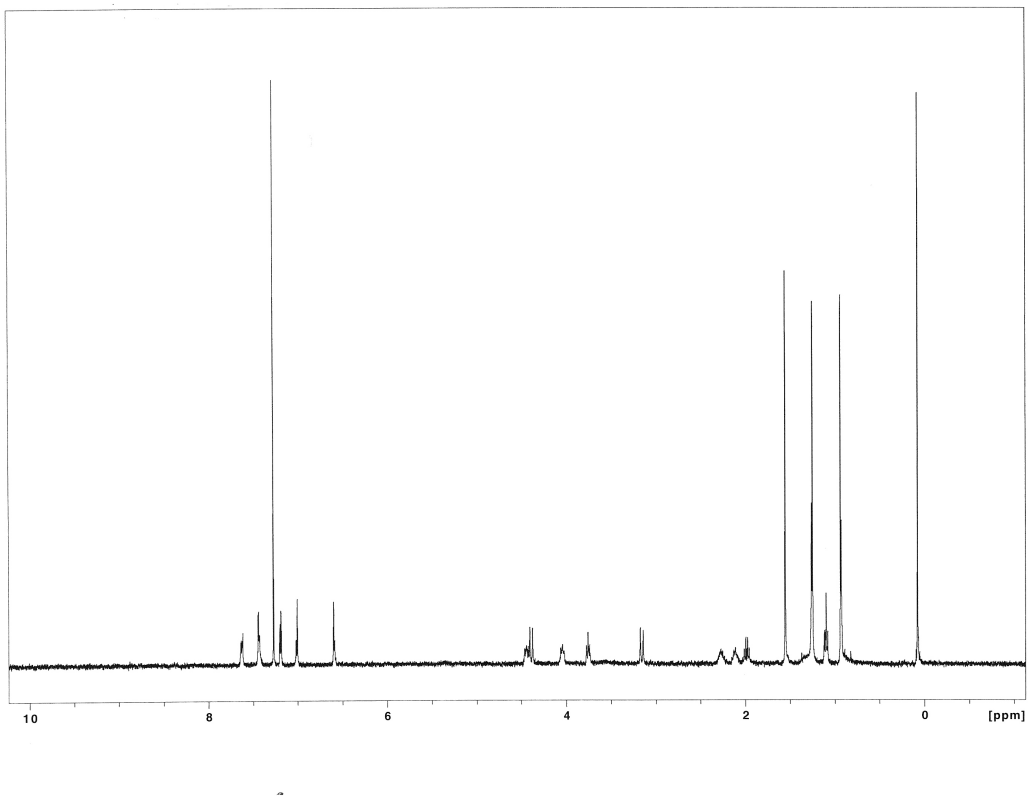

Figure 5.S.33: ^{1}H NMR data for **C2G**. ($CDCl_3$)

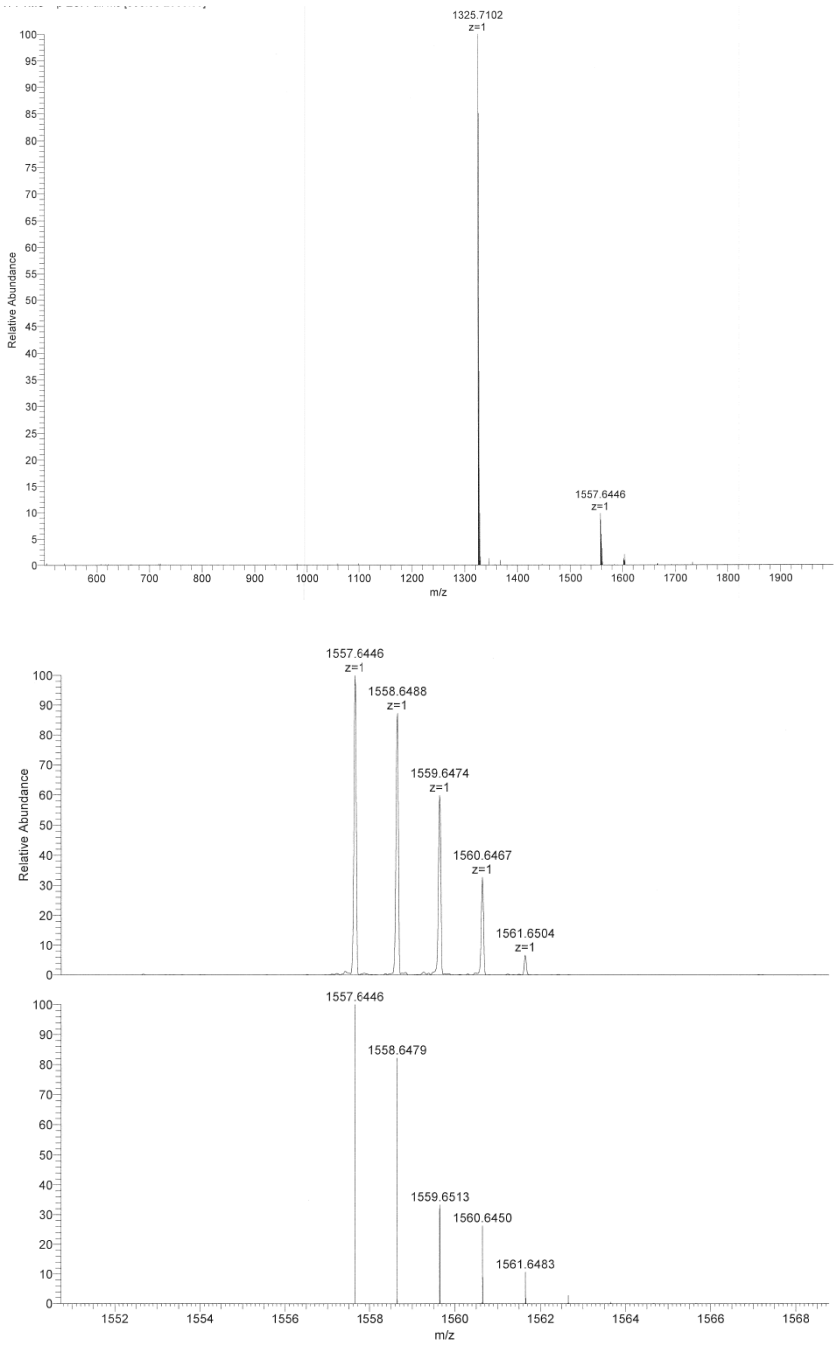

Figure 5.S.34: ESI-MS (+) data for **C2G**. Full range spectrum (top), relevant region zoom (middle) simulated spectrum (bottom)

5.9.2.5 Synthesis and Characterization of **C3G**

94 mg (0.08 mmol) ligand were dissolved in 10 mL dichloromethane and 22 mg (0.09 mmol) Ag_2O were added in the dark. The solution was stirred for 15 h and was subsequently filtered through celite. 46 mg (0.15 mmol) Me_2SAuCl were added to the obtained colorless solution. The mixture was stirred in the dark for 1 h. The solution was then filtered through celite and the solvent was evaporated. The obtained product was purified via column

chromatography (Selecto , dichloromethane : ethylacetate = 5 : 1). ^{1}H NMR (400 MHz, $CDCl_3$) δ 7.63 (m, 4H, C_6H_5), 7.47 (m, 6H, C_6H_5), 7.27 (s, 2H, ImH), 7.22 (s, 2H, ImH), 7.13 (br s, 4H, ArH), 6.49 (br s, 4H, ArH), 2.56, 3.19, 3.90, 4.07, 4.28, 4.66 (six br s, 26H, CH_2+OCH_3), 1.34 (s, 18H, t-C_4H_9), 1.05, 0.86 (two br s, 18H, t-C_4H_9); HR ES MS: $C_{70}H_{84}Au_2Cl_1N_4O_4^+$ m/z calculated 1473.5507, actual 1473.5518

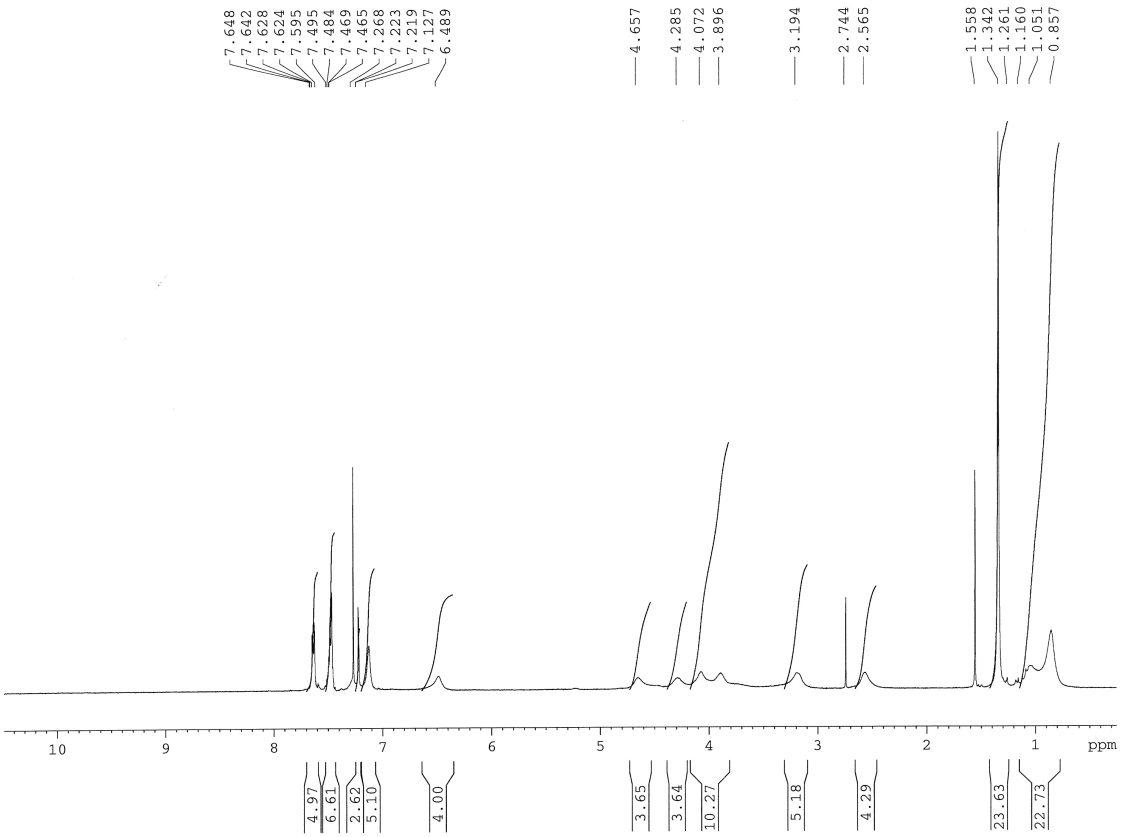

Figure 5.S.35: ^{1}H NMR of **C3G** ($CDCl_3$)

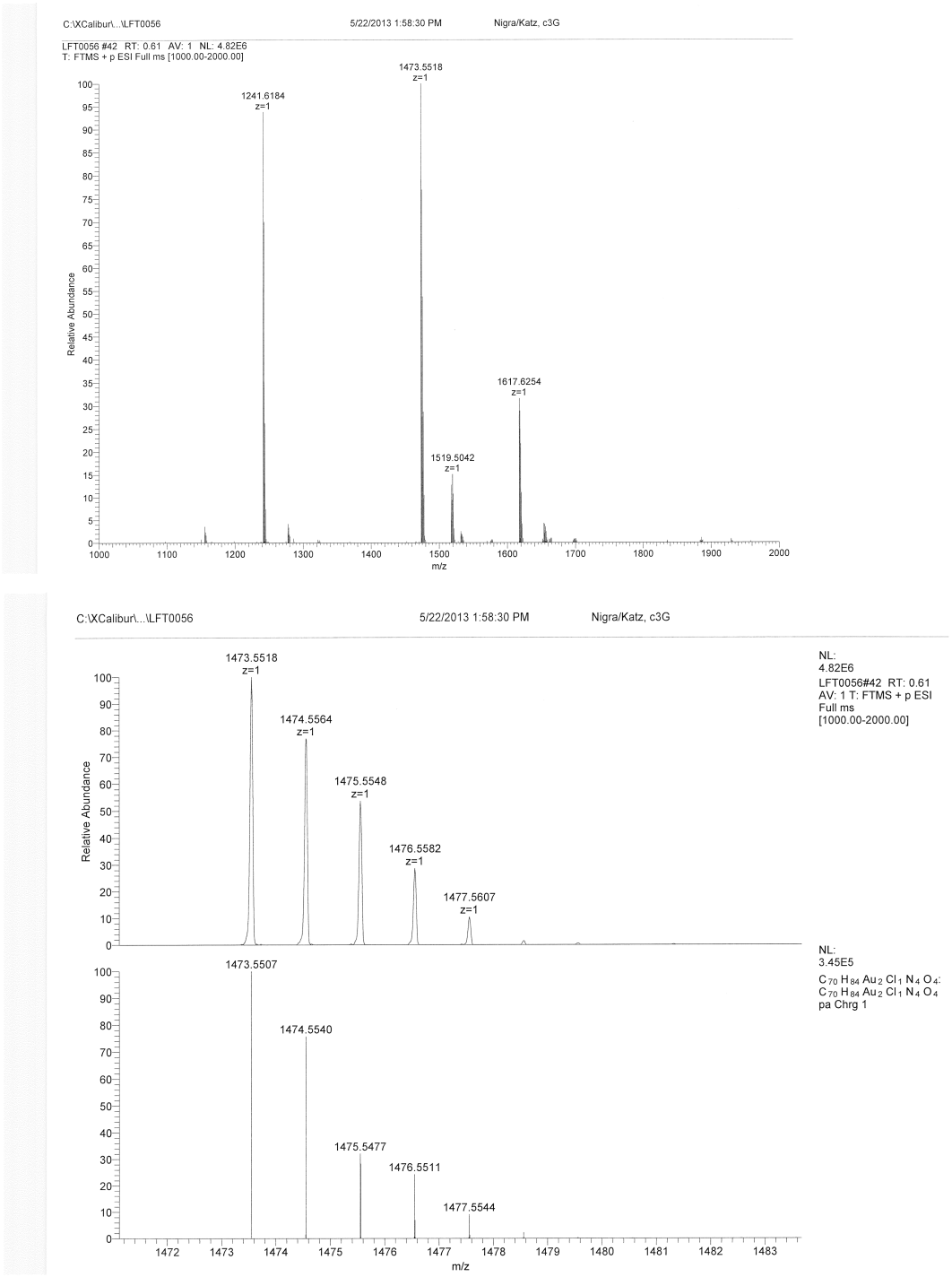

Figure 5.S.36: ESI-MS (+) of **C3G.** Full range spectrum (top), relevant region zoom (middle) simulated spectrum (bottom)

5.9.2.6 Synthesis and Characterization of **D1G**

235 mg (0.11 mmol) ligand were dissolved in 10 mL dichloromethane and 32 mg (0.14 mmol) Ag_2O were added in the dark. The solution was stirred for 15 h and was subsequently

filtered through celite. 68 mg (0.23 mmol) Me_2SAuCl were added to the obtained colorless solution. The mixture was stirred in the dark for 1 h. The solution was then filtered through celite and the solvent was evaporated. The obtained product was purified via column chromatography (Selecto G60, dichloromethane : ethylacetate = 5 : 1). ^{1}H NMR (400 MHz, $CDCl_3$) δ 6.88 (d, 2H, ^{3}J=2.0 Hz, ImH), 6.86 (s, 8H, ArH), 6.82 (d, 2H, ^{3}J=2.0 Hz, ImH), 6.69, 6.72 (two s, 4H+4H, ArH), 4.34, 4.38 (two d, 4H+4H, ^{2}J=12.4 Hz, $ArCH_2Ar$), 4.14 (m, 8H, CH_2), 3.83 (m, 16H, CH_2), 3.12, 3.13 (two d, 4H+4H, ^{2}J=12.4 Hz, $ArCH_2Ar$), 1.97, 2.04, 2.11 (three m, 18H, CH_2), 1.81 (m, 4H, CH_2), 1.34 (m, 8H, CH_2), 1.15 (s, 36H, t-C_4H_9), 1.02 (s, 36H, t-C_4H_9), 0.95 (m, 18H, CH_3); $C_{126}H_{178}Au_2Cl_2N_4O_8Na^+$, calculated: 2365.27 actual: 2365.24.

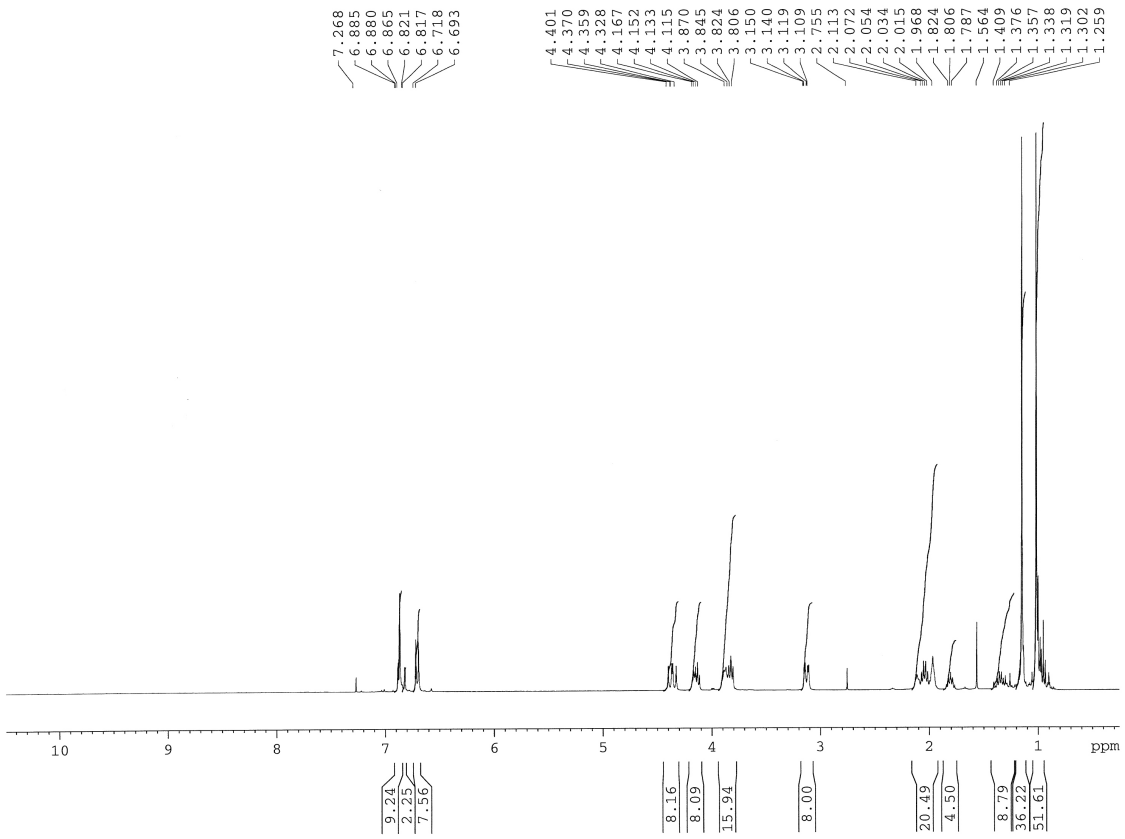

Figure 5.S.37 ^{1}H NMR of **D1G** ($CDCl_3$)

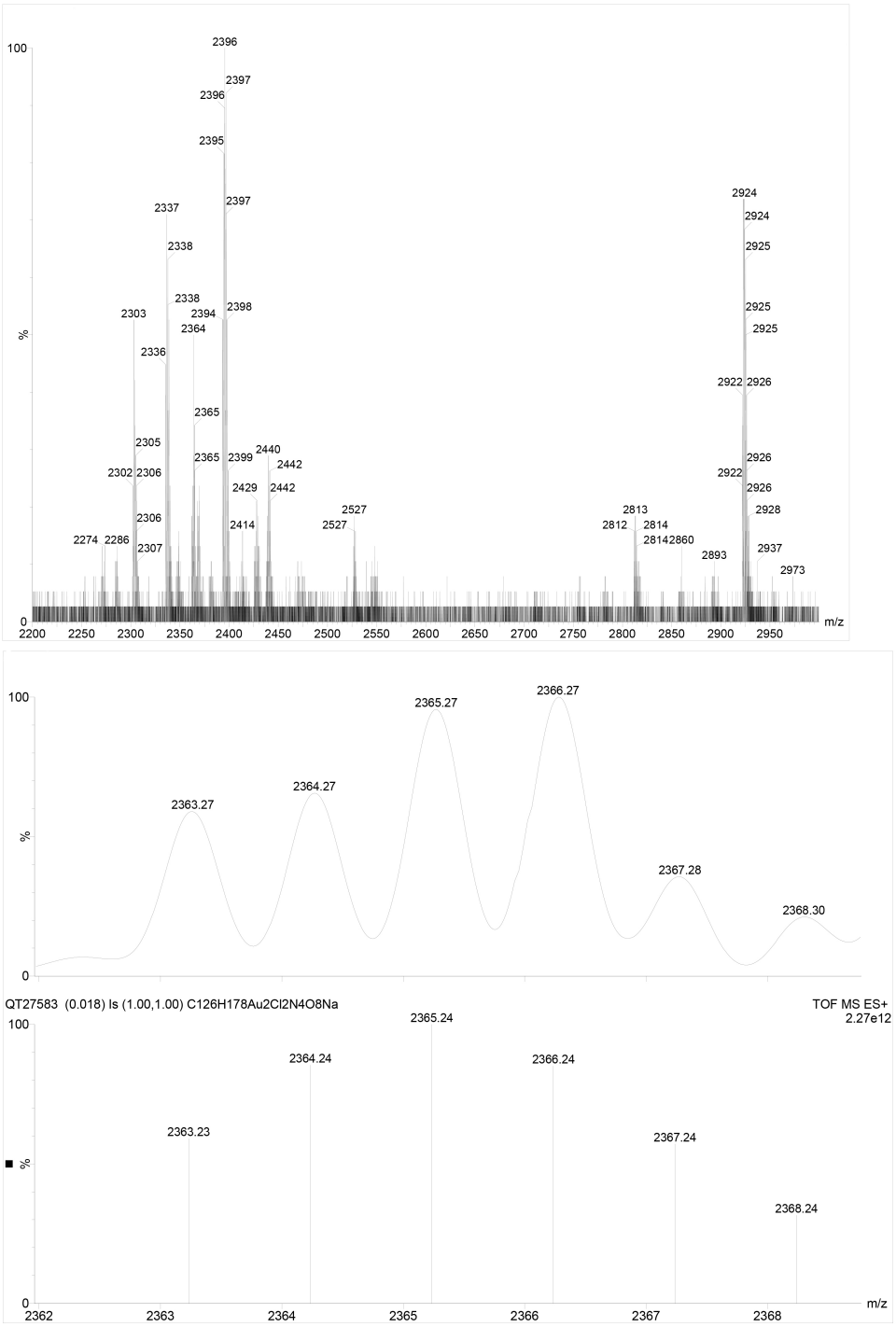

Figure 5.S.38: ESI-MS (+) of **D1G** Full range spectrum (top), relevant region zoom (middle) simulated spectrum (bottom).

5.9.3 Synthesis of Au(I) clusters by reduction of Au(I) complexes

Based on reduction procedures to synthesize calix[4]arene phosphine-bound Au clusters,[8] the following method was used to synthesize small Au clusters. A 2.0 mM suspension of an Au(I) complex (**C1G**, **C2G**, **C3G**, **D1G** or **H1G**) was suspended in anhydrous ethanol. (Aldrich)

4 eq. of sodium borohydride relative to Au atoms (Aldrich, 99.7%) was added to this suspension and stirred vigorously for 40 minutes at room temperature. The ethanol was evaporated *in vacuo*, and the resulting solid was washed with 100 mL of deionized water (18 MΩ) and then washed with 2 mL of hexane and filtered using vacuum filtration. The samples were dried overnight at room temperature under vacuum. An additional filtration was necessary for cluster **H1-red** where the sample was dissolved in dichloromethane and filtered through a syringe filter to remove the insoluble species. The solvent was then evaporated to recover the cluster. Yields for clusters are typically 20-50% of the initial Au(I) complex added.

5.9.4 UV-Vis characterization of Au clusters

Liquid phase UV-Vis measurements were recorded to characterize the reduced calixarene-bound Au(I) clusters. The clusters were dissolved in dichloromethane (Fisher, HPLC grade) to give a clear brown-colored solution. Absorption spectra were recorded from 700 to 350 nm with a step size of 0.5 nm and a time per data point of 0.166 s using a Varian Cary 4000 UV-Vis spectrometer at 25°C.

5.9.5 Transmission electron microscopy measurements of Au clusters

HAADF-STEM images were recorded using a 200kV F20 UT Tecnai electron microscope at the National Center for Electron Microscopy at Lawrence Berkeley National Laboratory. At least 200 particles were measured to obtain a particle size distribution. The samples were prepared by dissolving the cluster in dichloromethane and placing 2-3 drops on to a ultra-thin holey carbon coated copper grid (Ted Pella)

5.9.6 Fluorescence binding measurements

Based on procedures published for determining the accessibility of Au clusters using 2-NT as a probe molecule,[8,9] a similar titration experiment using adsorption of 2-NT onto cluster **H1-red** was performed and followed using steady-state fluorescence. The 2-NT fluorescence emission was measured on a Hitachi F-4500 Fluorimeter operating at 950 V and with an excitation/emission slit width of 5 nm (excitation wavelength was 283 nm). A typical procedure was as follows: 0.35 mg of **H1-red** were dissolved in 3 mL of dicholoromethane and 20 μL doses of 2-NT solution (1.0 mM 2-NT in dichloromethane) were added directly to the cuvette. The cuvette was shaken for 1 minute and equilibrated for 5 minutes before steady-state fluorescence measurements were recorded. All measurements and 2-NT titration experiments were conducted at 25°C. The peak of the 2-NT is observed at 350 nm.[8,9] Each fluorescence spectra is normalized at 308 nm, as described previously.[8,9] Each point on the titration curve represents a 20 μL dose of the 2-NT solution.

The large background fluorescence emission of all NHC-calixarene bound clusters (i.e. in the absence of any fluorophore probe molecule) was problematic from the standpoint of quantifying accessible and open surface sites via titration with 2-NT. This background fluorescence emission blocked our ability to accurately and reliably measure the binding of 2-NT to the gold surface. To exemplify this background fluorescence problem, Figure 5.S.39 shows the steady-state fluorescence emission spectra for solutions of **T1-red** and **C2-red** at a concentration of 120 μM (in Au atoms) for each cluster. The spectrum of the **C2-red** cluster

shows a broad band that extends into the range where the peak fluorescence emission of 2-NT is located, at 350 nm.

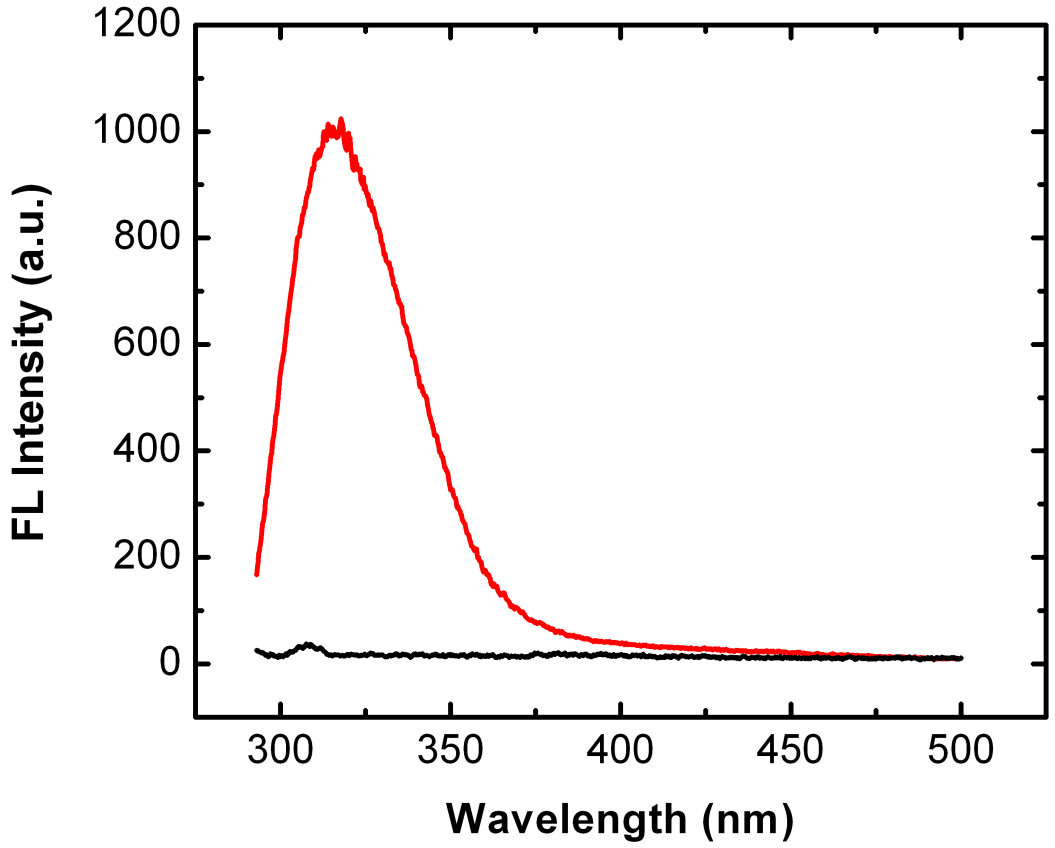

Figure 5.S.39: FL spectra of **T1-red** (black) and **C2-red** (red) excited at 283 nm at gold atom concentrations of 120 μM.

5.9.7 SAMSA-Fluorescein titrations

Due to the large background fluorescence of all calixarene NHC-bound gold clusters investigated here, we developed a new method for titrating and quantifying density of accessible, open "coordinatively unsaturated" sites on gold clusters. This method replaced 2-NT with a probe molecule that emits/excites at lower energy – to avoid the overlap with background fluorescence described above and shown in Figure 5.9.39. This new method is based on a SAMSA fluorescein dye as fluorescent probe molecule, which is able to bind to the gold surface by virtue of its pendant thioester/thiol functionality. The SAMSA fluorescein was activated according to procedures described by the manufacturer (Molecular Probes). To activate the SAMSA-fluorescein, 5 mg of SAMSA fluorescein was dissolved in 0.5 mL of 0.1 M NaOH solution for 15 minutes. The solution was then neutralized with 7 uL of 6 M HCl and buffered with 0.1 mL of 0.5 M sodium phosphate buffer at pH = 7. After the SAMSA fluorescein was activated, we proceeded with the titration experiments. In the titration experiments, our approach was to dissolve a known mass of gold cluster in 3 mL of isopropanol and add 20 μL

doses of 0.25 mM SAMSA fluorescein to the cluster. After the SAMSA fluorescein was added to the gold cluster, the resulting solution was shaken for 1 minute and stored in the dark for 15 minutes. Immediately following this, the steady-state fluorescence emission was measured using a Hitachi F-4500 Fluorimeter operating at 450 V and with an excitation/emission slit width of 5 nm exciting at 470 nm, and looking the peak height at 520 nm. The titrations were performed at 25°C.

To demonstrate the new approach, we used it on a cluster with a known number density of open "coordinatively unsaturated" sites, as measured by 2-NT titration. Our goal was to investigate whether or not a similar number density of open sites could be measured for both 2-NT and SAMSA fluorescein when using the same known cluster consisting of **T1-red**. Thus, 0.075 mg of cluster **T1-red** present was dissolved in 3 mL of isopropanol. When using a solution of 0.25 mM 2-NT to titrate, the expected uptake of 2-NT was measured, based on 2-NT titrations previously reported.[8]

$$(0.075 \text{ mg cluster } \mathbf{T1\text{-}red})\left(\frac{21.3 \text{ mg Au}}{100 \text{ mg cluster}}\right)\left(\frac{\text{g Au}}{1000 \text{ mg Au}}\right)\left(\frac{\text{mol Au}}{197 \text{ g Au}}\right)\left(\frac{2.7 \text{ open mol Au}}{11 \text{ mol Au}}\right) \times \left(\frac{1 \text{ mol 2-NT}}{1 \text{ open mol Au}}\right)\left(\frac{10^6 \text{ µL}}{0.25\ (10^{-3}) \text{ mol 2-NT}}\right) = 79.6 \text{ µL}$$

Based on previously reported 2.7 open sites per Au_{11} fragment in **T1-red**,[8] 79.6 µL of 0.25 mM 2-NT solution is expected to be needed to bind all of the open sites on **T1-red**.

Using the SAMSA-fluorescein titrant with the same mass of **T1-red** and the same concentration of titrant (0.25 mM), the amount of SAMSA fluorescein needed to titrate the open sites on cluster **T1-red** was measured. The equivalence point of the SAMSA-fluorescein titration was determined by finding the point of intersection of different slopes of fluorescence intensity versus amount of SAMSA-fluorescein added. This is based on the previously observed rationale that a fluorophore dye molecule with pendant thioester/thiol functionality emits at greater intensity when bound to a gold nanoparticle surface rather than when present in solution.[10] Linear regression was used to determine the point of intersection alluded to above.

An example titration plot using SAMSA fluorescein is shown below.

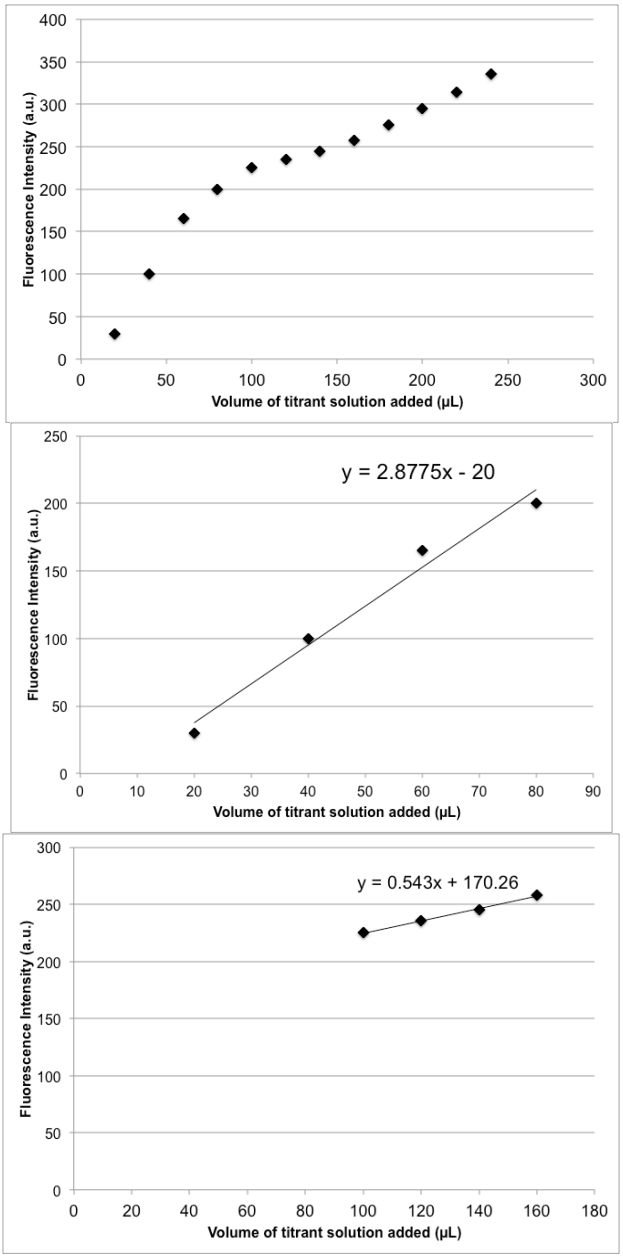

Figure 5.S.40: SAMSA-fluorescein titration data for **T1-red**. The linear regressions are shown for the two differently sloped regions of the graph. The equivalence point was shown to be when 81 µL of 0.25 mM SAMSA solution was added for 0.075 mg of **T1-red** in this experiment.

The data in Figure 5.S.40 illustrate a 1:1 correspondence with the amount of 2-NT needed to titrate an open site on **T1-red** and the amount of SAMSA fluorescein needed to titrate an open site on **T1-red**. The data in Figure 5.S.41 show that the amount of bound SAMSA fluorescein increases linearly with the mass of **T1-red** in solution, and that the slope of the line represents

the same accessible number density of open sites on **T1-red** when using SAMSA fluorescein as a probe molecule, relative to when using 2-NT as a probe molecule.

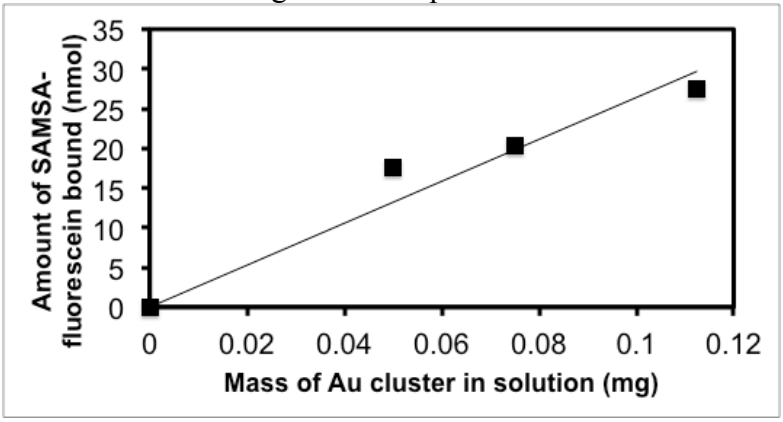

Figure 5.S.41: Linear dependence of SAMSA fluorescein bound as a function of **T1-red** in solution.

The new procedure based on using a SAMSA fluorescein probe was also used for determining the number of open sites on **C2-red**. An example is shown in Figure 5.S.42.

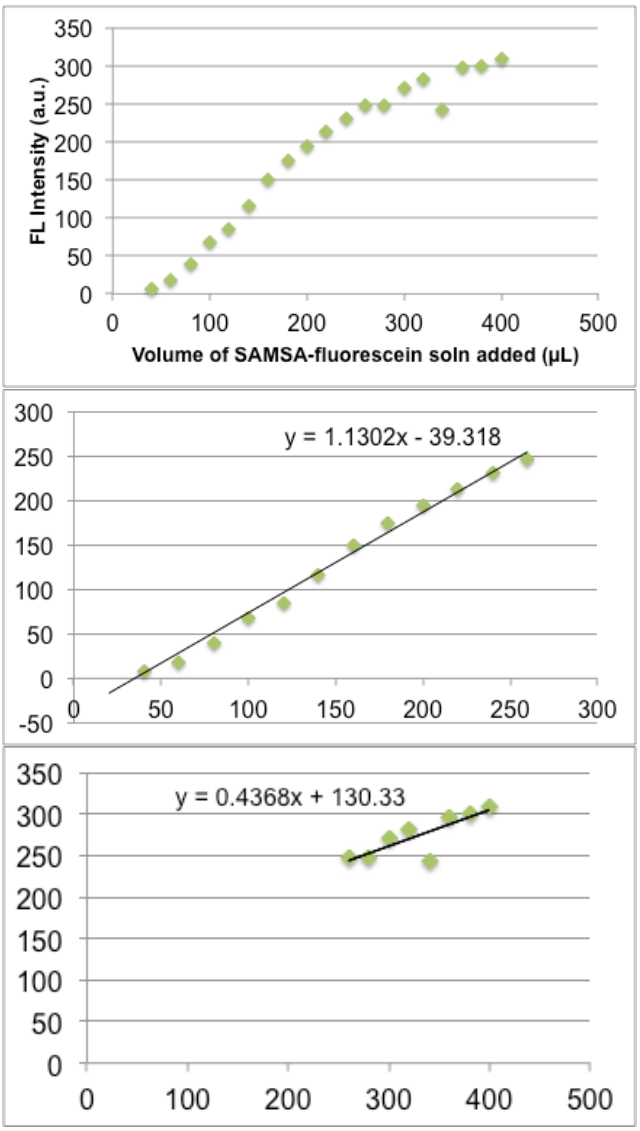

Figure 5.S.42: SAMSA-fluorescein titration data for **C2-red**. (top) The linear regressions of the data in the top panel are shown for the two differently sloped regions of the graph. (middle and bottom) The equivalence point was shown to be when 244 µL of SAMSA solution was added for 0.8 mg of **C2-red** in this experiment.

Knowing the equivalence point, the amount of open sites on **C2-red** was calculated as shown below.

Total number of open sites titrated by SAMSA fluorescein:

$$244(10^{-6})\text{ L solution}\left(\frac{0.25(10^{-3})\text{ mol SAMSA F}}{\text{L solution}}\right)\left(\frac{\text{mol open Au sites}}{\text{mol SAMSA F}}\right)\left(\frac{197\text{ g open Au sites}}{\text{mol open Au sites}}\right)$$
$$= 1.2(10^{-5})\text{ g open Au sites}$$

Total number of surface sites on a 1.2 nm particle:

$$0.8\text{ mg C2-red}\left(\frac{\text{g C2-red}}{10^{3}\text{ mg C2-red}}\right)\left(\frac{0.29\text{ g Au total}}{\text{g C2-red}}\right)\left(\frac{0.72\text{ g Au surface}}{\text{g Au total}}\right)$$
$$= 1.67(10^{-4})\text{g Au surface}$$
$$\frac{1.2(10^{-5})\text{g open Au sites}}{1.67(10^{-4})\text{g Au surface}} = 0.072$$

7.2% of the gold surface area of **C2-red** is accessible to SAMSA fluorescein at this data point.

Different masses of **C2-red** were used to determine the linearity of the response of the equivalence point of the titration and gold cluster mass. The results are shown in Figure 5.S.43. The equivalence point scales linearly with gold cluster mass as expected.

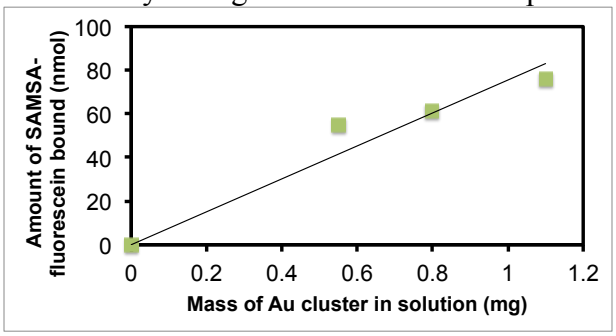

Figure 5.S.43: Amount of SAMSA-fluorescein bound per mass of **C2-red** in solution.

The dispersion of **C2-red** was calculated using a volume-weighted (based on diameter cubed rather than diameter to the first power) particle size distribution, rather than the particle size distribution based on diameter, which is shown in Figure 5.1. The volume-weighted average diameter was found to be 1.38 nm for **C2-red**. Using a spherical model and the bulk density of gold, the number of atoms in this particle was calculated.

$$\frac{4}{3}\pi\left(\frac{1.38(10^{-9})\text{m}}{2}\right)^{3}\left(\frac{1.93(10^{7})\text{g Au}}{\text{m}^3}\right)\left(\frac{\text{mol Au}}{197\text{ g Au}}\right)\left(\frac{6.022(10^{23})\text{ Au atoms}}{\text{mol Au}}\right) = 81\text{ Au atoms}$$

Assuming **C2-red** consists of an 81-atom cluster, the amount of surface atoms was calculated using correlations with a full shell model. (see p. 395 of "Supported Gold Nanoparticles as Oxidation Catalysts" by A. Corma and H. Garcia (Chapter 12) in *Nanoparticles and Catalysis*, Wiley-VCH (2008), Volume 1, Editor: Didier Astruc). Using linear interpolation between a 55 atom cluster having 76% of the atoms on the surface and a 147 atom cluster having 63% of the atoms on the surface, an 81 atom cluster is estimated to have 72% of the gold atoms on the surface. Using this knowledge of the dispersion, the data in Figure 5.S.43 leads to 7.1%

of the surface sites as open sites, using the slope of the line of best fit (75.5) from Figure 5.S.43. The calculation is shown below.

$$\frac{75.5(10^{-9})\text{mol SAMSA F}}{\text{mg C2-red}}\left(\frac{1\text{ mol open sites}}{1\text{ mol SAMSA F}}\right)\left(\frac{1000\text{ mg C2-red}}{1\text{ g C2-red}}\right)\left(\frac{100\text{ g C2-red}}{29\text{ g Au}}\right)\left(\frac{100\text{ g Au total}}{72\text{ g Au surface}}\right)$$

$$*\left(\frac{197\text{ g Au surface}}{\text{mol Au surface atoms}}\right) = 0.071\frac{\text{mol open sites}}{\text{mol Au surface atoms}}$$

5.9.8 TGA measurements of Au clusters

TGA measurements were performed using a TA instruments Model 2950 to determine the amount of organic material present in the reduced clusters. A mixture of 20% oxygen, balance argon was passed over the sample for 10 minutes under isothermal conditions and the sample was heated to 800°C at a rate of 5°C min^{-1}.

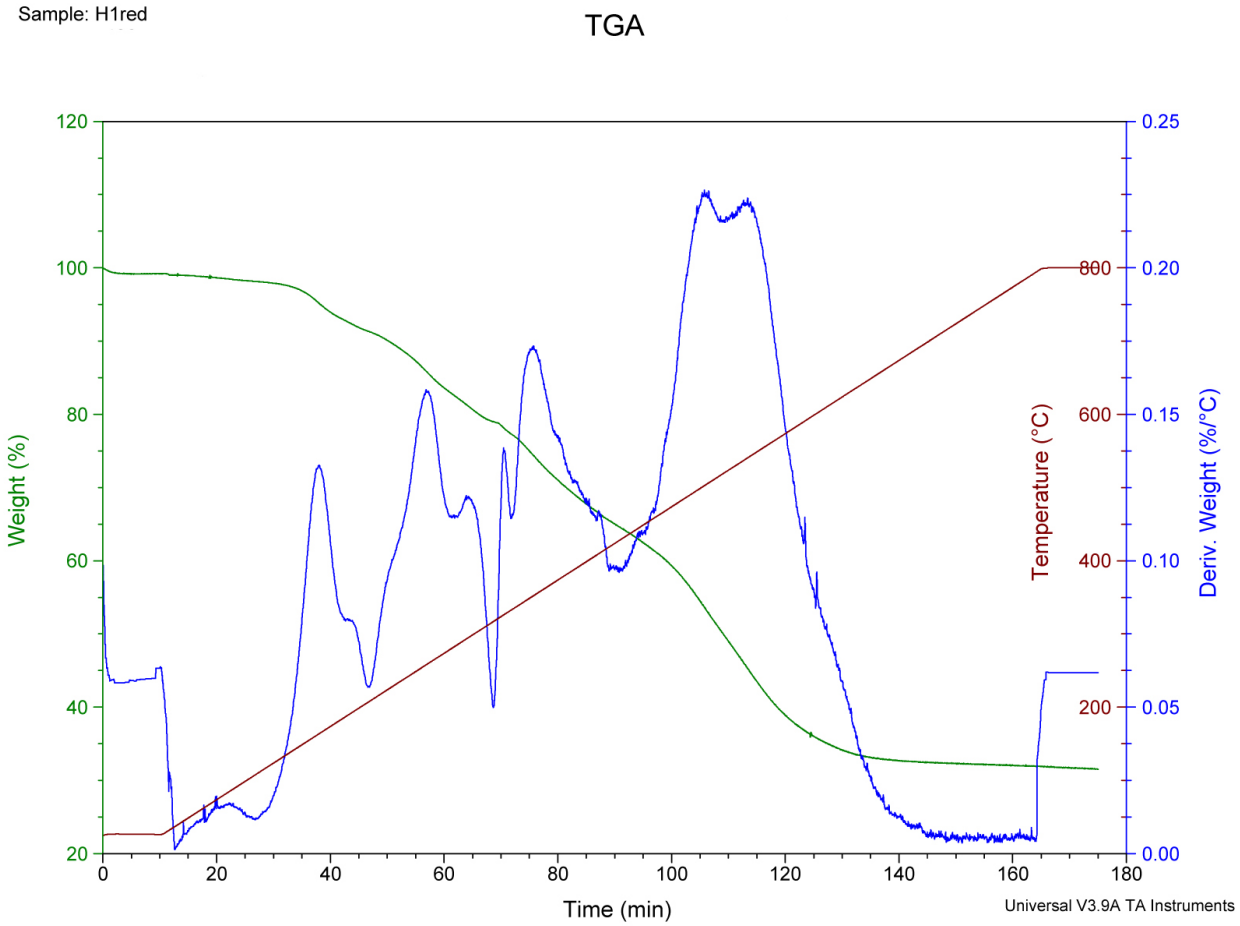

Figure 5.S.44: TGA of **H1-red**

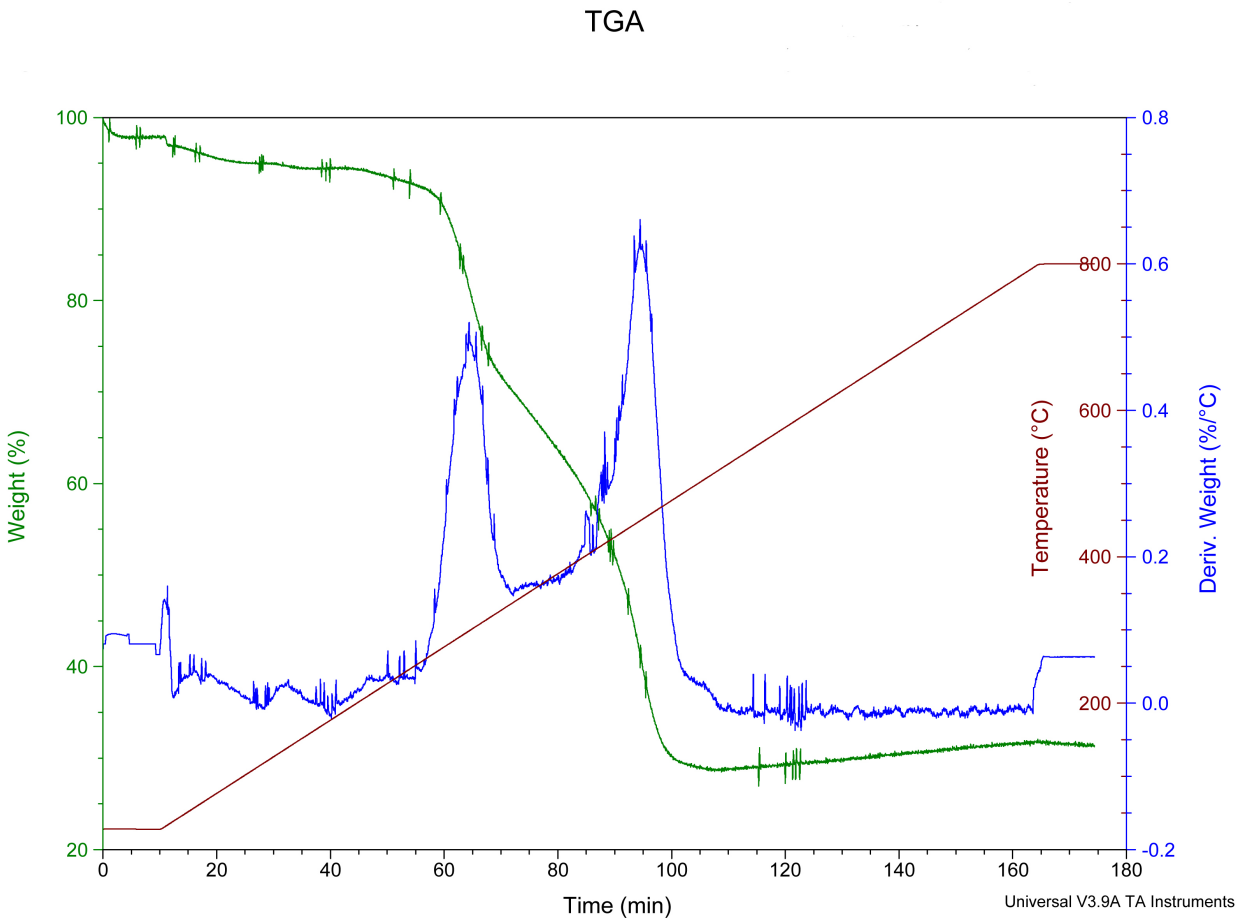

Figure 5.S.45: TGA of **C1-red**.

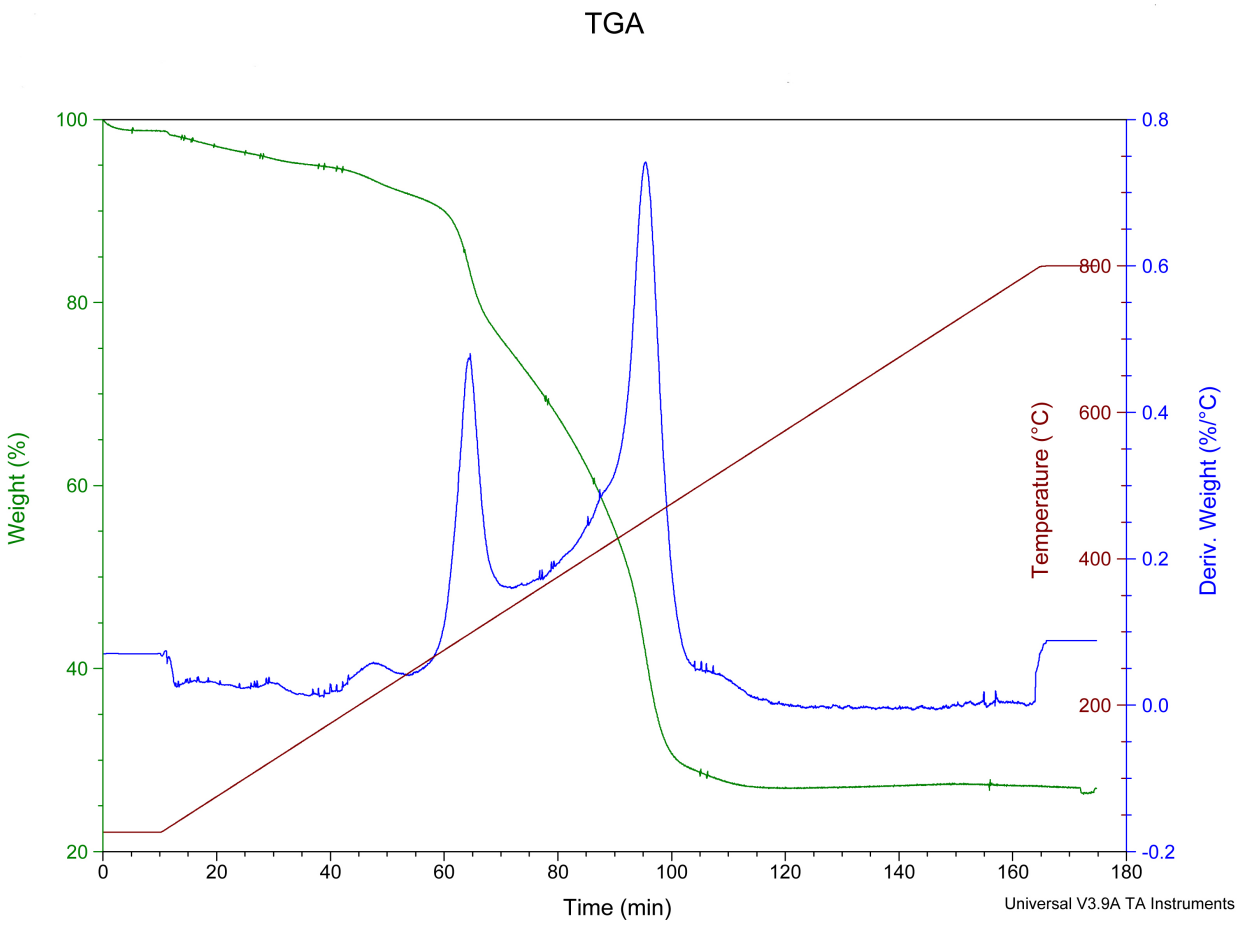

Figure 5.S.46 TGA of **C2-red**

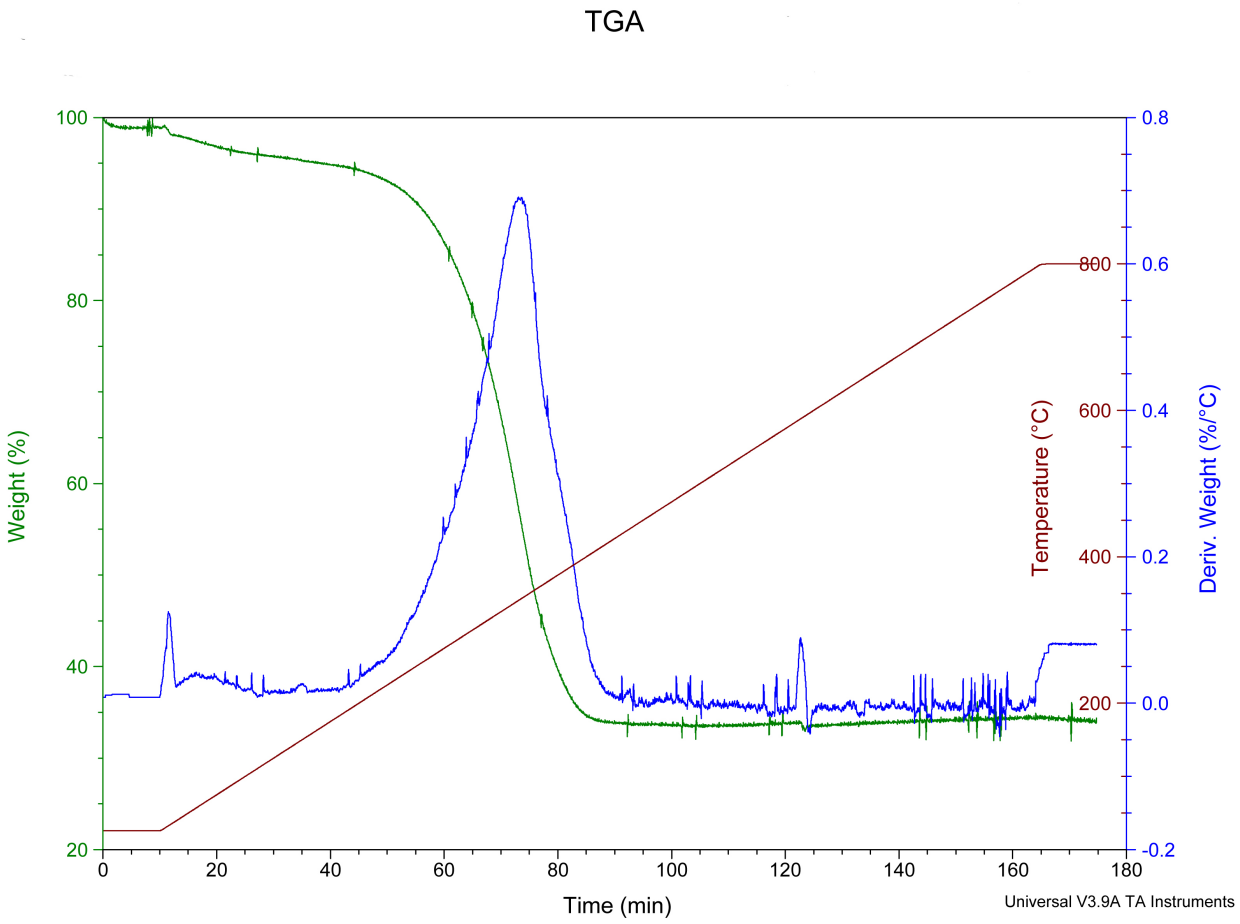

Figure 5.S.47: TGA of **C3-red**.

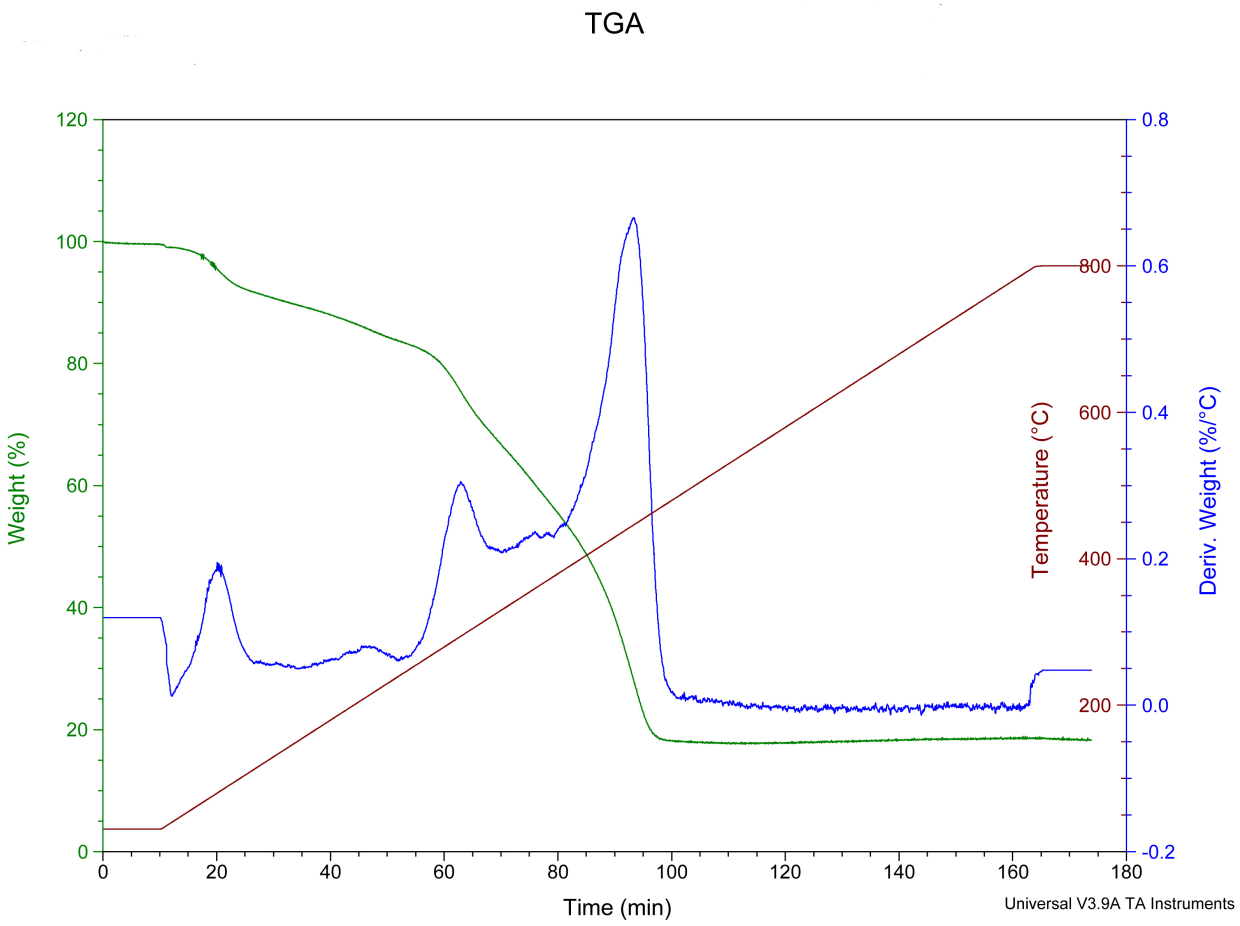

Figure 5.S.48: TGA of **D1-red**

5.9.9 XPS characterization data of **H1-red**

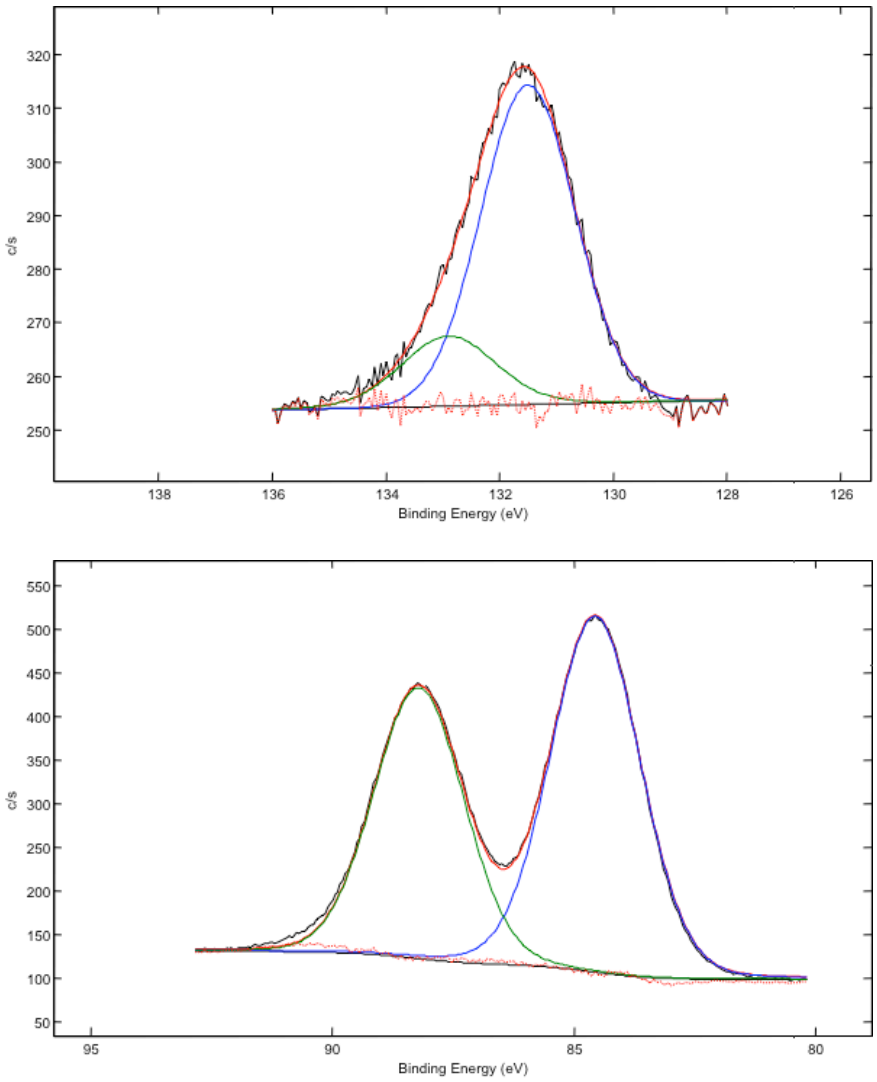

Figure 5.S.49 (top) P 2*p* and (bottom) Au 4f XPS results for **H1-red**. Deconvolution of the P 2*p* results shows the phosphine to phosphine oxide ratio to be 4.7 ± 1.5.

5.9.10 ESI-TOF MS data of **H1-red**

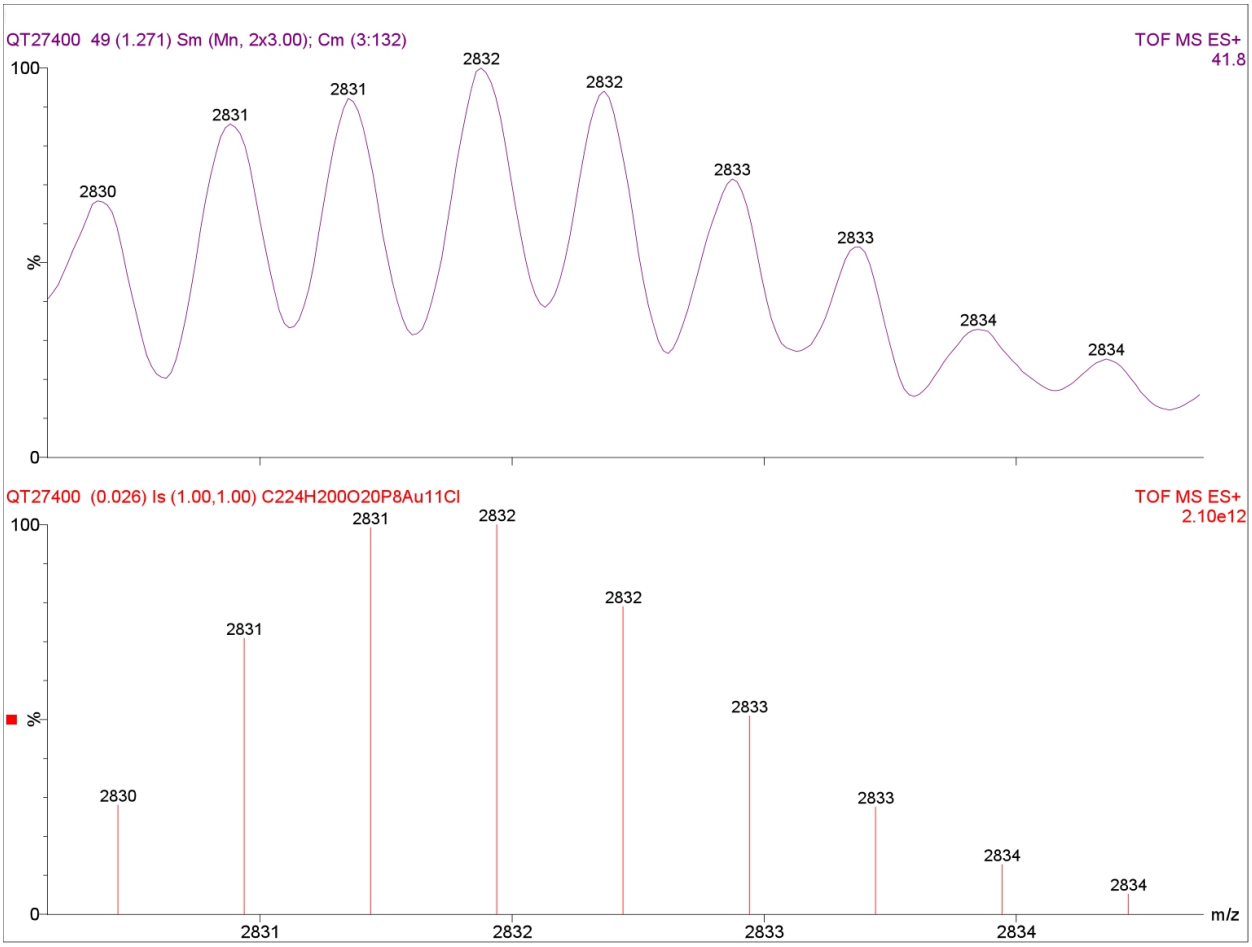

Figure 5.S.50: ESI mass spectrum (+) showing a molecular ion fragment in **H1-red** (top) and theoretical simulation of $[Au_{11}L_4Cl]^{2+}$. L = **H1** with one of the P present as phosphine and the other P present as phosphine oxide.

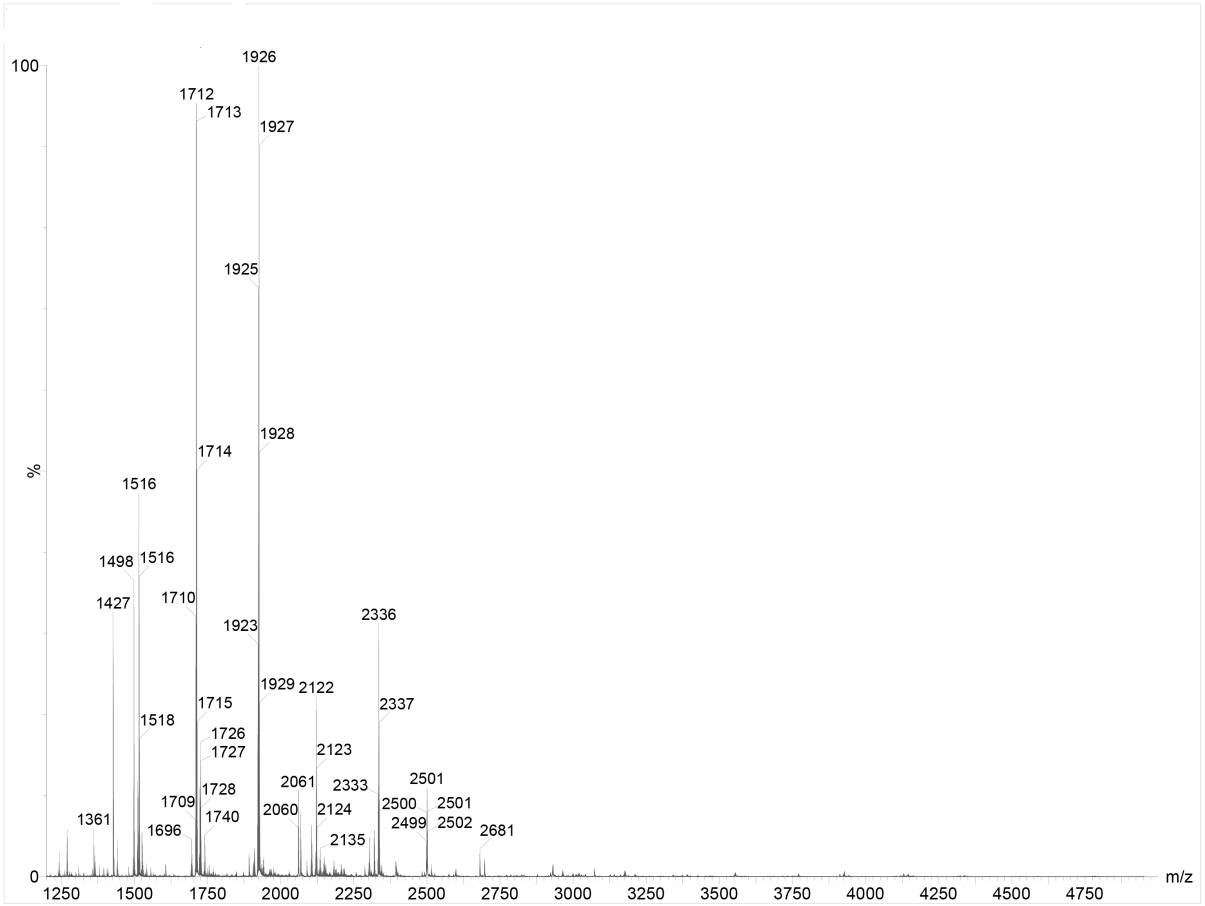

Figure 5.S.51: Full ESI mass spectrum (+) for **H1-red**

5.9.10 References for section 5.9

[1] K. Iwamoto, K. Araki, S. Shinkai, *Tetrahedron*, 47 (1991) 4325.

[2] P.J. Dijkstra, J.A.J. Brunink, K. E. Bugge, D. N. Reinhoudt, S. Harkema, R. Ungaro, F. Ugozzoli, E. Ghidini, *J. Am. Chem. Soc.,* 111 (1989) 7567.

[3] W. Wegener, *Z. Chem.,* 11(1971) 262.

[4] C.D. Gutsche, K.A. See, *J. Org. Chem.,* 57 (1992) 4527.

[5] C.B. Dieleman, D. Matt, P.G. Jones, *J. Organomet. Chem.,* 545-546 (1997) 461.

[6] N. de Silva, A. Solovyov, A. Katz, *Dalton Trans*. 39 (2010) 2194.

[7] C.D. Gutsche, B. Dhawan, J.A. Levine. K.H. No, L.J. Bauer. *Tetrahedron,* 39 (1983) 409.

[8] N. de Silva, J.-M. Ha, A. Solovyov, M.M. Nigra, I. Ogino, S.W. Yeh, K.A. Durkin, A. Katz, *Nat. Chem.*, 2(2010) 1062.

[9] J.-M. Ha, A. Solovyov, A. Katz, *Langmuir* 25 (2009) 10548.

[10] M. M. Y. Chen and A. Katz, *Langmuir*, 18 (2002) 2413.

5.10 References for Chapter 5

[1] H. Beinert, *JBIC, J. Biol. Inorg. Chem.*, 5 (2000) 2.

[2] L. Quintanar, J. Yoon, C.P. Aznar, A.E. Palmer, K.K. Andersson, R.D. Britt, E.I. Solomon, *J. Am. Chem. Soc.*, 127 (2005) 13832.
[3] A.H. Robbins, C.D. Stout, *Proc. Natl. Acad. Sci. U. S. A.*, 86 (1989) 3639.
[4] J.R. Banavar, A. Maritan, *Annu. Rev. Biophys. Biomol. Struct.*, 36 (2007) 261.
[5] N. de Silva, J.-M. Ha, A. Solovyov, M.M. Nigra, I. Ogino, S.W. Yeh, K.A. Durkin, A. Katz, *Nat. Chem.*, 2 (2010) 1062.
[6] J. Vignolle, T. D. Tilley, *Chem. Commun.*, 2009, 7230.
[7] Z.-T. Li, G.-Z. Ji, S.-D. Yuan, A.-L. Du, H. Ding, M. Wei, *Tetrahedron Lett.*, 39 (1998) 6517.
[8] Z.-T. Li, G.-Z. Ji, C.-X. Zhao, S.-D. Yuan, H. Ding, C. Huang, A.-L. Du, M. Wei, *J. Org. Chem.*, 64(1999) 3572.
[9] C.-M. Jin, J.M. Shreeve, *Inorg. Chem.*, 43 (2004) 7532.
[10] P. Schmitt, P.D. Beer, M.G.B. Drew, P.D. Sheen, *Angew. Chem., Int. Ed.*, 36 (1997) 1840.
[11] Z. Asfari, J. Weiss, S. Pappalardo, J. Vicens, *Pure Appl. Chem.*, 65 (1993) 585.
[12] N. Kerdpaiboon, B. Tomapatanaget, O. Chailapakul, T. Tuntulani, *J. Org. Chem.*, 70 (2005) 4797.
[13] P. R. A. Webber, P. D. Beer, G. Z. Chen, V. Felix, M. G. B. Drew, *J. Am. Chem. Soc.*, 125 (2003) 5774.
[14] B. Tomapatanaget, B. Pulpoka, T. Tuntulani, *Chem. Lett.*, 1998, 1037.
[15] C. Jaime, J. de Mendoza, P. Prados, P.N. Nieto, C. Sanchez, *J. Org. Chem.*, 56 (1991) 3372.
[16] C.B. Dieleman, D. Matt, P.G. Jones, *J. Organomet. Chem.*, 545-546 (1997) 461.
[17] *International Tables for Crystallography Volume A: Space Group Symmetry*, ed. T. Hahn, 2002, pp. 184
[18] Mercury: visualization and analysis of crystal structures. C.F. Macrae, P.R. Edgington, P. McCabe, E. Pidcock, G. P. Shields, R. Taylor, M. Towler, J. van de Streek, *J. Appl. Crystallogr.*, 39 (2006) 453.
[19] H.D. Flack, *Helv. Chim. Acta*, 86 (2003) 905.
[20] A.L. Spek, *J. Appl. Crystallogr.*, 36 (2003) 7.
[21] R. Ungaro, A. Pochini, G.D. Andreetti, P. Domiano, *J. Chem. Soc., Perkin Trans., 2*, (1985) 197.
[22] C.P. Brock, J.D. Dunitz, *Chem. Mater.*, 6 (1994) 1118.
[23] H.M.J. Wang, I.J.B. Lin, *Organometallics*, 17(1998) 972.
[24] K. Nunokawa, S. Onaka, T. Yamaguchi, T. Ito, S. Watase, M. Nakamoto, *Bull. Chem. Soc. Jpn.*, 76 (2003) 1601.
[25] D. Safer, L. Bolinger, J.S. Leigh, *J. Inorg. Biochem.*, 26 (1986) 77.
[26] Y. Yang, S. Chen, *Nano Lett.*, 3 (2003) 75.
[27] G.H. Woehrle, M.G. Warner, J.E. Hutchison, *J. Phys. Chem. B*, 106 (2002) 9979.
[28] Y. Yanagimoto, Y. Negishi, H. Fujihara, T. Tsukuda, *J. Phys. Chem. B*, 110 (2006) 11611.
[29] K.P. Hall, D.M.P. Mingos, *Prog. Inorg. Chem.*, 1984, **32**, 237.
[30] R.C.B. Copley, D.M.P. Mingos, *J. Chem. Soc., Dalton Trans.*, 1996, 479.
[31] J.M.M. Smits, J.J. Bour, F.A. Vollenbroek, P.T. Beurskens, *J. Crystallogr. Spectrosc. Res.*, 13 (1983) 355.
[32] Y. Shichibu, K. Konishi, *Chem. Commun.*, 2012, 7559.

[33] H.G. Alt, I.K. Böhmer, *Angew. Chem., Int. Ed.*, 47 (2008) 2619.
[34] J.S. Kirk, P.W. Bohn, *J. Am. Chem. Soc.*, 126 (2004) 5920.
[35] F. Cannone, G. Chirico, A.R. Bizzarri, S. Cannistraro, *J. Phys. Chem. B*, 110 (2006) 16491.
[36] M.M.Y. Chen, A. Katz, *Langmuir*, 18 (2002) 2413.

CHAPTER 6:

Delamination of layered zeolite precursors under mild conditions: synthesis of UCB-1 via fluoride/chloride anion-promoted exfoliation

a collaboration between
Isao Ogino, Michael Nigra, Son-Jong Hwang, Jeong-Myeong Ha, Thomas Rea,
Stacey Zones, and Alexander Katz

Abstract

New material UCB-1 is synthesized via the delamination of zeolite precursor MCM-22 (P) at pH 9 using an aqueous solution of cetyltrimethylammonium bromide, tetrabutylammonium fluoride, and tetrabutylammonium chloride at 353 K. Characterization by powder X-ray diffraction, transmission electron microscopy, and nitrogen physisorption at 77 K indicates the same degree of delamination in UCB-1 as previously reported for delaminated zeolite precursors, which require a pH of greater than 13.5 and sonication in order to achieve exfoliation. UCB-1 consists of a high degree of structural integrity via ^{29}Si MAS NMR and Fourier transform infrared spectroscopies, and no detectable formation of amorphous silica phase via transmission electron microscopy. Porosimetry measurements demonstrate a lack of hysteresis in the N_2 adsorption/desorption isotherms and macroporosity in UCB-1. The new method is generalizable to a variety of Si:Al ratios and leads to delaminated zeolite precursor materials lacking amorphization.

6.1 Main text

The emergence of a new class of catalysts consisting of exfoliated zeolite precursors expands the range of reactions that zeolites catalyze by providing access for larger reactant molecules. [1-4] ITQ-2 in particular represents the first example of such a material, and consists of pores derived from the zeolite precursor material MCM-22(P), which are embedded within thin, accessible sheets and enable shape-selective catalysis. [5-9] To date, the synthesis of exfoliated zeolite precursors has required a high-pH medium during precursor material swelling, typically in the pH range of 13.5–13.8. [10-12] On the basis of the high solubility of silica in such a basic aqueous solution, hypotheses of partial amorphization of the zeolite layers during delamination have been invoked. [10,11,13] This has motivated the search for milder conditions for delamination. While there has been notable success in decreasing the temperature from 353 K to room temperature during swelling of MCM-22 (P), it has been difficult to achieve delamination under these milder conditions, since the material reverts back to the zeolite precursor after acidification of the swollen sample. [11] Here, in this manuscript, we demonstrate the synthesis of UCB-1, which results from MCM-22 (P) exfoliation using a combination of tetrabutylammonium fluoride and chloride surfactants at pH 9 in aqueous solution, and is isolated in an aluminosilicate yield of 90% (versus ~75% aluminosilicate yield for ITQ-2 synthesis in our hands). We demonstrate unique morphology and high structural integrity of UCB-1, which are characterized by ^{29}Si MAS NMR spectroscopy, transmission electron microscopy (TEM), and porosimetry.

Delamination of layered zeolite precursors by the new method is guided by viewing exfoliation from the perspective of being a chemical deprotection process, involving breaking of Si–O and Al–O bonds in the interlayer region. Our approach uses fluoride anion because it is an established reagent for the deprotection of silyl ethers [14] and is known to form strong interactions to Si(IV) cations. [15,16] In addition, chloride is used because it is known to be the most aggressive anion for corroding anodized aluminum among a list of 12 investigated anions that include all four common halides. [17] We therefore hypothesized that delamination can be conducted using an aqueous mixture of fluoride and chloride anions. Thus, treatment of MCM-22 (P) at 353 K for 16 h using cetyltrimethylammonium bromide, tetrabutylammonium fluoride, and tetrabutylammonium chloride at a mild pH of 9 (typically associated with fluoride syntheses

of zeolites [18]) results in delamination. These conditions correspond to the same temperature and duration used under the conventional high-pH delamination method but, in contrast, crucially lack the requirement of sonication. After acidification of the slurry to pH 2, the delaminated zeolite precursor UCB-1 is collected via centrifugation.

Powder X-ray diffraction (PXRD) of as-made UCB-1 data are shown alongside data for zeolites MCM-22 (P) (Figure 6.1, pattern A) and ITQ-2 (pattern B), which match literature data (see the Supporting Information for details). [1,6,12]

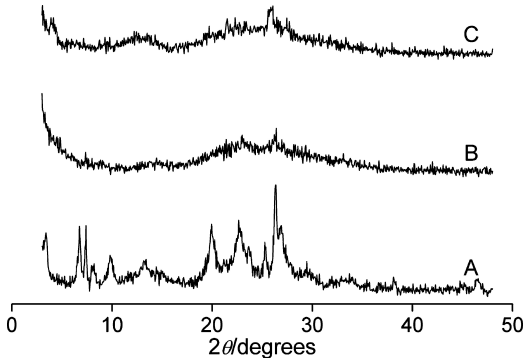

Figure 6.1: Powder X-ray diffraction patterns characterizing as-made zeolites (A) MCM-22 (P), (B) ITQ-2, and (C) UCB-1.

PXRD of as-made UCB-1 in Figure 1C demonstrates a powder pattern similar to that of ITQ-2 zeolite. The 001 (3.3°, ~27 Å) and 002 (6.7°, ~13 Å) peaks are significantly diminished in intensity; however, the 310 (26°) peak has a stronger intensity than for material ITQ-2. This suggests a greater degree of long-range order in the direction parallel to the sheet for the material synthesized by the fluoride/chloride delamination method.

Whereas TEM images of MCM-22 (P) show lamellar assemblies consisting of rectilinear sheets (Figure 6.S.1A and B in Supporting Information), images of UCB-1 clearly show curved layers (Figure 6.S.1C and D in the Supporting Information), which lack long-range order. Single layers of 2.5 nm thickness are evident in Figure 6.2 (see also Figure 6.S.2 in the Supporting Information).

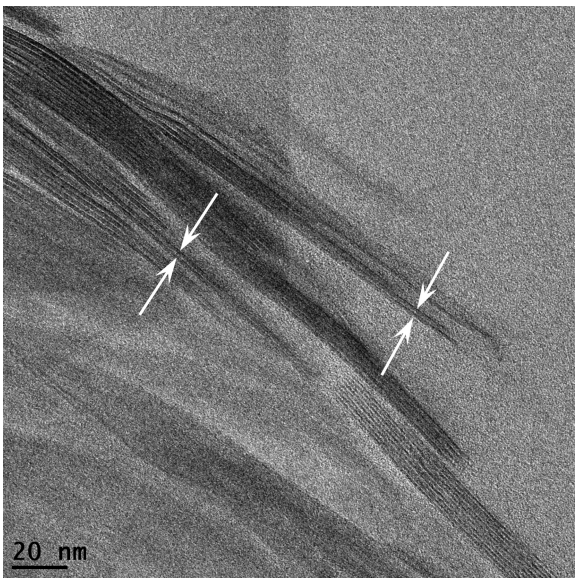

Figure 6.2: TEM image characterizing as-made UCB-1. The arrows indicate single-layers.

^{29}Si MAS and CP MAS NMR spectra in Figures 6.3 and 6.4 further compare MCM-22 (P) with as-made materials ITQ-2 and UCB-1. The well-resolved resonances in the Q^4 region ($-105 < \delta < -120$ ppm) and entire absence of Q^2 resonances for the spectrum in Figure 3C relative to Figure 3B reflect a higher degree of structural order for UCB-1 compared with ITQ-2.

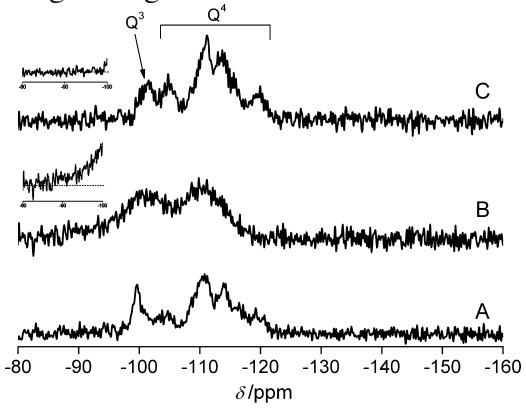

Figure 6.3: ^{29}Si MAS NMR data characterizing (A) MCM-22 (P), (B) as-made ITQ-2, (C) as-made UCB-1. Insets: Magnification of spectra in the range between –80 and –100 ppm.

The observed breadth of the Q^4 region and the appearance of downfield Q^2 resonances (≈ –91 ppm) in Figures 6.3B and 6.4A for as-made ITQ-2 are consistent with amorphization of the zeolite precursor material. Fourier-transform infrared (FTIR) spectra (Figure 6.S.3 in the Supporting information) of both as-made and calcined UCB-1 exhibit a well-resolved band at 563 cm^{-1}. This distinct band corresponds to pentasil rings in the framework [19] and is also similarly evident in MCM-22(P). The significantly diminished intensity of this band in the spectrum of ITQ-2 [1] is presumably the result of amorphization. [10,11,13] ^{27}Al MAS NMR spectroscopy (Figure 6.S.4 in the Supporting information) demonstrates retention of tetrahedral aluminum at 50–60 ppm and no octahedral aluminum at around 0 ppm in as-made UCB-1. [20]

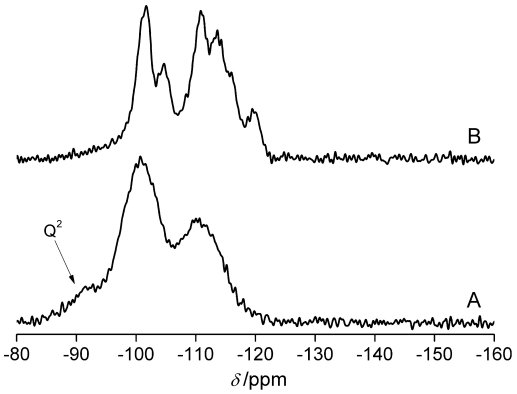

Figure 6.4: ^{29}Si CP MAS NMR data characterizing (A) as-made ITQ-2 and (B) as-made UCB-1. The spinning rate of the sample was 8 kHz, and contact time for cross-polarization was 2.0 ms.

Nitrogen physisorption isotherms at 77 K of calcined materials UCB-1 and ITQ-2, as well as calcined zeolites MCM-22, [21] TON, [22] and ultrastable HY (USY), are shown in Figure 6.5. The latter three are included as controls to elucidate where in the isotherm rings of a certain size physisorb nitrogen. Zeolite TON consists of only 10-membered-ring (MR) channels and shows pore filling of these channels starting at a relative pressure P/P_o of 10^{-7}. Zeolite USY consists of 12-MR windows and large (~13 Å) supercages, and shows pore filling of these pores at a relative pressure in the range of $10^{-5} < P/P_o < 10^{-4}$.

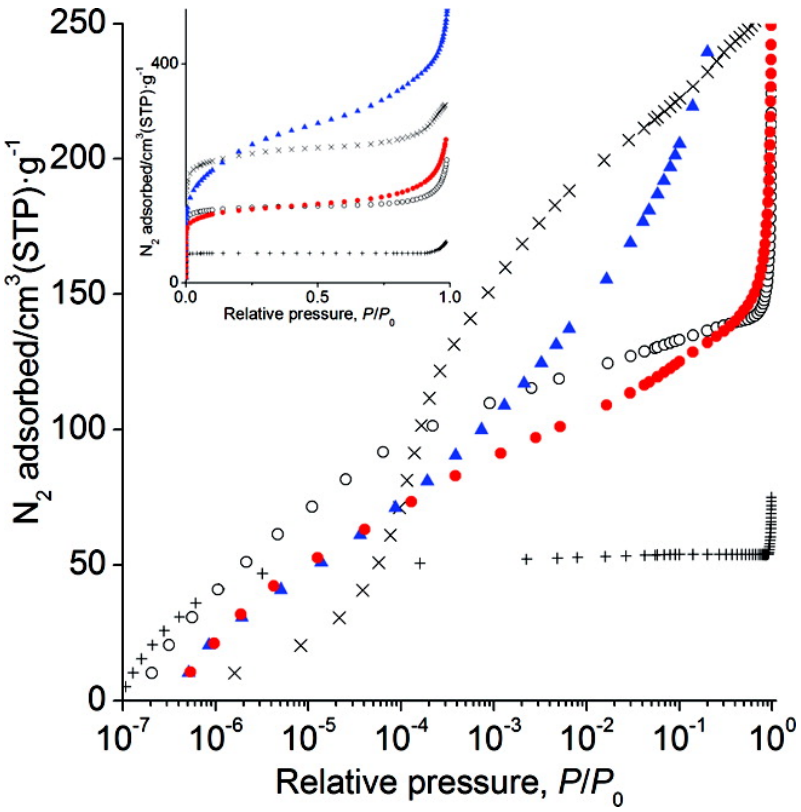

Figure 6.5: N_2 adsorption isotherms characterizing the following zeolites in a semilogarithmic scale: (○) MCM-22 zeolite, (▲ blue) ITQ-2 zeolite, (● red) UCB-1, (×) USY zeolite, and (+) TON zeolite. The inset shows the same data in a linear scale.

As a reference point, calcined zeolite MCM-22 consists of two independent 10-MR pore channels and 12-MR supercages, [21] with one of the 10-MR pore channel systems running through intralayers and the other through interlayers. Therefore, the delamination of MCM-22 (P) and its subsequent calcination is expected to form a material that retains 10-MR pore channels within each layer, while the other 10-MR pore channel is expected to be significantly reduced relative to calcined MCM-22 zeolite. [23] These expectations are indeed supported by a comparison of N_2 physisorption data for calcined MCM-22 and ITQ-2 in Figure 6.5. At a relative pressure of approximately $10^{-7} < P/P_o < 10^{-4}$, the total uptake of nitrogen into ITQ-2 is lower than that for MCM-22, which is consistent with loss of 10-MR during the delamination process. The isotherm for UCB-1 in Figure 6.5 essentially overlaps the isotherm for ITQ-2 in the region $10^{-7} < P/P_o < 10^{-4}$, which indicates that both materials have similar amounts of 10-MR channels (Table 6.S.1 in Supporting information). This in turn requires that the degree of delamination for both materials is similar. However, the significantly diminished uptake of UCB-1 for relative pressures P/P_o greater than 10^{-4} means that ITQ-2 consists of larger micropores and mesopores, which presumably originate from amorphous silica and are responsible for the hysteresis observed in the adsorption/desorption branches of the nitrogen physisorption isotherm of ITQ-2 (Figure 6.S.5 in Supporting information). This hysteresis is entirely absent in the corresponding

isotherms of UCB-1 (see Figure 6.S.5 in Supporting information). Mesoporosity in ITQ-2 and lack thereof in UCB-1 are additionally confirmed via TEM (Figure 6.S.6 in Supporting information). [10]

The structural integrity of layers in UCB-1 is evident in the large length scale of macroporosity via mercury porosimetry (Figure 6.S.7 in Supporting information). The average macropore diameter of 350 nm in UCB-1 is almost the same as the 0.5–1 μm microcrystalline diameter of the MCM-22 (P) used in the synthesis of UCB-1. Considering the curvature incorporated into UCB-1 layers upon delamination (vide supra), this is consistent with minimal intralayer fragmentation. TEM of calcined UCB-1 also demonstrates this macroporosity, which is formed between stacks of sheets. In contrast, though both materials are synthesized from the same layered zeolite precursor, the macropore diameter of calcined ITQ-2 is significantly smaller than that for UCB-1. This is consistent with fragmentation of ITQ-2 layers during the higher pH conventional delamination process.

When delamination is attempted using only fluoride in the absence of chloride, only partial delamination results. This is clearly demonstrated by the strong 001 and 002 peaks at 3.3° (*d*-spacing of ~ 27 Å) and 6.7° (*d*-spacing of ~ 13 Å) in Figure SS.6B. These features in the powder X-ray diffraction pattern indicate retention of layer stacking after delamination in the absence of chloride. The essential role of chloride demonstrated by the data above could be due to its ability to break Al–O bonds in the interlayer region, as demonstrated by its corrosivity of oxidized aluminum (*vide supra*). However, the crucial role of hybrid organic–inorganic self-assembly should also not be underestimated. There is much precedent for chloride-specific anion binding effects in the noncovalent stabilization of interfaces in general. In particular, chloride has been shown by classical Monte Carlo simulations to interact directly with Al–OH functionality in γ-alumina. [24] Furthermore, zeta potential measurements show chloride to be unique among other investigated halides consisting of bromide and iodide, in that chloride is able to specifically adsorb on an α-alumina surface. [25] Thus, chloride could also play an important role in stabilizing the supramolecular assembly that results during delamination by providing for required noncovalent interactions and space filling. [26]

Fluoride is also a necessary component for delamination because using only chloride in the absence of fluoride results in partial delamination as well. This is demonstrated by Figure 6.6C, which is similar to the powder X-ray diffraction pattern in Figure 6.6B. We hypothesize that coordination of fluoride to Si is critical for at least the partial replacement of Si–O with Si–F functionality in the interlayer region during MCM-22(P) delamination. Support for fluoride coordination to Si is contained in the ^{19}F NMR spectrum of as-made UCB-1 (Figure 6.S.8 in Supporting information), which exhibits a resonance at −128.6 ppm that is attributable to SiF_6^{2-}. [27]

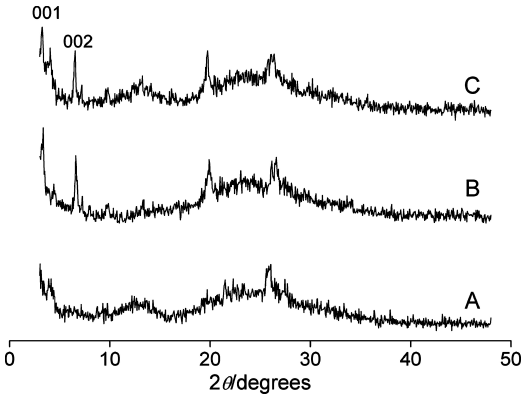

Figure 6.6: Powder X-ray diffraction patterns characterizing (A) as-made UCB-1, and MCM-22(P) (Si:Al ratio of 50) delaminated by the same method used for UCB-1, except in the absence of either (B) chloride or (C) fluoride.

The mild pH and lack of sonication used for UCB-1 synthesis are directly comparable with those used to synthesize ITQ-2, by applying both treatments to calcined zeolite MCM-22 as an aluminosilicate model. The treatment of calcined MCM-22 under UCB-1 synthesis conditions leads to a product with an intense powder pattern resembling parent MCM-22 (Figure 6.S.9 in Supporting information). However, treatment of calcined MCM-22 under ITQ-2 synthesis conditions leads to decreased zeolite crystallinity as evidenced by intense amorphous features and weaker overall peak intensity in the PXRD pattern (Figure 6.S.10 in Supporting information). This comparison demonstrates the milder nature of UCB-1 versus ITQ-2 synthetic conditions on the aluminosilicate framework.

While the results above have been demonstrated by using a MCM-22 (P) with a Si:Al ratio of 50, similar degrees of delamination via PXRD are achieved in materials having a Si:Al ratio of 20 (PXRD pattern is shown in Figure 6.S.11 in Supporting information). This has been performed using similar conditions to those reported here using the fluoride/chloride method, except that a swelling time of 3 d rather than 16 h is used.

In summary, the fluoride/chloride method presented here successfully delaminates layered zeolite precursors at a pH of 9 in aqueous solution and, as such, presents the mildest known method for the delamination of zeolite precursor materials. We anticipate that the method can be readily generalized to other layered zeolite precursors consisting of a variety of Si:Al ratios.

6.2 Supporting information

6.2.1 Experimental methods

6.2.1.1 Materials

All reagents used in zeolite synthesis and delamination were of reagent-grade quality and were used as received. USY zeolite used in N_2 gas physisorption was purchased from Zeolyst International (CBV760, Si/Al ratio of 60). TON zeolite was synthesized at Chevron Energy Technology Company according to the literature method, [1] except that the starting gel

composition used was SiO_2 : 0.10 NaOH : 0.01 Al_2O_3 (same ratio of H_2O/SiO_2 as that used in the literature).

6.2.1.2 Synthesis of MCM-22 (P)

The zeolite was synthesized according to the literature method. [2,3] Fumed silica (Sigma Aldrich, 3.54 g) was added to an aqueous solution containing sodium hydroxide (EMD Chemicals, 97%, 0.372 g), hexamethyleneimine (Sigma Aldrich, 99%, 2.87 g), and sodium aluminate (Riedel-de Haen, 0.108 g) in deionized water (46.6 g) under vigorously stirring. After stirring the mixture for 6 h, the gel was divided into four portions and each portion was loaded into a 23 mL Teflon- lined Parr reactor. Each reactor was tightly sealed and heated in a convection oven at 408 K for 11 days with tumbling of the reactor. After 11 days of heating, the reactors were cooled down to room temperature, and the product was separated by centrifugation. The separated product was washed with deionized water thoroughly, and finally dried at 313 K overnight.

6.2.1.3 Delamination of MCM-22 (P) by the Conventional Method (Synthesis of ITQ-2 Zeolite)

MCM-22 (P) synthesized according to the preceding section was delaminated by the literature method. [2] An aqueous slurry of MCM-22 (P) (3.00 g, 20 wt% solid) was mixed with cetyltrimethylammonium bromide (Sigma Aldrich, ≥98%, 3.38 g), deionized water (8.28 g), tetrapropylammonium hydroxide solution (Alfa Aesar, 40 wt%, 3.67 g), and the resulting mixture was heated at 353 K for 16 h. After 16 h of heating, the mixture was cooled to room temperature, and subjected to sonication for 1 h. The pH of the slurry was adjusted to 2 by adding concentrated HCl aqueous solution, upon which it was centrifuged to separate the product. Finally, the product was dried at 313 K overnight. The product yield was 75%. [4] The powder X-ray diffraction pattern of the product (Figure 6.1, pattern B) shows a significant decrease of all peaks characteristic of a lamellar structure of MCM-22 (P), in agreement with the literature results. [2,6,7] ITQ-2 was calcined at 823 K in flowing N_2/O_2.

6.2.1.4 Synthesis of UCB-1 via delamination of MCM-22 (P)

As-made MCM-22 (P) (1.00 g) was added to a mixture of cetyltrimethylammonium bromide (1.65 g), tetrabutylammonium fluoride (Fluka, ≥90%, 1.92 g) and tetrabutylammonium chloride (Sigma Aldrich, 1.68 g) in deionized water (25.9 g). The pH of the slurry was adjusted to approximately 9 by adding 40% tetrapropylammonium hydroxide solution, and the slurry was heated at 353 K for 16 h. After cooling, the pH of the mixture was adjusted to approximately 2 by adding concentrated HCl aqueous solution. The mixture was transferred to a centrifuge bottle with screw cap, and quickly centrifuged to separate solids. The supernatant solution was discarded, and the remaining solid was dried at 313 K overnight in the fume hood. The aluminosilicate product yield was 90%. UCB-1 was calcined at 823 K in flowing N_2/O_2.

6.2.1.5 Delamination of MCM-22 (P) without chloride

Delamination of MCM-22 (P) was attempted under similar conditions to those described

above, except without tetrabutylammonium chloride and with twice as much as tetrabutylammonium fluoride.

6.2.1.6 Delamination of MCM-22 (P) without fluoride

Delamination of MCM-22 (P) was attempted under similar conditions to those described above, except without tetrabutylammonium fluoride and with twice as much as tetrabutylammonium chloride.

6.2.1.7 Characterization

Powder X-ray diffraction (XRD) patterns were collected on a Siemens D5000 diffractometer using a Cu Kα radiation. Transmission electron microscopy images were recorded on a Tecnai 20 at the University of California at Berkeley or a JEOL JEM-2010 (200 kV) at Chevron Energy Technology Company. Nitrogen gas adsorption isotherms [8] were measured on a Micromeritics ASAP2020 at 77 K. Prior to measurement, samples were evacuated at 623 K for 4 h. ^{29}Si solid-state MAS NMR spectra were measured using a Bruker Avance 500 MHz spectrometer with a wide bore 11.7 T magnet and employing a Bruker 4 mm MAS probe. The spectral frequencies were 500.23 MHz for the ^{1}H nucleus and 99.4 MHz for the ^{29}Si nucleus. ^{29}Si MAS NMR spectra were acquired after a 4 μs-90 degree pulse with application of a strong 1H decoupling pulse. The spinning rate was 12 kHz, and the recycle delay time was 300 s. ^{29}Si CP MAS NMR spectra were collected on a Bruker DSX-500 spectrometer. The spectral frequency was 99.4 MHz for the ^{29}Si nucleus. The sample spinning rate was 8 kHz, and the cross polarization contact time was 2.0 ms. NMR shifts are reported in parts per million (ppm) when externally referenced to tetramethylsilane (TMS). One dimensional (1D) ^{27}Al MAS NMR spectra were recorded on a Bruker DSX-500 spectrometer (130 MHz for ^{27}Al) after a 0.5 ms single pulse ($< \pi/18$) with application of a strong 1H decoupling pulse, at a sample spinning rate of 14 kHz. Mercury porosimetry was conducted according to Standard Test Method for Determining Pore Volume Distribution of Catalysts by Mercury Intrusion Porosimetry (ASTM D 428).

6.2.2 Physisorption data

Table 6.S.1: Pore volume of MCM-22, UCB-1, and ITQ-2 determined from N2 gas adsorption data

Range of relative pressure	Pore volume (cm^3/g)		
	MCM-22	UCB-1	ITQ-2
$P/P_0 \leq 10^{-5}$	0.11	0.08	0.08
$10^{-5} < P/P_0 \leq 0.02$	0.08	0.09	0.17
$0.02 < P/P_0 < 1.0$	0.16	0.30	0.53

6.2.3 TEM micrographs of MCM-22 and UCB-1

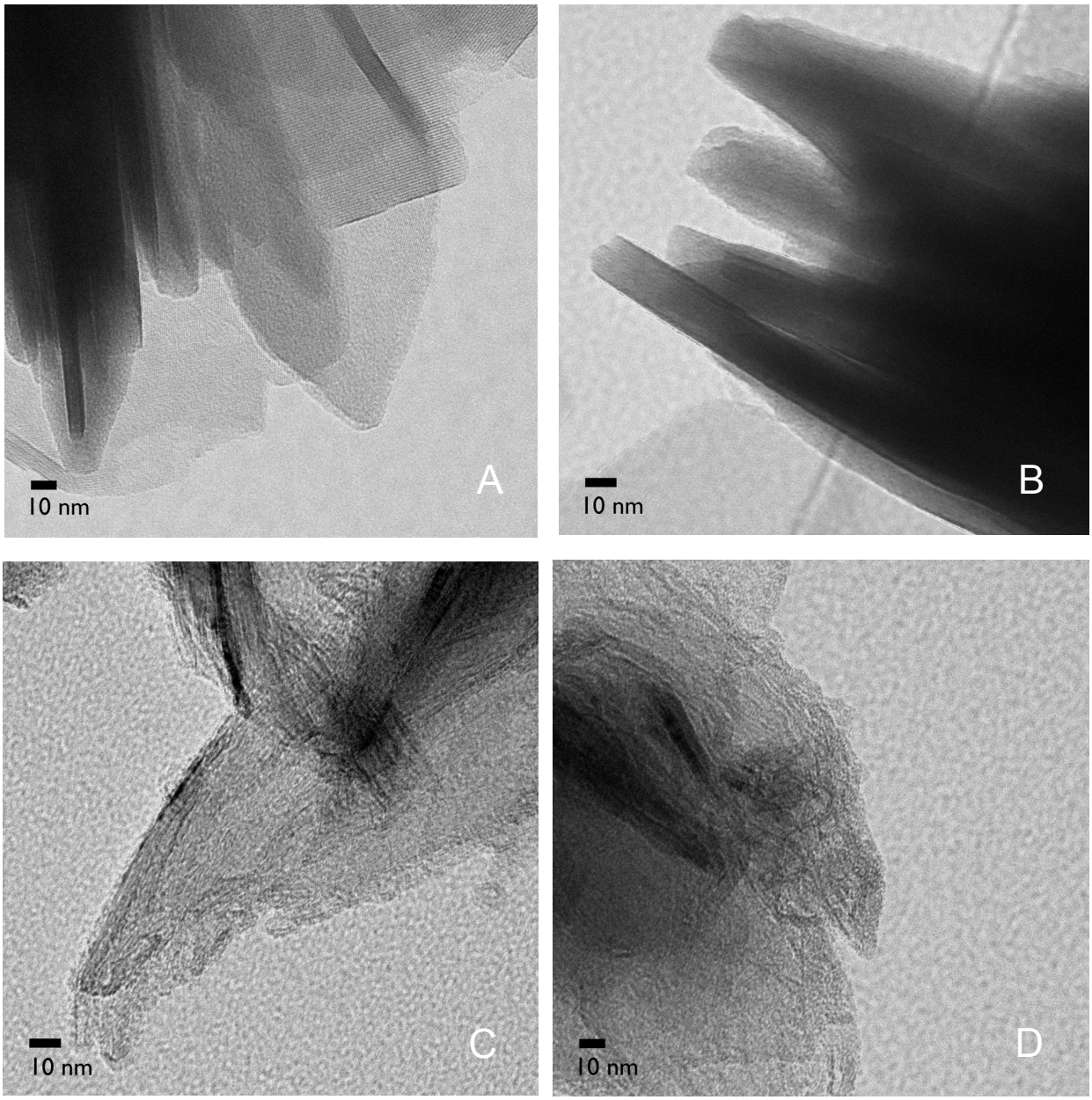

Figure 6.S.1: TEM images comparing MCM-22 (P) in (A) and (B) with as-made UCB-1 in (C) and (D) on similar length scales where MCM-22 (P) consists of an array of lamellar sheets, each of which consists of a rectilinear plate in (A) and (B). As-made UCB-1 consists of curved layers that have been split apart in (C) and (D), and lacks long-range order.

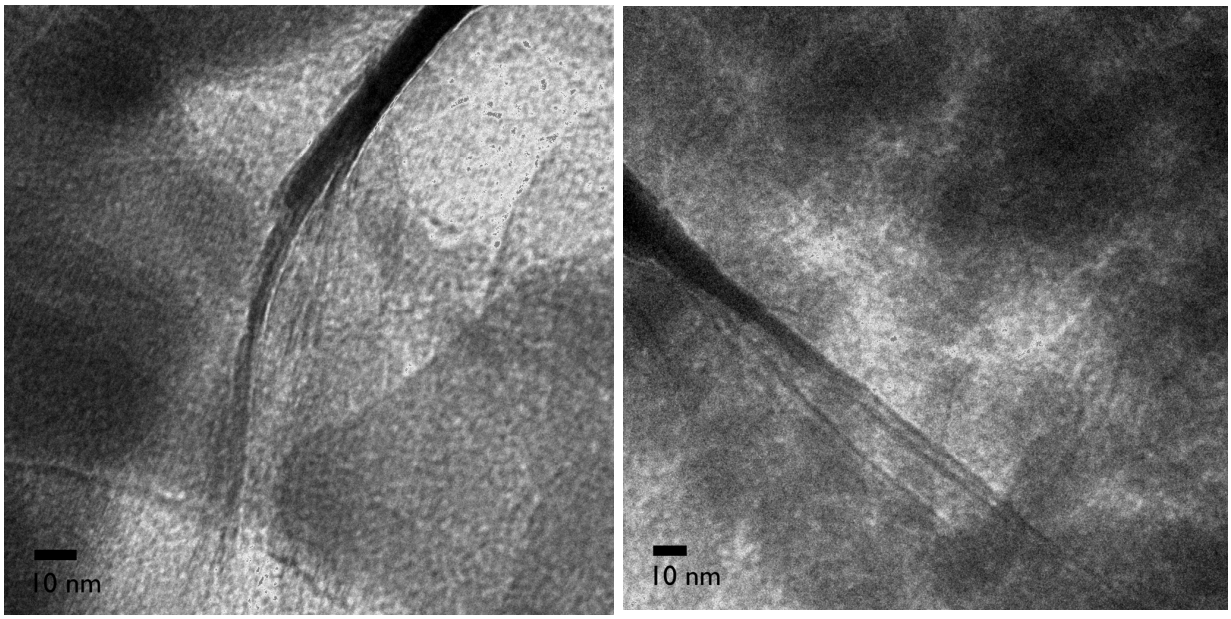

Figure 6.S.2: TEM images characterizing the splitting off of a layer as a consequence of the delamination process in as-made UCB-1.

6.2.4 FTIR Spectra

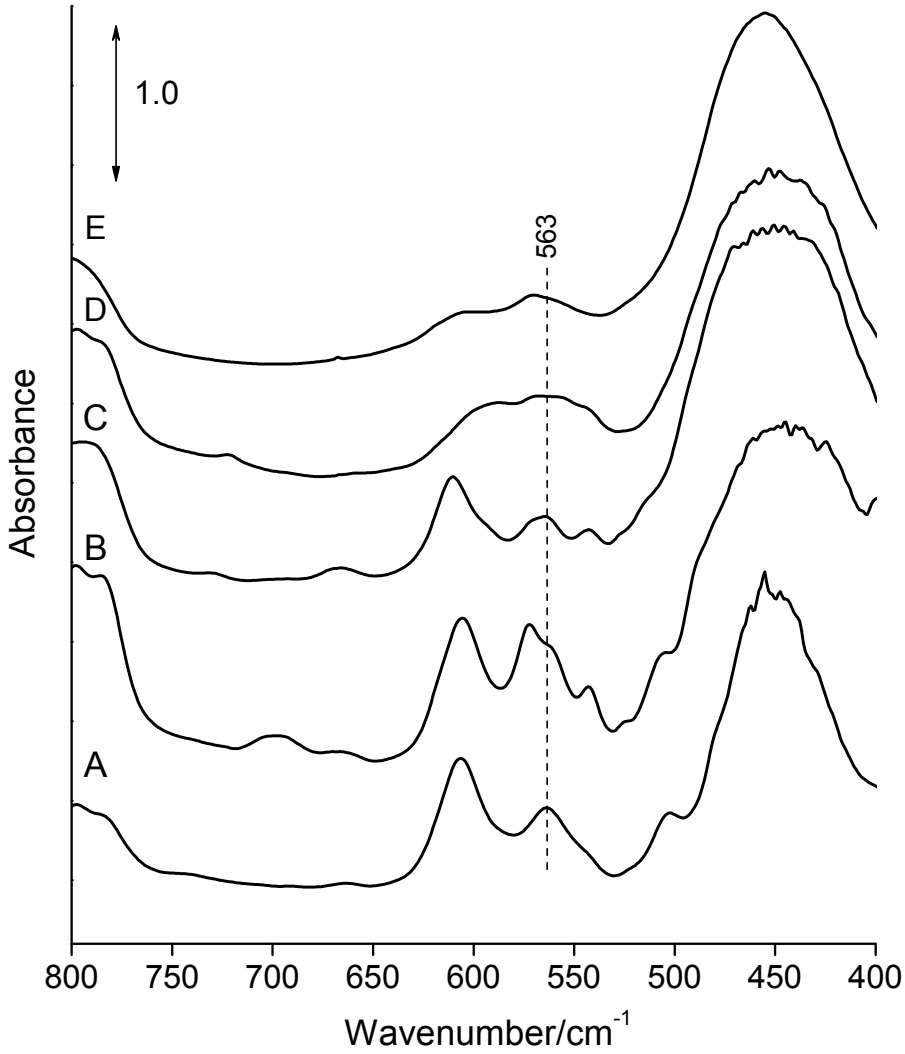

Figure 6.S.3: Fourier transform infrared (FTIR) spectrum of (A) MCM-22 (P) with Si/Al ratio of 50, (B) as-made UCB-1, (C) calcined UCB-1, (D) as-made ITQ-2, and (D) calcined ITQ-2. The labeled band at 563 cm^{-1} corresponds to a pentasil structure in the framework, which is slightly shifted from its previously reported value of 550 cm^{-1}. [9] This shift is due to the differing Si/Al ratios between MCM-22 in reference [9], which consists of a Si/Al ratio of 15, and materials investigated in Figure 6.S.3, which all consist of a Si/Al ratio of 50. Synthesis of both UCB-1 and ITQ-2 involved steps consisting of swelling of MCM-22 (P) at 353 K for 16 h, and acidification to pH 2. Both as-made UCB-1 and ITQ-2 were calcined at 823 K for 12 h in N_2/O_2.

6.2.5 NMR Spectra

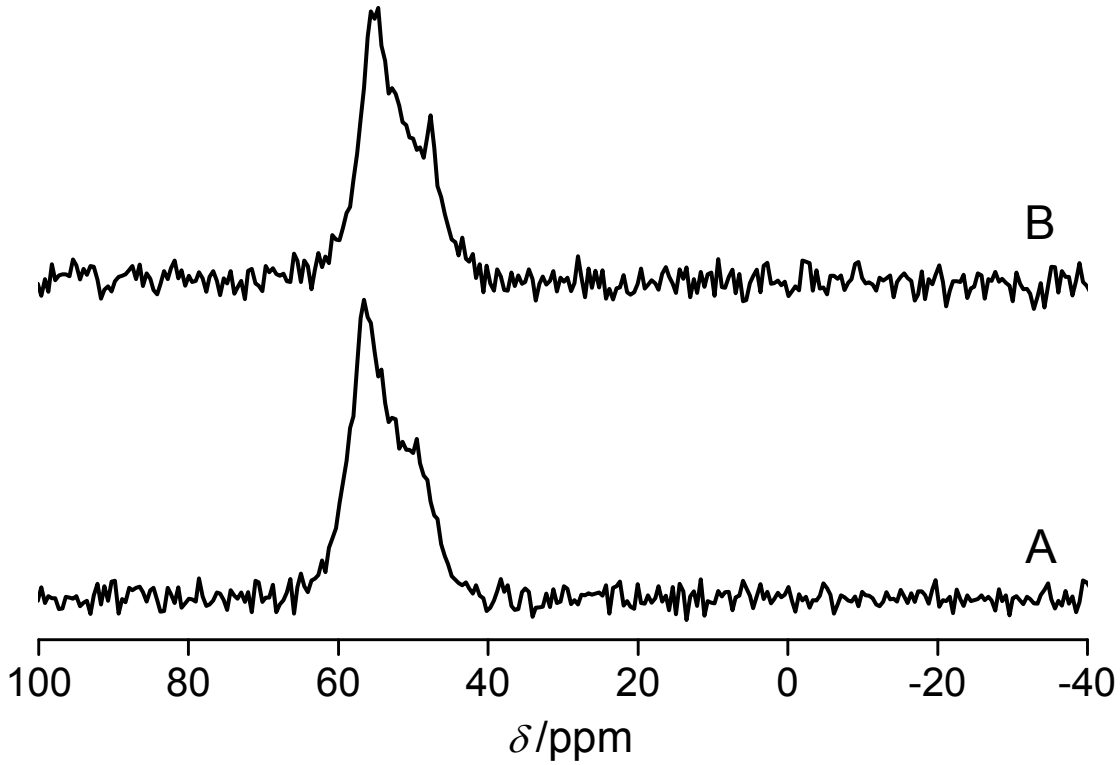

Figure 6.S.4: ^{27}Al MAS NMR spectra characterizing (A) MCM-22 (P) (Si/Al ratio = 50) and (B) the as- made UCB-1. The as-made UCB-1 was washed according to procedures described by Bein *et al*. [10] in order to remove templates.

6.2.6 Adsorption-desorption isotherms

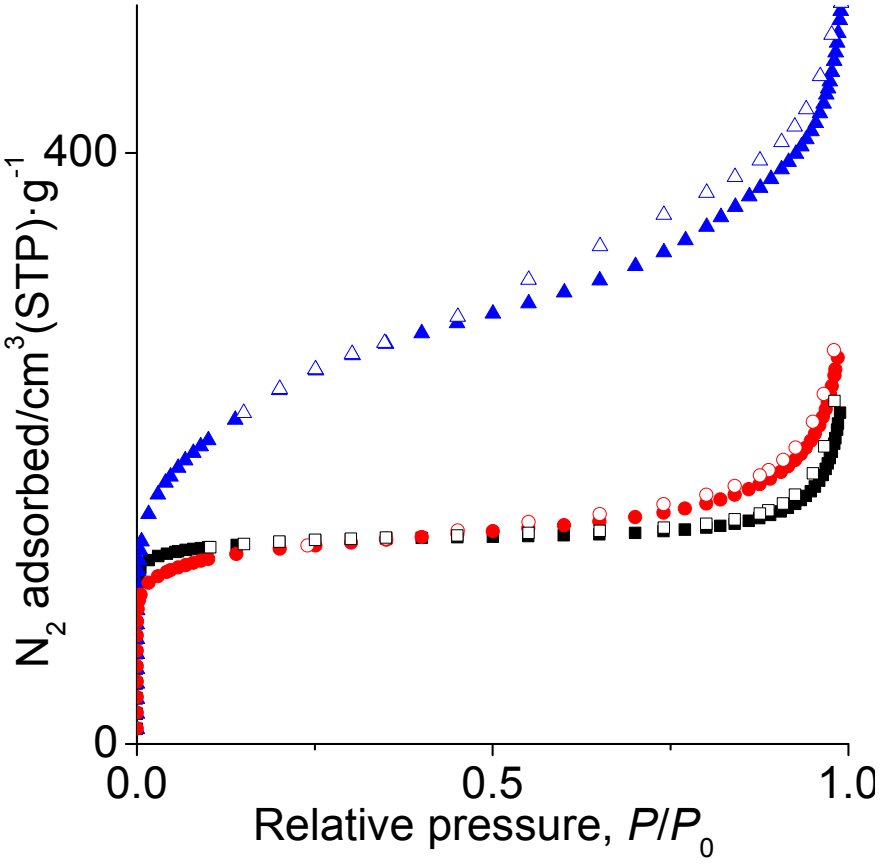

Figure 6.S.5: Adsorption-desorption isotherms of (▲: adsorption, △: desorption) ITQ-2, (●: adsorption,○:desorption) UCB-1, and (■: adsorption, □: desorption) MCM-22.

6.2.7 TEM of as-made ITQ-2

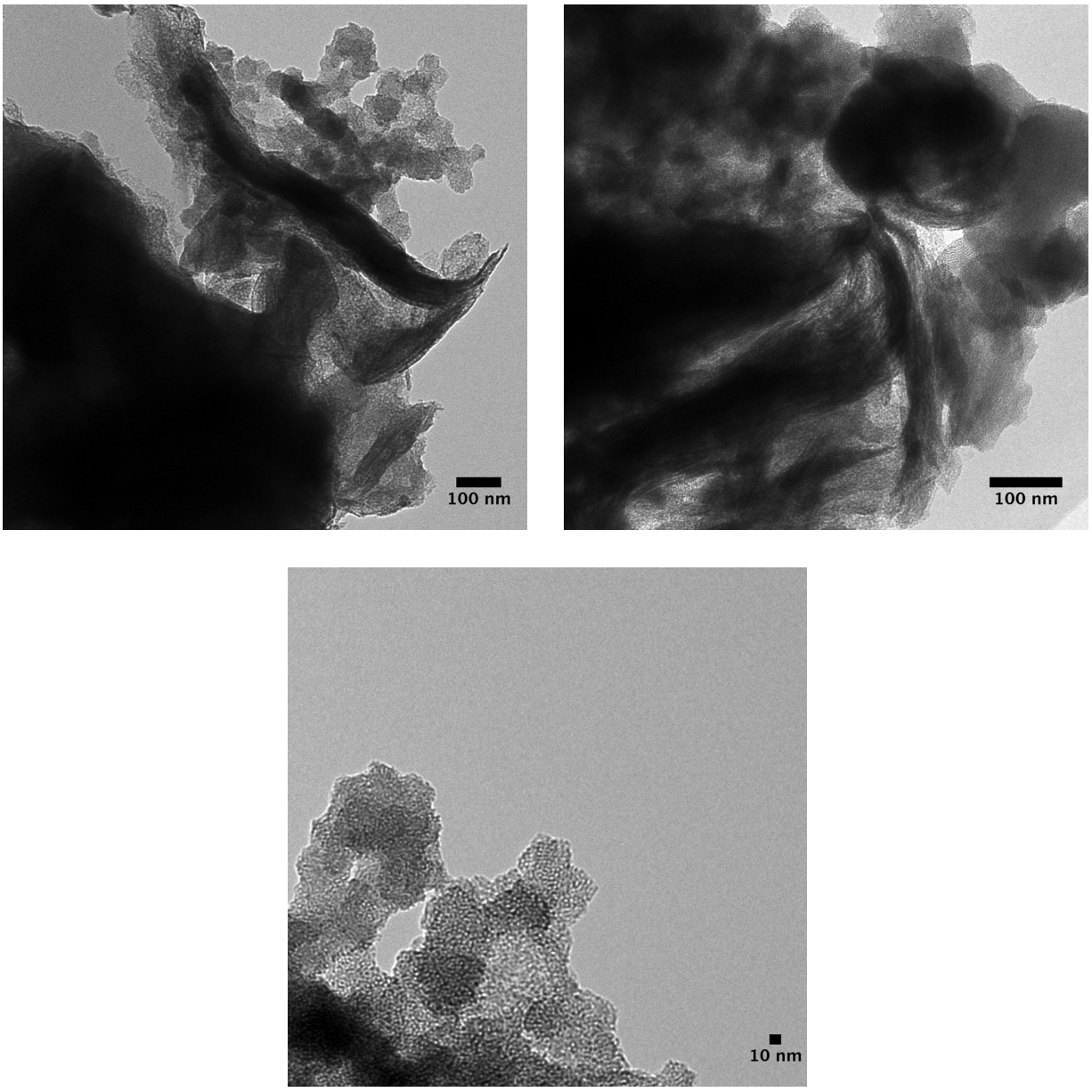

Figure 6.S.6: TEM images charactering as-made ITQ-2 zeolite show mesoporosity that is likely a consequence of silica amorphization during delamination.

6.2.8 Cumulative pore volume measurements

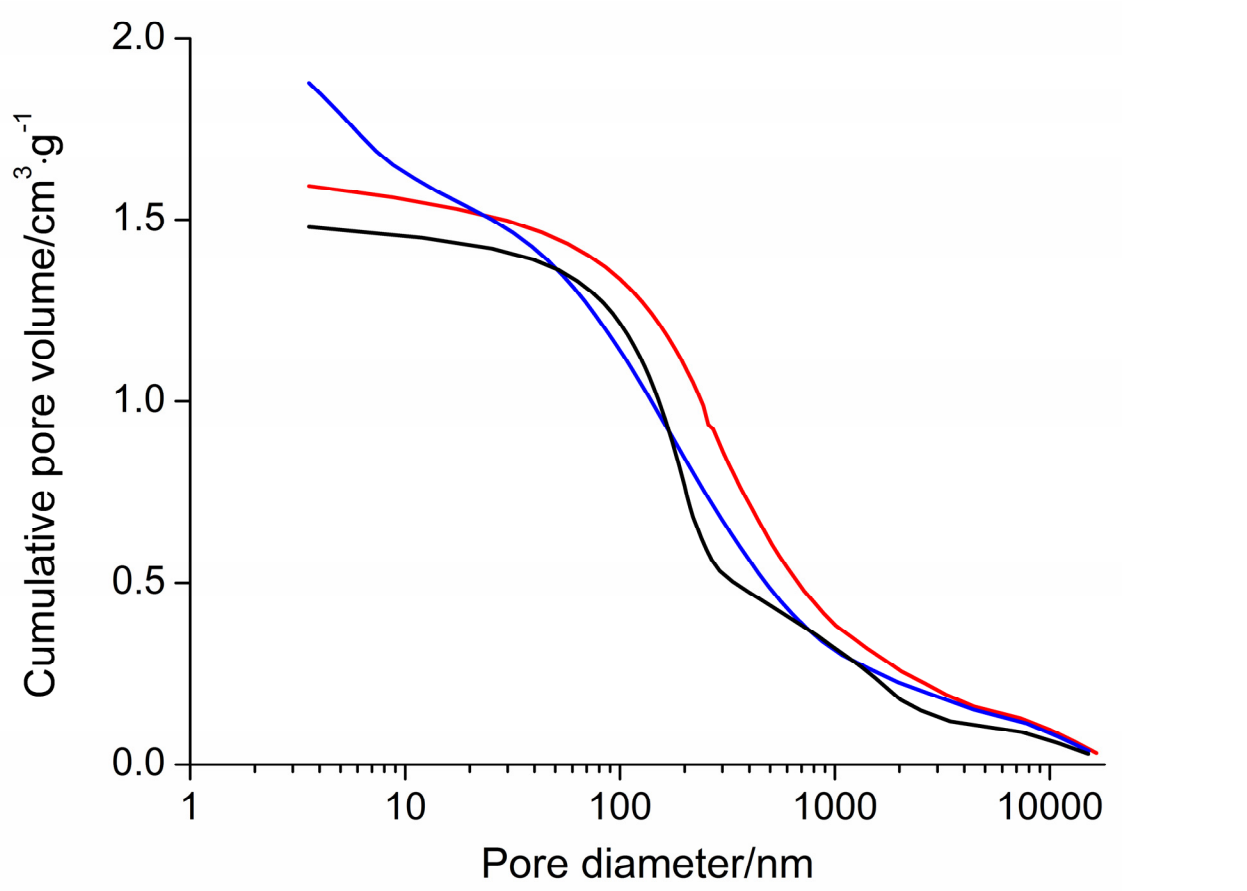

Figure 6.S.7: Cumulative pore volumes measured via mercury porosimetry for the following samples: black line, MCM-22 zeolite; blue line, ITQ-2 zeolite; red line, new material.

6.2.9 ^{19}F MAS NMR of as-made UCB-1

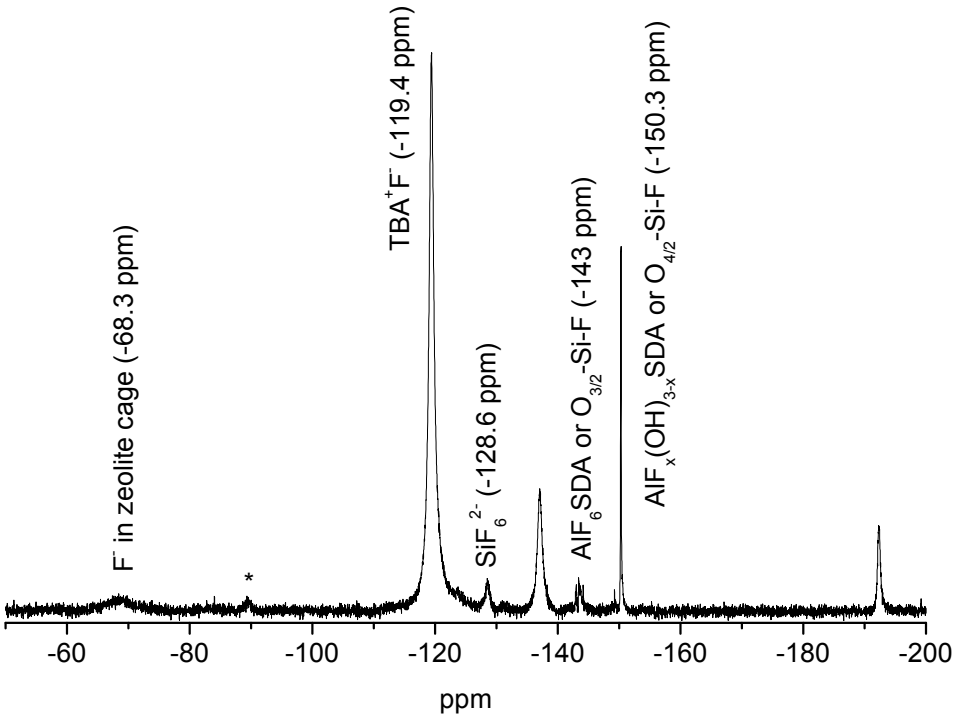

Figure 6.S.8: ^{19}F MAS NMR of as made UCB-1

6.2.10 PXRD of MCM-22

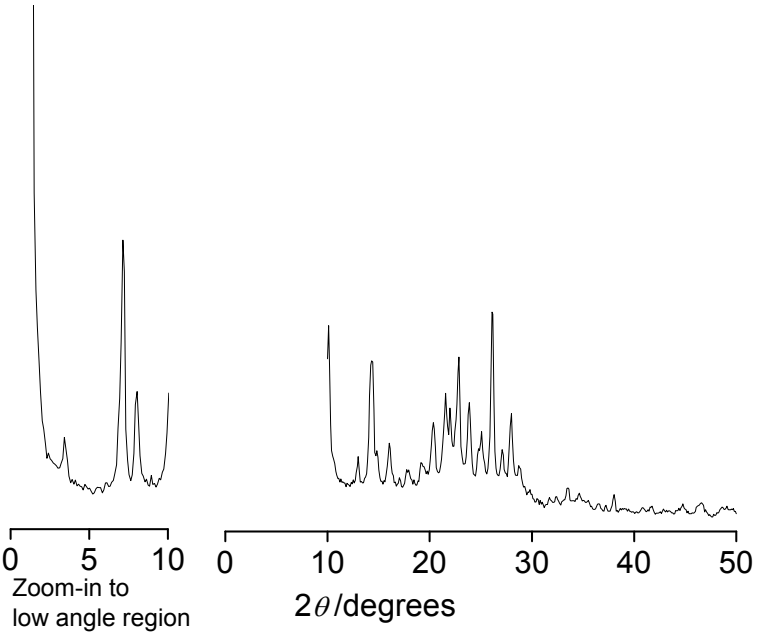

Figure 6.S.9: Powder X-ray diffraction pattern characterizing MCM-22 after the sample was treated under the same conditions as those used to synthesize UCB-1.

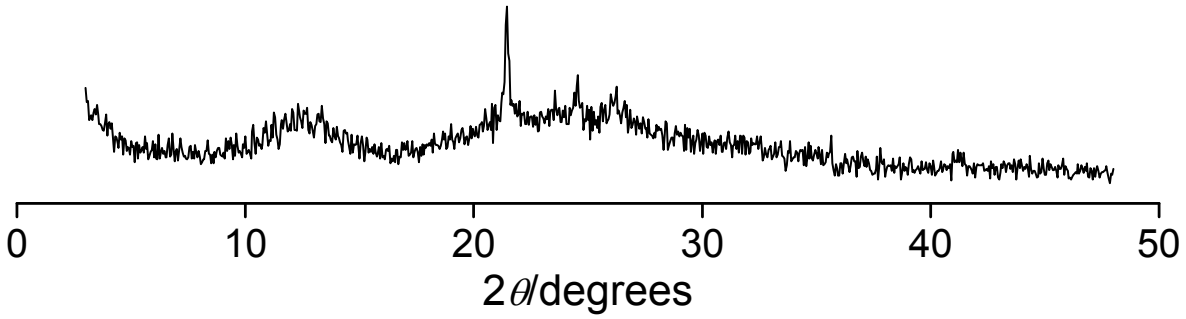

Figure 6.S.10: Powder X-ray diffraction pattern characterizing MCM-22 after the sample was treated under the same conditions as those used to synthesize ITQ-2 zeolite.

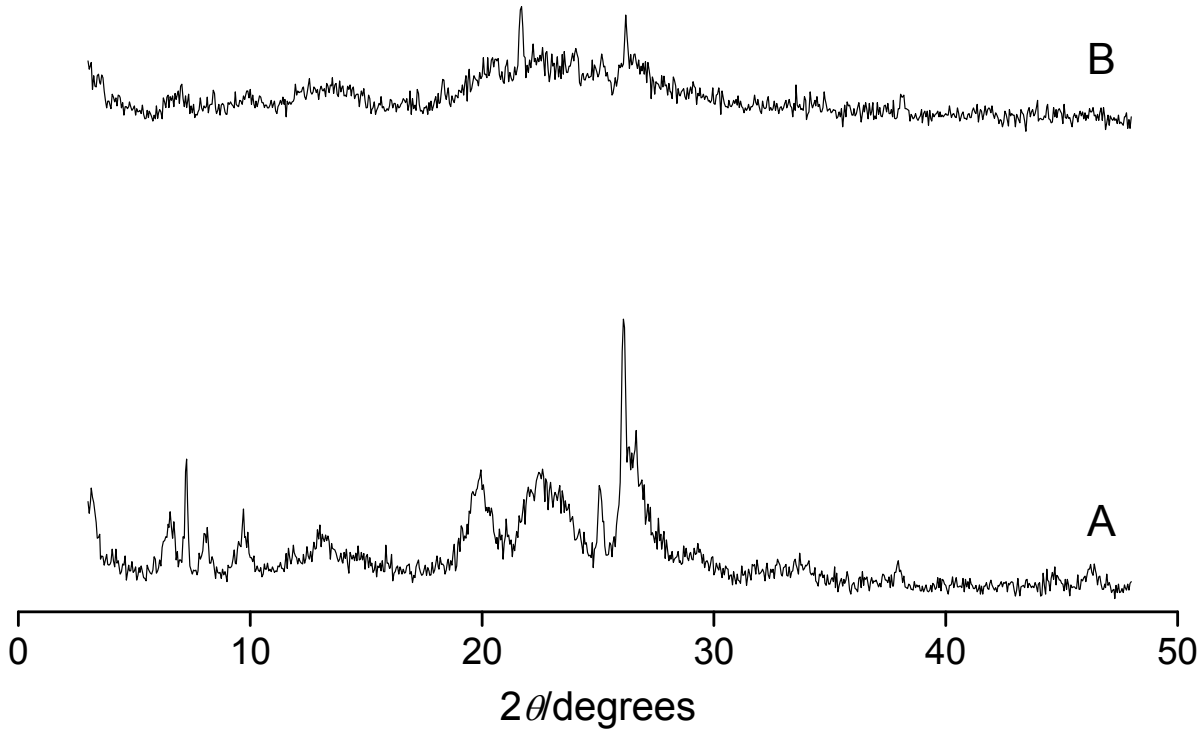

Figure 6.S.11: Powder X-ray diffraction patterns characterizing (A) MCM-22 (P) (Si/Al ratio = 20) and (B) the same sample after delamination by the fluoride/chloride anion-promoted method.

6.2.11: References for Section 6.2

[1] S.I. Zones, *Zeolites*, 9 (1989) 458.
[2] A. Corma, M. Díaz-Cabañas, J. Martínez-Triguero, F. Rey, J. Rius, *Nature*, 418 (2002) 514.
[3] S. Maheshwari, E. Jordan, S. Kumar, F.S. Bates, R.L. Penn, D.F. Shantz, M. Tsapatsis, *J. Am. Chem. Soc*., 130 (2008) 1507.
[4] Tatsumi *et al*. [5] reported the yield of 83% after swelling of MCM-22 (P) without sonication.
[5] P. Wu, D. Nuntasri, J.F. Ruan, Y.M. Liu, M.Y. He, W.B. Fan, O. Terasaki, T. Tatsumi, *J. Phys. Chem. B*, 108 (2004) 19126.
[6] W.J. Roth, J.C. Vartuli, *Stud. Surf. Sci. Catal*., 141 (2002) 273.
[7] A. Corma, V. Fornés, J. Martínez-Triguero, S.B. Pergher, *J. Catal*., 186 (1999) 57.
[8] S.J. Gregg, K.S.W. Sing, *Adsorption, surface area, and porosity*; U.S. ed.; Academic Press: London, New York, 1967.
[9] A. Corma, C. Corell, J. PérezPariente, J.M. Guil, R. López, S. Nicolopoulos, J.G. Calbet, M. ValletRegi, *Zeolites*, 16 (1996) 7.
[10] J. Kecht, T. Bein, *Microporous Mesoporous Mater*., 116 (2008) 123.

6.3 Acknowledgements

We acknowledge Prof. Enrique Iglesia for generosity in resources and for useful discussion about porosity in these types of materials, Dr. Alexander Kuperman at Chevron for helpful discussion regarding delamination mechanism, and Dr. Anja Rumplecker for assistance in the syntheses of MCM-22 (P) and ITQ-2 zeolites. We are grateful to the Management and Transfer of Hydrogen via Catalysis Program funded by Chevron Corporation for financial support. The NMR facility at Caltech is supported by the National Science Foundation (NSF) under the Grant Number 9724240 and partially supported by the MRSEC program of NSF under Award Number DMR-520565.

6.4 References

[1] A. Corma, V. Fornés, S.B. Pergher, T.L.M. Maesen, J.G. Buglass, *Nature*, 396 (1998) 353.
[2] A. Corma, U. Díaz, M.E. Domíne, V Fornés, *J. Am. Chem. Soc*., 122 (2000) 2804.
[3] A. Corma, U. Díaz, M.E. Domíne, V. Fornés, *Angew. Chem., Int. Ed*., 39 (2000) 1499.
[4] A. Corma, V. Fornés, U. Díaz, *Chem. Commun*., 2001, 2642.
[5] J. Aguilar, S.B.C. Pergher, C. Detoni, A. Corma, F.V. Melo, E. Sastre, *Catal. Today*, 133 (2008) 667.
[6] A. Corma, V. Fornés, J. Martínez-Triguero, S.B. Pergher, *J. Catal*., 186 (1999) 57.
[7] I. Rodríguez, M.J. Climent, S. Iborra, V. Fornés, A. Corma, *J. Catal*., 192 (2000) 441.
[8] P. Botella, A. Corma, S. Iborra, R. Montón, I. Rodríguez, V. Costa, *J. Catal*., 250 (2007) 161.
[9] A. Corma, H. García, J. Miralles, *Microporous Mesoporous Mater*., 43 (2001) 161.
[10] R. Schenkel, J.O. Barth, J. Kornatowski, J. Lercher, *Stud. Surf. Sci. Catal*. 142A (2002), 69.

[11] S. Maheshwari, E. Jordan, S. Kumar, F.S. Bates, R.L. Penn, D.F. Shantz, M. Tsapatsis, *J. Am. Chem. Soc*., 130 (2008) 1507.
[12] W.J. Roth, J.C. Vartuli, *Stud. Surf. Sci. Catal*., 141 (2002) 273.
[13] P. Wu, D. Nuntasri, J.F. Ruan, Y.M. Liu, M.Y. He, W.B. Fan, O. Terasaki, T. Tatsumi, *J. Phys. Chem. B*, 108 (2004) 19126.
[14] P.G.M Wuts, T.W. Greene, *Greene's Protective Groups in Organic Synthesis*; Wiley-Interscience: New York, 2007.
[15] H. Koller, A. Wölker, H. Eckert, C. Panz, P. Behrens, *Angew. Chem., Int. Ed*., 36 (1997) 2823.
[16] H. Koller, A. Wölker, L.A. Villaescusa, M.J. Díaz-Cabañas, S. Valencia, M.A. Camblor, *J. Am. Chem. Soc*., 121 (1999) 3368.
[17] J.L.Trompette, L. Arurault, S. Fontorbes, L. Massot, *Electrochim. Acta*, 55 (2010) 2901.
[18] M.A. Camblor, A. Corma, S. Valencia, *J. Chem. Soc., Chem. Commun*., 1996, 2365.
[19] A. Corma, C. Corell, J. Pérez-Pariente, J.M. Guil, R. Guil-López, S. Nicolopoulos, J.G. Calbet, M. Vallet-Regi, *Zeolites*, 16 (1996) 7.
[20] S.L. Lawton, A.S. Fung, G.J. Kennedy, L.B. Alemany, C.D. Chang, G.H. Hatzikos, D.N. Lissy, M.K. Rubin, H.K.C. Timken, S. Steuernagel, D.E. Woessner, *J. Phys. Chem*., 100 (1996) 3788.
[21] M.E. Leonowicz, J.A. Lawton, S.L. Lawton, M.K. Rubin, *Science*, 264 (1994) 1910.
[22] S.A.I. Barri, G.W. Smith, D. White, D. Young, *Nature*, 312 (1984) 533.
[23] A. Corma, V. Fornés, J.M. Guil, S. Pergher, T.L.M. Maesen, J.G. Buglass, *Microporous Mesoporous Mater*. 38 (2000) 301.
[24] L.J. Criscenti, R.T. Cygan, A.S. Kooser, H.K. Moffat, *Chem. Mater*., 20 (2008) 4682.
[25] M.R. Das, J.M. Borah, W. Kunz, B.W. Ninham, S. Mahiuddin, *J. Colloid Interface Sci*., 344 (2010) 482.
[26] B. W. Ninham, V. Yaminsky, *Langmuir*, 13 (1997) 2097.
[27] M.A. Camblor, P.A. Barrett, M.J. Díaz-Cabañas, L.A. Villaescusa, M. Puche, T. Boix, E. Pérez, H. Koller, *Microporous Mesoporous Mater*., 48 (2001) 11.

CHAPTER 7:

Single-pot synthesis of uniform glucan multilayers on oxide particles

a collaboration between
Joseph Jankolovits, Oz Gazit, Michael Nigra, and Alexander Katz

7.1 Main text

Nanoscale polymer coatings tune the surface chemistry of solids, and are used ubiquitously in functional materials for stabilizing dispersions, biocompatibilization, and controlled release, to name a few applications. [1-4] In an effort to increase sustainability, there is growing interest in developing functional materials from abundant biomass-derived polymers, such as poly(1→4)-β-glucan (β -glu) from crystalline cellulose. However, until now, it has not been possible to prepare polymer coatings directly from β -glu, the most prevalent polymer in biomass, without derivatization due in part to the propensity of β -glu strands to phase separate into dense microcrystalline domains. [5,6] In this manuscript, we synthesize nanocoatings consisting of multilayers of β -glu strands on a porous inorganic-oxide surface by leveraging on our recent success in synthesizing grafted β -glu monolayers. [7-9] We demonstrate that our method: (i) leads to remarkably stable nanocoatings due to the covalent connectivity between polymer layers, (ii) is accomplished in a single step and in high yield, (iii) generates uniform nanocoatings without catalysts or surfactants, and (iv) offers synthetic tunability.

Our novel Multilayers through Imbibed Crosslinker (MIC) approach is illustrated in Scheme 7.1. The β -glu grafts to a reactive surface, while simultaneously, imbibed $SiCl_4$ crosslinker diffuses from internal pores and covalently crosslinks the strands to generate a multilayered coating. [10] We demonstrate the MIC approach first with the synthesis of a β -glu nanocoating on R706, a commercially available TiO_2 paint pigment that contains a ~3 nm porous aluminosilicate overlayer. In the area of paints and related dispersions, uniform nanoscale coatings are invaluable for mitigating aggregation of pigment particles. Due to such aggregation, these particles must be used in large excess and currently represent the most energy-intensive component of commercial paint formulations. [11]

The MIC approach was conducted by treating dry R706 with $SiCl_4$ in an inert atmosphere, followed by partial removal of excess $SiCl_4$ under vacuum to yield powder that is dry in appearance but contains $SiCl_4$ imbibed within pores. $SiCl_4$ has a dual role in the MIC method. It activates the surface through a condensation reaction with surface OH-defect sites by forming ≡-O-$SiCl_3$ groups. Such activated surfaces have been previously been used to graft β-glu monolayers [7-9] and calixarene macrocycles. [12] The second role of $SiCl_4$ is to crosslink β-glu strands, since Cl-Si-Cl functional groups are known to achieve such crosslinking. [12] Thus, upon subsequent addition of a dilute and well-stirred β-glu solution in LiCl/dimethacetamide (DMAc) [14] to the porous oxide imbibed with $SiCl_4$, a β-glu layer is grafted on the activated R706 surface, and, concurrently, diffusion of imbibed $SiCl_4$ leads to β-glu crosslinking in the immediate vicinity of the surface, resulting in the formation of a multilayer β-glu coating.

Nanocoatings were prepared using the MIC approach in which the evacuation and β-glu treatment were performed at 0°C and room temperature (materials R706-MIC-0°C and R706-MIC-23°C, respectively). Thermogravimetric analysis of these materials (Table 7.1 and Figures 7.S.1, 7.S.2) reveals β-glu loadings consistent with an estimated 16 β-glu layers for R706-MIC-0°C and 9.6 β-glu layers for R706-MIC-23°C (see supporting information for a description of these estimates). We rationalize the reduced β-glu loading observed at room temperature relative to 0°C on the basis of less imbibed $SiCl_4$ being retained when evacuating at higher temperature. ^{13}C CPMAS NMR spectroscopy of R706-MIC-23°C shows a lack of crystalline cellulose resonances, as observed prevously for grafted glucan monolayers on inorganic-oxide surfaces, [8] suggesting that the multilayers in our nanocoating consist of discrete crosslinked β-glu strands and not cellulose crystallites (Figure 7.S.3). This conclusion was further supported by

observing the same ^{13}C CPMAS NMR spectum for R706-MIC-23°C as for a control material consisting of a monolayer of ^{13}C-labelled β-glu on R706 (Figure 7.S.4).

The β-glu-coated R706 particles were visualized with HAADF-STEM by using an $OsO_4/K_3Fe(CN)_6$ stain to provide sufficient contrast for the polymer multilayers. [15] This positive stain is known to interact with vicinal 1,2-diols at the C_2 and C_3 positions of the glucose units and has been previously used in histochemistry without disrupting the polymer backbone. [16] Typical images of the stained R706-control and R706-MIC-0°C are displayed in Figure 7.1. In Figure 7.1a and 7.1b, the ~3 nm aluminosilicate overlayer and polydispersity of R706 is evident. Upon prolonged exposure in our experiments, this overlayer did not experience beam damage. [17]

Table 7.1: TGA analysis of the mass loading and coverage of β-glu multilayers on R706 and SiO_2 supports

Sample	Mass loss vs. control[a] (%)	Est. β-glu loading[b] (mg/g support)	Est. # of β-glu layers[b]
R706-MIC-0°C	8.2	90	16.4
R706-MIC-23°C	5.0	53	9.6
R706-RC-0°C	4.0	42	7.7
R706-RC-23°C	1.2	12	2.2
R706-monolayer	0.2	1.6	0.3
R706-EC-MIC-23°C	5.2	55	10
SiO_2-MIC-23°C	16.8	215	5.0
SiO_2-monolayer	0.6	5.8	0.1

[a] R706-control from 220 - 750 °C, SiO_2-control from 250-750 °C, [b] See the supporting information for estimation details.

In Figures 7.1b – 7.1e, the nanocoating on R706-MIC-0°C is observed with less contrast than the R706 core and possesses a 15-20 nm thickness. As shown in Figure 7.1e, effectively each R706-MIC-0°C particle has this coating completely surrounding the R706 core with consistent thickness between particles. Beam damage is evident upon prolonged exposure in the microscope (Figure 7.S.5), demonstrating the coating is an organic material, [18] which contrasts the inorganic aluminosilicate coating imaged on R706-control (vide supra). Moreover, the coating thickness and coverage is consistent between different batches of R706-MIC-0°C (Figure 7.S.6). HAADF-STEM micrographs show that the coating on R706-MIC-23°C has comparable uniformity, though slightly lower thickness than R706-MIC-0°C (Figure 7.S.7). Crucially, there was no evidence in our HAADF-STEM micrographs for any crosslinked polymer colloids (CPCs), which in principle could have formed in bulk solution during nanocoating synthesis. Also, dynamic light scattering (DLS) data demonstrates that R706-MIC-0°C and R706-MIC-23°C consist of individual and separate particles, suggesting that bridging flocculation does not occur during the nanocoating synthesis (Table 7.S.1).

We investigated the necessity of crosslinker imbibing during the MIC approach by intentionally releasing the $SiCl_4$ from the R706 pores to the bulk solution prior to adding β-glu during the nanocoating synthesis (R706-RC-0°C and R706-RC-23°C). This crosslinker release was performed by adding dry LiCl/DMAc to R706 pretreated and imbibed with $SiCl_4$ prior to adding β-glu solution. This control ensured that the total quantity of crosslinker in the reaction mixture remains the same as when conducting the MIC approach, while the effect of imbibing is

eliminated because $SiCl_4$ has diffused to the bulk solution. TGA data in Table 7.1 demonstrated lower β-glu loadings when the $SiCl_4$ is released. HAADF-STEM micrographs show that R706-RC-23°C particles have a thinner and less uniform β-glu coating than R706-MIC-23°C (Figure 7.S.8). These data implicate imbibing as a required procedure for efficiently achieving thick and uniform multilayer β-glu coatings with the MIC approach.

The molecular accessibility of the nanocoatings prepared via the MIC approach was investigated through the adsorption of toluidine blue-O and acridine orange, as shown in Figure 7.2. The uncoated R706-control material adsorbs both dyes, as shown by the y-intercept in Figure 7.2. The R706-MIC materials exhibit 2- to 4-fold greater adsorption than R706-control, with the dye capacity increasing with the mass of the β-glu coating in the sample. This linear relationship demonstrates the accessibility of the nanocoating because these large dye molecules penetrate the coating and reach the core R706 surface. This linear relationship is also suggestive of molecular-scale uniformity of the nanocoating between R706-MIC-0°C and R706-MIC-23°C. The dye capacity in the R706-MIC materials corresponds to approximately a single dye molecule for every 8 cellubiose-repeat units in the nanocoating, whereas the *y*-intercept corresponds to approximately 0.6 dye molecules per nm^2 of surface area (internal and external) in the R706 core. The type-I profiles of the dye adsorption isotherms (inset of Figure 7.2) suggest the porosity in the nanocoatings is on a similar length scale to the dye molecules and therefore is in the microporous regime. Dye adsorption occurred faster than we could accurately measure (less than five minutes) presumably due to the small coating thickness (less than 20 nm). Unlike the cationic dyes above, the anionic dye fluorescein exhibited was not adsorbed by R706-control or the R706-MIC materials. Since the R706 surface is negatively charged based on zeta potential measurements (Figure 7.S.9), this selectivity suggests that the surface charge strongly influences adsorption in the nanocoating, which would be expected based on double-layer thickness considerations.

Given the importance of electrostatic effects in stabilizing dispersions,[4] we introduced carboxylate functional groups in the nanocoating using TEMPO-catalyzed oxidation of the primary alcohols in the β-glu strands (Figure 7.3A). [19] We subsequently studied dispersion stability by measuring light transmission through a suspension following centrifugation, as described in Figure 7.3b. Aggregation of the unstable R706 and R706-control dispersions results in their sedimentation to yield nearly transparent solutions after settling for a period of several hours, as shown in Figure 7.3c, or upon centrifugation. The nanocoating on R706-MIC-0°C and R706-MIC-23°C leads to modestly improved dispersion stability for the TiO_2 pigment, but the carboxylated coatings result in a greater stabilization effect. This improvement is attributed to the combined electrostatic effect of the increased charge from the carboxylates and sterics that result from swelling of the carboxylated β-glu coating. [20-23] These results suggest promise for using MIC coatings to enhance the dispersion stability of particles in paints and other suspensions.

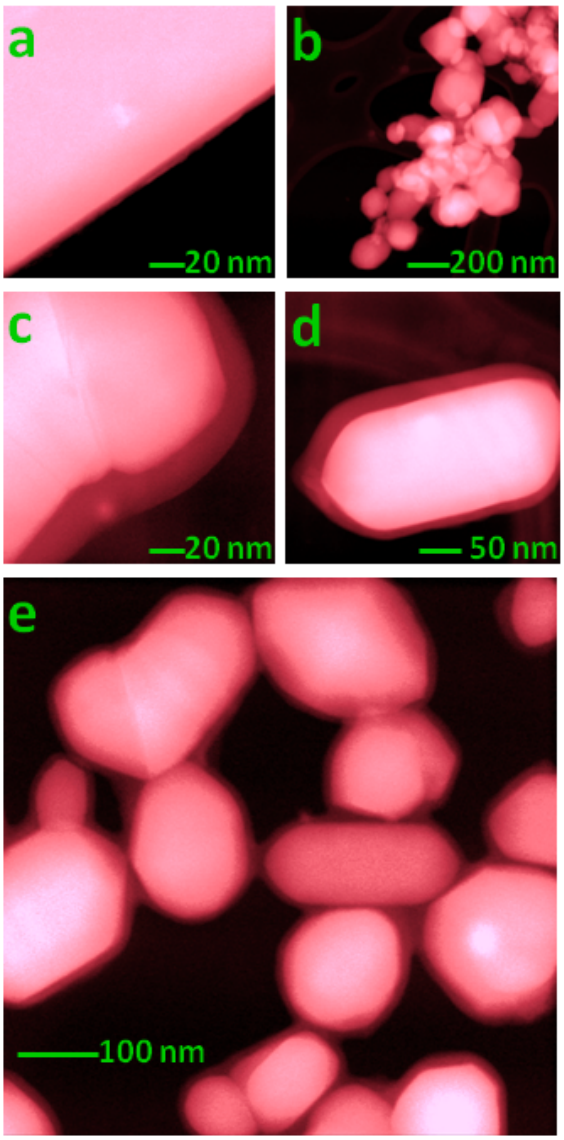

Figure 7.1: HAADF-STEM images of $OsO_4/K_3Fe(CN)_6$ stained a,b) R706-control and c,d,e) R706-MIC-0°C. The ~15-20 nm coating seen on R706-MIC-0°C experiences beam damage, while the R706-control does not.

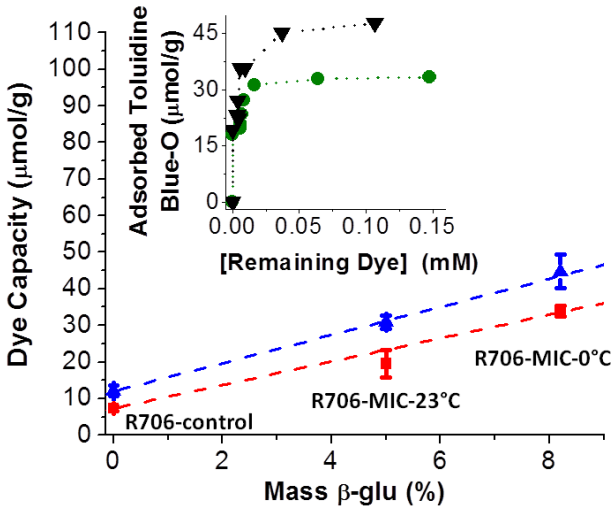

Figure 7.2: Relationship between the dye capacity of the R706-materials in pH 8.0 aq. tris buffer for toluidine blue-O (▲) and acridine orange (■) and the mass percent of β-glu in the nanocoating with best linear fits as dashed lines. The linearity suggests that the dyes penetrate the nanocoating and are adsorbed in the β-glu layers. Inset) Adsorption isotherm for toluidine blue-O and R706-MIC-0°C (▼) and R706-MIC-0°C (●) with dotted traces to guide the eye showing the steep type-1 behavior, consistent with the multilayer structure of the coating possessing microporosity.

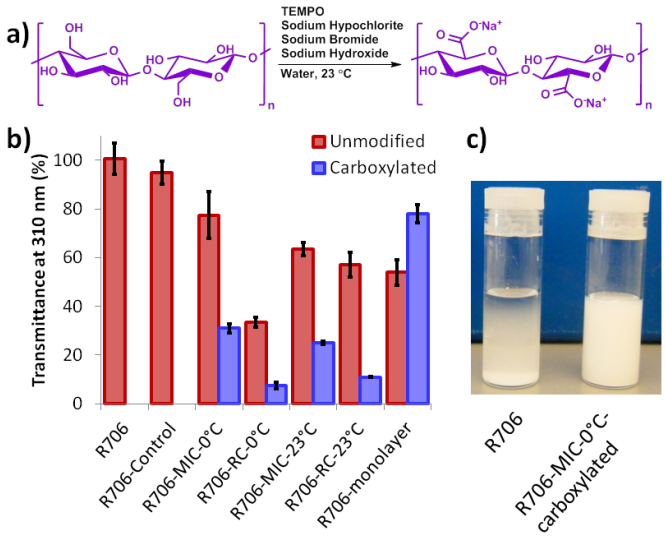

Figure 7.3: a) Reaction scheme for the TEMPO catalyzed oxidation of the β-glu coating to generate carboxylate groups, b,c) Demonstration of the enhanced dispersion stability of R706 coated with β-glu and carboxylated β-glu using b) light transmittance at 310 nm and c) photographs of 1 mg/mL suspensions in 10 mM pH 8.0 aq. tris buffer after settling for 2 hours.

To support the generality of the MIC aproach, R706 was coated with ethyl cellulose (R706-EC-MIC-23°C) using a nearly identical synthetic approach as when using β-glu for R706-

MIC-23°C. The R706-EC-MIC-23°C material has a 10-15 nm coating thickness based on HAADF-STEM (Figure S10), and the ethyl-cellulose mass loading is approximately 55 mg/g, which is similar to R706-MIC-23°C. To further demonstrate generality, β-glu multilayers were synthesized on microporous silica particles (SiO_2-MIC-23°C). TGA of SiO_2-MIC-23°C revealed an estimated 5.0 β-glu layers were grafted via the MIC procedure, which starkly contrasts the modest loading on the same SiO_2—prepared with monolayer coverage by complete removal of the imbibed $SiCl_4$. The Bloch-decay ^{13}C NMR spectrum of this SiO_2-monolayer material (synthesized using ^{13}C-labeled β-glu) exhibited resonances consistent with grafted, amorphous β-glu (Figure S11), [8] while quantitative integration of the Bloch-decay NMR spectrum supports the β-glu loading measured via TGA.

In summary, this work contributes to two goals for the sustainable production of polymer coatings: the use of renewable polymers directly from biomass and single-pot synthesis. A novel contribution to the synthetic toolbox for preparing polymer coatings in a single-pot [24-30] was presented that relies on imbibed crosslinker to localize polymer multilayer growth to the surface proximity of the support during synthesis. The resulting β-glu multilayer coating has uniform nanoscale thickness and surface coverage, is permeable to organic molecules, and can be functionalized with established cellulose modification chemistry. Because the single-pot MIC approach avoids cumbersome multiple-pot synthesis of crosslinked materials and utilizes biocompatible building blocks, it is expected to find broad usage in a wide array of applications in the future. The demonstrated capability for stabilizing pigment dispersions is one such possibility.

7.2 Experimental

Complete experimental details are provided in the supporting information. A representative MIC synthesis is described below.

R706-MIC-0°C) 1 g of R706 was dried under vacuum at 190 °C overnight in a 100 mL Schlenk flask. At room temperature, 6 mL of neat silicon tetrachloride ($SiCl_4$) was added under argon and stirred overnight. In an ice-water bath, the suspension was *partially* dried by first removing excess $SiCl_4$ under vacuum such that the solid has a dry appearance and constant pressure was reached on a digital vacuum gauge, and secondly by continuing the application of a vacuum for 10 minutes. Separately, 20 g of 0.6 % wt. β-glu dissolved in 0.8 % wt. LiCl in DMAc solution was passed through a 0.2 μm nylon syringe filter in a glovebox and cooled in an ice-water bath. The β-glu solution was added via cannula to the *partially* dried solid while stirring at 400 rpm under argon in an ice-water bath. After stirring for 3 minutes, the suspension was sonicated for 1 minute and then stirred overnight. The particles were isolated by room temperature centrifugation at 10 kG, and then washed using a general washing procedure: 8 % wt. LiCl in DMAc (twice, once overnight), DMAc (once), 10 % formic acid in methanol by volume (twice, once overnight), and water (twice, once overnight) by subsequent immersion, stirring, centrifugation, and decantation. The particles were dried first on a freeze dryer and lastly under vacuum at 120 °C overnight. Yield = 0.489 g.

7.3 Supporting information

7.3.1 Full experimental details

All reagents were used as received unless described otherwise. The chlorination and grafting procedures were performed in dry glassware using standard Schlenk techniques in an argon atmosphere or glove box techniques in a nitrogen atmosphere. Dimethylacetamide was dried by distillation over CaH_2 under argon. Dichloromethane was dried over alumina on a Glass Contour solvent system. Lithium chloride was dried at 190 °C under vacuum. The silica support consisted of Aldrich 10-20 nm particle size amorphous silica nanopowder. The silica surface was fully hydroxylated by refluxing in water overnight. R706 is a commercial pigment sold by DuPont under the trade name Ti-Pure R-706. R706 has a median particle size of 360 nm and is composed of a minimum of 93% rutile titanium dioxide prepared by the chloride process, coated with precipitated alumina (2.5 % wt.) and amorphous silica (3% wt.).

Dry amorphous poly(1→4,β-glucan) powder was prepared from Avicel following a reported method.[1] The 0.6% wt. β-glu in 0.8% wt. LiCl in DMAc solution was wet with dry amorphous poly(1→4,β-glucan) powder with anhydrous methanol in a nitrogen glove box, followed by solvent exchange with methanol once and DMAc three times, with the third being performed overnight. The amorphous poly(1→4,β-glucan) powder was then dissolved with vigorous magnetic stirring in 8% wt. LiCl/DMAc to make a 6% wt. β-glu solution. This solution was then diluted with dry DMAc to 0.6 wt% β-glu and passed through a 0.2 μm nylon filter in a nitrogen glovebox.

Ethyl cellulose solutions were prepared by first drying ethyl cellulose (Aldrich, 48% ethoxy groups) at 120 °C under vacuum. In a glovebox, ethyl cellulose was dissolved at room temperature in dry DMAc to prepare a 3% wt. solution.

TGA was performed on a Netzsch 449C Jupiter TGA equipped with a QMS 403 Aëlos quadrupole mass spectrometer. The carrier gas was 20% O_2/ 80% Ar. 20-30 mg of the samples were loaded in alumina crucibles and equilibrated in the instrument for 30 minutes prior to the measurement. Samples were subject to a temperature ramping at 5 °C/min from room temperature to 120 °C, holding for 1 hour, and then increasing the temperature at 5 °C/min to 800 °C. Volatiles were sent through a 230 °C fused silica capillary to the mass spectrometer.

Dynamic light scattering (DLS) and zeta potential measurements were performed on a Malvern Nano-Zetasizer. Size measurements were performed in disposable plastic cuvettes at 25 °C. All solutions were filtered through a 0.2 μm syringe filter. Samples were prepared by vortexing and sonicating ~0.1 mg/mL suspensions for at least 15 minutes. After vortexing again to suspend the sedimented particles, the suspensions were diluted approximately 10 fold and given sufficient time to equilibrate to 25 °C before measuring. The results from at least four measurements are averaged and the number-average particle size values are reported.

N_2 Physisorption analysis was performed on a Micrometrics ASAP 2020 instrument. Samples were degassed at 110 °C and nitrogen adsorption-desorption isotherms were measured at 77 K.

Dispersion stability was analyzed using UV-visible spectroscopy on an Agilent 8453 spectrometer. 1 mg/mL dispersions were vortexed and sonicated for at least 15 minutes. In 1.5 mL Eppindorf tubes, the suspensions were centrifuged at 1500 G for 90 seconds at room temperature. 1 mL of the solution was then carefully removed via pipet and transferred to a low volume cuvette and its absorption spectrum was collected immediately.

Solid-state ^{13}C DP NMR spectra are obtained using a Bruker DSX-500 spectrometer and a 4 mm Bruker CPMAS probe. Powder samples (~80 mg) are packed in ZrO_2 rotors and are spun at 8 kHz. Typical CP contact time is 1 ms, and the signal is averaged with a recycle delay time of 6 sec. The chemical shift is referenced to TMS.

HAADF-STEM micrographs were recorded using a 200 kV F20 UT Tecnai microscope at the National Center for Electron Microscopy at Lawrence Berkeley National Laboratory. Microscopy samples were prepared by staining with OsO_4 and $K_3Fe(CN)_6$ following a modified version of the reported method.[2] 10 mg of the material was immersed in 1 mL of a 1% osmium tetroxide solution 0.05 M potassium ferricyanide, 0.01 M pH 8.0 aqueous tris buffer. The suspensions were vortexed and sonicated for 30 seconds and set to react. After two hours, the solid was isolated by centrifugation, washed twice with 1 mL water and twice with methanol for 15 minutes each, and air dried. To prepare the grids, 0.1 mg/mL of the stained powder was suspended in 1 mL of deionized water. This suspension was sonicated for 15 minutes and one drop was placed on a copper/carbon mesh grid and allowed to evaporate. The black and white HAADF-STEM micrographs were given a red-hue by adjusting the picture temperature and tint in Windows Photo Gallery.

Dye adsorption experiments were performed in suspensions containing 1.5-5 mg of carefully weighed solid in 1-10 mL of 5 mM pH 8 aqueous tris buffer solution. The dye concentration ranged from 0.01-750 mM. The suspensions were sonicated and then stirred for at least 15 hours. The suspensions were then centrifuged at 14000 rpm for 5 minutes and the mother liquor was transferred via pipet to a 96 well plate. The plate was analyzed on a Spectramax M2 spectrophotometer at the absorption maximum for the dyes: 625 nm for toluidine blue-O and 490 nm for fluorescein. The quantity of adsorbed dye was determined by comparison to a control sample containing no absorbent.

7.3.2 Standard washing and drying procedures

After the reaction, the suspension was subject to centrifugation at 10 kG for 10 minutes at room temperature. The mother liquor was decanted and the solid was resuspended in about 20 mL of solution with the aid of vortexing and sonication and then agitated for at least 2 hours on a spinner. The solid was isolated by centrifugation at 10 kG and decantation of the solvent. The order of the solvent washes is as follows: twice with 8% wt. lithium chloride (LiCl) in dimethylacetamide (DMAc) (one of which is performed overnight), once with DMAc, twice with 10% by volume formic acid in methanol (one of which is performed overnight), and twice with water (one of which is performed overnight). After all washing steps, the solid was dried on a freeze dryer and subsequently dried under vacuum at 120 °C overnight.

7.3.3. Synthesis of β-glu coated materials

7.3.3.1 R706-MIC-23 °C

1 g of R706 was dried under vacuum at 190 °C overnight in a 100 mL schlenk flask. At room temperature, 6 mL of neat $SiCl_4$ was added via cannula transfer under argon and stirred overnight. In a room temperature water bath, the suspension was *partially* dried under vacuum by first removing excess $SiCl_4$ by vacuum such that the solid has a dry appearance and constant pressure was reached on a digital vacuum gauge, and secondly by continuing the application of a vacuum for 10 minutes. Separately, 20 g of a solution of 0.6% wt. β-glu dissolved in 0.8% wt. LiCl in DMAc was passed through a 0.2 μm nylon syringe filter in a glovebox. The filtered β-glu solution was added via cannula to the *partially* dried solid while stirring at 400 rpm under argon at room temperature. After stirring for 3 minutes, the suspension was sonicated for 1 minute and

then stirred overnight under argon. The β-glu coated particles were isolated by room temperature centrifugation at 10 kG, and then subject to the standard washing and drying procedure. Yield = 0.9693 g.

7.3.3.2 R706-RC-0 °C

1 g of R706 was dried under vacuum at 190 °C overnight in a 100 mL schlenk flask. At room temperature, 6 mL of neat $SiCl_4$ was added via cannula transfer under argon and stirred overnight. In an ice-water bath, the suspension was *partially* dried under vacuum by first removing excess $SiCl_4$ by vacuum such that the solid has a dry appearance and constant pressure was reached on a digital vacuum gauge, and secondly by continuing the application of a vacuum for 10 minutes. Next, 10 mL of 0.8 % wt. LiCl in DMAc was cooled in an ice bath and added via cannula to the *partially* dried solid. After three minutes of stirring, the suspension was sonicated for one minute, and then subjected to further stirring for one hour at 0 °C. Separately, 20 g of a solution of 0.6% wt. β-glu dissolved in 0.8% wt. LiCl in DMAc was passed through a 0.2 μm nylon syringe filter in a glovebox and cooled in an ice-water bath. The cold β-glu solution was added via cannula to the *partially* dried solid while stirring at 400 rpm under argon in an ice-water bath. After stirring for 3 minutes, the suspension was sonicated for 1 minute and then stirred overnight under argon. The β-glu coated particles were isolated by room temperature centrifugation at 10 kG, and then subject to the standard washing and drying procedure. Yield = 1.0299 g.

7.3.3.3 R706-RC-23 °C

1 g of R706 was dried under vacuum at 190 °C overnight in a 100 mL schlenk flask. At room temperature, 6 mL of neat silicon tetrachloride ($SiCl_4$) was added via cannula transfer under argon and stirred overnight. In a room temperature water bath, the suspension was *partially* dried under vacuum by first removing excess $SiCl_4$ by vacuum such that the solid has a dry appearance and constant pressure was reached on a digital vacuum gauge, and secondly by continuing the application of a vacuum for 10 minutes. Next, 10 mL of 0.8% wt. LiCl in DMAc was added via cannula to the *partially* dried solid at room temperature. After three minutes of stirring, the suspension was sonicated for one minute, and then subjected to further stirring for one hour at 4 °C. Separately, 20 g of a solution of 0.6% wt. β-glu dissolved in 0.8% wt. LiCl in DMAc was passed through a 0.2 μm nylon syringe filter in a glovebox. The room temperature β-glu solution was added via cannula to the *partially* dried solid while stirring at 400 rpm under argon in a room temperature water bath. After stirring for 3 minutes, the suspension was sonicated for 1 minute and then stirred overnight under argon. The β-glu coated particles were isolated by room temperature centrifugation at 10 kG, and then subject to the standard washing and drying procedure. Yield = 0.9679 g.

7.3.3.4 R706-monolayer

2 g of R706 was dried under vacuum at 190 °C overnight in a 100 mL schlenk flask. At room temperature, 11 mL of a dichloromethane solution containing 9 % by volume $SiCl_4$ was added via cannula transfer under argon and stirred overnight. The suspension was *completely* dried under vacuum at 60 °C for four hours. Separately, 40 g of a solution of 0.6% wt. β-glu

dissolved in 0.8% wt. LiCl in DMAc was passed through a 0.2 μm nylon syringe filter in a glovebox. The room temperature β-glu solution was added via cannula to the dry, chlorinated R706 while stirring at 400 rpm under argon in a room temperature water bath. After stirring for 3 minutes, the suspension was sonicated for 1 minute and then stirred overnight. The particles were isolated by room temperature centrifugation at 10 kG, and then subject to the standard washing and drying procedure. Yield = 1.9788 g.

7.3.3.5 R706-control

2 g of R706 was dried under vacuum at 190 °C overnight in a 100 mL schlenk flask. At room temperature, 11 mL of a dichloromethane solution containing 9 % by volume $SiCl_4$ was added via cannula transfer under argon and stirred overnight. The suspension was *completely* dried under vacuum at 60 °C for four hours. Separately, 40 g of a solution of 0.6% wt. β-glu dissolved in 0.8% wt. LiCl in DMAc was passed through a 0.2 μm nylon syringe filter in a glovebox. The room temperature β-glu solution was added via cannula to the dry, chlorinated R706 while stirring at 400 rpm under argon in a room temperature water bath. After stirring for 3 minutes, the suspension was sonicated for 1 minute and then stirred overnight. The particles were isolated by room temperature centrifugation at 10 kG, and then subject to the standard washing and drying procedure. Yield = 1.8304 g.

7.3.3.6 R706-EC-MIC-23 °C

1 g of R706 was dried under vacuum at 190 °C overnight in a 100 mL schlenk flask. At room temperature, 6 mL of neat $SiCl_4$ was added via cannula transfer under argon and stirred overnight. In a room temperature water bath, the suspension was *partially* dried under vacuum by first removing excess $SiCl_4$ by vacuum such that the solid has a dry appearance and constant pressure was reached on a digital vacuum gauge, and secondly by continuing the application of a vacuum for 10 minutes. 20 g of a 0.6% wt. ethyl cellulose solution was added via cannula to the *partially* dried solid while stirring at 400 rpm under argon at room temperature. After stirring for 3 minutes, the suspension was sonicated for 1 minute and then stirred overnight under argon. The ethyl cellulose coated particles were isolated by room temperature centrifugation at 10 kG, and then washed twice with DMAc (one of which is performed overnight), twice with 10% by volume formic acid in methanol (one of which is performed overnight), and twice with water (one of which is performed overnight). The solid was dried on a freeze dryer and subsequently dried under vacuum at 120 °C overnight. (. Yield = 0.9712 g.

7.3.3.7 SiO_2-MIC-23 °C

0.5 g of SiO_2 was dried under vacuum at 190 °C overnight in a 100 mL schlenk flask. At room temperature, 6 mL of neat $SiCl_4$ was added via cannula transfer under argon and stirred overnight. In a room temperature water bath, the suspension was *partially* dried under vacuum by first removing excess $SiCl_4$ by vacuum such that the solid has a dry appearance and constant pressure was reached on a digital vacuum gauge, and secondly by continuing the application of a vacuum for 10 minutes. Separately, 20 g of a solution of 0.6% wt. β-glu dissolved in 0.8% wt. LiCl in DMAc was passed through a 0.2 μm nylon syringe filter in a glovebox. The filtered β-glu solution was added via cannula to the *partially* dried solid while stirring at 400 rpm under argon

at room temperature. After stirring for 3 minutes, the suspension was sonicated for 1 minute and then stirred overnight under argon. The β-glu coated particles were isolated by room temperature centrifugation at 10 kG, and then subject to the standard washing and drying procedure. Yield = 0.4998 g.

7.3.3.8 SiO_2-control

1 g of SiO2 was dried under vacuum at 190 °C overnight in a 100 mL schlenk flask. At room temperature, 11 mL of a dichloromethane solution containing 9 % by volume $SiCl_4$ was added via cannula transfer under argon and stirred overnight. The suspension was *completely* dried under vacuum at 60 °C for four hours. Separately, 40 g of a solution of 0.6% wt. β-glu dissolved in 0.8% wt. LiCl in DMAc was passed through a 0.2 μm nylon syringe filter in a glovebox. The room temperature β-glu solution was added via cannula to the dry, chlorinated R706 while stirring at 400 rpm under argon in a room temperature water bath. After stirring for 3 minutes, the suspension was sonicated for 1 minute and then stirred overnight. The particles were isolated by room temperature centrifugation at 10 kG, and then subject to the standard washing and drying procedure. Yield = 0.8941 g.

7.3.4 Comments on Crosslinked Polymer Colloid Impurities

CPCs are common impurities in organic-inorganic composites. To assess whether it was possible to isolate CPCs under the synthesis conditions, β-glu was reacted with varying quantities of $SiCl_4$. 20 g of the 0.6 % wt. β-glu in 0.8 % wt. LiCl/DMAc solution were mixed with 10-250 μL of $SiCl_4$. The isolation of CPCs was significantly reduced by centrifuging at 10 kG compared with higher forces. The maximum quantity of isolated CPCs obtained while centrifuging at 10 kG was with 50 μL $SiCl_4$ per 20 g of β-glu solution, which yielded merely 9.4 mg. No CPCs were isolated with 10 or 25 μL $SiCl_4$ per 20 g of β-glu solution. R706 has a low internal pore volume of ~30 μL/g. Given that the partial evacuation step likely removes some of the imbibed crosslinker, the 10-25 μL of $SiCl_4$ should be a representative volume of the imbibed crosslinker. Therefore, the quantity of imbibed $SiCl_4$ is likely insufficient for isolating CPCs. Three additional observations support that the MIC materials are free of CPC impurities. First, no CPCs were observed by HAADF-STEM. Secondly, the dye uptake and selectivity in the dye adsorption experiments are consistent with the β-glu being immobilized on the surface. Only cationic dyes are adsorbed, not neutral or negatively charged dyes, which is consistent with the surface charge on the R706 core dictating uptake in the nanocoating. CPCs might be expected to adsorb negatively charged or neutral dyes. Moreover, the linear correlation between dye uptake and β-glu loading on R706-control, R706-MIC-23°C, and R706-MIC-0°C further supports that the β-glu in the sample is in the coating and not in CPC impurities. Lastly, the R706-RC-0°C and R706-RC-23°C had very low β-glu loading. Conceptually, more CPCs should form when the crosslinker is released than when it is imbibed. Therefore the significant β-glu loading in the MIC materials (up to 90 mg/g of R706, 216 mg/g of SiO_2) likely originates overwhelmingly from grafted polymer. Overall, the evidence suggests that CPC impurities should be an insignificant fraction of the β-glu in MIC coated materials.

7.3.5 TEMPO catalyzed oxidation of the β-glu coating

200 mg of the β-glu coated R706 material was mixed with TEMPO (0.005 mmol, 0.8 mg), sodium bromide (0.05 mmol, 5.1 mg), and a 10-15% aqueous solution of sodium hypochlorite (Aldrich, ~0.2 mmol, 560 μL) in 15 mL of water. The pH was adjusted to between 10.5 and 11.0 with a 0.5 M solution of sodium hydroxide. As the reaction progressed over the course of ~90 minutes, additional sodium hydroxide was added to maintain a pH between 10.5 and 11.0. Once the pH ceased to decrease, the solid was isolated by centrifugation and washed twice with water for 30 minutes and once with water overnight. The solid was dried on a freeze dryer and further dried at 120 °C overnight. Complete conversion of the primary alcohols to carboxylates is expected based on the accessibility of the nanocoating to the cationic dyes and the known treatment times for TEMPO oxidation.[3]

Yields: R706-MIC-0°C = 189.4 mg
R706-MIC-23°C = 177.1 mg
R706-RC-0°C = 168.3 mg
R706-RC-23°C = 158.6 mg
R706-monolayer = 129.8 mg

7.3.6 TGA analysis

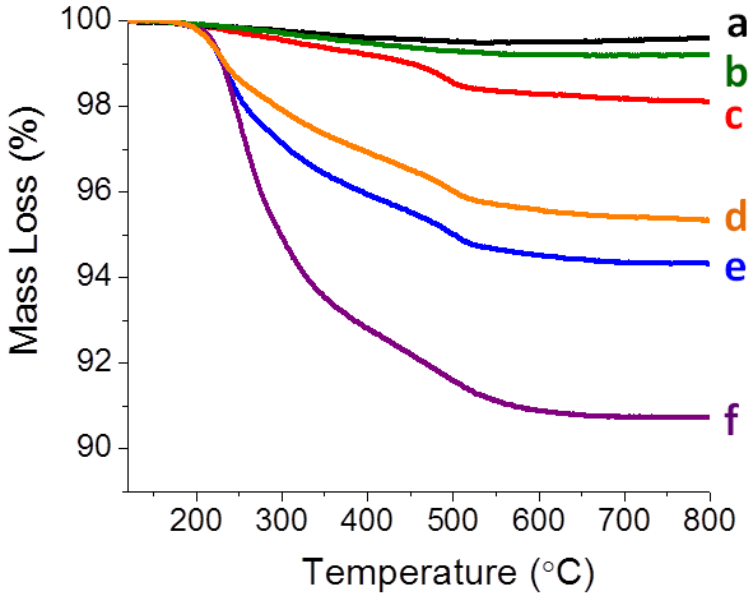

Figure 7.S.1: Thermogravimetric analysis of a) R706-control, b) R706-monolayer, c) R706-RC-23°C, d) R706-RC-0°C, e) R706-MIC-23°C, and f) R706-MIC-0°C. Surface hydroxyl groups are removed starting at roughly 200 °C. TGA-MS reveals the glucan combustion products CO and CO_2 from 250 - 750 °C (figure S2). The significant mass loss from 250 - 750 °C in e and f support that high glucan loadings are achieved with the impregnated crosslinker strategy. The combustion profile of R706-MIC-0°C matches previous studies of amorphous β-glu grafted on SiO_2 by random irreversible chemisorption. [1]

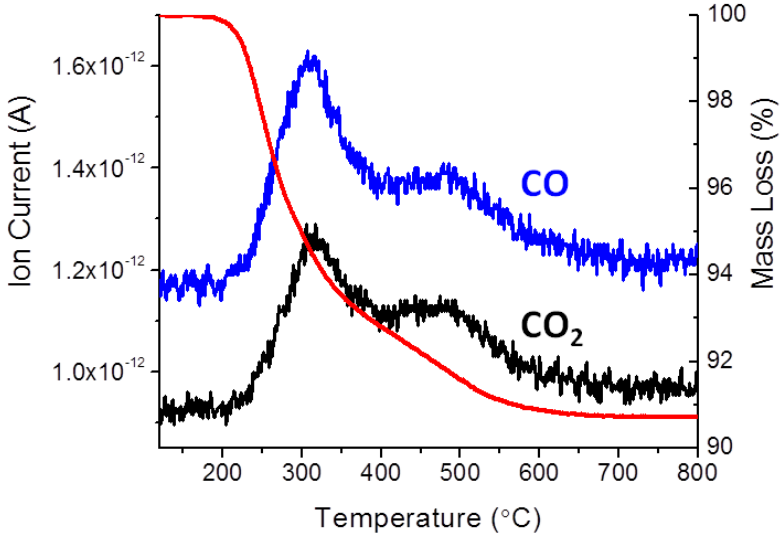

Figure 7.S.2: TGA-MS data for R706-MIC-0°C highlighting the β-glu combustion products CO and CO_2 released over the 220-750 °C temperature range.

7.3.7 NMR Spectra

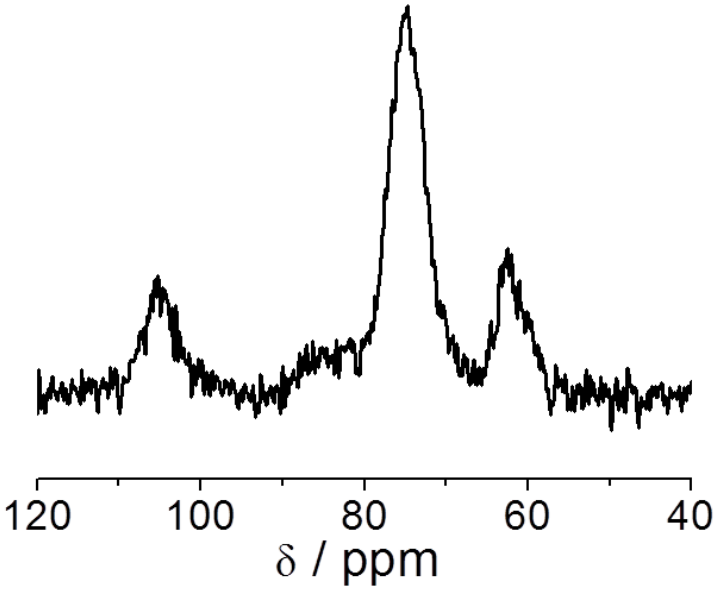

Figure 7.S.3: ^{13}C CPMAS NMR spectrum of R706-MIC-23°C.

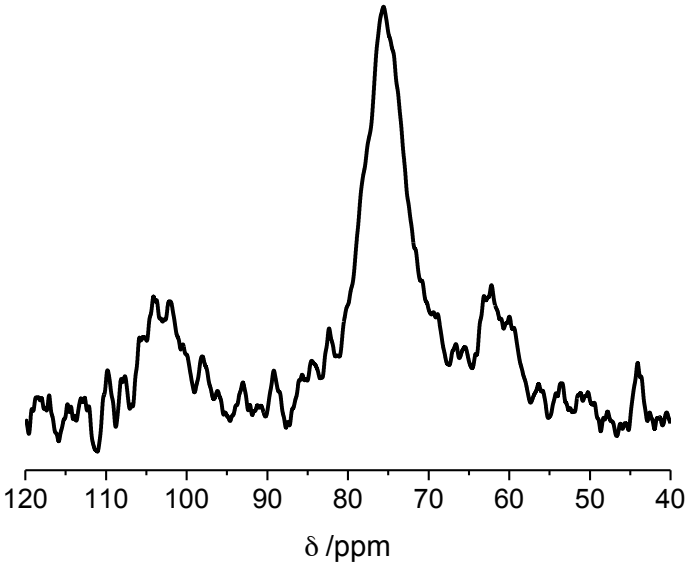

Figure 7.S.4: ^{13}C Bloch-decay NMR spectrum of R706-monolayer prepared with ^{13}C-labelled β-glu.

7.3.8 HAADF-STEM images

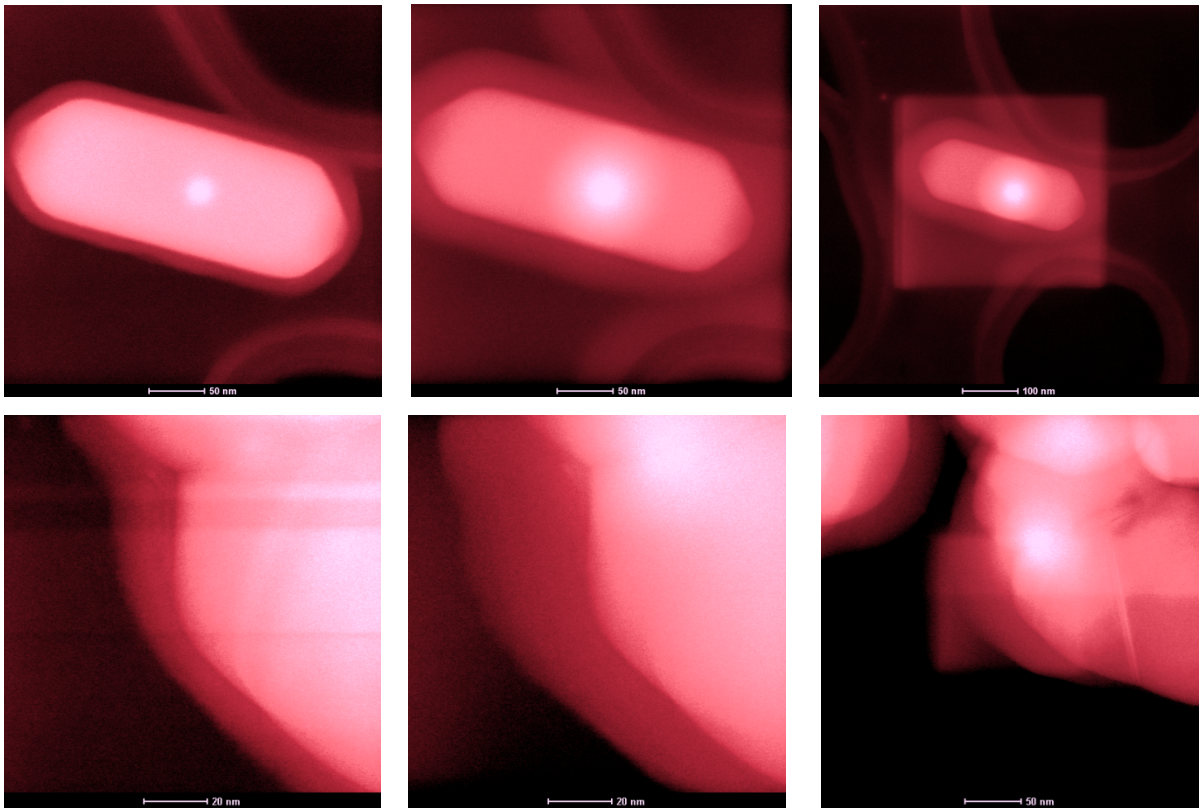

Figure 7.S.5: HAADF-STEM micrographs of R706-MIC-0°C highlighting the beam damage in the particles. After the initial exposure (left), coating expansion and the growth of regions of concentrated contrast on the particle are evident from extended exposure (middle). The micrograph with decreased magnification after extended exposure (right) reveals a box with greater contrast within the exposure window.

Batch # 1

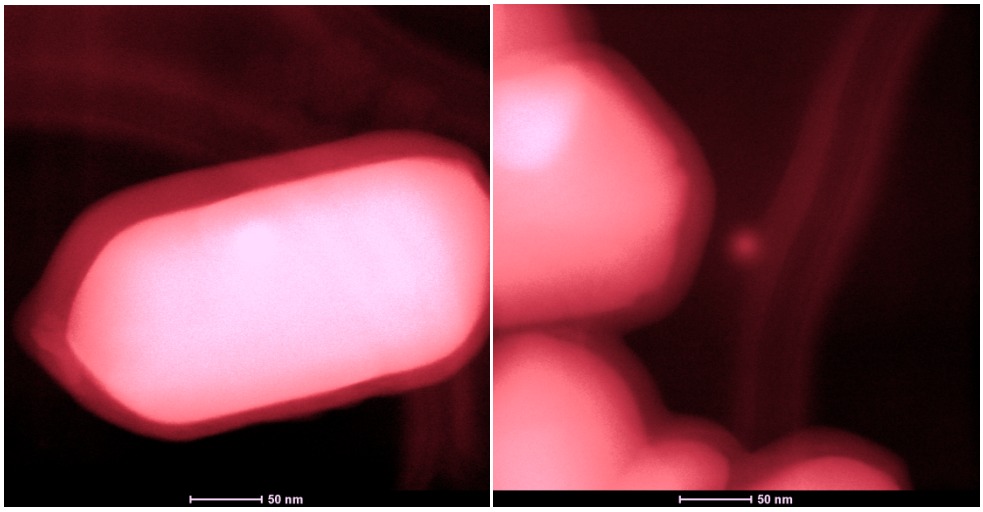

Batch # 2

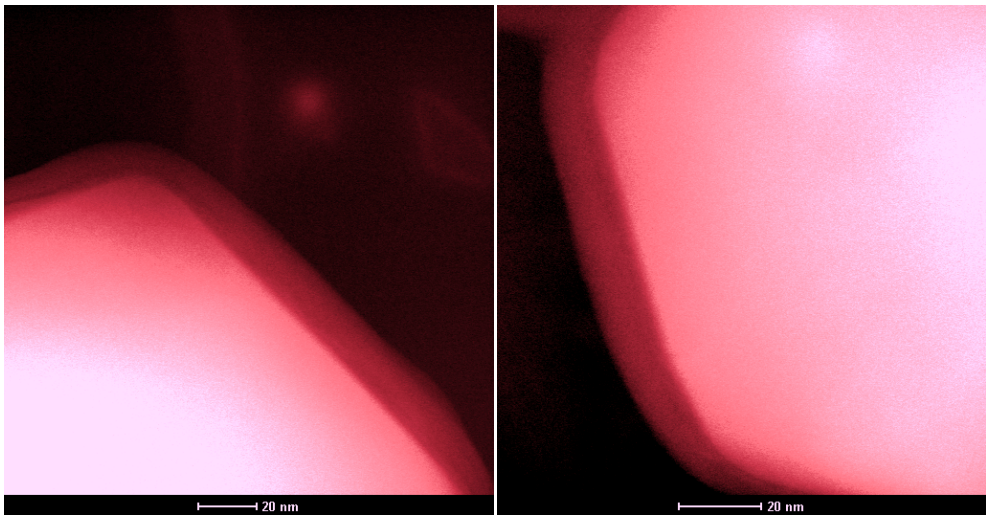

Figure 7.S.6: HAADF-STEM micrographs of R706-MIC-0°C highlighting the reproducibility of the coating from two different batches.

7.3.9 Measurement of hydrodynamic diameters

Table 7.S.1: The number-average hydrodynamic diameter of R706 materials in 1% ethylene glycol in water (by volume) and 10 mM pH 8.0 aq. tris buffer measured by DLS.

	Hydrodynamic Diameter (nm)	
Sample	**1% ethylene glycol butyl ether in water (by volume)**	**10 mM pH 8.0 aq. tris buffer**
Untreated R706	480	440
R706-control	480	480
R706-monolayer	480	370
R706-MIC-0°C	420	360
R706-MIC-23°C	410	340
R706-RC-0°C	380	320
R706-RC-23°C	350	330
R706-EC-MIC-23°C	360	380

The greater hydrodynamic diameter of untreated R706 and R706 control is attributed to intractable aggregation of these particles. The similar particle sizes of all materials is consistent with a negligible degree of particle flocculation during the nanocoating synthesis.

7.3.10 HAADF-STEM of MIC-prepared samples at 23°C

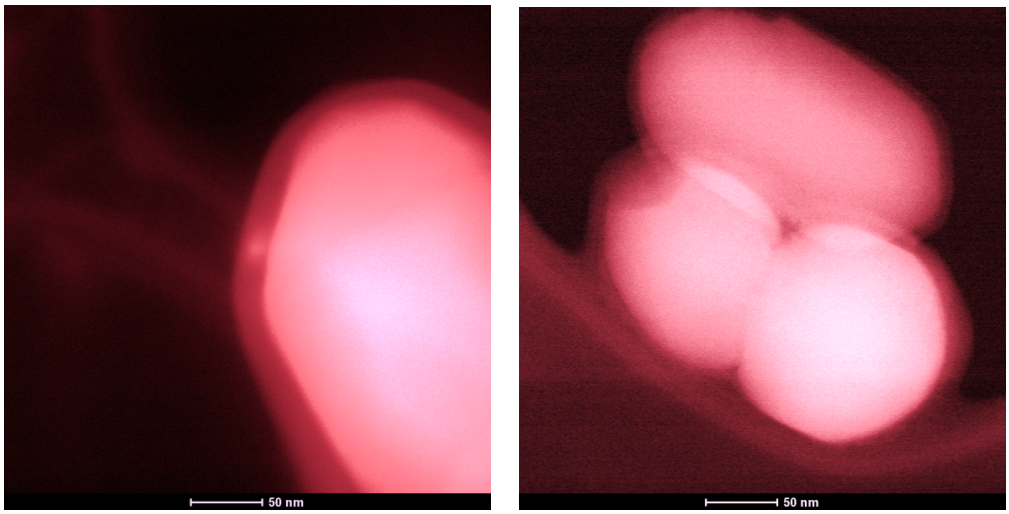

Figure 7.S.7: HAADF-STEM micrographs of R706-MIC-23°C.

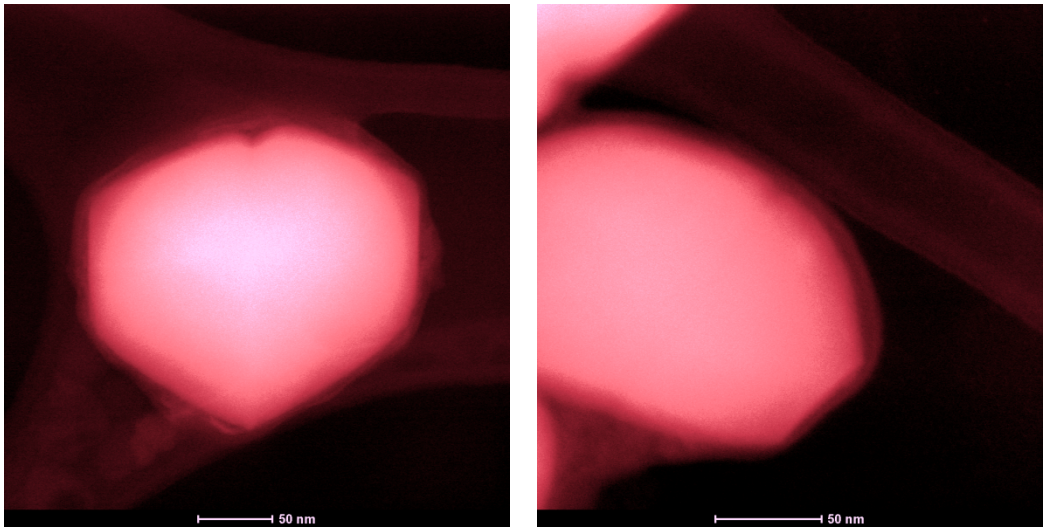

Figure 7.S.8: HAADF-STEM micrographs of R706-RC-23°C.

7.3.11 Zeta potential measurements at varying pH levels for R706-MIC-23°C

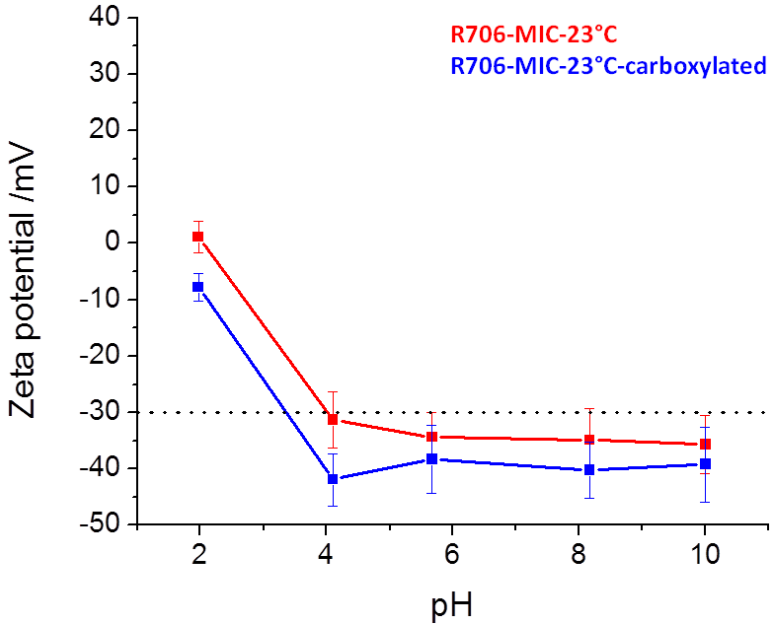

Figure 7.S.9: Plot of the zeta potential at varying pH for R706-MIC-23°C and R706-MIC-23°C-carboxylated.

7.3.12 HAADF-STEM images of R706-EC-MIC-23°C

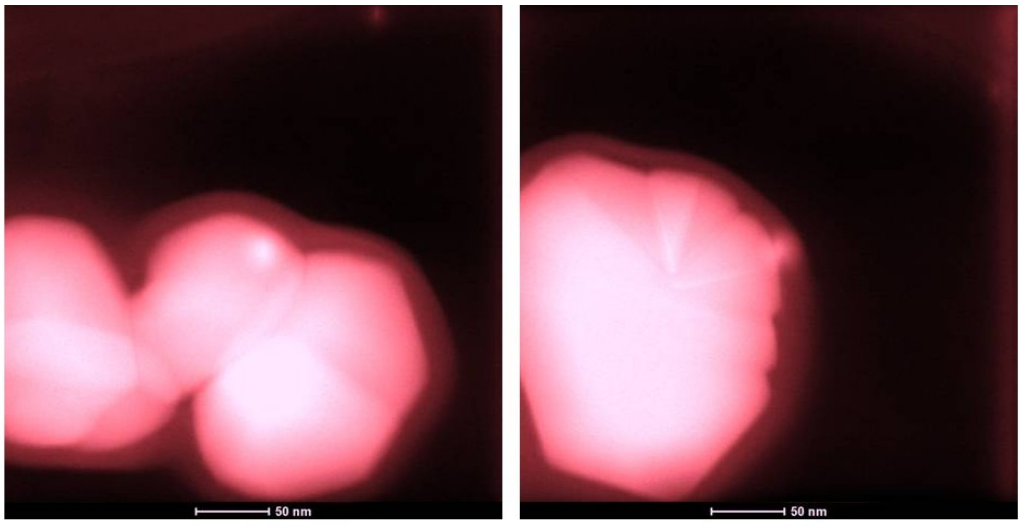

Figure 7.S.10: HAADF-STEM micrographs of R706-EC-MIC-23°C.

7.3.13 NMR spectrum of SiO_2-monolayer prepared with ^{13}C-labelled β-glu

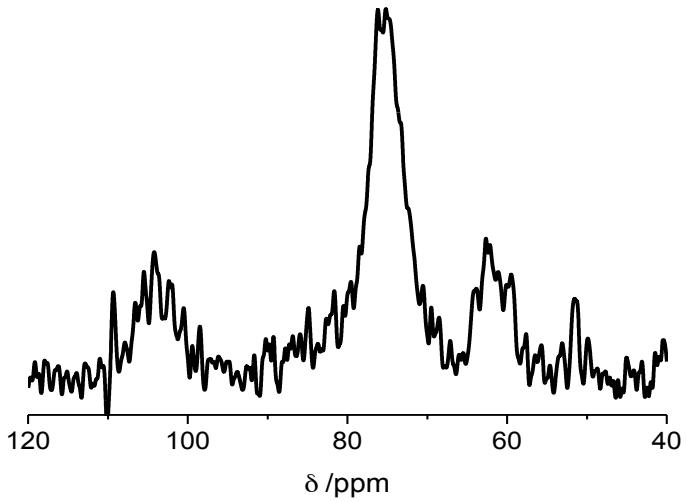

Figure 7.S.11: ^{13}C Bloch-decay NMR NMR spectrum of SiO_2-monolayer prepared with ^{13}C-labelled β-glu.

7.3.14 Estimations of β-Glu Loading and Number of Layers using TGA Data

To estimate the mass of β-glu for a monolayer coverage on R706, the theoretical maximum packing density of a polymer deposited by random irreversible chemisorption of 0.65[4] was used, where m = mass and SA = external surface area, and the area of a cellobiose monomer in cellulose is taken from the crystal structure of cellulose [5] :

$$Monolayer\ Packing\ density = 0.65$$
$$= \frac{area_{cellobiose} \times molecules_{cellobiose}}{m_{R706} \times SA}$$
$$= \frac{1.034\ nm \times 0.778\ nm \times molecules_{cellobiose}}{1\ g_{R706} \times 1.2x10^{19}\ \frac{nm^2}{g_{R706}}}$$

$$monolayer_{\frac{\beta-glu}{g_{R706}}} = 9.7x10^{18}\ molecules_{cellobiose} = 5.5\ mg_{cellobiose}$$

Following a similar treatment for the silica, the theoretical mass of a monolayer is 43.1 mg.

To estimate the β-glu mass loading using TGA, the % mass remaining at 800 °C was taken as the sum of the support, the added mass from $SiCl_4$ treatment of the surface, and the added mass from the crosslinks. All of $SiCl_4$ molecules that react with the surface or via crosslinking glucan strands are presumed to add the mass of SiO_2 to the material. The added

mass from $SiCl_4$ treatment was estimated based on the BET surface area measurements (12 and 600 m^2/g for R706 and SiO_2, respectively) and the estimated hydroxyl density on the surface of 4.5 per nm^2. The number of crosslinks was estimated based on the internal pore volume (30 and 210 μL per g of R706 and SiO_2, respectively). It was assumed that every surface hydroxyl group reacts with $SiCl_4$, that the imbibed $SiCl_4$ completely fills the internal pores after the partial evacuation step, and that each imbibed $SiCl_4$ results in a crosslink. Using these assumptions, the absolute mass of the nonvolatile material in the sample could be estimated based on the % mass measured by TGA and the amount of support used in the reaction.

The % mass removed over the range of β-glu combustion (220-750 and 250-750 °C on R706 and SiO_2, respectively) on R706 control or SiO_2-control was subtracted from the sample to give the % mass of β-glu. The absolute mass of the β-glu in the sample was estimated using the absolute mass of the nonvolatile material in the sample (see above). Using this absolute mass of β-glu, the number of multilayers was estimated by dividing by the theoretical mass of a monolayer.

7.3.15 References for section 7.3

[1] O.M. Gazit, A. Katz, *Langmuir*, 28 (2012) 431.
[2] W.C.d. Bruijn, *J. Ultrastruct. Res.*, 42 (1973) 29.
[3] A. Isogai, Y. Kato, *Cellulose*, 5 (1998) 153.
[4] J.-S. Wang, R.B. Pandey, *Phys. Rev. Lett.*, 77 (1996) 1773.
[5] A.C. Sullivan, *Cellulose*, 4 (1997) 173.

7.4 Acknowledgements

The authors would like to thank The Dow Chemical Company for financial support as well as for useful discussions in preparing this paper, particularly James Bohling and John Roper III. The authors acknowledge support of the National Center for Electron Microscopy, Lawrence Berkeley Lab, which is supported by the U.S. Department of Energy under Contract # DE-AC02-05CH11231.

7.5 References for main text

[1] J.Z.W. Wicks, F.N. Jones, S.P. Pappas, D.A. Wicks, *Organic Coatings: Science and Technology, Third Edition*, 3rd ed., John Wiley & Sons, Inc., Hoboken, NJ, 2007.
[2] I. Banerjee, R.C. Pangule, R.S. Kane, *Adv. Mater.*, 23 (2011) 690.
[3] P.T. Hammond, *Nanomedicine*, 7 (2012) 619.
[4] T.F. Tadros, *Dispersion of Powders in Liquids and Stabilization of Suspensions*, Wiley-VCH Verlag GmbH & Co., Weinheim, 2012.
[5] D. Klemm, B. Heublein, H.P. Fink, A. Bohn, *Angew. Chem. Int. Ed.*, 44 (2005) 3358.
[6] R.J. Moon, A. Martini, J. Nairn, J. Simonsen, J. Youngblood, *Chem. Soc. Rev.*, 40 (2011) 3941.
[7] O.M. Gazit, A. Charmot, A. Katz, *Chem. Commun.*, 47 (2011) 376.
[8] O.M. Gazit, A. Katz, *Langmuir*, 28 (2012) 431.
[9] O.M. Gazit, A. Katz, *J. Am. Chem. Soc.*, 135 (2013) 4398.
[10] G. Rydzek, P. Schaaf, J.-C. Voegel, L. Jierry, F. Boulmedais, *Soft Matter*, 8 (2012) 9738.

[11] S. Farrokhpay, *Adv. Colloid Interface. Sci.*, 151 (2009) 24.
[12] A. Katz, P.D. Costa, A.C.P. Lam, J.M. Notestein, *Chem. Mater.*, 14 (2002) 3364.
[13] J.F. Klebe, H.L. Finkbeiner, *J. Polym. Sci. A1*, 7 (1969) 1947.
[14] T. Roder, B. Morgenstern, N. Schelosky, O. Glatter, *Polymer*, 42 (2001) 6765.
[15] W.C.d. Bruijn, *J. Ultrastruct. Res.*, 42 (1973) 29.
[16] W.C.d. Bruijn, P.D. Breejen, *Histochem. J.*, 8 (1976) 121.
[17] R.F. Egerton, P. Li, M. Malac, *Micron*, (2004) 399.
[18] G.H. Michler, *Electron Microscopy of Polymers*, Springer Berlin Heidelberg, Berlin Heidelberg, 2008.
[19] A. Isogai, Y. Kato, *Cellulose*, 5 (1998) 153.
[20] S.G.J. Heijman, H.N. Stein, *Langmuir*, 11 (1995) 422.
[21] H.J. Taunton, C. Toprakcioglu, L.J. Fetters, J. Klein, *Macromolecules*, 23 (1990) 571.
[22] K. Bridger, D. Fairhurst, B. Vincent, *J. Colloid Interf. Sci.,* 68 (1979) 190.
[23] K.K. Das, P. Somasundaran, *Colloids Surf. A*, 223 (2003) 17.
[24] H. Ejima, J.J. Richardson, K. Liang, J.P. Best, M.P. van Koeverden, G.K. Such, J. Cui, F. Caruso, *Science*, 341 (2013) 154.
[25] E.H.H. Wong, S.N. Guntari, A. Blencowe, M.P. van Koeverden, F. Caruso, G.G. Qiao, *ACS Macro Lett.*, 1 (2012) 1020.
[26] D. Mertz, C. J. Ochs, Z. Zhu, L. Lee, S. N. Guntari, G. K. Such, T. K. Goh, L. A. Connal, A. Blencowe, G. G. Qiao, F. Caruso, *Chem. Comm.*, 47 (2011) 12601.
[27] G. Rydzek, A. Parat, P. Polavarapu, C. Baehr, J.-C. Voegel, J. Hemmerlé, B. Senger, B. Frisch, P. Schaaf, L. Jierry, F. Boulmedais, *Soft Matter*, 8 (2012) 446.
[28] G. Rydzek, L. Jierry, A. Parat, J.S. Thomann, J.C. Voegel, B. Senger, J. Hemmerle, A. Ponche, B. Frisch, P. Schaaf, F. Boulmedais, *Angew. Chem. Int. Ed.*, 50 (2011) 4374.
[29] Y. Jiao, Y. Sun, B. Chang, D. Lu, W. Yang, *Chem. Eur. J.*, 2013, *DOI: 10.1002/chem.201301060*.
[30] Q. Gao, Y. Xu, D. Wu, Y. Sun, X. Li, *J. Phys. Chem. C*, 113 (2009) 12753.

CHAPTER 8:

Conclusions and future outlook

The synthesis and characterization of materials at the nanoscale in order to control surface properties of materials is a major goal in the field of materials synthesis and design in the recent decades and will continue to be in the future. This dissertation explored the synthesis and characterization of many new materials from glucan coated metal oxide particles to delaminated zeolites to calixarene-bound gold nanoparticles that aim to control the surface properties of materials in order to display unprecedented control of their properties.

The main thrust of this dissertation was in the synthesis and characterization of organic ligand-bound, specifically calixarene-bound, gold clusters. Catalytic activity arising from minority fraction of sites, first postulated by Taylor, has been demonstrated in practice in many catalytic systems through the decades since then. Most of these examples show that coordinatively unsaturated sites are responsible for the majority of the catalytic activity. Chapter 2 of this dissertation gives what we believe to be the first demonstration of the quantification of the relative activities of corner versus edge sites in a supported nanoparticle system. Using a supported gold nanoparticle system, where the particles have an average size of approximately 3.5 nm, sites on the gold nanoparticle surface were titrated with strongly binding thiol or phosphine ligands at sub-monolayer coverages to demonstrate that the corner sites comprising approximately 1% of the total gold surface were the most active sites by a factor of 17 over the edge sites, and the terrace sites comprised 70% of the surface and 0% of the total activity of the catalyst. While this method was used in the model reaction of resazurin to resorufin, other reactions could be investigated using this titration method to observe the catalytic contributions of different sites in those systems too. A limitation of this method is that organic ligands were used which would not be stable at elevated temperatures, however titration procedures using inorganic species could also be developed for reactions at high temperatures. Another application of this method could be in systems where selectivity is important and the undercoordinated sites are very active, but not selective. One could titrate the undercoordinated sites with a strongly binding ligand and observe that the less active, but more selective terrace sites are available to perform the reaction. An example of this approach using atomic-layer deposition of Al_2O_3 to block the coordinatively unsaturated sites on palladium affecting selectivity has already been successfully demonstrated. [1]

Another example from Chapter 3 in this dissertation uses 2-napthalenethiol to block sites on calixarene phosphine- or calixarene thiol-bound gold nanoparticles of a similar size (4 nm) as the supported system in Chapter 2. It was observed in the reduction of 4-nitrophenol that when the sites on the gold nanoparticle surface were blocked with the strongly binding thiol, that the reaction rate did not decrease significantly. An induction time for this reaction was observed and increased with the amount of thiol bound to the gold nanoparticle surface. Presumably, the leaching rate is controlled by the amount of the thiol present on the gold surface in this system.

Knowing that in many systems coordinatively unsaturated sites are responsible for a large fraction of the catalytic activity of a cluster/nanoparticle, one goal was to create very small particles that by virtue of their small size would have a large fraction of undercoordinated sites on the surface. Our hypothesis was that by using an organic ligand such as a bulky calixarene that is commensurate with the size of the metal cluster, that there would be pockets of accessible surface area on the metal cluster where substrates could bind to the metal particle surface due to a packing problem. An additional goal was to tune the electronic state of the cluster through electron-donating groups of the calixarene ligands that were bound to the surface of the metal cluster. Our approach was demonstrated in Chapter 4 using calixarene phosphine ligands with gold clusters. Depending on the identity of the groups on the lower-rim of the calixarene,

different average particle sizes ranging from 0.9 nm to 1.8 nm in average size as well as different degrees of polydispersity were observed with different calixarene phosphine ligands. The smallest particles synthesized were Au_{11}-type particles that demonstrated a remarkable degree of accessibility displaying approximately 3 binding sites per Au_{11} cluster. The larger clusters demonstrated less accessibility as a function of increasing particle size, as the calixarene molecules were able to pack more efficiently on the gold surface with larger particles. XPS results revealed very electron-rich gold in the Au_{11} clusters, which may be useful in systems where it is believed that electron-rich gold promotes catalysis, such as with oxidation reactions. [2,3] Chapter 5 expands the synthetic portfolio of the calixarene-bound gold clusters to include N-heterocyclic carbene clusters. These particles ranged in average size from 1.2 to 1.6 nm. Using the smallest of the carbene bound gold clusters, similar accessibility was demonstrated as with the 1.1 nm calixarene phosphine bound gold cluster indicating that a mechanical model of accessibility was in place that did not depend on the identity of the functional groups that where bound to the gold cluster, whether it be phosphine or carbene. Investigation of catalytic applications of these particles will prove to be an interesting endeavor, particularly with oxidation reactions that have been predicted to prefer an electron-rich gold surface.

In the synthesis of delaminated zeolites, a new procedure was developed to delaminate zeolites using conditions that were much milder than had been reported in the literature using a new fluoride/chloride method at slightly basic pH to synthesize UCB-1, while the previous literature used a high pH environment for delamination. A wide variety of characterization techniques including nitrogen physisorption, x-ray diffraction and high resolution TEM were used to provide evidence for delamination of the parent MCM-22 to the delaminated UCB-1 material. The delamination of the zeolite structure allows for larger reactants to access the inside of the pore structure as well as creating more external surface sites/area. Since publication of this paper in 2011, this method has been successfully utilized in delaminating additional zeolites. [4,5] Current and future directions for this work include comparative studies of delaminated versus non-delaminated zeolites in catalytic applications as well as immobilizing metal clusters onto these materials for additional catalytic applications.

The grafting of glucans to the surface of metal oxide particles using a novel one-step method Multilayers through Imbibed Crosslinker (MIC) approach created a new material from readily available raw materials such as metal oxide particles and biomass derived polymers like poly β-glucans. There are many opportunities for applications of these materials including the described application of stabilizing dispersions of particles in paint pigments as well as using these particles where biocompatibility is necessary such as in drug delivery. The facile tunability of these coatings through synthesis will lead to many more applications.

[1] J. Lu, B. Fu, M.C. Kung, G. Xiao, J. W. Elam, H.H. Kung, P. Stair. *Science* 335 (2012) 1205.

[2] M. Okumura, Y. Kitagawa, M. Haruta, K. Yamaguchi, *Chem. Phys. Lett.*, 346 (2001), 163.

[3] M. Okumura, M. Haruta, Y. Kitagawa, K. Yamaguchi, *Gold Bulletin*, 40 (2007) 40.

[4] I. Ogino, E.A. Eilertsen, S.-J. Hwang, T. Rea, D. Xie, X. Ouyang, S.I. Zones, A. Katz, *Chem. Mater.*, 25 (2013) 1502.

[5] E.A. Eilertsen, I. Ogino, S.-J. Hwang, T. Rea, S. Yeh, S.I. Zones, A. Katz, *Chem. Mater.*, 23 (2011) 5404.